UNIVERSITAT POLITÈCNICA DE CATALUNYA BARCELONATECH

Corrosion studies on Cu-based alloys

by
Chenyang Xie

PhD program in Computational and Applied Physics

Corrosion studies on Cu-based alloys

Doctoral thesis by:

Chenyang Xie

Thesis advisor:

Daniel Crespo and Frank Renner

Department of Physics, INTE & Barcelona Multiscale Res. Center, Universitat Politècnica de Catalunya, Barcelona, Catalunya and Institute for Materials Research (IMO) & IMOMEC,Hasselt University, Diepenbeek, Belgium

Barcelona, November 2020

Acknowledgements

This thesis is a story about corrosion and inhibition of Cu-based alloy. Moreover, all this story begins with a boy deciding to go abroad to study for a doctoral degree. So I will first acknowledge my family, including my girlfriend, to support my idea of going to Spain. As the Chinese always have a strong family connection, this is not an easy thing for them. The encouragements and considerations from them conduct a significant amount of power for the steps along these years. Besides, I must conduct my sincere thank to my master supervisor Prof. Wu Chunjing, who teach me the primary research skill and a broader vision for the future. The economic support from China Scholarship Council (CSC) makes the study possible and colorful life in Barcelona; I'm very thankful for this support.

My supervisor and friend, Daniel Crespo, from Universitat Politècnica de Catalunya, offer me so much help in research and life in Europe. He always introduces me to scientific research from the strategy to details; the patience and willingness give me a deep impression. Even though he always forgets what he had taught me, I still remember the sentences, which will lead me to better performance. Furthermore, he helps me understand the culture and ideas here and teaches me how to have a good life. This relationship will be a treasure for my whole life, and I am so grateful for his help. Frank Renner, another supervisor of me in University Hasselt, also conduct significant help in both research and life there. Thank you so much, and I still remember the journey with his bike on bicycle highway from Belgium to Lussenberg. Besides my advisors, I would like to thank Prof. Eloi, Prof. Pere, and Prof. Trinitat in the GCM group, their kindly help enlighten my research life here. Thank for my fellow labmates and technicians in UPC and Uhasselt for the stimulating discussions, for the sleepless nights we were working together before deadlines, and for all the fun we have had in the last four years.

For the thesis, I especially appreciate the assistance of Prof. Ingrid and Prof. Tone from Jožef Stefan Institute. Their guidance helped me in all the time of research and writing of this thesis. Besides my advisor, I would like to thank the rest of my thesis committee: Dr. Peyman and Dr. Patricia, and Prof. Rojas, for their insightful comments and encouragement, but also for the hard question which incented me to widen my research from various perspectives.

Finally, I would like to thank all the people who helped me in these years. The four years of experience give me an open and inclusive mind on research and life and introduce me to a better understanding of the world. I wish a better future for all species on the earth, especially in this challenging moment of the pandemic of Covid-19.

致谢

异国他乡，游子求学，中文致谢献给我的家人、同学和朋友。

首先，感谢给予我无限力量的家人们。

在欧洲的这几年，我对东西方家庭观念的认知已在潜移默化中发生改变。印象中独立的西方家庭，实际上 子女成年后与父母的联系，甚至比中国还要紧密，家人间相互扶持的纽带，能维系几十年乃至更久。

三十而立，这四年我与家人相聚团圆的次数屈指无数，若没有来自他们的支持，我便失去了安心学习的环 境，就无法顺利地完成博士学业，每每想到这，内心不胜感激。

古语云：树欲静而风不止，子欲养而亲不待。衰老与死亡是每个人都无法避免的，如何看待这些则是一门学问。年华老去，我的姥姥姥爷已年过八旬，常从父母口中听闻他们犯糊涂或犯病入院的消息。我对此已学会泰然处之，虽然不能给予他们无微不至的陪伴，但搭乘技术的便车，实时网络交流也极大地满足 需求，获得慰藉。每月 1 至 2 次的视频聊天，令彼此间的亲昵不曾远去。

而我最大的力量支持，则源于父母。从本科开始，习惯无微不至照顾我生活起居的他们，也渐渐适应了 我的独立人格，开始重新审视自己的定位。我们之间最大的幸福莫过于互相理解与包容，以及逐渐建立起 对当今社会的深度认知与共情。这使得那条由年代认知产生的鸿沟不断弥合，这也是一个学会与自己和 解的过程。

不仅学业上他们没有让我有后顾之忧，生活中我的每一次决定，也得到了他们充分支持。比如骑自行车去 青藏高原，去中国东北开拓视野，磨砺自我，独立人格与社会历练密不可分，感谢他们让我的兴趣得以开 展和延续，赋予了我一部分精神食粮。

另外，我的大舅，二舅二舅妈，小姨姨夫，他们也都是我坚实的后盾。如果哪一天我需要什么，相信他们 都会随时站出来帮助我。而表弟表妹们的生活也都步入正轨，他们的进步与成长让我倍感欣慰，希望在未 来的岁月里，我们能继续互相帮助与理解。

除家人之外，我国内的同学和朋友也为我提供了很多无私的帮助，作为我的后援团，每当有一些手续或者 疑难，他们总能快速地帮我解决。每次回国，都会受到他们热情地邀请，时间和距离没有疏远彼此，没有 淡化曾经的感情，也没有改变纯真的友谊。希望此生的喜怒哀乐能够与这些好友们共同分享。

人生何处不相逢，在西班牙求学认识的同窗、朋友也给予了我莫大的帮助，让远在异国的我身边充满了温 暖和阳光，让一些艰难的时刻能平稳度过。而推心置腹的交流，也让那些压抑在内心的想法得到纾解。

说到这，我还想提及一个可爱的人——我的女朋友。我们相识于 2015 年的一场奇妙的骑行之旅，始于缘分 ，陷于才华，忠于三观，从聚少离多的异地恋发展成相隔万里的异国恋，青涩的感情早已凝练成如今的深 沉。这种深沉不是表达的深沉，而是发自内心的相互理解、支持和灵魂的共鸣。而且她养的橘猫阿黄很可 爱，云吸猫让我紧张的科研读博生涯多了一丝丝惬意。感谢彭珊和阿黄，回国之后我会带着小鱼干去看望 阿黄的。

感谢这一路上给我无数帮助的人们，是你们让我获得更广阔多元的视野，去审视自己的人生，反思过往， 重新定义生命的价值与意义。漫漫人生路，我是何其幸运能得到你们的支持。我爱你们，正如你们对我的 爱，人生的辽阔与美好，从与你们相遇开始。

最后，我要把诚挚的感谢献给祖国，在海外的这些岁月里，广泛的书籍阅读和信息摄入，关于中国世界历 史、社会变迁知识的学习，令我对人类社会的认知更加的宽泛深刻。我深知自己不是没有根的流浪汉，我 是一名中国人，并因此而骄傲，希望未来我能为这个古老而充满生机的国家贡献一己之力！

Table of Content

List of Figures

alloys with or without addition of mercapto-benzimidazole derivatives in aqueous 3 wt. % NaCl solution after 1 h at the open circuit conditions.

Figure 6.9. Electrochemical impedance spectra of $Cu_{40}Zr_{60}$ alloy in the form of Bode impedance plot, phase angle plot and Nyquist plot recorded for a), c), e) crystalline and b), d), f) amorphous alloys with or without addition of hydroxy-benzimidazole derivatives in aqueous 3 wt. % NaCl solution after 1 h at the open circuit conditions.

Figure 6.10 Polar graphs of impedance modulus at 0.01 Hz, measured after 1 h immersion, for Zr (top) and Cu (bottom) metals and crystalline (left) and amorphous (right) Cu_xZr_{100-x} alloys in 3 wt.% NaCl aqueous solution (blank) and in the presence of different organic compounds added at 1 mM concentration. Note the logarithmic scale.

Figure 6.11. Potentiodynamic polarization curves of crystalline (left) and amorphous (right) $Cu_{50}Zr_{50}$ in 3 wt.% NaCl aqueous solution with and without 1 mM of different organic compounds: (top) imidazole derivatives, (middle) mercapto-benzimidazole derivatives, and (bottom) hydroxy-benzimidazole derivatives. Quantitative electrochemical parameters are presented in **Table A3.5** and **Table A3.6**.

Figure 6.12. Electrochemical impedance spectra of $Cu_{50}Zr_{50}$ alloy in the form of Bode impedance plot, phase angle plot and Nyquist plot recorded for a), c), e) crystalline and b), d), f) amorphous alloys with or without addition of imidazole derivatives in aqueous 3 wt. % NaCl solution after 1 h at the open circuit conditions.

Figure 6.13. Electrochemical impedance spectra of $Cu_{50}Zr_{50}$ alloy in the form of Bode impedance plot, phase angle plot and Nyquist plot recorded for a), c), e) crystalline and b), d), f) amorphous alloys with or without addition of mercapto-benzimidazole derivatives in aqueous 3 wt. % NaCl solution after 1 h at the open circuit conditions.

Figure 6.14. Electrochemical impedance spectra of $Cu_{50}Zr_{50}$ alloy in the form of Bode impedance plot, phase angle plot and Nyquist plot recorded for a), c), e) crystalline and b), d), f) amorphous alloys with or without addition of hydroxy-benzimidazole derivatives in aqueous 3 wt. % NaCl solution after 1 h at the open circuit conditions.

Figure 6.15. Potentiodynamic polarization curves of crystalline (left) and amorphous (right) $Cu_{64}Zr_{36}$ in 3 wt.% NaCl aqueous solution with or without added 1 mM concentration of different organic compounds: (top) imidazole derivatives, (middle) mercapto-benzimidazole derivatives, and (bottom) hydroxy-benzimidazole derivatives. Quantitative electrochemical parameters are presented in **Table A3.11**Table A3.12.

Figure 6.18 Electrochemical impedance spectra of $Cu_{64}Zr_{36}$ alloy in the form of Bode impedance plot, phase angle plot and Nyquist plot recorded for a), c), e) crystalline and b), d), f) amorphous alloys with or without addition of imidazole derivatives in aqueous 3 wt. % NaCl solution after 1 h at the open circuit conditions.

Figure 6.19 Electrochemical impedance spectra of $Cu_{64}Zr_{36}$ alloy in the form of Bode impedance plot, phase angle plot and Nyquist plot recorded for a), c), e) crystalline and b), d), f) amorphous alloys with or without addition of mercapto-benzimidazole derivatives in aqueous 3 wt.% NaCl solution after 1 h at the open circuit conditions.

Figure 6.20 Electrochemical impedance spectra of $Cu_{64}Zr_{36}$ alloy in the form of Bode impedance plot, phase angle plot and Nyquist plot recorded for a), c), e) crystalline and b), d), f) amorphous alloys with or without addition of hydroxy-benzimidazole derivatives in aqueous 3 wt.% NaCl solution after 1 h at the open circuit conditions.

Figure A1.14 Long-term EIS impedance and phase diagram of pure Cu in NaCl, in period of 120h with SH-BimH

Figure A1.15 Long-term EIS impedance and phase diagram of pure Cu in NaCl, in period of 120h with Me-S-BimH

Figure A1.16 Long-term EIS impedance and phase diagram of pure Cu in NaCl, in period of 120h with SH-BimH-5OMe

Figure A1.17 Long-term EIS impedance and phase diagram of pure Cu in NaCl, in period of 120h with SH-ImiH-4Ph

Figure A1.18 Long-term EIS impedance and phase diagram of pure Cu in NaCl, in period of 120h without SH-BimH-5NH_2

Figure A1.19 Long-term EIS impedance and phase diagram of pure Cu in NaCl, in period of 120h with SH-ImiMe

Figure A1.20 Long-term EIS impedance and phase diagram of pure Cu in NaCl, in period of 120h with OH-BimH

Figure A1.21 Long-term EIS impedance and phase diagram of pure Cu in NaCl, in period of 120h with OH-Me-BimH

Figure A1.22 Normalized survey XPS spectrums for the surface of pure Cu after polishing and pickling, and after immersion in 3wt.% NaCl with and without added of SH-BimH, Me-S-BimH, SH-BimH-5OMe and SH-ImiH-4Ph. Dash lines represent the position of peaks of reference compounds. Upper: Immersion for 24h. Down: Immersion for 120h.

Figure A1.23 EDX elemental map analysis of the bare pure Cu sample under 10000x magnification

Figure A1.24 EDX elemental map analysis of pure Cu immersed in 3 wt.% NaCl solution for 60 day

Figure A1.25 Pure Cu immersed in 3 wt.% NaCl with added 1mM ImiH solution for 60 days (a) surface under 320x magnification with all typical features (b) surface under 1000x magnification (c) surface under 5000x magnification (d) surface features in black part (e) 3D topography under 320x magnification by SEM

Figure A1.26 EDS elemental map analysis of Pure Cu immersed in 3 wt.% NaCl solution with added 1mM ImiH for 60 days

Figure A1.27 EDS elemental point analysis spectrum of Pure Cu immersed in 3 wt.% NaCl solution with added 1mM ImiH for 60 days (a) spectrum of point a, flat homogenous surface (b) (c) spectrum of point b and c, black part on the surface.

Figure A1.28 EDS elemental map analysis of Pure Cu immersed in 3 wt.% NaCl solution with added 1mM SH-BimH for 60 days

Figure A1.29 EDS elemental map analysis of pure Cu immersed in 3 wt.% NaCl solution with added 1mM Me-S-BimH for 60 days

Figure A1.30 EDS elemental map analysis of pure Cu immersed in 3 wt.% NaCl solution with added 1mM SH-BimH-5OMe for 60 days

Figure A1.31 EDS elemental map analysis of pure Cu immersed in 3 wt.% NaCl solution with added 1mM SH-ImiH-4Ph for 60 days

Figure A1.32 Pure Cu immersed in 3 wt.% NaCl with added 1mM SH-BimH-5NH_2 solution for 60 days (a) surface under 320x magnification (b) surface under 320x magnification (c) surface of black part in figure (a) (d) surface of black part in figure (b) (e) 3D topography under 320x magnification by SEM

Figure A1.33 EDS elemental map analysis of pure Cu immersed in 3 wt.% NaCl solution with added 1mM SH-BimH-5NH_2 for 60 days

Figure A1.34 EDS elemental point analysis spectrum of pure Cu immersed in 3 wt.% NaCl solution with added 1mM SH-BimH-5NH_2 for 60 days (a) spectrum of point a, white surface (b) (c) spectrum of point b and c, black film on the surface.

Figure A1.35 Pure Cu immersed in 3 wt.% NaCl with added 1mM SH-ImiMe solution for 60 days (a) surface under 320x magnification with all typical features (b) surface under 320x magnification (c) surface under 1000x magnification (d) surface 2500x magnification (e) 3D topography under 320x magnification by SEM

Figure A1.36 EDS elemental map analysis of pure Cu immersed in 3 wt.% NaCl solution with added 1mM SH-ImiMe for 60 days

Figure A1.37 EDS elemental point analysis spectrum of pure Cu immersed in 3 wt.% NaCl solution with added 1mM SH-ImiMe for 60 days (a) (b) spectrum of point a and b, dendritic structure (c) spectrum of point c, white bulk.

Figure A1.38 Pure Cu immersed in 3 wt.% NaCl with added 1mM OH-BimH solution for 60 days (a) surface under 320x magnification with all typical features (b) surface under 10000x magnification (c) surface with different features under 320x magnification (d) local attacks on the surface (e) 3D topography under 320x magnification by SEM

Figure A1.39 EDS elemental map analysis of pure Cu immersed in 3 wt.% NaCl solution with added 1mM OH-BimH for 60 days

Figure A1.40 EDS elemental point analysis spectrum of pure Cu immersed in 3 wt.% NaCl solution with added 1mM OH-BimH for 60 days (a) spectrum of point a, porous surface (b) spectrum of point b, cubic particles on the surface (c) spectrum of point c, black part of the surface.

Figure A1.41 EDS elemental map analysis of pure Cu immersed in 3 wt.% NaCl solution with added 1mM OH-Me-BimH for 60 days

Figure A1.42 All linear polarization resistance curves of pure Zn with and without inhibitors in 3 wt.% NaCl solution after immersion for 1 h

Figure A1.43 Long-term linear polarization curves of pure Zn under the 120h period of testing of the alloy in the presence of the inhibitor in the 3 wt.% NaCl aqueous solution without inhibitors

Figure A1.44 Long-term linear polarization curves of pure Zn under the 120h period of testing of the alloy in the presence of the inhibitor in the 3 wt.% NaCl aqueous solution with ImiH

Figure A1.45 Long-term linear polarization curves of pure Zn under the 120h period of testing of the alloy in the presence of the inhibitor in the 3 wt.% NaCl aqueous solution with SH-BimH

Figure A1.46 Long-term linear polarization curves of pure Zn under the 120h period of testing of the alloy in the presence of the inhibitor in the 3 wt.% NaCl aqueous solution with Me-S-BimH

Figure A1.47 Long-term linear polarization curves of pure Zn under the 120h period of testing of the alloy in the presence of the inhibitor in the 3 wt.% NaCl aqueous solution with SH-BimH-5OMe

Figure A1.48 Long-term linear polarization curves of pure Zn under the 120h period of testing of the alloy in the presence of the inhibitor in the 3 wt.% NaCl aqueous solution with SH-ImiH-4Ph

Figure A1.49 Long-term linear polarization curves of pure Zn under the 120h period of testing of the alloy in the presence of the inhibitor in the 3 wt.% NaCl aqueous solution with SH-BimH-$5NH_2$

Figure A1.50 Long-term linear polarization curves of pure Zn under the 120h period of testing of the alloy in the presence of the inhibitor in the 3 wt.% NaCl aqueous solution with SH-ImiMe

Figure A1.51 Long-term EIS impedance and phase diagram of pure Zn in NaCl, in period of 120h without inhibitor

Figure A1.52 Long-term EIS impedance and phase diagram of pure Zn in NaCl, in period of 120h with ImiH

Figure A1.53 Long-term EIS impedance and phase diagram of pure Zn in NaCl, in period of 120h with SH-BimH

Figure A1.54 Long-term EIS impedance and phase diagram of pure Zn in NaCl, in period of 120h with Me-S-BimH

Figure A1.55 Long-term EIS impedance and phase diagram of pure Zn in NaCl, in period of 120h with SH-BimH-5OMe

Figure A1.56 Long-term EIS impedance and phase diagram of pure Zn in NaCl, in period of 120h with SH-ImiH-4Ph

Figure A1.57 Long-term EIS impedance and phase diagram of pure Zn in NaCl, in period of 120h without SH-BimH-$5NH_2$

Figure A1.58 Long-term EIS impedance and phase diagram of pure Zn in NaCl, in period of 120h with SH-ImiMe

Figure A1.59 EDX elemental map analysis of the bare sample under 1000x magnification

Figure A1.60 EDX elemental map analysis of Pure Zn immersed in 3 wt.% NaCl solution for 12 days

Figure A1.61 Pure Zn immersed in 3 wt.% NaCl with added 1mM ImiH solution for 12 days (a) surface under 320x magnification with all typical features (b) surface under 1000x magnification (c) cracks on the surface (d) hemisphere (e) 3D topography under 320x magnification by SEM

Figure A1.62 EDS elemental map analysis of Pure Zn immersed in 3 wt.% NaCl solution with added 1mM ImiH for 12 days

Figure A1.63 EDS elemental point analysis spectrum of Pure Zn immersed in 3 wt.% NaCl solution with added 1mM ImiH for 12 days (a) and (c) spectrum of point a and c, hemisphere on the surface (b) spectrum of point b, boundary between hemisphere

Figure A1.64 Pure Zn immersed in 3 wt.% NaCl with added 1mM SH-BimH solution for 12 days (a) surface under 320x magnification with all typical features (b) surface under 320x magnification (c) surface under 1000x magnification (d) cracks and holes on the surface (e) 3D topography under 1000x magnification by SEM

Figure A1.65 EDS elemental map analysis of Pure Zn immersed in 3 wt.% NaCl solution with added 1mM SH-BimH for 12 days

Figure A1.66 EDS elemental point analysis spectrum of Pure Zn immersed in 3 wt.% NaCl solution with added 1mM SH-BimH for 12 days (a) spectrum of point a, white part on the surface (b) spectrum of point b, black corroded part (c) spectrum of point c, grey part on the surface.

Figure A1.67 Pure Zn immersed in 3 wt.% NaCl with added 1mM Me-S-BimH solution for 12 days (a) surface under 320x magnification with all typical features (b) surface under 1000x magnification (c) surface under 5000x magnification (d) surface features on white part (e) 3D topography under 320x magnification by SEM

Figure A1.68 EDS elemental map analysis of Pure Zn immersed in 3 wt.% NaCl solution with added 1mM Me-S-BimH for 12 days

Figure A1.69 EDS elemental point analysis spectrum of Pure Zn immersed in 3 wt.% NaCl solution with added 1mM Me-S-BimH for 12 days (a) spectrum of point a, white part of the surface (b) spectrum of point b, black part of the surface (c) spectrum of point c, dark grey part of the surface.

Figure A1.70 Pure Zn immersed in 3 wt.% NaCl with added 1mM SH-BimH-5OMe solution for 12 days (a) surface under 320x magnification with all typical features (b) long bulge on surface under 1000x magnification (c) white flat surface under 2500x magnification (d) cracks and corrosion products (e) 3D topography under 320x magnification by SEM

Figure A1.71 EDS elemental map analysis of Pure Zn immersed in 3 wt.% NaCl solution with added 1mM SH-BimH-5OMe for 12 days

Figure A1.72 EDS elemental point analysis spectrum of Pure Zn immersed in 3 wt.% NaCl solution with added 1mM SH-BimH-5OMe for 12 days (a) spectrum of point a, white bulge on the surface (b) spectrum of point b, white flat surface (c) spectrum of point c, black corrosion products.

Figure A1.73 EDS elemental map analysis of Pure Zn immersed in 3 wt.% NaCl solution with added 1mM SH-ImiH-4Ph for 12 days

Figure A1.74 EDS elemental map analysis of Pure Zn immersed in 3 wt.% NaCl solution with added 1mM SH-BimH-5NH_2 for 12 days

Figure A1.75 Pure Zn immersed in 3 wt.% NaCl with added 1mM SH-ImiMe solution for 12 days (a) surface under 320x magnification with all typical features (b) dark part of surface under 1000x magnification (c) white part of the surface under 5000x magnification (d) porous of dark part (e) 3D topography under 320x magnification by SEM

Figure A1.76 EDS elemental map analysis of Pure Zn immersed in 3 wt.% NaCl solution with added 1mM SH-ImiMe for 12 days

Figure A1.77 EDS elemental point analysis spectrum of Pure Zn immersed in 3 wt.% NaCl solution with added 1mM SH-ImiMe for 12 days (a) spectrum of point a, white part of the surface (b) spectrum of point b and c, dark part of the surface

Figure A1.78 All linear polarization resistance curves of pure copper Zr with and without inhibitors

Figure A2.1 All linear polarization resistance curves of $Cu_{70}Zn_{30}$ alloy with and without inhibitors in 3 wt.% NaCl solution after immersion for 1 h

Figure A2.2 All linear polarization resistance curves of $Cu_{30}Zn_{70}$ alloy with and without inhibitors in 3 wt.% NaCl solution after immersion for 1 h

Figure A2.3 Long-term linear polarization curves of $Cu_{70}Zn_{30}$ alloy under the 120h period of testing of the alloy in the presence of the inhibitor in the 3 wt.% NaCl aqueous solution without inhibitors

Figure A2.4 Long-term linear polarization curves of $Cu_{70}Zn_{30}$ alloy under the 120h period of testing of the alloy in the presence of the inhibitor in the 3 wt.% NaCl aqueous solution with ImiH

Figure A2.5 Long-term linear polarization curves of $Cu_{70}Zn_{30}$ alloy under the 120h period of testing of the alloy in the presence of the inhibitor in the 3 wt.% NaCl aqueous solution with SH-BimH

Figure A2.6 Long-term linear polarization curves of $Cu_{70}Zn_{30}$ alloy under the 120h period of testing of the alloy in the presence of the inhibitor in the 3 wt.% NaCl aqueous solution with Me-S-BimH

Figure A2.7 Long-term linear polarization curves of $Cu_{70}Zn_{30}$ alloy under the 120h period of testing of the alloy in the presence of the inhibitor in the 3 wt.% NaCl aqueous solution with SH-BimH-5OMe

Figure A2.8 Long-term linear polarization curves of $Cu_{70}Zn_{30}$ alloy under the 120h period of testing of the alloy in the presence of the inhibitor in the 3 wt.% NaCl aqueous solution with SH-ImiH-4Ph

Figure A2.9 Long-term linear polarization curves of $Cu_{70}Zn_{30}$ alloy under the 120h period of testing of the alloy in the presence of the inhibitor in the 3 wt.% NaCl aqueous solution with SH-BimH-5NH_2

Figure A2.10 Long-term linear polarization curves of $Cu_{70}Zn_{30}$ alloy under the 120h period of testing of the alloy in the presence of the inhibitor in the 3 wt.% NaCl aqueous solution with SH-ImiMe

Figure A2.11 All linear polarization resistance curves of $Cu_{30}Zn_{70}$ alloy with and without inhibitors in 3 wt.% NaCl solution after immersion for 1 h

Figure A2.12 Long-term linear polarization curves of $Cu_{30}Zn_{70}$ alloy under the 120h period of testing of the alloy in the presence of the inhibitor in the 3 wt.% NaCl aqueous solution without inhibitors

Figure A2.13 Long-term linear polarization curves of $Cu_{30}Zn_{70}$ alloy under the 120h period of testing of the alloy in the presence of the inhibitor in the 3 wt.% NaCl aqueous solution with SH-BImH

Figure A2.14 Long-term linear polarization curves of $Cu_{30}Zn_{70}$ alloy under the 120h period of testing of the alloy in the presence of the inhibitor in the 3 wt.% NaCl aqueous solution with SH-BimH-5OMe

Figure A2.15 Long-term linear polarization curves of $Cu_{30}Zn_{70}$ alloy under the 120h period of testing of the alloy in the presence of the inhibitor in the 3 wt.% NaCl aqueous solution with SH-ImiH-4Ph

Figure A2.16 Long-term linear polarization curves of $Cu_{30}Zn_{70}$ alloy under the 120h period of testing of the alloy in the presence of the inhibitor in the 3 wt.% NaCl aqueous solution with SH-BimH-5NH_2

Figure A2.17 Normalized survey XPS spectrums for the surface of $Cu_{70}Zn_{30}$ alloy after polishing and pickling, and after immersion in 3wt.% NaCl with and without added of SH-BimH, Me-S-

BimH, SH-BimH-5OMe and SH-ImiH-4Ph. Dash lines represent the position of peaks of reference compounds. Upper: Immersion for 24h. Down: Immersion for 120h.

Figure A2.18 EDX elemental map analysis of the bare sample under 1000x magnification

Figure A2.19 EDX elemental map analysis of $Cu_{70}Zn_{30}$ alloy immersed in 3 wt.% NaCl solution for 60 days

Figure A2.20 $Cu_{70}Zn_{30}$ alloy immersed in 3 wt.% NaCl with added 1mM ImiH solution for 60 days (a) surface under 2500x magnification with all typical features (b) surface under 320x magnification (c) surface under 1000x magnification (d) surface features in the valley (e) 3D topography under 1000x magnification by SEM

Figure A2.21 EDS elemental map analysis of $Cu_{70}Zn_{30}$ alloy immersed in 3 wt.% NaCl solution with added 1mM ImiH for 60 days

Figure A2.22 EDS elemental point analysis spectrum of $Cu_{70}Zn_{30}$ alloy immersed in 3 wt.% NaCl solution with added 1mM ImiH for 60 days (a) spectrum of point a, white clusters on the surface (b) spectrum of point b, grey cubic particles under the clusters (c) spectrum of point c, grey pieces in the valley.

Figure A2.23 EDS elemental map analysis of Cu70Zn30 alloy immersed in 3 wt.% NaCl solution with added 1mM SH-BimH for 60 days

Figure A2.24 EDS elemental map analysis of $Cu_{70}Zn_{30}$ alloy immersed in 3 wt.% NaCl solution with added 1mM Me-S-BimH for 60 days

Figure A2.25 EDS elemental map analysis of $Cu_{70}Zn_{30}$ alloy immersed in 3 wt.% NaCl solution with added 1mM SH-BimH-5OMe for 60 days

Figure A2.26 EDS elemental map analysis of $Cu_{70}Zn_{30}$ alloy immersed in 3 wt.% NaCl solution with added 1mM SH-ImiH-4Ph for 60 days

Figure A2.27 $Cu_{70}Zn_{30}$ alloy immersed in 3 wt.% NaCl with added 1mM SH-BimH-5NH_2 solution for 60 days (a) surface under 2500x magnification with all typical features (b) surface under 320x magnification (c) surface under 1000x magnification (d) surface features in the valley (e) 3D topography under 1000x magnification by SEM

Figure A2. 28 EDS elemental map analysis of $Cu_{70}Zn_{30}$ alloy immersed in 3 wt.% NaCl solution with added 1mM SH-BimH-5NH_2 for 60 days

Figure A2.29 EDS elemental point analysis spectrum of Cu70Zn30 alloy immersed in 3 wt.% NaCl solution with added 1mM SH-BimH-5NH2 for 60 days (a) spectrum of point a, white part under BSE detector (b) spectrum of point b, grey film on the surface (c) spectrum of point c, particles in porous

Figure A2.30 $Cu_{70}Zn_{30}$ alloy immersed in 3 wt.% NaCl with added 1mM SH-ImiMe solution for 60 days (a) surface under 2500x magnification with all typical features (b) surface under 320x magnification (c) surface under 1000x magnification (d) surface features in the valley (e) 3D topography under 1000x magnification by SEM

Figure A2.31 EDS elemental map analysis of $Cu_{70}Zn_{30}$ alloy immersed in 3 wt.% NaCl solution with added 1mM SH-ImiMe for 60 days

Figure A2.32 EDS elemental point analysis spectrum of $Cu_{70}Zn_{30}$ alloy immersed in 3 wt.% NaCl solution with added 1mM SH-ImiMe for 60 days (a) spectrum of point a, white part under BSE

detector (b) spectrum of point b, grey film on the surface (c) spectrum of point c, particles in porous

Figure A2.33 EDX elemental map analysis of the bare $Cu_{30}Zn_{70}$ alloy sample under 1000x magnification

Figure A2.34 EDX elemental map analysis of $Cu_{30}Zn_{70}$ alloy immersed in 3 wt.% NaCl solution for 12 days

Figure A2.35 $Cu_{30}Zn_{70}$ alloy immersed in 3 wt.% NaCl with added 1mM SH-BimH solution for 12 days (a) surface under 320x magnification with all typical features (b) surface under 2500x magnification (c) bulk material under porous film (d) big corrosion products on the surface (e) 3D topography under 320x magnification by SEM

Figure A2.36 EDS elemental map analysis of $Cu_{30}Zn_{70}$ alloy immersed in 3 wt.% NaCl solution with added 1mM SH-BimH for 12 days

Figure A2.37 EDS elemental point analysis spectrum of $Cu_{30}Zn_{70}$ alloy immersed in 3 wt.% NaCl solution with added 1mM SH-BimH for 12 days (a) spectrum of point a, bulk material under the porous film (b) spectrum of point b, grey porous film (c) spectrum of point c, clusters on the surface.

Figure A2.38 $Cu_{30}Zn_{70}$ alloy immersed in 3 wt.% NaCl with added 1mM SH-BimH-5OMe solution for 12 days (a) surface under 320x magnification with all typical features (b) particles and cracks on the surface (c) surface under 320x magnification (d) porous structure of the surface (e) 3D topography under 320x magnification by SEM

Figure A2.39 EDS elemental map analysis of $Cu_{30}Zn_{70}$ alloy immersed in 3 wt.% NaCl solution with added 1mM SH-BimH-5OMe for 12 days

Figure A2.40 EDS elemental point analysis spectrum of $Cu_{30}Zn_{70}$ alloy immersed in 3 wt.% NaCl solution with added 1mM SH-BimH-5OMe for 12 days (a) spectrum of point a, grey flat surface (b) spectrum of point b, white flat surface (c) spectrum of point c, porous substance on the surface.

Figure A2.41 $Cu_{30}Zn_{70}$ alloy immersed in 3 wt.% NaCl with added 1mM SH-ImiH-4Ph solution for 12 days (a) surface under 320x magnification with all typical features (b) surface under 1000x magnification (c) surface under 1000x magnification (d) structure of flower-like substance (e) 3D topography under 320x magnification by SEM

Figure A2.42 EDS elemental map analysis of $Cu_{30}Zn_{70}$ alloy immersed in 3 wt.% NaCl solution with added 1mM SH-ImiH-4Ph for 12 days

Figure A2.43 EDS elemental point analysis spectrum of $Cu_{30}Zn_{70}$ alloy immersed in 3 wt.% NaCl solution with added 1mM SH-ImiH-4Ph for 12 days (a) spectrum of point a, small flower-like substance (b) spectrum of point b and c, large flower-like substance.

Figure A2.44 EDS elemental map analysis of $Cu_{30}Zn_{70}$ alloy immersed in 3 wt.% NaCl solution with added 1mM SH-BimH-5NH_2 for 12 days

Figure A2.45 Raman spectrum of OH-Me-BimH powder (bottom), pure Cu surface after 60 days' immersion with added 1mM OH-Me-BimH (top).

List of Tables

List of Academic Publications and Activities

- Anton Kokalj, Matic Lozinšsek, Barbara Kapun, Peyman Taheri, Shova Neupane, Patricia Losada-Pérez, Chenyang Xie, Stojan Stavber, Daniel Crespo, Frank U. Renner, Arjan Mol, Ingrid Milošev, Simplistic correlations between molecular electronic properties and inhibition efficiencies: Do they really exist? Corrosion Science, 2020, 108856, ISSN 0010-938X, https://doi.org/10.1016/j.corsci.2020.108856. Published.

- Yufen Chen, Lluís Soler, Chenyang Xie, Xavier Vendrell, Jarosław Serafin, Daniel Crespo, Jordi Llorca, A straightforward method to prepare supported Au clusters by mechanochemistry and its application in photocatalysis, Applied Materials Today, Volume21, 2020, 100873, ISSN 2352-9407, https://doi.org/10.1016/j.apmt.2020.100873. Published.

- Chenyang Xie, Pere Bruna, Anton Kokalj, Frank U Renner, Ingrid Milosev Daniel Crespo, Corrosion resistance of crystalline and amorphous CuZr alloys in NaCl aqueous environment and effect of corrosion inhibitors. Journal of Alloys and Compounds. Submitted.

- Presentation in EUROCORR 2019 in Sevilla, Spain:
  Chenyang Xie, Inhibition properties of benzimidazole-based compounds on crystalline and amorphous CuZr alloys (ID: 20759)

Abstract

Cu-based alloys are widely applied in corrosive environments. The improvement of the alloys' corrosion resistance will significantly reduce energy consumption and overexploitation of resources. To increase the resistance of copper as less corrosion alloy component, nine imidazole-based compounds with different functional groups were tested as potential corrosion inhibitors. Besides, CuZn alloys, CuZr crystalline and amorphous alloys, and their pure metals are tested to explore the correlations between inhibition and structure and elements. For CuZn alloys, the α-Cu phase $Cu_{70}Zn_{30}$ alloy and non-α-Cu phase $Cu_{30}Zn_{70}$ alloy were tested. CuZr alloys are the basis of a family of metallic glasses with large glass forming ability and remarkable mechanical properties. The corrosion response of as-produced crystalline and amorphous Cu_xZr_{100-x} alloys (x = 40, 50, 64 at. %) were tested. The alloys were immersed in 3 wt.% NaCl aqueous solution. Potentiodynamic polarization measurements, electrochemical impedance spectroscopy and long-term immersion tests followed by microscopy analysis and Raman spectroscopic analysis were carried out. Comparative analysis of pure Cu and $Cu_{70}Zn_{30}$ alloy shows that the same inhibitors are effective in both alloys. A similar behavior is found with pure Zn and $Cu_{30}Zn_{70}$ alloy. However, the inhibition power shows a different value, which should be attributed to the healing effect. Defects present in most of the polished samples accelerate the pitting on these locations. The healing effect will lead to a patch on those positions, which will slow down the local attacks. All the tested amorphous alloys exhibit a much better corrosion resistance than their crystalline counterparts in the presence and absence of inhibitors. The main factor controlling the corrosion resistance of the alloys appears to be the Zr-rich (or at least equiatomic) amorphous structure, the effect of the inhibitors being secondary. Results therefore show a complex relationship between inhibitor performance, microstructure and composition of CuZr alloys. SH-ImiH-4Ph shows potential to become a global α-Cu phase alloy inhibitor and SH-BimH-5NH_2 shows potential for Zn-based and CuZr alloys. Electrochemical measurements, especially long-term measurements, display a significant correlation to immersion tests.

Chapter 1: Introduction

The usage of materials shapes the history of humanity. The conventional periodization of the distant prehistoric time reflects this fact, as we talk of the Stone Age, the Bronze Age, or the Iron Age, for instance. In particular, the first usage of bronze, a copper alloy, changed history. However, copper and its alloys still play an essential role in modern society. The industrial revolution increased productivity and reduced impurities. In parallel, booming global demands of electricity in the late 19th century boosted the production of Cu for generators and transmission lines and brought more research work on Cu, extending the application range of its alloys. The most important copper alloys are at present brass, which adds zinc as the additional principal element, cupronickel with nickel, and aluminum bronzes with aluminum [1]. Copper and its alloys are present in a variety of ways in our life and still play an essential role in modern society. Electronics, in particular, made extensive use of copper and its alloys as well.

However, demand and proved reserves of resources, as well as environmental issues, are the biggest concern for the sustainable development of human beings. Since 1994, sixteen European continent countries established a system for specialized copper treatment along all its life cycle [2]. Moreover, the researchers also revealed that citizens of most of the countries waste 1-3 kg Cu/year, mostly in obsolete electronics and end-of-life vehicles [3]. According to Elshkaki et al. [4], the requirements of copper may increase between 275% and 350% and exceed the known copper reserves by 2050. The energy consumed in the production of copper is expected to reach 1.0 - 2.4% of total energy demand by 2050, compared to only 0.3% today [4]. Grade decline must also be expected as copper mining reserves be exhausted. Recycling of the material and reducing the waste will be the core research on copper and its alloys in the future.

Most Cu alloys are not served as bearing parts. Thus, the life cycle is determined by their resistance to corrosion. As shown in **Table 1.1**, corrosion has a substantial impact on the economy of all countries. On account of the excellent corrosion resistance of copper and its alloys, they have been applied in corrosive environments like heat transfer system, valves handling freshwater, seawater, etc.. The knowledge of the corrosion mechanisms of copper alloys and the research on possible corrosion prevention or inhibition strategies are therefore subjects of utmost interest. A wide range of methods of corrosion prevention are applied in modern society, such as protective coating, alloying, cathodic protection, design modification, and there is a recent research surge on corrosion inhibitors.

Furthermore, the brisk demand for new materials by the development of technology pushes the study and application of new Cu-based alloys, such as new applications in electronic devices and microdevices, as well as new materials such as Cu-based metallic glasses. Corrosion will be an essential research topic of the new alloys since it is present in every application. Since metallic glasses show a completely different structure than crystalline alloys, it is worth exploring the potential prevention effect arising from this

difference. In this research, it may also provide a view of the interaction between organic self-assembled monolayers and metallic glass.

Table 1.1 Corrosion cost in some countries [5–10]
*: Transfer based on the currency of the time.

Country	Cost in USD	Percentage of GDP/GNP	Report Year
China [5]	~ 310 billion	3.34% GDP	2017
Japan* [6]	~ 47.7 billion	1.02% GNP	1999
USA [7]	~ 276 billion	3.1% GDP	1998
Kuwait [8]	~ 1 billion	5.2% GDP	1995
Australia* [9]	~ 1.3 billion	1.5% GNP	1983
UK* [10]	~ 840 million	3.5% GNP	1971

The introduction will focus on three aspects: surface characterization of copper and its alloys, corrosion of copper and its alloys, an inhibitor for Cu and its alloys, including Cu-based metallic glasses. Given the lightning speed of oxidation in air and water, the first task to be performed is the characterization of the specimens' surface. Although there is no universal corrosion mechanism of copper and its alloys, much work has been carried out on specific alloys and solutions. These studies will offer an expectation of corrosion; thus, the prevention effect can be analyzed. Organic inhibitors are one of the hotspots in corrosion due to its universality and flexibility, especially for copper. The proper application of organic inhibitors on copper in a corrosive environment can be a corrosion prevention method applicable to many copper alloys.

Metallic glasses, on their side, show different properties compared to their crystalline counterpart, which are reflected in their corrosion resistance as well. A brief introduction on metallic glasses and its corrosion performance may help to understand the latter difference of the inhibition effect.

1.1 Corrosion of copper and its alloys

Copper and its alloys are widely used in many environments and applications due to their excellent corrosion resistance coupled with combinations of other desirable properties such as their superior electrical conductivity for electric appliances and electronic devices, large thermal conductivity for cooling and heat exchange systems, ease of fabricating and joining, and convenient mechanical properties. The corrosion rate of copper in clean air and water is negligible, and copper alloys resist many saline solutions, alkaline solutions, and organic chemicals [11]. However, copper is sensitive to oxidizing acids, oxidizing heavy-metal salts, sulfur, ammonia (NH_3), and some sulfur and NH_3 compounds, which will result in fast corrosion [12].

Corrosion is an omnibus subject, which involves the interaction between the environment and materials. Here the environment comprises the pH, the presence of absence of flow, the available ions and or gases, and all need to be considered to figure out the corrosion

process. For the materials side, the impurities, manufacture methods, elements, and so on, all are influence factors as well. Owing to this complexity, the review in this section will focus on the corrosion process on Cu and CuZn alloys, i.e., the formation of the film in air, water and sodium chloride solution, and the corrosion in sodium chloride solution.

1.1.1 Oxidation of copper: initial stages

When talking about the metal surface and interface, oxidation cannot be ignored. Oxidation proceeds ultra-fast on newly created metal surfaces, both in air and in solution, creating different surface structures by diverse mechanisms [13,14]. These films on the metal surfaces influence the posterior development of corrosion and inhibition effect; therefore, they must be considered before further study.

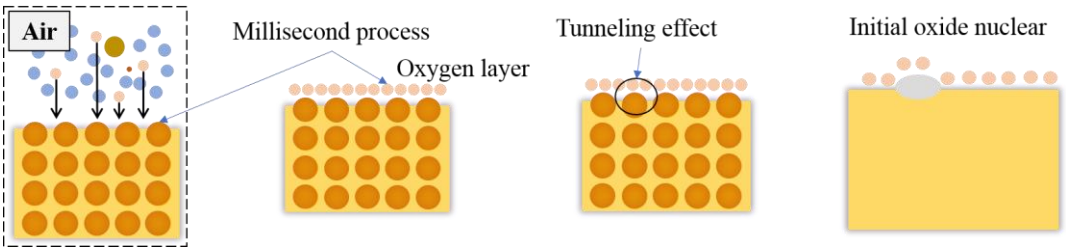

Figure 1.1 Schematic diagram of initial nucleation of oxide in air [15]

In an air environment and at room temperature, a thin oxide film of the base metal usually develops on a newly created surface. This film, invisible to the naked eyes, often protects the metal from further reaction and therefore slows down corrosion. The formation of this oxide film always happens in the millisecond range and forms a nanometer thickness oxide layer in hours [16]. **Figure 1.1** shows the mechanism of the initial nucleation of oxide in the air, as described by Cabrera and Mott [15]. The bare surface of metal contains a layer of atoms not entirely surrounded, which act as metal radicals and combine with the highly electronegative oxygen atoms of air. The high concentration of oxygen in air makes this reaction happens in some milliseconds. The resulting energy barrier will prevent the oxidation but not wholly, as the tunneling effect can make it possible. Then the oxide will grow laterally two-dimensionally across the surface at tremendous speed, as shown in . After the formation of a thin oxide film, an electric field appears, which lowers the activation energy for ions to move into the oxide, which continues increasing the layer thickness[15]. When the layer reaches a critical thickness, about 100 Å, the intensity of the electric field becomes too low, and the growth speed of the layer decreases substantially. Aluminum, silver and zirconium show this kind of oxidation (see **Figure 1.2** (a)). **Figure 1.2** (b) shows the growth rate of some of the oxides. Then Fehlner and Mott [17] expanded the theory, considering the fast incorporation of oxygen into the metal substrate by place exchange. The voltage built up across the film induces a slow logarithmic growth of the oxide, and the film will reorder, allowing island growth, which results in faster logarithmic growth. However, further research showed that not all metals

show two-dimensional growth at first. Instead, three-dimensional oxidation was found in copper.

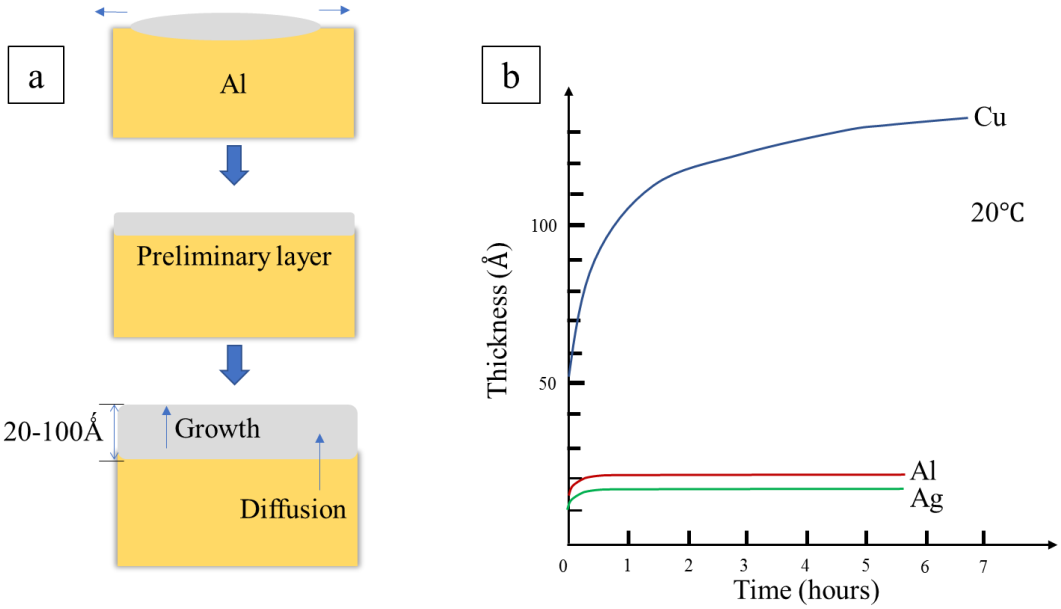

Figure 1.2 (a). Schematic diagram of the unified-type formation of the oxide. (b) Oxidation at room temperature and pressures of oxygen between 10^{-4} and 10^{-2} mm. Hg (Redraw from Garforth [15]).

Oxidation of copper

Cuprous oxide (Cu_2O) is the oxidation and corrosion product responsible for the protection of copper at low temperatures. This oxide is a p-type semiconductor in which defects are uniformly distributed in the oxide. It forms spontaneously in air, faster with a humid environment, and even faster in water. Oxygen surface diffusion is the dominant mechanism for transport, nucleation and growth for copper oxide [20], in a mechanism different from the theory proposed by Cabrera and Mott. Interfacial anion diffusion under

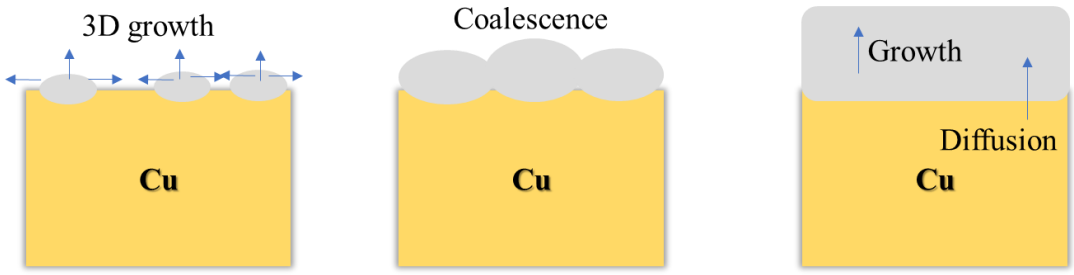

Figure 1.3 Schematic diagram of oxidation of pure copper (derive from ref. [18] [19][20]).

atmosphere conditions accounts for the initial stage of Cu_2O island growth [20]. The process is shown in **Figure 1.3**; the formation of islands happens in several nucleation points. These islands grow three-dimensionally until they coalesce with their neighbor islands. After the formation of the continuous oxide layer, the surface diffusion route is shut down, and a much slower bulk diffusion is required for further oxidation. The process at atmospheric pressure is different from the surface diffusion-controlled process observed under low oxygen pressure[18]. Compared with the metals which form amorphous oxide layers like aluminum and silicon, more defects are observed in the cuprous oxide layer. The interface between oxide and copper is explained as metaphase containing Cu_4O-S1, Cu_4O-S2, Cu_8O, $Cu_{64}O$ from the research work of Guan et al. [21–24]. This may offer a further understanding of the formation of the oxide layer, but this transition region does not seem to be significant on the global behavior of the oxide. The Cu_2O film is a highly defective film and the structure may be described as one with some missing Cu^+ cations, and the otherwise deficient positive charge is balanced by a single positive charge (positive hole) in the vicinity of each cation vacancy [25]. Due to the existence of abundant vacancies in this structure, the cation transportation will be straightforward and electronic resistance will be small.

Oxide of Brass in air

The oxidation behavior of copper shows the formation of cuprous oxide. As the most applicable alloy, brass, the oxidation behavior is also worth to illustrate. The oxidation of Cu/Zn(64/36) brass studied by Van Ooij [26] under the different surface and environmental conditions showed that the formation of the thin oxide layer of zinc results in surface composition of 40% Cu; increasing temperatures would increase the zinc oxide layer thickness. A copper-rich layer exists under the zinc oxides. The reaction

$$Cu_2O + Zn = ZnO + 2Cu$$

is the major effect of the result of the balance between the different oxidation behavior of copper and brass. Maroie et al. [27][28] studied the growth of oxides on α(75%Cu/25%Zn) and β(53%Cu/47%Zn) brass surface by XPS at controlled low pressure. The α-brass initially forms ZnO on different sites, and then it will stop or keep an extremely low growth rate. The formation of Cu_2O oxides will take place as well, but slower than ZnO. However, the growth of Cu_2O is faster than that of ZnO when the pressure reached 10^{-4} Torr (0.013 Pa) [27]. ZnO forms a continuous layer in β brass. Increasing temperature will also induce an increase in the ZnO layer thickness due to the acceleration of Zn diffusion through the oxide layer. Moreover, the influence of the diffusion of oxygen through the oxide-metal interface is negligible [28]. Besides, Qiu et al. [29] analyzed the initial oxidation on a brass (Cu–20Zn) surface exposed to humidified air at 90% RH. The natural oxides consist of some Zn-enriched areas, which means a local growth of ZnO, which retards the formation of a more uniform growth of a Cu_2O-like oxide due to galvanic effects.

1.1.2 Corrosion of pure copper

Corrosion happens in a variety of ways, in atmosphere, marine and soil environments, and can be accelerated by stress; therefore, different parameters should be considered. As this thesis focus on the corrosion and the corrosion inhibition in aqueous condition, the corrosion review will emphasize corrosion in this condition. When the workpiece is put into the aqueous working condition, the first process on the surface is usually the removal of adsorbed gas by the aqueous solution. Therefore, a new film will develop, and its growth is attributed to the interaction with the solution, which contains part of dissolved gas from the air and the other ions. The mechanism of formation of this film depends on the different species in the solution and the properties of the materials themselves. Which is extraordinarily complex, thus, not well understood in some cases. However, the reviewed bibliography shows that the corrosion mechanisms are very sensitive to the experimental conditions.

Kruger [30,31] studied the formation of oxides of Cu in pure water under different conditions. At room temperature and atmospheric pressure, the oxidation was comparatively more natural in water than in air, and the oxygen in water plays the primary role in the formation of the oxide film. Besides, different crystallographic planes showed different oxidation rates and orientation of the epitaxy films, similar to what happens in dry air. Identical to the oxides in the air, the films were not continuous, and light influenced the process in water as a kind of catalytic reaction. If the atmosphere changed to oxygen-helium mixtures, CuO was also found when the oxygen was more than 10%, and depending on the presence of CO_2, which influences the pH, CuO will be further oxidized to Cu_2O. The O_2 and CO_2 concentration will control the thickness with the competing reactions[30,31]:

$$Cu + Cu^{2+} \rightarrow 2Cu^{+}$$
$$Cu^{+} \rightarrow Cu^{2+} + e^{-}$$

The rapid formation and more prominent nuclei of oxides in water can be explained as due to the influence of the ion transformation, and thus it was experimentally observed that stirring decreased the formation rate of CuO. **Table 1.2** shows the free energies, corrosion reaction constant and equilibrium ionic products in water derived from the research of D. J. G. Ives and A. E. Rawson [32]. Reaction ① and ② are accompanied by a free energy loss of ~20 and 2.4 kcal at one total atm pressure. This means the copper is inclined to dissolve in water containing oxygen and carbon dioxide. Oxygen accounts for the equilibrium concentration of cupric bicarbonate in solution [32]. Despite the corrosion may be dominated by these two reactions, reverse reactions ③ to ⑦ can further reduce the free energy of the system. They also revealed that the increasing thickness might accelerate the dissolution instead of offering more protection. Furthermore, neither carbon dioxide nor oxygen is particularly aggressive towards copper without each other.

Table 1.2 Standard free energies, ΔG°, and equilibrium ionic products, K' = $(Cu^{2+})(HCO_3^-)^2$, for copper corrosion reactions at 25℃ (reproduced from D. J. G. Ives and A. E. Rawson [32])

	Reaction	ΔG°, kcal	log K'
①	$Cu + H_2O + CO_2 = Cu(HCO_3)_2$	-19.88	$14.57 + 2\log P_{CO_2} + 1/2 \log P_{O_2}$
②	$1/2Cu_2O + H_2O + 2CO_2 + 1/4O_2 = Cu(HCO_3)_2$	-2.39	$1.75 + 2\log P_{CO_2} + 1/4\log \log P_{O_2}$
③	$Cu(OH)_2 + 2CO_2 = Cu(HCO_3)_2$	8.73	$-6.40 + 2\log P_{CO_2}$
④	$CuO + H_2O + 2CO_2 = Cu(HCO_3)_2$	10.52	$-7.71 + 2\log P_{CO_2}$
⑤	$1/2[CuCO_3{\cdot}Cu(OH)_2] + 1/2\ H_2O + 3/2CO_2 = Cu(HCO_3)_2$	11.90	$-8.69 + 3/2\log P_{CO_2}$
⑥	$1/3[2CuCO_3{\cdot}Cu(OH)_2] + 2/3H_2O + 4/3CO_2 = Cu(HCO_3)_2$	12.10	$-8.84 + 4/3\log P_{CO_2}$
⑦	$Cu_2O - Cu + H_2O + 2CO_2 = Cu(HCO_3)_2$	15.10	$-11.07 + 2\log P_{CO_2}$

The dissolution of Cu^{2+} and the growth of a cuprous oxide film under a fixed pressure of CO_2 follows first-order kinetics with respect to oxygen [33]. A duplex film structure was proposed, composed of an inner compact Cu_2O thin layer and an outer layer taking the form of a porous layer formed later, but this mechanism neglects the influence of CO_2 [34]. At low O_2 pressure, the dissolution of Cu and the film growth increases, while it decreases at low CO_2 pressure. Further, the increase in oxygen pressure will restrict the dissolution and film formation. However, carbon dioxide will have the opposite effect [35].

Table 1.3 Corrosion rate of copper and brasses (reproduced from ref. [36])

Alloy	Composition			Corrosion Rate / MPY(*)
Copper, O free	≥ 99.9%	-	-	0.1 – 1.6
Commercial Bronze	90	10	-	0.1 – 1.1
Red Brass	85	15	-	0.2 – 1.8
Yellow Brass	66.47	33.51	Fe: 0.02, Pb: < 0.01	0.2 – 2.5
Copper, O free	≥ 99.9%	-	-	0.1 – 1.6

(*)MPY stands for Mils per year, and 1 Mil = 0.0254 mm

Different from pure water, the addition of chloride ions generates a more complex corrosion process and film. Typically, in aqueous conditions and in the absence of external polarization, copper and its alloys show simultaneously general corrosion and pitting corrosion. The essential corrosive environment in Cu applications is the seawater, which contains about 19000 mg/L chloride, and general corrosion always occurs in such conditions. The corrosion rates of some common copper alloys in seawater are shown in **Table 1.3**. With the increase of Zn concentration, at first, the corrosion rate is decreasing, but when the zinc content reaches ~33%, the corrosion rate is higher than that of pure copper.

North and Pryor [37] studied the formation of oxide film on Cu and Cu-Ni alloys, revealing that the film was continuous and consisted entirely of Cu_2O. Moreover, $Cu_2(OH)_3Cl$ was also found at longer immersion times. However, the film on Cu was less protective than the layer on Cu-Ni alloys, presenting a significant ohmic and ionic

resistance. The reason that leads to this difference may be attributed to Ni substitution in the Cu_2O reaction product film. The film thickness growth in the Cl^- solution was 11,000 Å(66h), quite more significant than in dry air, 146Å (66h), and in distilled water ~500Å (~100h) [31]. The presence of Cl^- induces a tremendous acceleration of the film thickness growth, compared to that of pure water. This can be attributed to the modification of defect structure, as Cl^- replaces some O_2 in the oxide lattice and introduces a charge imbalance. This replacement helps Cu^+ ions to pass into the solution and create additional neutral cation vacancies, faster than in pure water where only the OH^- are present. Besides, we should note that the concentration of Cl^- is relatively higher than that of OH^- in pure water. With this kind of increasing film and Cu^+ ion transformation, the copper alloy workpiece will be reduced gradually [31]. **Figure 1.4** shows the Pourbaix diagram for copper in seawater. Under equilibrium conditions, Cu_2O is only stable down to pH 5 at normal potentials. However, it can still give a comprehensive view of the corrosion under different pH in the presence of Cl^- [38].

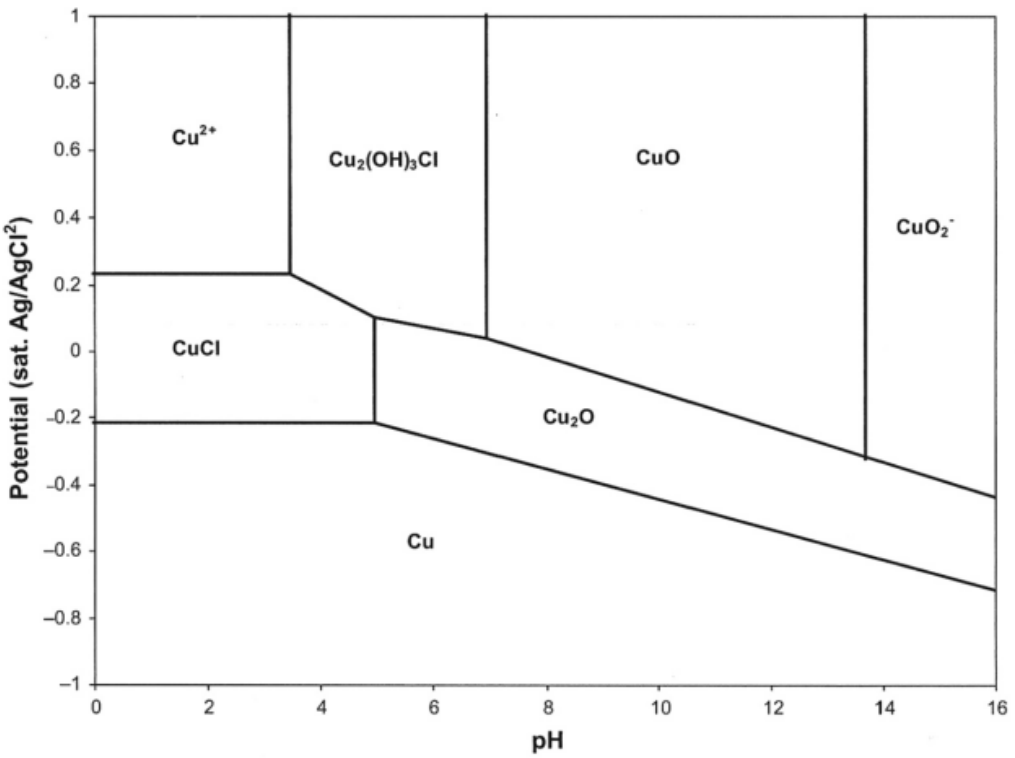

Figure 1.4 Pourbaix diagram for seawater (copper-chloride-water system) [39].

Pitting corrosion

Pitting is a localized form of corrosion by which cavities or "holes" are produced in the material. The pitting of copper was initially found in copper pipes with water by Campbell [40]. Thomas and Tiller found that the presence of chloride and carbonate would assist the pitting process [41], and research of Al-Kharafi et al. [42] agreed on the effect of

chloride and cuprous chloride inside the pits. Mattsson proposed three types of pitting [40]: Type 1 occurs on annealed or half-hard pipes in cold tap water, caused by a continuous carbon film formed on the inner pipe surface during bright annealing; type 2 occurs on hard drawn pipes in the hot tap water of low (< 7:4) pH and low (< 1) [HCO3-]/[SO42-] ratio; type 3 occurs on both hard and annealed pipes in the cold tap water of high pH, with low salt concentration [11]. Frommeyer [43] studied the composition of type 1 pits by electron spectroscopic methods, revealing the schematic of the structure reproduced in **Figure 1.5**. Another layer of Cu_2O on the metal surface due to the oxidation was also found. The hole inside the bulk copper resulted from pitting; a thin layer of CuCl was present on the interface, some Cu_2O particles were found close to the CuCl layer, and the corrosion products of pitting were found around the hole and above the oxidation layer.

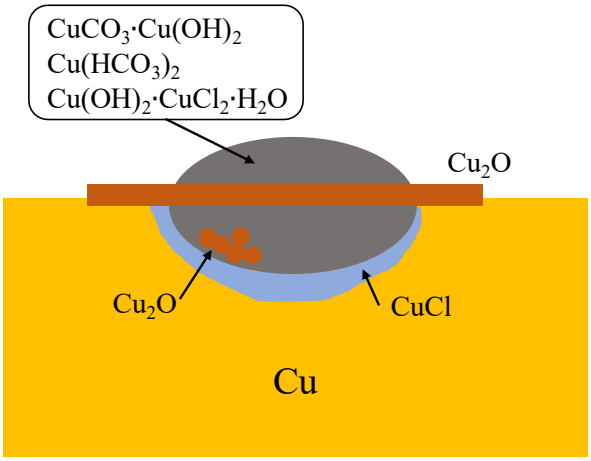

Figure 1.5 Schematic structure of pits from type1 pitting

Cornwell et al. [43] suggested the reaction mechanism of copper pitting in aerated and chloride supply waters. Copper ions produced by anodic dissolution combine with the chloride ions to form cuprous chloride:

$$Cu^+ + Cl^- = CuCl$$

Cuprous chloride is not stable in near-neutral pH ranges, hydrolyzes to form Cu_2O, which is precipitated on the metal surface:

$$2CuCl + H_2O = Cu_2O + 2HCl$$

The cathodic reaction supporting the anodic dissolution process is oxygen reduction:

$$O_2 + 2H_2O + 4e^- = 4OH^-$$

For corrosion to proceed, the hydroxyl ions produced at the cathodic sites must be removed. This occurs more rapidly in acid supplied water or water that contains bicarbonate ions:

$$OH^- + HCO_3^- = CO_3^{2-} + H_2O$$

The final reaction causes precipitation of mixed calcium carbonate and basic copper carbonate scale.

1.1.3 Corrosion of brass

Standard brasses are alloys of copper with 10 – 50% zinc and often other elements such as tin, iron, manganese, aluminum, and lead. Zinc addition in copper up to 39% will maintain a single-phase alloy, α-brass, and 47–50% for another single-phase, β-brass. Between 39 and 47%, the alloy contains both phases. The copper/zinc ratio is the dominating factor of corrosion of the α-brasses; the duplex alloy leads to more zinc dissolution. Dezincification takes place by the preferential dissolution of the less noble β phase, and in the pure β alloys, only zinc appears in the corrosion products, the copper mostly being redeposited as metal. The corrosion behavior of brasses depends on several parameters, such as the dissolved salts, dissolved gases, and the formation of protective films. As shown in Table 1.3 Corrosion rate of copper and brasses (reproduced from ref. [36]) the corrosion rate of brass increased when the addition of Zn was below ~20% and increased when reached ~33% in seawater.

Dealloying is an electrochemical reaction in which one element constituting an alloy is selectively separated and removed from the alloy, causing deterioration of its essential properties. Since the selective dissolution, it is difficult to find the severity of the attack. As mentioned before, selective dissolution of the active component zinc had its specific name, dezincification, since the epidemicity in dealloying. It can lead to many problems, especially in hard water, solution with ammonia, and chloride as well. The commonest happens on brasses containing > 15% zinc. Dealuminification and denickelification have been reported for aluminum bronzes and cupronickels as well, but not as frequently as dezincification. As shown in **Figure 1.6**, two types of dezincification always are also observed. Brass that contain the β phase suffer much than the single α phase ones. Lucey [44] studied the dezincification of α-brass and β-brass; the simultaneous dissolution of Cu and Zn were found, observing that copper will be redeposited at the position dissolved, as well as Stillwell and Turnipseed [45] found in ϵ-brass. Besides, the new underlying copper frequently shows alternating formation layers; less dense copper layers incorporate with bands of cuprous oxides and a narrow band of dense copper. The first copper corrosion product is believed to be cuprous chloride and β- or non-arsenical α-brass will reduce cuprous chloride to copper. Dezincification may take place in layers over the whole surface, but it may also form plugs in localized regions, see **Figure 1.6**. T. L. Barr and J. J. Hackenberg [46] proposed the onset dezincification process:

a) Migration to subsurface and surface of Zn^{2+} from bulk alloy to form ZnO.
b) Dissolution of some of the protective (passivating) oxides:
    a. all Cu^{2+} quickly dissolved (~5 h, 3% NaC1); (B) a little of the Cu^{+} may dissolve; (C) some of (original) ZnO also dissolves

c) Extensive thickening of the ZnO sublayer.
d) A new, thicker Cu oxide layer forms below the surface layer of ZnO.
e) Overlap of layer boundaries increases dramatically.
f) Termination of surface secretion of Zn.
g) Island growth of clusters of ZnO at outer surface encapsulating some Cu oxides.

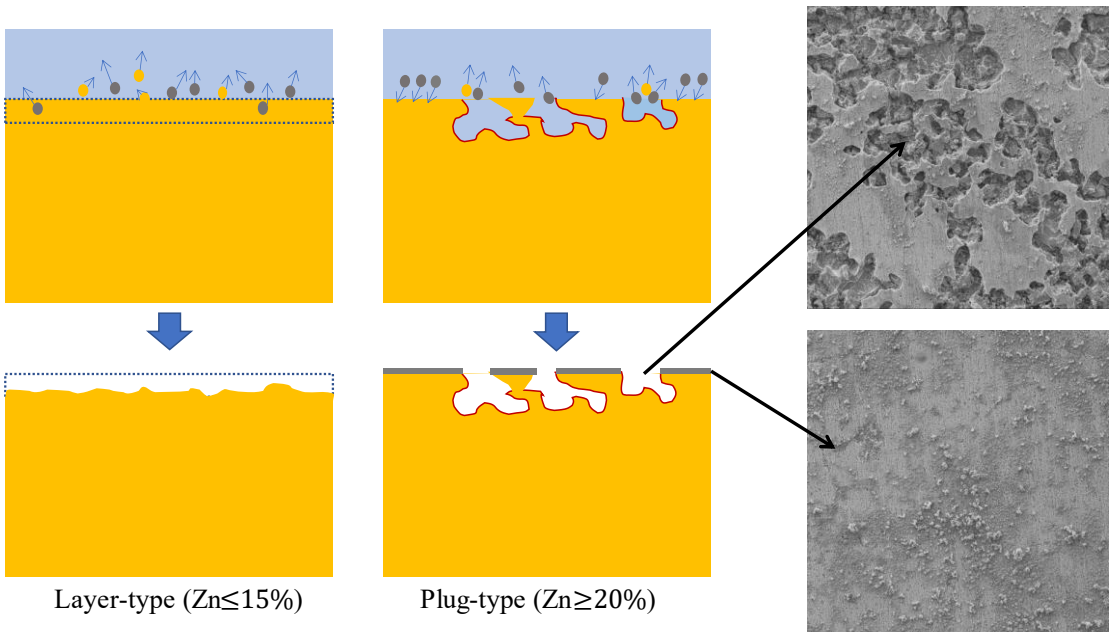

Figure 1.6 Two different types of dezincification

Warraky [47] observed that on the initial stage of dezincification of brass(70/30), from seconds to minutes, the growth of the initially formed Cu_2O eventually stopped. Furthermore, a high concentration of the ZnO layer was formed in a few seconds. As described before, a rough reaction procedure can be listed, and the first step is the oxidation in saltwater

$$Zn^{2+} + H_2O = ZnO + 2H^+$$
$$2Cu^+ + H_2O = Cu_2O + 2H^+$$

After the surface has become covered by both ZnO and Cu_2O, CuCl is formed on the surface by the reaction

$$Cu^+ + Cl^- = CuCl$$

And a disproportionation reaction may present [48]

$$2CuCl = Cu + CuCl_2$$

other reactions which results in the formation of $CuCl_2^-$ may happen [49][50]

$$CuCl + Cl^- = CuCl_2^-$$
$$Cu + 2Cl^- = CuCl_2^-$$

Additionally, ZnOX ($HZnO_2^-$) and ZnCl2 was observed and indicate that zinc dissolves as

$$ZnO + OH- = HZnO_2^-$$
$$CuCl_2 + Zn = ZnCl_2 + Cu$$

1.2 Prevention of corrosion of copper and its alloy

Corrosion prevention is essential for all technological materials. The typical methods include surface coating, cathodic protection, alloying and inhibition. For copper, in freshwater and seawater, the corrosion rate can be controlled under low flow velocity and less harmful components. pH also has a dominating effect and should be larger than 6. However, cuprosolvency will always be a challenge, and the water treatment may also affect the corrosion rate. A protective Cu_2O layer should be built before formal application or painting of organic coatings. This kind of film always is applied to improve the corrosion resistance of copper alloys. Microalloying can also improve corrosion resistance. Also, for high Zn containing brass alloys, the prevention of dezincification always focuses on the selection of the alloy for a given application. According to the required application, alloying and cathode protection are the most popular methods to reduce the corrosion rate of copper and its alloys. However, organic inhibitors have recently shown a remarkable protective effect on the copper, opening the path for a new corrosion protection strategy applicable for microdevices, which can be combined with other prevention methods.

1.2.1 Traditional methods

Since the reactions which occur on the copper alloys' surface should follow the fundamental kinetics of electrochemistry, several electrochemical tests had been put into practice. Cornwell et al. [43] and Pourbaix [51] found that the different processes during corrosion showed different potential under chloride water. If one of the potentials cannot be satisfied, the reaction will slow down, and thus the corrosion will be inhibited. It should also work for brasses with the α-phase. The kinetics of cathodic protection of copper under soil [52] and seawater [53] environment was investigated. Although cathodic protection and alloying could provide protection, the problem is still present. Cathodic protection always needs a careful design for all components.

Minor addition of elements such as Fe is another protection method. From the study of North and Pryor [54], ferrous ions are oxidized and form colloids, and then a layer of lepidocrocite will cover the surface and inhibit the corrosion. The dezincification is accelerated by high-temperature, chloride content, low flow rates, and differential aeration, which means that reducing each of the factors will slow down the process. Under

the selection rule of brass, to avoid the dezincification, usually, 0% to 15% zinc will not dezincify, 15% to 36% zinc will resist dezincification if arsenic is added [55], >36% zinc will dezincify, the addition of 1% tin will slow it down [12]. The traditional methods are widely used in applications, but all of them have their own yields as well. Coating and the alloying may cause harmful dissolution like pollution of arsenic.

1.2.2 Corrosion Inhibitors

A corrosion inhibitor is a chemical compound that, when added to a liquid or gas, decreases the corrosion rate of the material, typically a metal or an alloy, that comes into contact with the fluid [56]. When a thick layer of film can not be applied, inhibitors show relatively high potential for protection. However, the performance of the inhibitors relies on the surface condition of the alloy, liquid flow and composition of the solution. Corrosion inhibitors are common in the industry, but since the toxicity of the applied organic and inorganic compounds, they can not be applied in all environments. Inorganic inhibitors always involve the formation of a passivation layer, which prevents access of the corrosive substance to the metal. On the contrary, organic inhibitors show adsorption behaviour on the metal surface; an organic-metal complex layer will be formed on the surface and provide the protection, known as self-assembled monolayers (SAMs) as well. As a comparison, the passive film typically produces a micrometer thickness layer, but the SAMs are only one to a few molecules thick, which is nanometre thickness. This results in a particular advantage for modern areas of materials research, such as microelectronic devices or micromechanics. Besides, the stability of the passive layer can be affected by the pH of the environment.

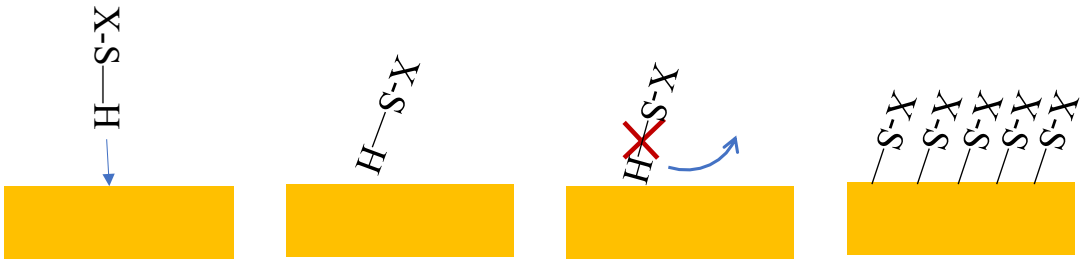

Figure 1.7 Formation of SAMs of thiol on Au

The first SAMs, reported by Bigelow et al. [57], consisted of monomolecular layers obtained by adsorption (self-assembly) of a surfactant onto a clean metal surface. Compared with other ultrathin films such as chemical vapor deposited (CVD) film, they are highly ordered and oriented, and the dense and stable structure leads to a potential application of SAMs on corrosion prevention. Specific research was carried on the typical self-assemble phenomenon between thiols and gold. Bain et al. [58] pointed out that there is evidence that binding of thiols to gold through a thiolate moiety, but throw no light on the mechanism for the conversion of the thiol to thiolate. Moreover, their study also observed two kinds of kinetic at relatively dilute solutions (10^{-3} M). Rapid adsorption in

few minutes is described well by diffusion-controlled Langmuir adsorption. Furthermore, slow adsorption lasts several hours, at the end of which the thickness and contact angles reach their final values, which can be interpreted as a surface crystallization process. **Figure 1.7** shows an estimated procedure of adsorption of thiol onto the gold surface, and the adsorption includes two processes, physisorption and chemisorption.

As illustrated before, adsorption on gold benefits from an oxide-free surface, but oxides always exist on the base metals, which suffer corrosion. Several approaches have been used to control, inhibit and eventually suppress corrosion in metals, and specifically in copper. Between them, corrosion control in aqueous solution has been attempted by adding both inorganic and organic inhibitors. Organic inhibitors show, in general, a better performance than inorganic ones [59]. As mentioned before, the strategy includes the production of the passive film and the addition of other elements. The inhibitor also can assist the passivation of the alloy; as the research showed, heterocyclic compound benzotriazole inhibits corrosion of copper and copper alloys by the blocking action of the copper-benzotriazole complex [60,61]. Among them, azole compounds are known for their ability to inhibit the corrosion of Cu based materials [62,63], with benzotriazole being a notable example that has been widely used.[64] The mechanism of complex formation is proposed and described by the following reactions [65]:

$$Cu_{(s)} + BTAH_{(aq)} = Cu{:}BTAH_{(ads)} + H^{+}_{(aq)}$$

Mercapto based azoles are also promising [66,67]. Several amino derivatives have been studied. Sherif et al. investigated the copper inhibition of N-phenyl-1,4-phenylenediamine (NPPD) in de-aerated, aerated, and oxygenated HCl [68] and NaCl [69], finding that the oxidation of copper to a Cu^{+}-NPPD complex film protects the surface. A.A.El Warraky [70] investigated the influence of ethylenediamine (EDA) on Cu in 0.01M HCl with and without the addition of Na_2S.

The thiol group compounds have been widely studied with Au for quite a long period, and it also presents an adsorption behaviour with Cu. Y.S.Tan et al. [71] studied the effect of a series of benzenethiol(SAMs) on copper in 0.5 M H_2SO_4. The inhibition with different additional functional groups increases in the following order: $–CH(CH_3)_2$ > $–CH_3$ > –F > $–NHCOCH_3$ > $–NH_2$. H. Baba et al. found large inhibition by anodic treatment with triazinedithiols (TDT) in 3% NaCl solutions, and polymerization in the surface film improved the inhibition as well[72]. Other organic inhibitors were investigated, such as amino acid [73], phosphates [74], aniline derivatives [75], and so on. However, the search for less toxic and effective alternatives is still an active research subject. The low- and non-toxic imidazole derivatives corrosion inhibitors were studied by Stupnišek-Lisac [76,77], and showed an inhibition close to the commercial ones.

1.3 Cu-based Metallic glasses and its corrosion

Glasses have a long history in human society, in the form of natural and artificial products, which significantly changed our lives. Metallic glasses have a much shorter history, but since the publication of Klement et al. [78] they have been used in a variety of areas such as aerospace, power transmission, electronic devices, etc. Moreover, the uniqueness of the metallic glass structure provides a chance for a deeper understanding of materials science and condensed matter physics. Metallic glasses are amorphous metallic alloys produced by fast quenching from the melt; crystallization is suppressed by the sudden increase of viscosity during the cooling; this causes the alloys to retain the disordered atomic structure of the parent liquid, as sketched in Figure 1.8a. Metallic glasses can also be produced by alternative methods such as physical vapor deposition, ion irradiation or mechanical alloying. The resulting materials lack medium- and long-range order. Their surfaces are smooth and free of voids, dislocations and/or atomic terraces, features that often contribute to improved corrosion resistance. Unlike ordinary glasses, which are typically electrical insulators, metallic glasses always show good electrical conductivity. Besides, metallic glasses do not have the defects (such as dislocations) and grain boundaries characteristic of crystalline metals, which helps them to present a better resistance to corrosion.

1.3.1 CuZr-based metallic glasses

Zirconium metal has much less industrial importance than Cu, although it is essential in the nuclear industry. It is a very reactive metal, prone to fast oxidation. Zirconium oxide is an essential component of fine ceramics. CuZr alloys are the basis of one of the most exciting families of metallic glasses. From early work, it is known that $Cu_{100-x}Zr_x$ (at.%) metallic glasses can be obtained by melt-spinning in a wide composition range of x = 25 to 60 at.%.[79] The amorphous CuZr system is an excellent glass former, and although the amorphous surfaces are wavy and irregular, they show considerable chemical homogeneity and improved corrosion resistance.[80] It is worth noting that many corrosion studies on CuZr based amorphous alloys were performed in low concentration NaCl solutions, from 0.01 to 0.1 M [81].

1.3.2 Corrosion of Cu-based metallic glasses

Oxidation of amorphous glasses

Oxidation of amorphous glasses is particularly important for its corrosion resistance, since the oxide layer established on the surface will provide improved corrosion resistance. Furthermore, the corrosion resistance will depend on the type and structure of the oxide layer on the surface. Early research on CuZr metallic glass showed preferential oxidation of Zr [82]. Moreover, much more work had been done; **Figure 1.8**

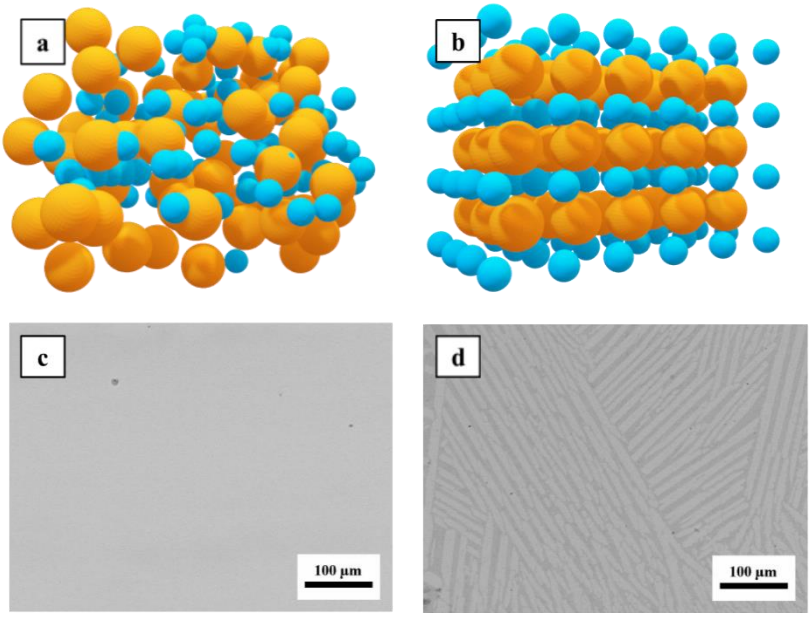

Figure 1.8 Schematic presentation of atomic structures of (a) amorphous and (b) crystalline CuZr alloys. SEM images of (c) amorphous and (d) crystalline $Cu_{40}Zr_{60}$ alloys.

schematically shows the interface structure between electrode and electrolyte, based on the model postulated by Xu et al.[83] The natural oxide passive layer of the CuZr amorphous turns out to be ZrO_2 oxide, developed over a Cu-rich region above the amorphous matrix. The thickness of the ZrO_2 layer increases with the concentration of Zr, and the formation of the Cu-rich region is caused by the diffusion of Zr to the surface. Due to the ultrafast initial oxidation process, the ZrO_2 ultrathin passive film becomes the interface between the sample surface and electrolyte. Besides, the research in the higher temperature of Cu-Ti metallic glass by Park et al. [84] also showed an amorphous TiO_2 – Cu-enriched – metallic glass structure below Tg temperature, similar to that of CuZr amorphous glass at RT. All the researches [82,84–87] on CuZr-based metallic glasses show similar results: Zr will form an amorphous ZrO_2 layer at low temperature, other elements such as Ti, Be will oxide if the temperature increased[84,88], Cu is always the one didn't appear to be oxidized.

Corrosion of Cu-based metallic glass

The comparison of the corrosion mechanisms of crystalline and amorphous alloys of the same stoichiometry would give valuable data regarding the effect of the atomic structure on the inhibitor performance. A number of literature studies are available discussing the properties and corrosion mechanisms of CuZr-based metallic glasses[81,89–91]. Although many CuZr based alloys show good corrosion resistance, such as $Zr_{55}Cu_{20}Ni_{10}Al_{10}Ta_5$ (at.%), $Zr_{50}Cu_{20}Ni_{10}Al_{10}Ta_{10}$ (at.%) or $Zr_{55}Cu_{20}Ni_{10}Al_{10}Ti_5$ (at.%), the parent CuZr alloy is not particularly corrosion resistant. Thus, the observed

differences in corrosion resistance and inhibition may be attributed mostly to the different surface crystalline structures, i.e., the ordered – probably polycrystalline – atomic structure in the crystal vs. the disordered but chemically homogeneous atomic distribution in amorphous alloys[92,93]. This is one argument to choose a binary alloy when comparing the response of crystalline and amorphous alloys; the comparison of corrosion resistant multicomponent alloys with their crystalline counterparts has much less significant as the role of the minor elements would be undiscernible. It has also been noted that an additional source of protection against corrosion in amorphous materials might be the development of amorphous oxide layers; the absence of grain boundaries in these oxide layers may reduce the ion mobility[94].

Chapter 2: Objectives

Organic inhibitor shows immense potential for corrosion prevention. However, a number of aspects influence the inhibitor performance, and a complete analysis goes beyond the possibilities of a Ph.D. This work will focus on the following subjects to contribute to a better understanding of inhibitors.

Correlation between inhibitor and chemical composition of the alloy. Alloying and microalloying always change the properties of the material, which affects the performance of inhibitors. Exploration of this correlation is complicated but significantly important.

Correlation between inhibitor and structure of the material. The understanding of the structure of metallic materials experienced a revolution since the discovery of metallic glasses. And this glass-like structure highly affects the properties and performance of the materials. It offers an opportunity for researching the correlation between inhibition on the amorphous and crystalline structure.

Figure 2.1 Correlation between inhibitor and other two important aspects: structure and alloy composition.

Mechanism and effect of corrosion inhibition of imidazole derivatives, mercapto-benzimidazole derivatives and hydroxy-benzimidazole derivatives on Cu and its alloys. Three related derivatives will assist in exploring the influence of different functional groups added to inhibitors.

Selection of potential inhibitors for Cu-based alloys. The broad application of Cu and its alloys in corrosive environments encourages the search for competitive inhibitors for different applications. This research will explore the potential of inhibitors based on imidazole organic compounds.

Development of a reliable analysis protocol for inhibition measurements. Organic inhibitors show many advantages on corrosion prevention, but since the formation of monolayer, the stability and measurement of this kind of inhibitor present specific difficulties. This research will try to build a series of measurement methods for the characterization of the inhibition performance of organic compounds.

Chapter 3: Materials and Methodology

In this chapter, all the materials applied in experiments will be illustrated. Methods include preparation of the samples and solutions, characterization of samples, setup of the immersion test and their details will be stated as well.

3.1 Materials and chemicals

Materials applied during the experiments obtain in two ways: preparation in our lab and commercial ones. All the chemicals are commercial ones. This section will introduce all the preparation methods of the materials for experiments and the specification of the commercial materials and chemicals.

3.1.1 Pure Metals and Raw Materials

Raw Materials

In the following **Table 3.1**, the purity, form, size and company of raw materials are listed. Before weighing and melting the materials, all the oxide layer were removed by polishing.

Table 3.1 List of raw materials with details

Material	Purity / %	Form	Size	Company
Pure Copper	99.99	Wire	d = 0.5mm	Advent Research Materials Ltd
Pure Copper	99.99	Foil	t = 1.0mm	Alfa Aesar
Pure Zirconium	99.94 excluding Hf, Hf nominal 3%	Foil	t = 0.25mm	Alfa Aesar
Pure Zirconium	99.95 excluding Hf, Hf nominal 3%	Slug	d = 6.35mm	Alfa Aesar
Pure Zinc	99.9	Foil	t = 0.62mm	Alfa Aesar

Pure Metal Samples

Pure Cu and Zn samples for electrochemical measurements are cut from the foil materials from raw materials to around $1cm^2$ triangle pieces. Pure Zr samples for electrochemical measurements are cut from the slug to 6.35mm diameter discs. The preparation of electrochemical samples followed protocol 3.1. Pure Cu, Zn and Zr samples for immersion tests are illustrated in protocol 3.2. Pure Cu and Zn samples were immersed in 0.5M H_2SO_4 solution for 30s and 10s respectively for removing the oxidation from

grounding. Then the samples were cleaned with ethanol in an ultrasonic bath for 3 min, double-rinsed with distilled water and dried with a vacuum desiccator.

Protocol 3.1 Preparing bulk samples of electrochemical measurements

1. As shown in **Figure 3.1**, soldering with a rubber protected copper wire.
2. Embed in epoxy resin and keep the testing side on the bottom in the mould.
3. Take out from the mould and sequentially ground with P600, P1200, P2000, P4000 SiC (CarbiMet) abrasive paper.
4. Polish with 6 μm, 3 μm and 1 μm MetaDi diamond suspensions (Buehler).
5. Clean with ethanol in an ultrasonic bath for 3 min, double-rinsed with distilled water and dried with vacuum desiccator.

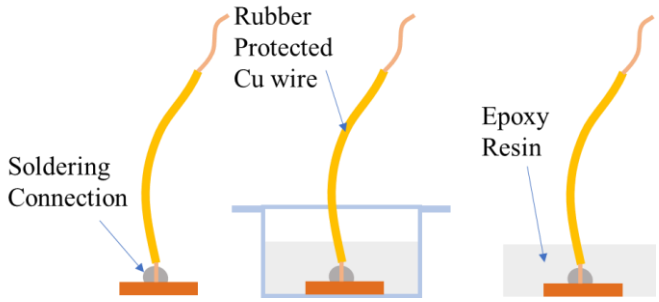

Figure 3.1 Preparation method of bulk samples for electrochemical measurements

Protocol 3.2 Preparing bulk samples of immersion test

1. Cut a triangle piece from the foil materials and then sequentially ground with P600, P1200, P2000, P4000 SiC (CarbiMet) abrasive paper.
2. Clean with ethanol in an ultrasonic bath for 3 min, double-rinsed with distilled water and dried with vacuum desiccator.
3. Pickling the surface and rinse with DI water. (Depends on the materials)
4. As shown in **Figure 3.2**, prepare two pieces of PTFE tape, and cut a window around 1 × 1 cm2 from one piece.
5. Put the window to the centre of the sample surface and cover the sample by two pieces of the tape.
6. Measure the sample surface area and put the sample vertical to the bottle, keep a distance from the sample surface to the bottle and other samples.
7. Pour the solution into the bottle with a solution/surface ratio of 25ml/cm^2.
8. Seal the bottle and keep it in the box covered the sunshine.

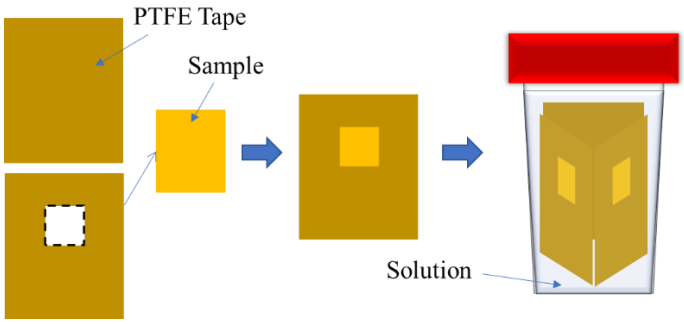

Figure 3.2 Preparation of bulk sample for immersion test

3.1.2 CuZn and other alloys

Cu/Zn (70/30) brass (alloy 260) sheet with a typical composition of alloy: Cu 68.5-71.5%, Pb 0.07% max, Fe 0.05% max, Zn remainder, and the thickness is 0.81mm, from Alfa Aesar. Cu/Zn (30/70) brass was melted by induction melting in melt spinner in a quartz crucible. The alloy was melted for 10min around 900℃ and cooling down slightly by control heating frequency. The bulk cylinder sample was then heated to 700℃ in 1 hour and stay for 1h for annealing in a muffle furnace, then cooling down in a furnace. The cylinder sample was cut into discs around 10mm diameter by a low-speed diamond saw. The Cu/Si (95/5), Cu/Al (95/5), Cu/Ni (95/5) and Cu/Ni (70/30) alloys are followed the same procedure to prepare the electrochemical samples. And preparation of the electrochemical samples is illustrated in the protocol. Preparation of the immersion test for Cu/Zn (70/30) and Cu/Zn (30/70) brass is illustrated in protocol and samples were immersed in 0.5M H_2SO_4 solution for 30s and 15s respectively for removing the oxidation from grounding. Then the samples were cleaned with ethanol in an ultrasonic bath for 3 min, double-rinsed with distilled water and dried with a vacuum desiccator.

3.1.3 CuZr Crystalline and Amorphous alloys

Crystalline CuZr samples for corrosion tests were produced from high purity raw materials were melted in high vacuum induction with a quartz crucible for 15mins and cooled gradually. Crystalline CuZr samples for corrosion tests were produced from high purity raw materials shown in **Table 3.1**. Samples were melted twice on an arc melter oven (Compact Arc Melter MAM-1, Edmund Bühler GmbH) provided with a water-cooled plate, on a Ti-gettered Ar (99.995% Nippon gases) atmosphere at a pressure of ~700 hPa. Heat treatment was at ~650 ℃ for 1h and cooling down in the furnace. Circular samples and brass sheets were cut with a low speed diamond saw from the arc melted alloy, having a surface area of 0.5 – 1.0 cm^2. Preparation for electrochemical and immersion test samples were introduced in protocols 3.1 and 3.2.

Amorphous ribbon materials of approximately 40 μm thickness and 1.5 mm in width were produced on an Edmund Bühler melt spinner in Ar (99.995%) atmosphere at 1 mm of crucible-wheel distance surface and wheel velocity of 40 ± 1 m/s (**Figure 3.3** a, b).

Corrosion tests for amorphous samples were performed on the free side of the ribbons which acted as the working electrode. For preparing the ribbon for measurements, it was connected to a pure copper (99.9%) strip by a PTFE tape to get an electrical connection; the copper strip and the wheel side of the ribbon were then covered by PTFE tape (**Figure 3.3** c).

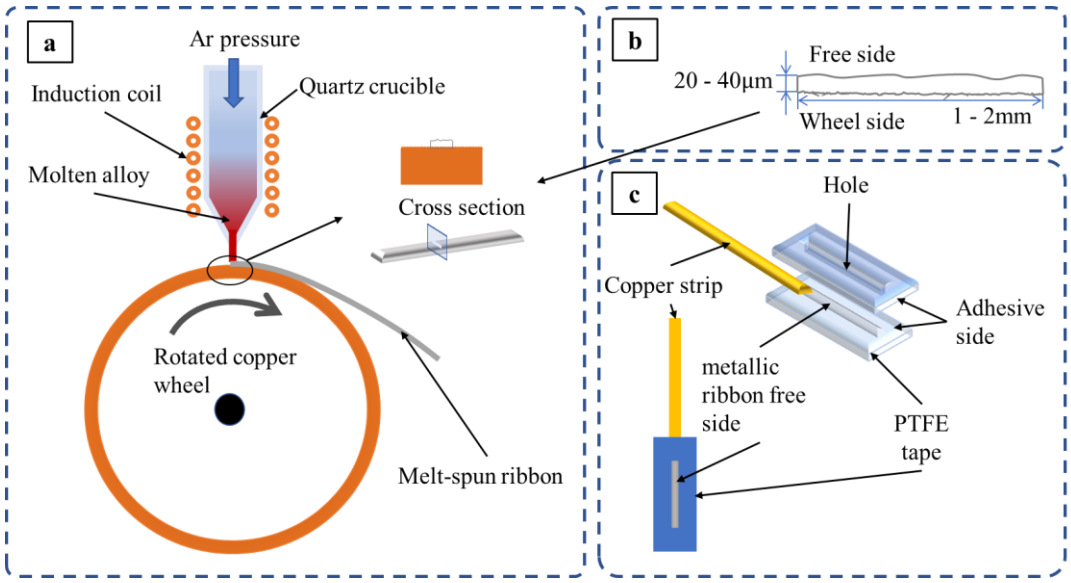

Figure 3.3 Preparation of amorphous samples. (a) Synthesis of amorphous ribbons. (b) Sketch of the surface cross-section of the amorphous ribbons. (c) Preparation method of amorphous ribbon samples for corrosion testing.

3.1.4 Chemicals

Electrochemical corrosion tests and immersion tests were carried out in 3 wt.% (0.51 M) NaCl (Panreac Quimica (p.a.)) aqueous solution with or without the addition of organic compounds tested as corrosion inhibitors. Nine compounds were tested. To facilitate the presentation, they are divided into three groups:

(1) imidazole derivatives: imidazole (ImiH, 99.5%), 2-mercapto-1-methylimidazole (SH-ImiMe, 99%), 2-mercapto-4-phenylimidazole (SH-ImiH-4Ph, 97%),

(2) mercapto-benzimidazole derivatives: 2-mercaptobenzimidazole (SH-BimH, 98%),

2-mercapto-5-methoxybenzimidazole (SH-BimH-5OMe, 99%), 5-amino-2-mercapto-benzimidazole (SH-BimH-5NH_2, 96%), 2-(methylthio)benzimidazole (Me-S-BimH, 97%), and

(3) hydroxy-benzimidazole derivates: 2-hydroxybenzimidazole (OH-BimH, 97%), benzimidazole-2-methanol (OH-Me-BimH, 97%.

All compounds were used at a concentration of 1mM. Skeletal formulae of the inhibitors are presented in **Figure 3.4**. Benzimidazole-2-methanol was supplied by Fluorochem, and other inhibitors were supplied by Sigma–Aldrich. Compounds were used as supplied.

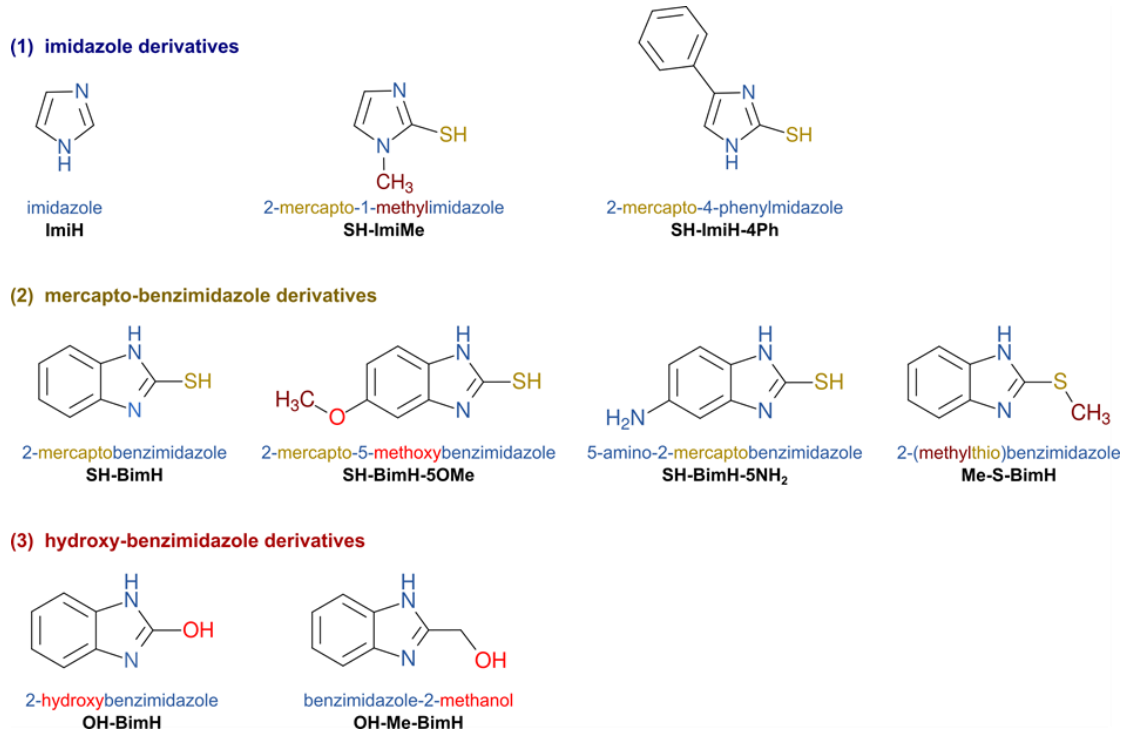

Figure 3.4 Skeletal formulae of the organic molecules and their shorthand labels, tested as corrosion inhibitors in this work, and their classification into three groups: (1) imidazole derivatives, (2) mercapto-benzimidazole derivatives, and (3) hydroxy-benzimidazole derivatives.

3.2 Structural characterization

The crystalline and as-cast ribbons were examined using Bruker D8 Advance X-ray diffractometer (XRD) equipped with Cu Kα X-ray tube with radiation (λ=1.5418 Å) in Bragg-Brentano geometry. The thermal stability of the amorphous samples was evaluated using a NETZSCH DSC 404 F3 differential scanning calorimeter (DSC) at a heating rate of 20 K/min under a flow of high purity N_2.

3.3 Electrochemical measurements

Electrochemical tests were performed in a three-electrode corrosion cell (volume 0.1 L, Bio-logic SP-200, France) at 25 ºC in 3 wt.% NaCl. An Ag/AgCl (3.5 M KCl) electrode (+0.205 V vs. saturated hydrogen electrode at 25 ºC) was used as a reference electrode and a spiral platinum wire (~3.6 cm^2) was used as a counter electrode. Specimens' surface exposed to the solution was around 0.5−1.0 cm^2 for crystalline samples and around 0.05−0.2 cm^2 for amorphous ones. Measurements were carried out with a SP-200 Bio-

Logic (Bio-Logic Science Instruments, France) potentiostat/galvanostat operated by the EC-Lab software. The specimens were stabilized under open circuit condition for 1 hour before the measurements. During that time, the open circuit potential was measured as a function of time. The stable, quasi-steady state potential reached at the end of the stabilization period is denoted the open circuit potential (OCP). Electrochemical tests and immersion tests were both under the dark condition based on ref. [95] to avoid the influence of the light.

3.3.1 Linear Polarization Resistance

This measurement only applied to the crystalline samples and due to the uniform dielectric of ZrO_2 on CuZr amorphous alloy, it will not show a stable result. Linear potentiodynamic polarization curves were recorded starting at −10 mV negative to OCP, then increasing the potential in the anodic direction to 10 mV at a potential scan rate of 0.1 mV/s. All the measurements were performed at least three times, and the typical standard deviation is below 12%. Then a line regression was applied on the curves and the linear polarization resistance (R_p) will be obtained. Crystalline samples were polished before every measurement. Another long-term measurement was carried out after 1 h at the OCP and up to 120 h immersion in periods of 24 h.

3.3.2 Potentiodynamic measurements

Potentiodynamic polarization curves were recorded starting at 250 mV negative to OCP, then increasing the potential in the anodic direction at a potential scan rate of 1 mV/s. A maximum positive potential of 650 mV, relative to OCP, was applied to crystalline samples, and of 250 mV for amorphous due to the thickness of the ribbon. All the measurements were performed at least twice, and the typical standard deviation is below 12%. Crystalline samples were polished before every measurement, while all measurements on amorphous samples were performed on fresh ribbons.

3.3.3 Electrochemical impedance spectroscopy

Electrochemical impedance spectroscopy (EIS) measurements were performed at open circuit conditions in the frequency range from 10^5 Hz to 10^{-2} Hz. AC excitation voltage was 10 mV. EIS spectra were recorded after 1 h at the OCP and up to 120 h immersion in periods of 24 h.

The modulus of impedance $|Z|$ at a frequency of 10^{-2} Hz was taken as a significant parameter of the corrosion resistance of the metal covered by an inhibitor layer. The typical standard deviation of the measurements is around 15%, and in all cases below 30%

3.4 Immersion Tests

Immersion tests were carried out in a sealed polyethylene container with an electrolyte volume/sample surface ratio larger than 25 mL/cm^2. Cu/Zn (70/30) brass sheets were polished to P4000 and clean with ethanol in ultrasonic for 3 minutes, and then rinsed with DI water. Cu/Zn (70/30) brasses and pure Cu samples were immersed for 2 months. Cu/Zn (30/70) brasses and pure Zn were immersed for 12 days. Pure Zr samples were immersed for one year due to the great corrosion resistance. Amorphous alloys $Cu_{50}Zr_{50}$ and $Cu_{64}Zr_{36}$ were immersed for 5 days and $Cu_{40}Zr_{60}$ for 12 days due to its good corrosion resistance, immersion method was shown in **Figure 3.5**. All crystalline alloys were immersed for 5 days.

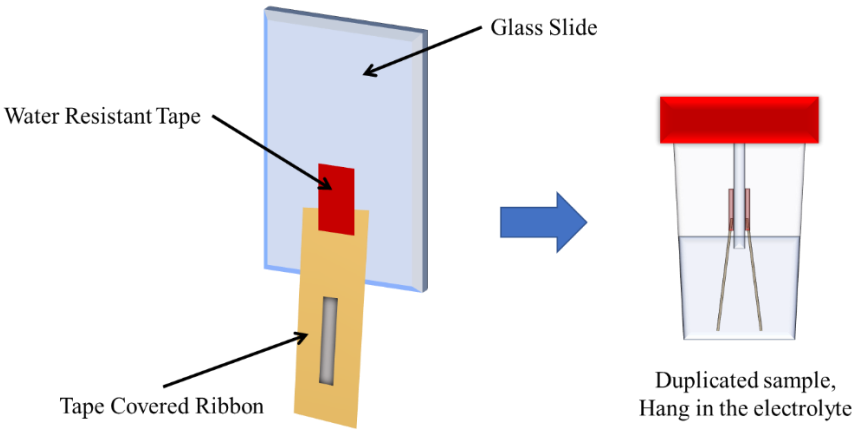

Figure 3.5 Preparation of immersion test for amorphous alloys

3.4.1 X-ray Photoelectron Spectroscopy

X-ray photoelectron spectroscopy (XPS) was performed with a SPECS system equipped with a Phoibos 150 MCD-9 detector and an Al anode XR50 source operating at 150 W. Scan step for high-resolution analysis is 0.1 eV. Due to the complexity of the surface conditions, qualitative analysis was applied to these spectra instead of quantitative analysis. The diameter of the analyzed spot was 1 mm^2. CasaXPS program (Casa Software Ltd., UK) was used to evaluate the XPS data (Shirley type background). The analyzed elements of pure Cu and $Cu_{70}Zn_{30}$ alloy are the same: Cu 2p, Cu LMM. O 1s, Cl 2p. C 1s, N 1s and S 2p.

3.4.2 Photography

The photos after the immersion test were taken by a Nikon D750 camera with a Lens of 28-300. The light condition was under a KAISER RS1 system equipped a pair of Kaiser RB 218 Daylight Set, with a colour temperature (Kelvin) of 5400K. The photographic parameters were fixed at the focus of F16, ISO of 200 and shutter speed of 1/13s. Distortion correction was based on the official database and useless parts were cropped

from the photo. All the photos were taken after rinsed with DI water. And some of the photos of Cu/Zn (70/30) were taken after rinsing with ethanol in the ultrasonic base.

3.4.3 Optical Microscopy

Optical microscopy Nikon ECLIPSE LV100D was only applied to CuZr alloys, pure Cu and Zr alloys for immersion tests. Other alloys presented a thick organic layer and optical microscopy can hardly offer information.

3.4.4 SEM-EDX

For pure Cu and Zn and CuZn alloys, the surfaces were analysed with a scanning electron microscope (SEM) from Phenom XL Desktop SEM with a Backscattered electron detector. And the elements were analysed by energy-dispersive X-ray spectroscopy equipped with the SEM. 3D roughness reconstruction by using the ProSuite software application platform was applied. EDX equipped with silicon drift detector (SDD), thermoelectrically cooled (LN_2 free) system and ultra-thin silicon nitride (Si_3N_4) window allowing detection of elements B to Am, the energy resolution Mn K$\alpha \leq$ 132 eV. The CuZr sample surface was analysed with a scanning electron microscope (SEM) at electron beam energy of 15 keV on a Neon40 Crossbeam™ workstation.

3.4.5 Raman Spectroscopy

The micro-Raman spectroscopy system from Renishaw's inVia Qontor Raman microscope and its Windows-based Raman Environment (Wire™) software are applied for the measurements of Cu, Zn and CuZn alloy samples. A monochromatic light source of the visible laser at 532 nm with a nominal 100 mW output power was used.

3.5 Experimental plan

A series of experiments will be applied to understand the mechanism of inhibition in pure metals and alloys. The first measurement will be a couple of electrochemical tests include linear polarization resistance, impedance spectroscopy and potentiodynamic polarization after 1 h immersion in 3wt% NaCl aqueous solution and in the presence of different organic compounds added at 1 mM concentration. This will show a roughly inhibition ability. The inhibitor will be identified as a useless inhibitor if there is no significant improvement. But the initial result can only offer a view of inhibition after 1 h immersion. Then a couple of long-term (~120h) electrochemical tests include LPR and EIS will be carried out to figure out the durable inhibitors. LPR and EIS are nearly effect-free measurements that will not destroy the adsorption between inhibitors and material surface. In this part, Rp and impedance modulus at 0.01Hz will be the indicator for inhibition, and Nyquist plots can show the corrosion behavior during the long-term immersion. Then, the inhibitors present great inhibition will be analyzed by XPS after 1 day and 5 days'

immersion. This will offer a view of bonding, such as bonding type and which function group bond on the surface. However, this kind of measurements are still not long enough to check the inhibition close to the real application. Immersion test will be applied for a longer period, immersion duration depends on the corrosion resistance of each material. After the immersion, the samples will be analyzed by photography, OM, SEM-EDX and Raman spectroscopy. All these methods are aimed to reveal the influence of inhibitor during immersion and build the connection with previous tests.

4 Corrosion Inhibition of Pure Materials

As introduced before (add some ref.), Cu and its alloys show great potential for applying organic inhibitors to improve corrosion resistance. Therefore, the measurements will initially focus on the interaction of pure Cu and inhibitors, which is the most important indicator for the inhibition ability. This introduces the possibility to improve the corrosion resistance of pure Cu and its alloys, especially when they present the same α-Cu phase. There is much less information on the inhibition efficiency of Zn and Zr. Therefore, here we will report the inhibition efficiency of the three pure metals.

4.1 Corrosion Inhibition of Copper

Short- and long-term electrochemical tests were performed on pure Cu. Based on the results from electrochemical measurements and visual analysis, XPS was performed to identify the adsorption mechanism. 60 days' immersion tests will assist in understanding the influence of inhibitors in a near practical condition. Furthermore, the immersion tests were analyzed by means of SEM-EDX, OM and Raman spectroscopy for a better understanding of the surface evolution.

4.1.1 Short-term electrochemical tests

Linear polarization resistance can be derived from Volmer-Butler equation

$$i = i_0\left[e^{-\alpha f\eta} - e^{(1-\alpha)f\eta}\right]$$

where i is the current, i_0 is exchange current, α is the transfer coefficient, η is the overpotential and $f = \frac{F}{RT}$ is a constant. When the overpotential η is close to 0, the exponentials can be approximated by their Taylor expansion, $e^x \sim 1 + x$, and the current can be expressed as:

$$\mathrm{i} = -i_0 f\eta$$

and by dividing both sides by i, the linear polarization resistance is $R_p = -\frac{\eta}{i}$ and it is often identified with the charge transfer resistance, hence

$$R_{ct} = \frac{RT}{Fi_0}$$

Low frequency impedance can also be taken as a good indicator of corrosion resistance. Let's consider the effect of inhibitor addition to corrosive solution. As illustrated in the introduction part, the physisorption takes place significantly fast and good inhibitors arrange on the surface, as shown in **Figure 4.1**. Since the interference is quite small as in LPR, when the frequency reaches a value low enough the slow alternating potential can

allow enough time for driving the charge transfer process. The modulus of the low frequency impedance is taken as a convenient figure of merit. Therefore, linear polarization resistance and impedance both reflect the combined action of coverage rate and adsorption stability of inhibitors.

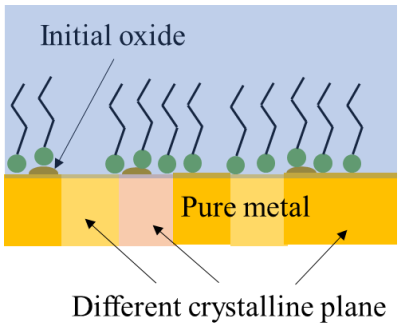

Figure 4.1 Schematic diagram of inhibitor adsorb on the sample surface at 1h

Figure 4.2 left shows the polar plot of R_p of Cu in the presence of the tested inhibitors in logarithmic scale. The corresponding short-term linear polarization curves are presented in **Figure A1.1**. **Figure 4.2** right displays a polar graph of the modulus of the impedance at 0.01Hz. Compared to each other, the impedance and resistance in logarithmic scale are relatively close. Furthermore, inhibition behaviors are the same. From these measurements, it is found that SH-BimH, Me-S-BimH, SH-BimH-5OMe, SH-ImiH-4Ph and OH-Me-BimH are effective inhibitors while ImiH, SH-BimH-5NH_2, SH-ImiMe and OH-BimH act as corrosion accelerators. The effect of every functional group is complex. In imidazole derivatives, ImiH induces corrosion acceleration, while it shows the best inhibition among all inhibitors by adding -SH and -Ph group; the addition of -SH and -Me is almost neutral. In mercapto-benzimidazole derivatives, the addition of -Me on -SH and -OMe on the benzene ring both improve the resistance, but the -NH2 on the benzene ring accelerates the corrosion process. The addition of -SH on -OH turns the accelerator OH-BimH into a good inhibitor in the hydroxy-benzimidazole group. Furthermore, other factors may influence the adsorption process, such as the crystalline plane, the initial oxide on the surface, the presence of grain boundaries, etc..

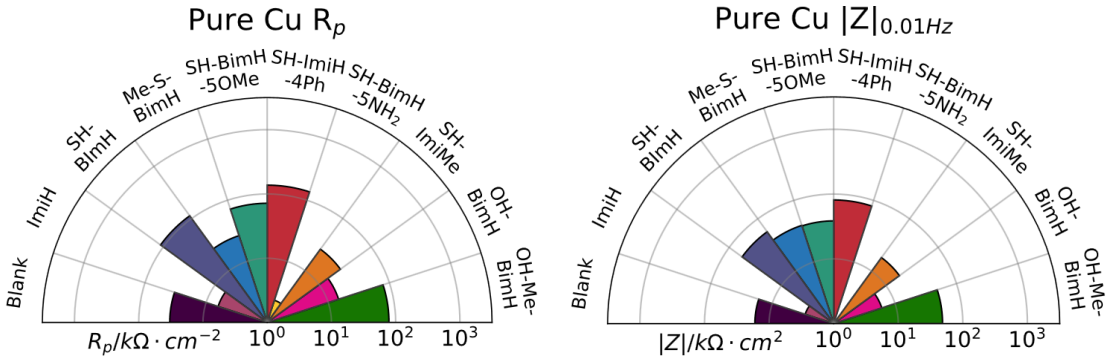

Figure 4.2 Polar graphs of linear polarization resistance (left) and impedance modulus at 0.01 Hz (right) of pure Cu, measured after 1 h immersion in 3 wt.% NaCl aqueous solution (blank) and in the presence of different organic compounds added at 1 mM concentration. Note the logarithmic scale.

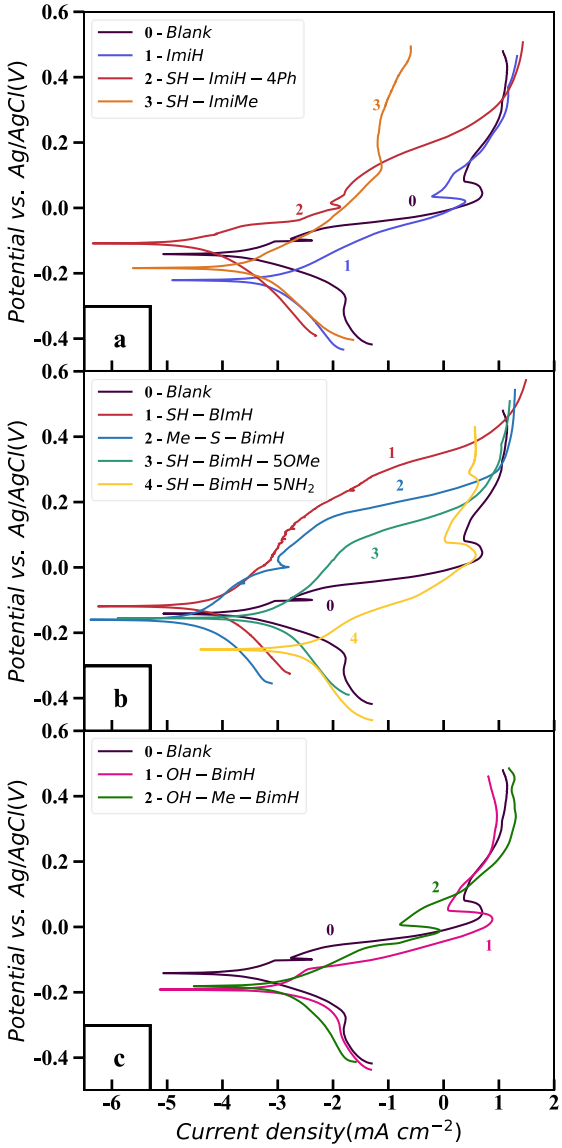

Figure 4.3 Potentiodynamic polarization curves of pure Cu in 3 wt.% NaCl aqueous solution with and without 1 mM of different organic compounds: (top) imidazole derivatives, (middle) mercapto-benzimidazole derivatives, and (bottom) hydroxy-benzimidazole derivatives. Quantitative electrochemical parameters are presented in **Table 4.1**.

The value of Rp and |Z| offers a first glance of the potential as corrosion inhibitors of the tested molecules, but the influence on kinetics must be assessed. The schematic diagram of **Figure 4.1** can be used to describe the material's response to a bigger range of potentiodynamic polarization. From a quantum mechanics description, the energy of electrons at the interface between the solution and the Cu surface depends on the potential applied on the electrode [96]. If the potential is driven towards a positive value, the energy of electrons at the Cu surface will decrease. At a given energy level electrons will be released and the neutral Cu atoms become ions. This is the onset of the anodic reaction. However, inhibitor adsorption may inhibit this process, reducing the corrosion rate, which means that the kinetics of the corrosion process will be modified. At higher positive potential values desorption may take place due to the higher energy level. On the contrary, cathodic reactions resulting of negative polarization result typically into Hydrogen production and are in principle less damaging for the alloy. Potentiodynamic polarization curves and quantitative electrochemical parameters derived from the polarization curves for Cu in the presence of potential inhibitors are presented in **Figure 4.3** and **Table 4.1,** respectively. In the case of Cu in NaCl solution with imidazole derivatives (**Figure 4.3** a), ImiH acted as an activator, while SH-ImiH-4Ph and SH-ImiMe acted as inhibitors causing a decrease in current density and shifting in E_{corr} to more anodic values [66,97]. As shown in **Figure 1.4**, the Pourbaix diagram for copper-chloride-water system, at a pH~7(expected for a 0.51 M NaCl solution), a transition happens around -0.1V in the blank curve corresponding to the switch between oxidation to CuO and Cu_2O. It is also observed on SH-ImiH-4Ph. However, it is not observed in

both ImiH and SH-ImiMe. ImiH, SH-ImiMe and blank curve show a passivation region around 0 – 0.1V, but the behavior of SH-ImiMe is quite different from that of the other two; this may indicate a different kind of passivation introduced by the inhibitor. For SH-ImiH-4Ph, passivation appears above 0.3V.

In **Figure 4.3** b, Mercapto-based derivatives showed better performance with the corrosion current densities j_{corr} decreasing in the following order: j_{corr}(SH-BimH) > j_{corr}(Me-S-BimH). SH-BimH-5OMe and SH-BimH-5NH_2 acted as activators. Similarly than for imidazole derivatives, SH-BimH, SH-BimH-5OMe and SH-BimH-5NH_2, seem to delay oxidation on the cathodic side, and passivation was also extended to more than 0.2 V. Hydroxy-benzimidazole derivatives also acted as corrosion activators.

Efficient inhibitors on Cu acted as mixed type inhibitors with a strong inhibition of the anodic reaction. The inhibitors have different influences on surface reaction, as some of the inhibitors can stop the oxidation to Cu_2O, SH-ImiMe changed the passivation process due to the appearance of a new passivation region in the anodic range. But the common feature of effective inhibitors in the figures is the extension of passivation range and a slower current increasing rate in anodic polarization range.

Table 4.1 Cu Metal Tafel Parameters (cf. **Figure 4.3**).

Solution	E_{corr} (mV) vs. Ag/AgCl	j_{corr} （μA/cm^2）	$-\beta_c$ (mV/dec)	β_a (mV/dec)
3 wt.% NaCl	−139	0.657	84	81
ImiH	−218	1.030	83	200
SH-ImiMe	−184	0.437	117	152
SH-ImiH-4Ph	−76	0.055	27	155
SH-BimH	−119	0.117	186	185
SH-BimH-5OMe	−153	1.045	177	215
SH-BimH-5NH_2	−239	2.258	82	206
Me-S-BimH	−161	0.030	146	103
OH-BimH	−133	5.372	34	447
OH-Me-BimH	−164	1.860	76	245

Figure 4.4 shows the Electrochemical impedance spectra of pure Cu alloy in the form of Bode impedance plot, phase angle plot and Nyquist plot. The observable first semicircle is an indication of Warburg impedance and its radius gives an idea of the inhibition effect. The appearance of Warburg impedance indicates that semi-infinite diffusion appears at low frequency, which means that charge transfer can be big enough and diffusion is the controlling factor of the corrosion behavior. Good inhibitors reduce the process of charge transfer in the corrosion reaction. The radius of the first semicircle indicates the impedance of the charge transfer, so a larger radius indicates better inhibition on the charge transfer process. As for the phase angle diagram, a peak and valley mean that a new time constant appears at a given frequency, indicating a new reaction happens. The presence of an inhibitor will increase the complexity of the corrosion reaction. Therefore,

if a single time constant can be identified a uniform layer is built, while multiple time constants may indicate partial coverage or different corrosion mechanisms in different areas. This will assist in understanding how inhibitor works during tests. However, this is a short term measurement which has to be confirmed with long term tests.

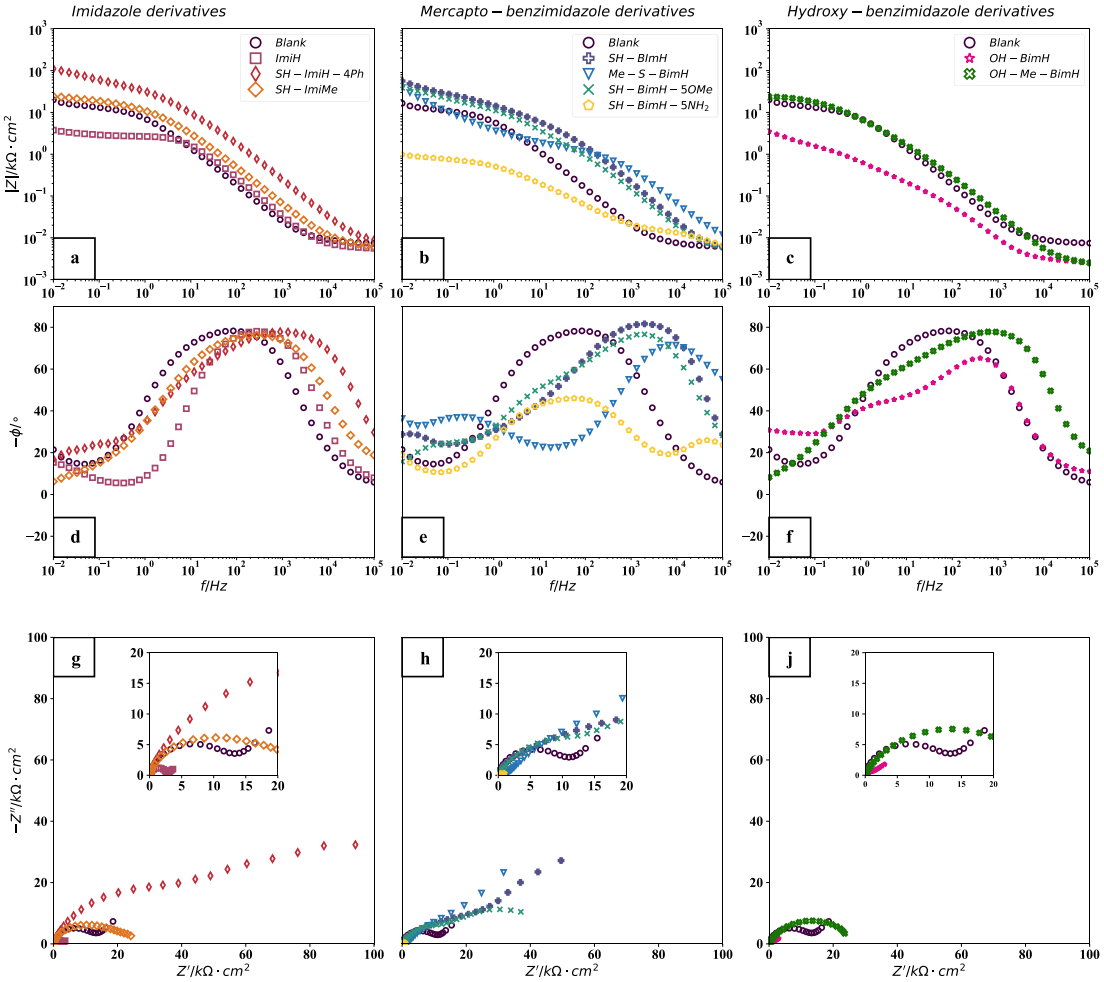

Figure 4.4 Electrochemical impedance spectra of pure Cu alloy in the form of Bode impedance plot, phase angle plot and Nyquist plot with or without addition of 1 mM of different organic compounds in aqueous 3 wt. % NaCl solution: a), d), g) imidazole derivatives, b), e), h) mercapto-benzimidazole derivatives, and c), f), j) hydroxy-benzimidazole derivatives.

As shown in figure 4.4, pure Cu in NaCl solution shows a typical charge transfer domain semicircle, and the semi-infinite diffusion domain region appears as a straight line with a slope of 45°. Only a clear time constant is observed in the phase angle diagram. The figures of the left column (a, d and g) show the curves obtained in presence of imidazole derivatives. In **Figure 4.4** d, all these derivatives show only one clear time constant, which may indicate that only one uniform layer was formed or no significant inhibition effect happened. Imidazole shows a corrosion behavior similar to that of the blank curve, but with smaller impedance. **Figure 4.4** g shows the Nyquist plot, the appearance of ImiH is again like the blank curve, with a smaller semicircle, which indicates acceleration of

corrosion by reduction of charge transfer. Combined with the phase angle diagram, it may be concluded that ImiH cannot form a layer to protect Cu but can even assist the corrosion reaction. SH-ImiH-4Ph shows a large semicircle and the curve continues with an angle smaller than 45°; the phase angle diagram shows that the smallest angle is larger than ~20°. Both results indicate that SH-ImiH-4Ph contributes to control the diffusion. SH-ImiMe shows a larger semicircle than the blank solution, and the curve shows no diffusion-controlled region.

The middle column of **Figure 4.4** (b, e and h) shows the EIS spectra of mercapto-benzimidazole derivatives, SH-BimH and Me-S-BimH show a similar curve in the Nyquist plot and phase angle plot, SH-BimH-5OMe is much more close to SH-ImiH-4Ph, and SH-BimH-5NH_2 shows a significantly smaller semicircle and phase angle, which indicates that the acceleration of corrosion is quite strong. SH-BimH and Me-S-BimH show another time constant at low frequency, and in the Nyquist plot, a second larger semicircle seems to appear at low frequency. SH-BimH-5OMe shows a larger semicircle than blank and the second semicircle appears at low frequency similarly than for SH-ImiH-4Ph, who shows two smaller semicircles. Hydroxy-benzimidazole derivatives are presented in the right column of **Figure 4.4** (c, f and j). OH-BimH shows active corrosion behavior with a very small semicircle. OH-Me-BimH shows a larger semicircle with a single time constant.

Overall, SH-ImiH-4Ph, SH-ImiMe, SH-BimH, Me-S-BimH, SH-BimH-5OMe and OH-Me-BimH are good inhibitors by inhibiting the charge transfer process, and some of them show another pressed semicircle as well. Me-S-BimH and SH-BimH-5OMe show two time constants, which indicates that the inhibition effect is sensitive to frequency. The short-term tests show that SH-ImiH-4Ph, SH-BimH, SH-BimH-5OMe, Me-S-BimH are good corrosion inhibitors for pure Cu. Subsequent long-term tests will reveal the stability of the inhibitors.

4.1.2 Long-term electrochemical tests

Short-term electrochemical tests offer a quick test of the inhibition efficiency. However, corrosion is a long-lasting process; hence, long-term electrochemical tests are necessary to figure out which molecules are actually good corrosion inhibitors. In this section, long-term test of linear polarization resistance and EIS will be analyzed for a better description of corrosion inhibition on pure Cu.

Figure 4.5 exhibits two plots of long-term measurements. The left figure shows the linear polarization resistance versus time, while the right figure shows the impedance modulus at 0.01 Hz versus time. Both vertical axes are displayed with a logarithmic scale. LPR plots show the error bars obtained from three different measurements, as they are simple and fast. The results of both measurements are mutually consistent; the LPR measurements of almost all the inhibitors follow the same trends than the EIS measurements.

Pure Cu in 3 wt. % NaCl solution shows good corrosion resistance since there is no big drop in the resistance and impedance. This may result from the formation of a film of Cu_2O as discussed in ref. [37]. SH-ImiH-4Ph shows the best resistance and impedance after 120h, and the value keeps increasing with time. SH-BimH, OH-BimH and OH-Me-BimH show a good inhibition as well, the values at 120h are all larger than the one at 1h. However, OH-BimH has a different inhibition behavior; it didn't show any inhibition effect at the first 1 h, but it reached a relatively high resistance and impedance after 120 h. At the first measurements carried at 1 h, the resistance and impedance of SH-BimH, Me-S-BimH, SH-BimH-5OMe and SH-ImiH-4Ph are close, but Me-S-BimH and SH-BimH-5OMe show an increasing-decreasing transfer after 96 h. This behavior can be related to the growth mode of Cu_2O, which may begin to grow in 3D and then show the coalescence of oxide islands illustrated in ref. [18][19][20]. The behavior of SH-ImiMe is similar to that of OH-BimH; at short times, there is almost no inhibition effect, but after 24 hours, the inhibition was largely increased. This kind of behavior is suspected to be due to the growth of a stable passive film, and will be studied later by means of immersion test. ImiH and SH-BimH-5NH_2 kept their low resistance and impedance, which means that they provide no inhibition at all, and they will accelerate corrosion process.

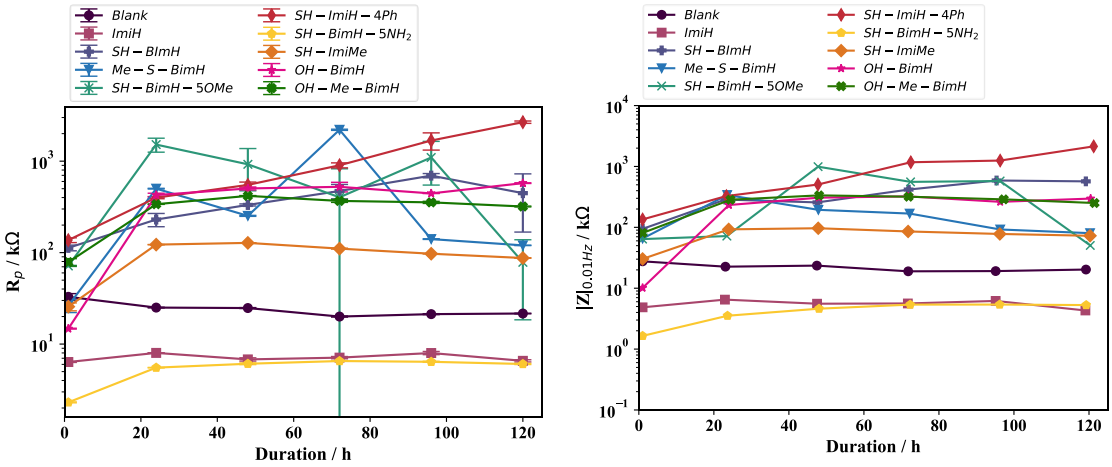

Figure 4.5 Long-term graph of linear polarization resistance (left) and impedance modulus at 0.01 Hz (right) of pure Cu, measured in a period of 120 h immersion in 3 wt.% NaCl aqueous solution (blank) and in the presence of different organic compounds added at 1 mM concentration. Note the logarithmic scale.

The information on the variation of resistance and impedance is completed by **Figure 4.6** , which shows the dynamic Nyquist plot of pure Cu versus time in NaCl solution without and with inhibitors. With increasing immersion time the reference (Blank) shows that the whole frequency range is dominated by charge transfer domain; the same data is the plot as a usual phase angle diagram in **Figure A1.12** in supplementary materials. The highest angle at 0.01 Hz is observed at the beginning of the immersion, (~0.1 Hz @1h), and the maximum angle decreases down to ~65° a 120 h; it is observed that after the initial transient, the corrosion process remains almost the same for the next 120h immersion.

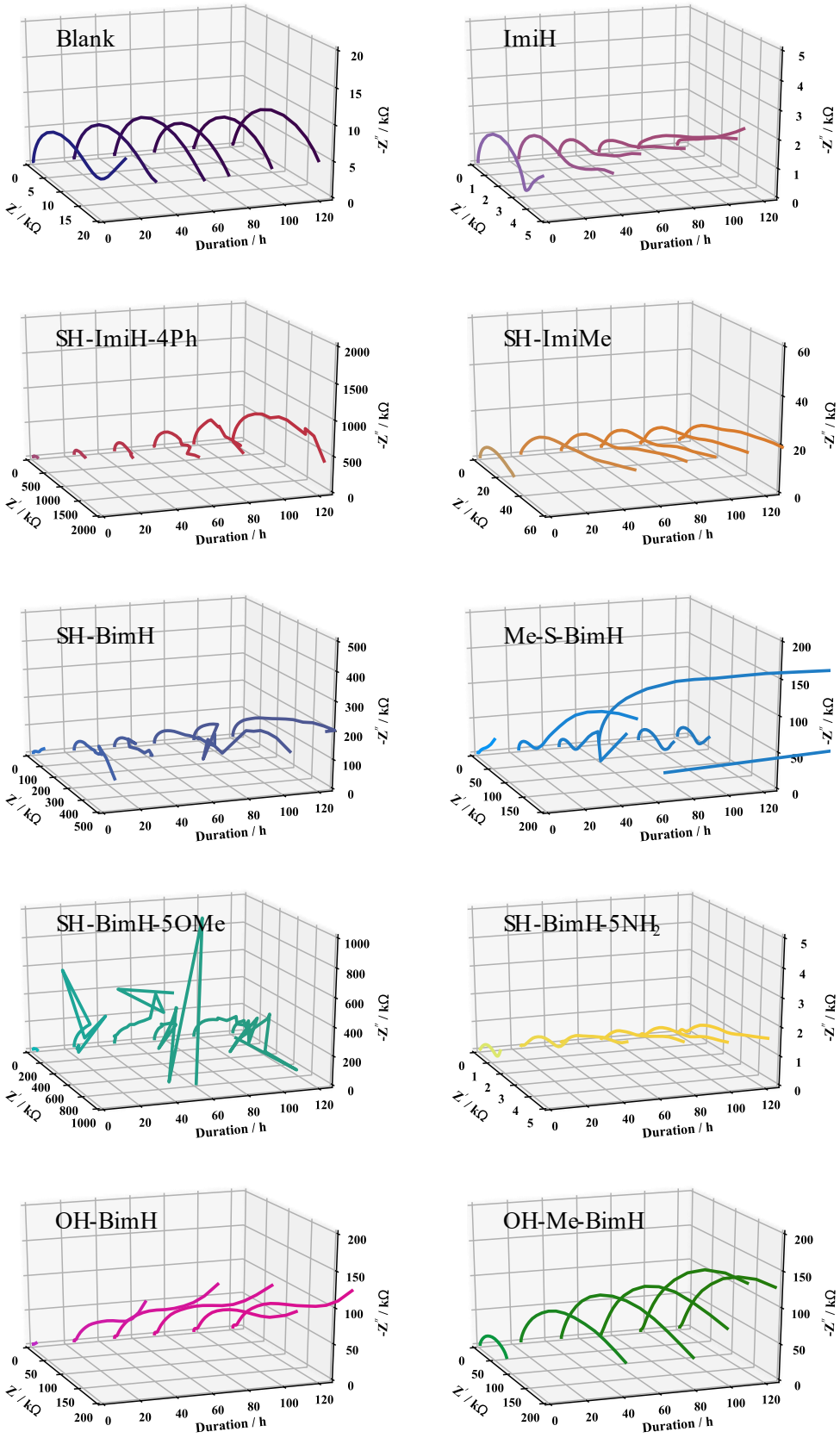

Figure 4.6 Long-term Nyquist plot of pure Cu in NaCl solution without and with 1 mM inhibitor, in a period of 120 h.

ImiH shows a first semicircle which keeps decreasing with time, and the and phase diagram (**Figure A1.13**) does not show much difference from the blank solution. On the contrary, SH-ImiH-4Ph is the best inhibitor from electrochemical measurements; the shape of the successive Nyquist plots is almost the same, but the semicircles increases continually; this is also shown in the phase plots (see **Figure A1.17**). SH-ImiMe shows a fast increase in the impedance after 24h, but later a whole pressed semicircle is transferred to a circle as a straight line; in the phase diagram (**Figure A1.19**), two time constants were found after 24 h and the minimum phase angle increased up to ~20°. This may indicate the formation of a film different than those formed on pure Cu.

SH-BimH also shows a good inhibition effect for both long- and short-term electrochemical measurements. In the figure, the semicircle increases with time, but the stability of the test decreased at low frequency. In **Figure A1.14**, the phase plots at different times show similar behavior, the maximum phase increases with immersion time, but measurements become unstable for frequencies below 1 Hz. As in the case of SH-ImiH-4Ph, SH-BimH-5OMe also shows unstable measurements, which may indicate that some of the inhibitors at the interface is not stable enough when a potential difference is applied. Nevertheless, the combination of EIS and LPR can be validated results to prove the inhibition effect.

As for Me-S-BimH, the double semicircle increases until 72 h immersion, and then we observe a massive drop of the semicircle and a new straight line appears after the first semicircle. Inspecting the phase angle diagram (**Figure A1.15**), it is observed that the first three curves show a similar look. The curve at 72 h begins to change as the second time constant disappears, and the curves obtained at 96 h and 120 h show a lower minimum phase angle degree. This significant change may indicate that part of the inhibitor is not stable, but the fact that the maximum phase angle is kept means that the capacitance behavior did not vanish. Therefore, part of the inhibitor molecules are still bonding on the surface.

SH-BimH-5OMe shows complex behavior. The measurements are not stable and the Nyquist plots are difficult to read. But the phase angle diagram (**Figure A1.16**) shows that the maximum phase increase to more than ~80°, and the chaotic behavior appears when the frequency is lower than 1 Hz. This may indicate that with increasing time stability of part of the inhibitor on the surface decreases and even a small perturbation will affect the inhibition effect. SH-BimH-5NH_2 is a bad inhibition, regardless of the immersion time. Inhibition of OH-BimH significantly changed with time, the radius of the first semicircle increases with time and the shape of the Nyquist plot does not change much after 24 h. The two time constants are clearer after 24 h in the phase plot (**Figure A1.20**), and the maximum phase degree shifts to ~80°. OH-Me-BimH shows the same Nyquist plot shape with an increasing semicircle, and the phase angle plot (**Figure A1.21**) does not change much, showing two time constants which become more differentiated at larger immersion times.

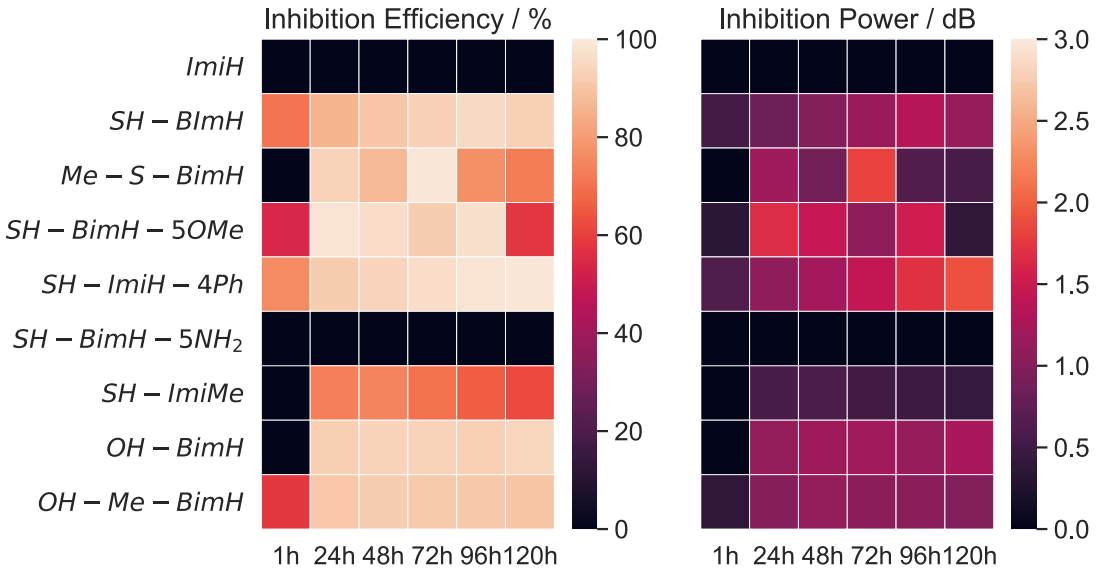

Figure 4.7 Long-term LPR R_p inhibitor efficiency and inhibitor power with different inhibitors in period of 120h

In inhibitor research, inhibition efficiency is a general indicator defined as:

$$IE = \frac{R_p^{Inh} - R_p^{Blank}}{R_p^{Inh}} \times 100\%$$

where IE is the inhibitor efficiency, R_p^{Inh} is the linear polarization resistance in presence of the inhibitor, and R_p^{Blank} is the linear polarization of the material without inhibitor. As we can see, for example, in **Figure 4.7**, the resistance and impedance changes are large. Therefore, the IE computed from this definition saturates when R_p^{Inh} is above one order of magnitude larger than R_p^{Blank}, precisely when considering good inhibitors. To solve this issue, Kokalj et al. [97], defined a new parameter to evaluate the performance of corrosion inhibitors, the so-called inhibition power:

$$IP = 10log\frac{R_p^{Inh}}{R_p^{blank}}$$

With this definition, the inhibition power is measured in deciBels (dB). Furthermore, the impedance can also be used to calculate IE and IP, replacing the linear resistance by impedance at 0.01 Hz. **Figure 4.7** and **Figure 4.8** show the IE and IP computed from linear polarization resistance and impedance, respectively. The inhibition efficiency is remarkably high after 120h for SH-BimH, SH-ImiH-4Ph, OH-BimH and OH-Me-BimH. However, in inhibition power, the color shows clear hierarchal data; SH-ImiH-4Ph is significantly the best inhibitor, followed by SH-BimH. OH-BimH and OH-Me-BimH show a close inhibition effect.

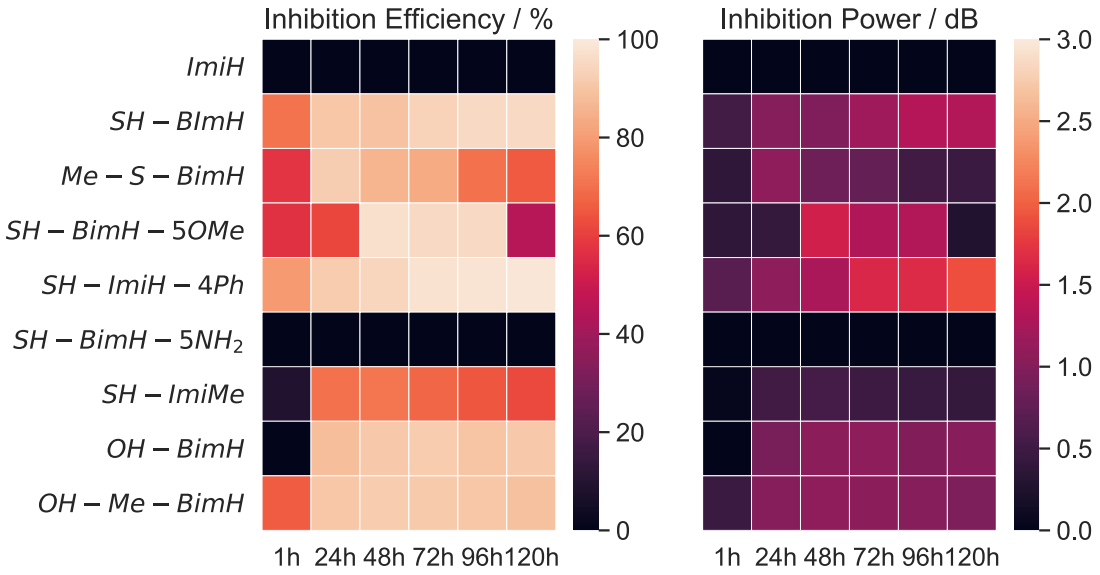

Figure 4.8 Long-term EIS |Z| at 0.01 Hz inhibitor efficiency and inhibitor power with different inhibitors in period of 120h

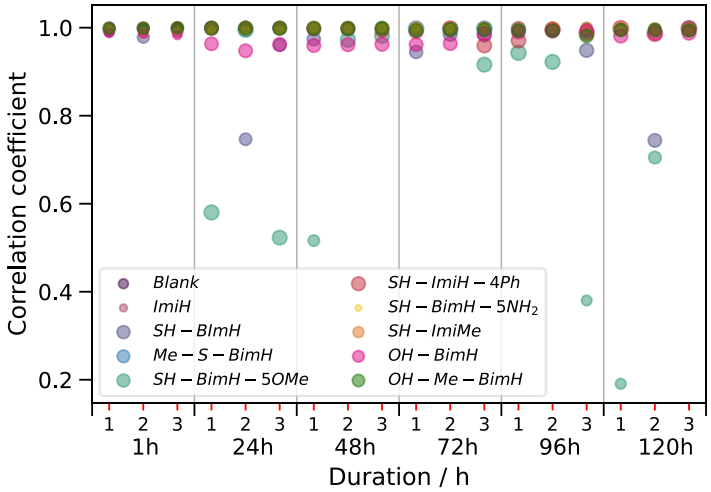

Figure 4.9 Statistical analysis of LPR data based on correlation coefficient in Long-term measurements of pure Cu

The linear polarization curve is a simple and useful tool for the evaluation of corrosion. But there are concerns about its applicability in the evaluation of corrosion inhibition. Comparing the two figures above, it appears that LPR is a powerful tool, but it is convenient to assess its stability on such a large set of measurements. **Figure 4.9** shows the correlation coefficient obtained from the linear regression of the LPR data for all the individual measurements used in **Figure 4.7**. Here, the x axis shows the measurement sequence at each given time, and the y axis shows the coefficient. Most of the values are above 0.9 and only SH-BimH-5OMe repeatedly shows low correlation coefficients for

measurements after 24 hours' immersion. However, EIS of the same inhibitor shows also similar chaotic data at low frequency. Therefore, we conclude that EIS measurements are reliable in the analysis of the corrosion inhibition performance, and the correlation of the measurement as well as its repeatability is its own quality check.

4.1.3 Immersion Test

Short-term immersion tests characterized by XPS

X-ray photoelectron spectroscopy is a sensitive surface characterization method, hence it is a proper technique for analyzing the ultrathin film on the metal surface. Typical depth penetration is around 10nm, and the high-resolution scan could introduce details about the binding energy of different elements in various states. Four effective inhibitors for pure Cu were selected for 24 and 120 hours immersion test, and later analyzed by XPS. The selected inhibitors are SH-BimH, Me-S-BimH, SH-BimH-5OMe and SH-ImiH-4Ph. The survey XPS spectra of pure Cu bare surface and after 24h and 120h immersion are shown in **Figure A1.22**. The different dash lines are guides to the eye to show the presence of different chemical compounds. The spectra of the bare surface shows the presence of Cu, C, O and Si. Si appears in all spectra, but it is neither alloyed to the metal nor in solution; it corresponds to SiC particles embedded on the surface during polishing. Since polishing must be performed with water and polishing fluid, slight oxidation and corrosion are inevitable; this is proved by presence of O. C is everywhere in environment, it is difficult to precise it origin, so it will be discussed on high-resolution spectra. For the curves obtained after immersion in presence of inhibitors, the existence of S and N indicates the formation of an inhibitor film on the surface, as expected for effective inhibitors. In these cases, the intensity of Cu peaks decreases accordingly.

Figure 4.10 shows the normalized high-resolution XPS spectra of Cu 2p, Cu LMM, O 1s and Cl 2p, for the surface of pure Cu after polishing and pickling and after immersion in 3wt.% NaCl with and without added inhibitors. Dash lines correspond to the position of the peaks of reference compounds. Upper and lower plots show the spectra of samples curves immersed for 24h and 120h, respectively. High-resolution spectra will assist in identifying the chemical environment of elements and to relate particular chemical species to each other. The analysis of the spectra will be focused on the peak position instead of quantitative analysis, due to the complexity introduced by the variety of organic compounds and its interaction with the surface. There are no precise peaks for specific element states, since different kind of bonds are present in organic compounds. The features of XPS spectra of Cu and Cu oxides have been widely studied [98–101]. The principal Cu LMM peak and Cu2p peak are always collected by XPS high-resolution spectra of Cu. The Cu2p peak has significantly split spin-orbit components, and it is possible to distinguish Cu oxidation states using satellite features of Cu2p. Cu (II) and Cu

(I) oxide have an observable collection of satellite features at ~943 eV and ~945 eV, respectively. And the satellite features of Cu (I) oxide are very weak. Besides, the precise location of the binding energy is not well defined, as it depends on the status of the surface. In this research, the bare surface spectrum is recorded to set up a reference of the energy locations of Cu and its oxides. The dash lines allow a comparison of the shift and energy difference with the reference states. The Cu2p3/2 peak in Cu (II) oxide is shifted and is much broader when compared to Cu (I) oxide. The chemical shifts in the Cu LMM peak of Cu (I) oxide and Cu (II) oxide show a large difference. In **Figure 4.10** (a), weak satellite features appear in both bare and blank samples after 24h immersion, as well as the 120h immersion, which indicates the presence of Cu_2O. Samples with inhibitors show no clear features at this position, which is attributed to the interaction between inhibitor and Cu_2O. As shown in **Figure 4.10** (b), the CuO LMM peak almost disappeared. The oxidation state of Cu depends on the presence of CO_2 during immersion, which influences the pH and favors the further oxidation of CuO to Cu_2O. The O_2 and CO_2 concentration will control the thickness with the competing reactions[30,31]:

$$Cu + Cu^{2+} \rightarrow 2Cu^{+}$$
$$Cu^{+} \rightarrow Cu^{2+} + e^{-}$$

The peak intensities for the solutions with inhibitors decrease in both **Figure 4.10** (a) and (b). This indicates the thin film formation on the surface that reduces the x-ray that reaches to the Cu substrate. The Cu2p peaks indicate the Cu are still in Cu or Cu_2O state. However, Cu LMM peaks show the shift of Cu to higher binding energy; this accounts for the effect of inhibitor adsorption on the Cu/ Cu_2O states, as observed previously [102]. The Cu LMM peak of Me-S-BimH shows a larger shift than the rest, which decreases after 120h immersion. This agrees with the deceasing of inhibition efficiency in the electrochemical measurements. However, other efficiency-decreasing inhibitors do not show this behavior, which merits further study. The O1s peaks are also shown in **Figure 4.10** (c); the bare surface shows a wide peak around three binding energies, $O^{2=}$, OH^{-}, H_2O; this indicates the presence of all three species on the surface. With 24h immersion, the blank sample presents a peak in the middle of $O^{2=}$ and OH^{-}, but it shifts to the O2- peak after immersion for 120h. This can be attributed to further oxidation. All inhibitor O1s peaks shift to the peak around H_2O. It is difficult to explain since the presence of organic compounds may interact with O. Besides, SH-BimH-5OMe O1s peak become wider and reach the energy of OH^{-}. Considering the fast decrease of inhibitor efficiency at 120h in the electrochemical measurements in **Figure 4.7** and **Figure 4.8**, it is indicative that corrosion proceeds in some locations on the surface. Chloride ions in the solution are highly aggressive, thus the presence of the Cl 2p peak is an indicator of the corrosion process. It is interesting that the Cl 2p peak appears already in the bare surface, this may account for the contamination from the polishing agent. The peak of the blank sample increases in the 120h immersed sample, and the peaks of all other samples are smaller. The larger Cl 2p peak in SH-BimH-5OMe shows slightly stronger corrosion than the rest inhibitors after 120h immersion.

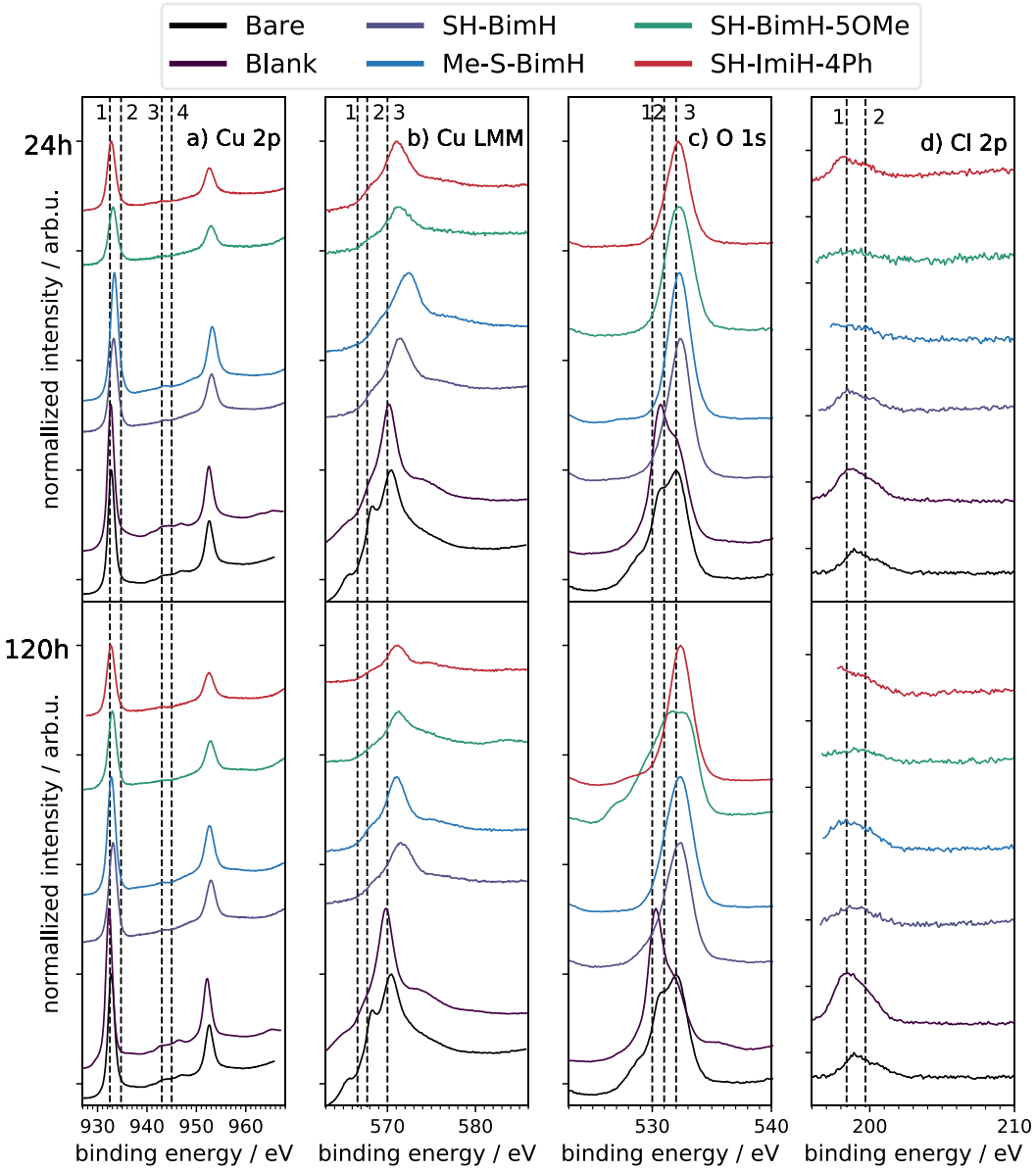

Figure 4.10 Normalized high-resolution XPS spectra for the surface of pure Cu after polishing and pickling, and after immersion in 3wt.% NaCl with and without added 1mM of SH-BimH, Me-S-BimH, SH-BimH-5OMe and SH-ImiH-4Ph. Dash lines represent the position of peaks of reference compounds: (a) 1: Cu/Cu2O, 2: Cu(OH)2, 3: Cu(II) satellite peak, 4: Cu(I) satellite peak, (b) 1: Cu, 2: CuO, 3: Cu2O, (c) 1: O2-, 2: OH-, 3: H2O, (d) 1: Cl 2p3/2, 2: Cl 2p1/2. Up: Immersion for 24h. Down: Immersion for 120h.

Figure 4.11 shows the normalized high-resolution XPS spectra of C 1s, N 1s and S 2p of the surface of pure Cu after polishing and pickling and after immersion in 3wt.% NaCl with and without added inhibitors. The reference binding energy of C 1s and N 1s shown as dash lines are derived from the work of I. Milošev [66]. The inhibitors are composed

mainly of carbon, nitrogen and sulfur; these peaks can assist in understanding the chemical composition and condition on the surface in chloride solutions containing inhibitors. As shown in **Figure 4.11** (a), carbon peaks appear in all spectra, and the intensity of bare and blank sample is lower than that with inhibitors. The peak width of inhibited ones is wider as well. Since the carbon peaks of different carbon bond is close, it is difficult to identify the peaks. However, the wider peaks prove the presence of more types of carbon bonds to other elements, i.e. nitrogen, oxygen and sulfur, and the higher intensity shows that more carbon appears on the surface, contained in the inhibitors. The higher C 1s main peaks in 120h immersed samples with inhibitor indicate that more inhibitors appear on the surface. As for the N 1s peaks in (b), two reference binding energies are presented by dash lines [66], C-N (400.4 eV) and C=N (399.0 eV). There is almost no signal of these two peaks in the bare and blank samples. In the upper figure, a wide peak with a plateau appears on SH-BimH, SH-BimH-5OMe, SH-ImiH-4Ph, but the presence of the C-N bond is not clear in Me-S-BimH. The presence of both pyridine and pyrrole type N atoms is important, it can indicate the formation of thiol tautomer forms because thione lacks the pyridine type N atoms. Thus, for SH-BimH, SH-BimH-5OMe, SH-ImiH-4Ph the thione tautomer are stable after 24h immersion. However, the peaks of pyrrole type N atoms disappear in SH-BimH, while this peak appears in Me-S-BimH. The formation of thiol tautomer is slower in Me-S-BimH and is not stable for SH-BimH. The intensity of the peaks corresponding to these two kinds of bonds also changes in SH-BimH-5OMe, which indicates that the thiol tautomer will change with the time. SH-ImiH-4Ph is the only inhibitor whose peak keeps the same shape, which accounts for the rapid formation of the thiol tautomer and a long-lasting bond to the surface. From this point of view, SH-ImiH-4Ph is the most stable inhibitor. Two different peaks exist in the S 2p spectra which only show a difference of 1.1eV, corresponding to the S 2p 3/2 and 2p 1/2 states respectively. They are not usually differentiated as two separate peaks. In samples immersed with solutions containing SH-BimH, Me-S-BimH, SH-BimH-5OMe, the S 2p 3/2 and 2p 1/2 peaks are single and located between 162.2eV and 164.4eV, agreeing with the literature [66,102–105]. The oxidation-dimerization reaction of C–S or C=S group is converted to an S–S bridge. Then further oxidation will introduce a peak ~4eV above the main peak [102]. Interestingly, only SH-ImiH-4Ph shows a split peak in both 24h immersed and 120h immersed samples. This fact can only be due to the existence of two kinds of chemical bond on the surface, which might be the reason why this compound shows the best inhibition performance.

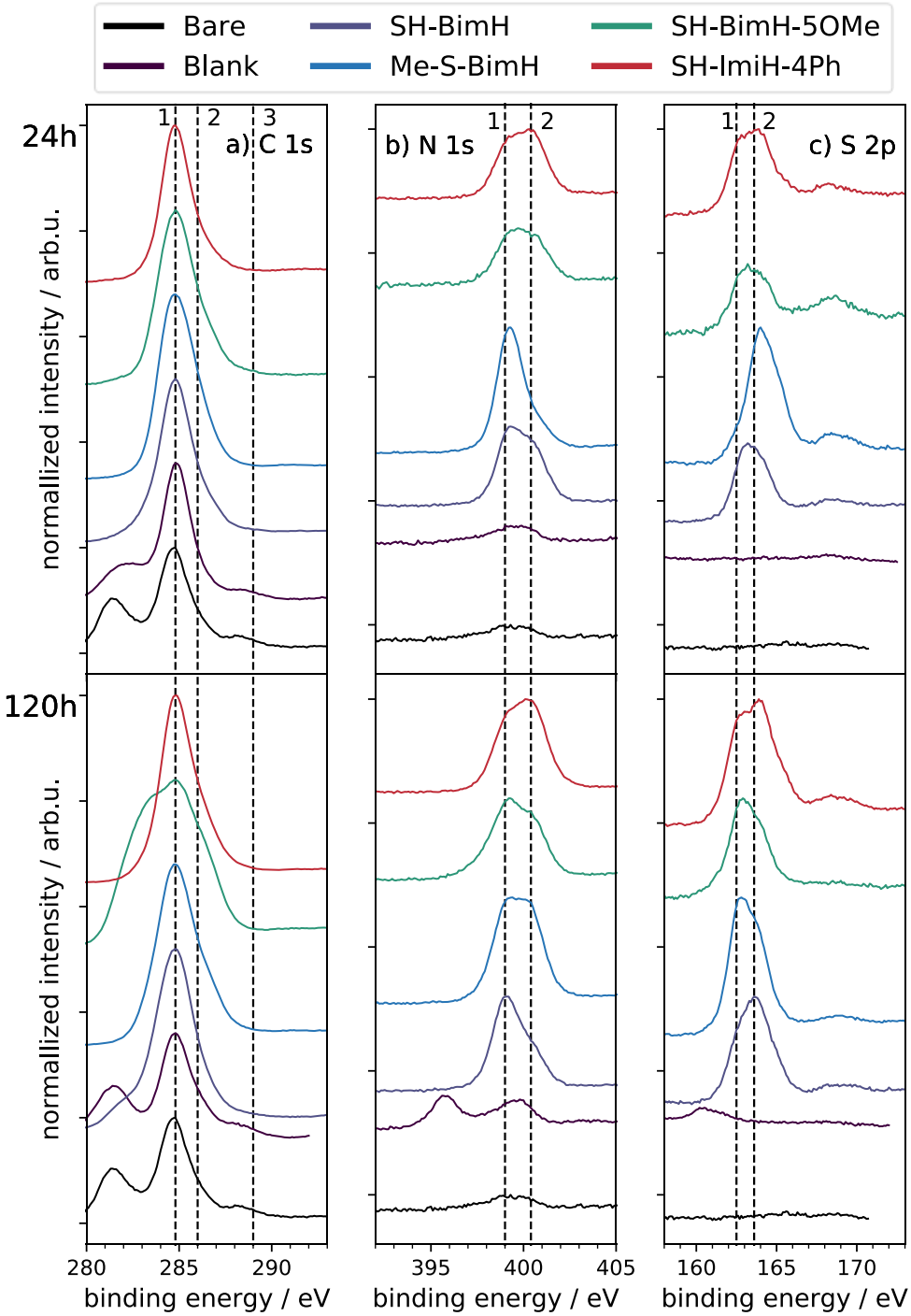

Figure 4.11 Normalized high-resolution XPS spectrums for the surface of pure Cu after polishing and pickling and after immersion in 3wt.% NaCl with and without added of SH-BimH, Me-S-BimH, SH-BimH-5OMe and SH-ImiH-4Ph. Dash lines represent the position of peaks of reference compounds: (a) 1: C–C,C–H, 2: C–O, 3: C=O, (b) 1: - C=N-C, 2: C-NH-C, (c) 1: S $2p_{3/2}$, 2: S $2p_{1/2}$. Upper: Immersion for 24h. Down: Immersion for 120h.

60 days' immersion test

Photographic analysis

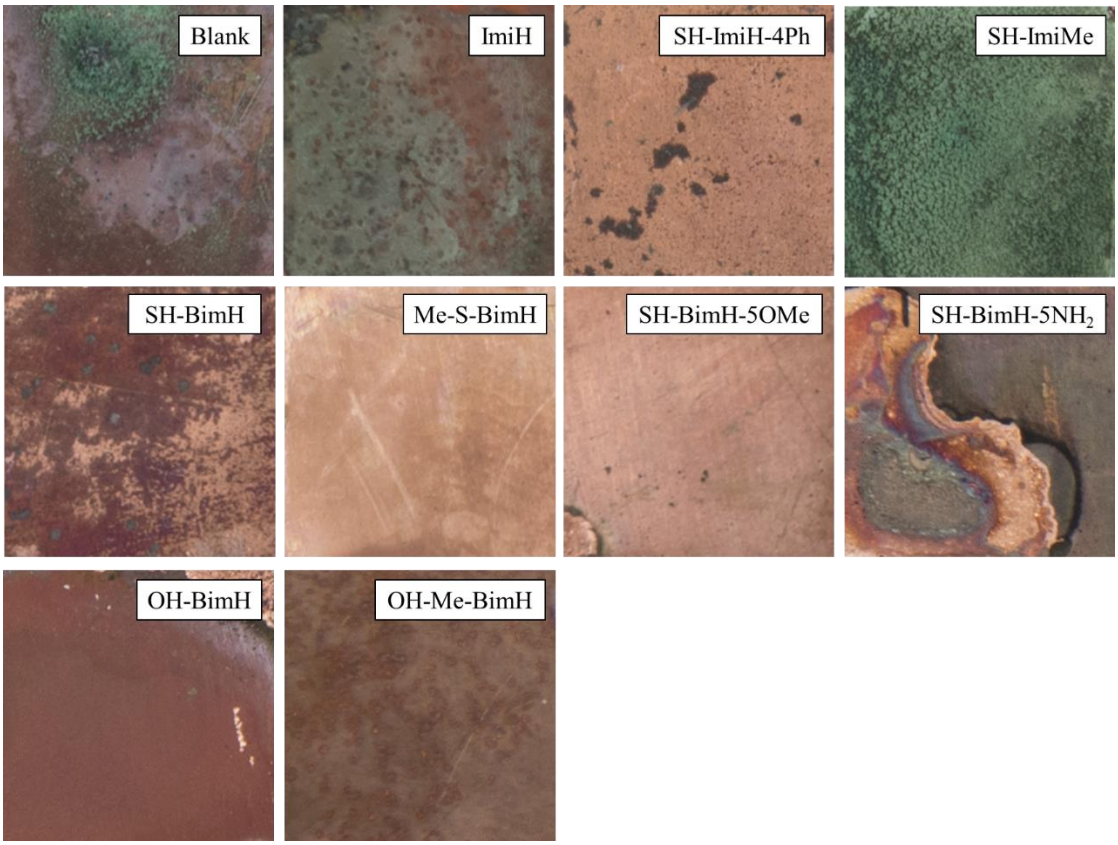

Figure 4.12 Photographs of pure Cu immersed in 3 wt.% NaCl solution with and without inhibitor for 60 days (real size of each photo is around 0.9×0.9 cm^2)

Figure 4.12 shows the photographs of pure Cu surface after immersion in 3 wt. NaCl with and without inhibitors for 60 days. Imidazole derivatives, ImiH and SH-ImiMe show similar corrosion products as no, they do not inhibit the sample corrosion. SH-ImiH-4Ph shows a good surface for the most area; however, part of the surface is covered by a black film, which needs further check by SEM-EDX. Mercapto-benzimidazole derivatives show a diverse result; the presence of SH-BimH-5NH_2 produced different, white corrosion products. However, the surface of the sample immersed in presence of Me-S-BimH appears almost unchanged. Sample immersed in presence of SH-BimH-5OMe shows a good surface as well. A dark red film and black areas appear on the surface of the sample after immersion in presence of SH-BimH, which needs to be checked by SEM-EDX. For hydroxy-benzimidazole derivatives, immersion in presence of OH-BimH produced a dark red film on the surface, which shows no inhibition. Finally, the sample immersed in presence of OH-Me-BimH shows a good surface with a little darken look.

SEM-EDX analysis

The characteristic X-ray energies of related elements were listed in **Table A1.1**.**Figure 4.13** shows the bare surface of pure Cu of the backscattered electron image (BSE). (a) and (b) show some exfoliations and scratches due to polishing. The close look in (c) and (d) shows that the exfoliations have different sizes. The 3D plot in figure (e) shows that exfoliations and scratches are not deep; the surface roughness Sa (arithmetical mean height) is 0.825 μm. Please note that the roughness calculated by SEM is not precise, and must merely be taken as a reference. **Figure A1.23** shows the EDS elements map of Cu and Si. Distribution of Cu is uniform except at exfoliations, and Si appears in the exfoliations, which indicates that some SiC particles embed in the exfoliations. **Figure 4.14** shows the EDS elemental point analysis spectrum of pure Cu in different locations. Owing to the fact that EDS cannot show an exact element ratio and the non-conductive organic layer on the surface, the analysis of the spectrum will be focused on analyzing the distribution of the elements on the surface. For higher energy resolution, the spectrum was separated into two energy ranges. The low energy range, from 0 to 3 keV, allows one to identify C, N, O, Cu, Zn, Si, S, Cl, while the high energy range from 7 to 10 keV allows the identification of Cu and Zn. The EDX energy intensity was normalized by dividing the maximum value in each range to help the comparison of elements. The value of C_{max} in each subplot accounts for the maximum counts of the spectrum in the range 0.5 – 3.0 keV and 7 – 10 keV. All the characteristic x-ray energies are given in **Table A1.1**. Point (a) is on the flat surface. Two small peaks are found from 0.2 to 0.4 keV, which may correspond to C (K_α ~ 0.277 keV).

Initial oxidation of brass is very fast in air and water, as we discussed before. After polishing, the oxide layer will be an interference factor. Thus, samples were immersed in 0.1 M H_2SO_4 for 30s' pickling. In **Figure 4.14**, as shown in the spectrum (a), the peak of oxygen was quite low, compared to others. Pickling reduces the influence of the oxides, but it was impossible to remove them entirely for the practical application of the inhibitors. The highest peak around 1 keV corresponds to Cu ($L\alpha$ ~ 0.93 keV). In the right spectrum of (a) point, we note that the relative intensity of these peaks is small. The peak around 8.1 keV corresponds to Cu-$K\alpha_1$ (~ 8.046 keV) and that at 9 keV for Cu-$K\beta_1$ (~ 8.904 keV). Since the CuZn alloy will be tested in the same way, the advantage of peaks in this range is that we can eliminate other interference to show an apparent Cu/Zn ratio, which will help to figure out the surface composition when the organic film exists. Points (a) is taken at the flat surface; no oxygen appears in the spectrum which means no severe oxidation happened on the surface. Points (b) and (c) show the elemental spectrum inside the exfoliation; a Si peak appears in both of the spectrums. This kind of embedding introduce new defects on the surface but can not be avoided during practical application. The interaction between this defect and inhibitor should be noticed in the following experiments.

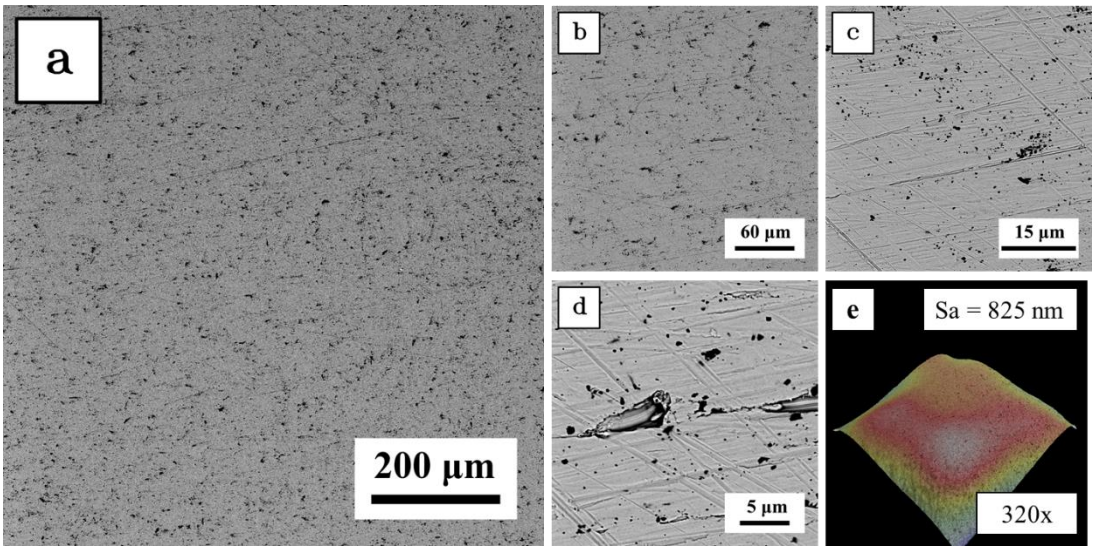

Figure 4.13 Bare surface of pure Cu after polishing and rinse. Magnification of (a) 320x (b), 1000x and (c) 5000x. (d) detail of the scratch and exfoliation. (e) 3D topography under 320x magnification by SEM

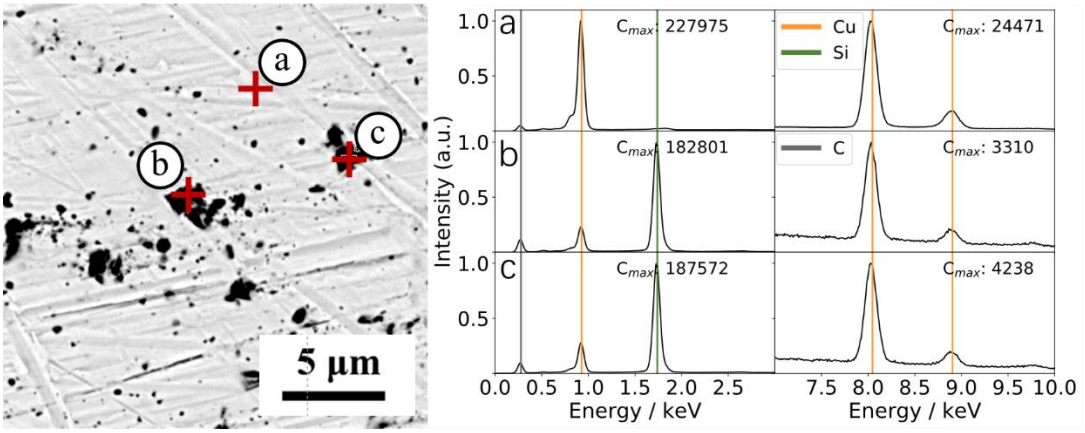

Figure 4.14 EDX elemental point analysis spectrum of bare surface of pure Cu in (a) flat surface, (b) exfoliation hole and (c) exfoliation hole.

Figure 4.15 shows the look of pure Cu surface after 60 days' immersion in 3 wt.% NaCl solution in sealed bottle. (a) and (b) show different features on the surface. Part of the surface is flat and shows white under BSE, while some parts look black. By adjusting the contrast on the black part in (b), some dendritic structures are observed on the surface, magnified in (c). The roughness of the dendritic structure may be responsible for the low BSE contrast, hence this area should correspond to the green area in **Figure 4.12**. Magnification of the flat surface (d) shows the presence of small islands with smaller dendritic crystals as well. **Figure A1.24** shows the elemental map of the surface. O, C and Cl appear on the surface, and the Cl-rich area shows less Cu concentration. The distribution of Cu and O are highly correlated, which means the islands on the flat surface should be CuO or Cu_2O, as also mentioned in [37]. **Figure 4.16** shows elemental points analysis of surface on different features. Point (a) is on the flat surface; no chloride is found, and oxygen appears to come from Cu oxide on the surface. Point (b) is on the dendritic substance and point (c) is on the grey surface under BSE, but they both show a

similar elemental distribution. Chloride appears on these two locations, which indicate the formation of CuCl or $CuCl_2$. As introduced in chapter 1, pitting corrosion of pure Cu proceeds by local attacks on the surface with formation of chloride compounds with Cu ions. This sample will be a reference for evaluating the inhibition effect in the following analysis and will be referred to as blank.

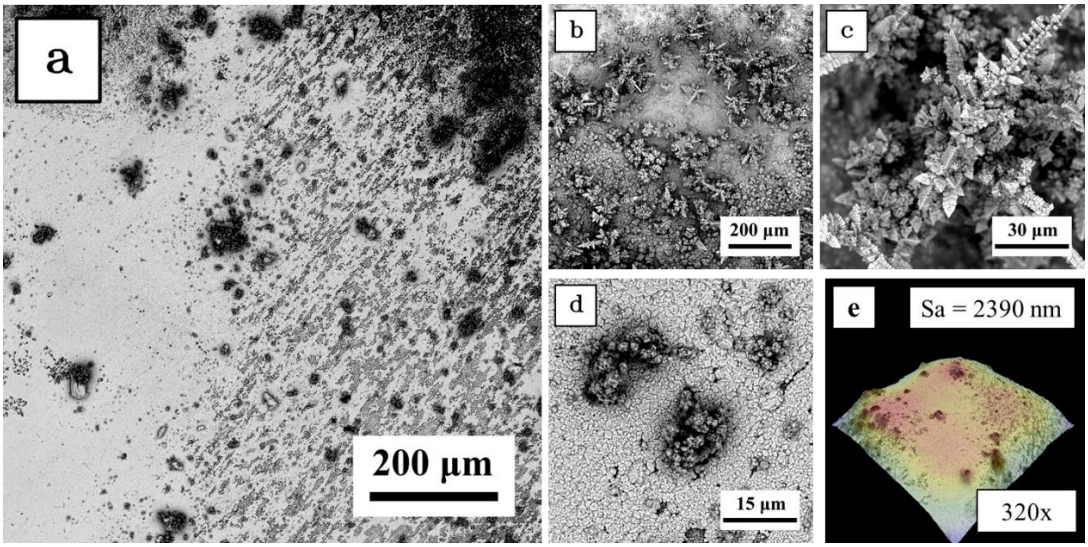

Figure 4.15 Pure Cu immersed in 3 wt.% NaCl solution for 60 days. (a) surface under 320x magnification with all typical features (b) surface under 320x magnification on the dendritic structure (c) surface under 2500x magnification on dendritic structure (d) surface features in flat part (e) 3D topography under 320x magnification by SEM

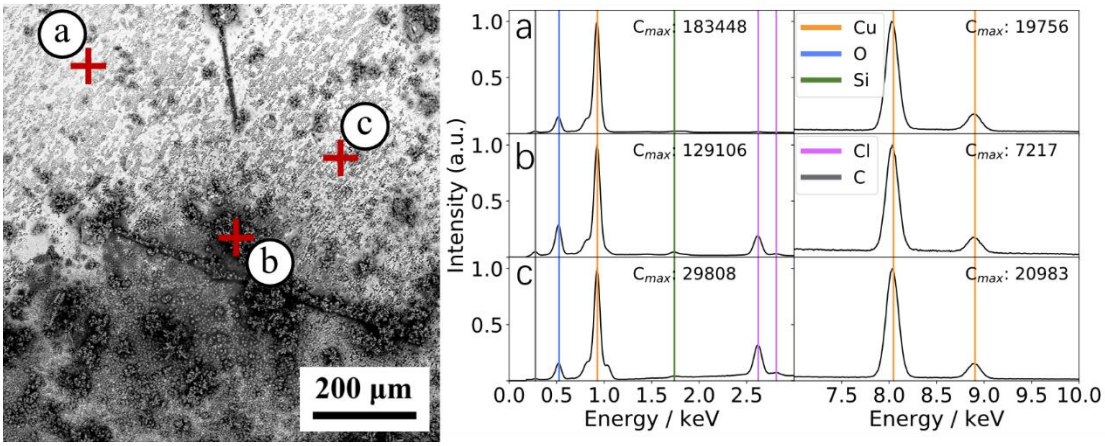

Figure 4.16 EDX elemental point analysis spectrum of pure Cu immersed in 3 wt.% NaCl solution for 60 days. (a) white flat part under BSE detector, (b) dendritic structure on the surface and (c) particles on the surface.

As shown in **Figure 4.17**, the surface after immersion 60 days in 3w% NaCl with added 1mM SH-BimH shows a better look than that of the blank sample. (a) shows most of surface is like the bare surface but a little darker, and some dark irregular parts appear. As shown in (b) and (d), the surface is as good as bare surface. (c) shows the look of dark irregular area on the surface; the porous structure indicates local attacks on this region. (e) shows this area is higher than the surface around. The elemental distribution displayed

in **Figure A1.28** shows an increased concentration of S, C and Cl on this attacked part. Contrarily, Cu shows a lower concentration in the same region. **Figure 4.18** shows the point analysis of EDX spectra. Point (a) is on the white flat surface; there is no oxygen detected and only shows presence of Cu. Grey surface analyzed by point (b) shows the presence of oxygen, indicating oxidation of the surface. Point (c) shows the presence of S, O, Cl, which indicates the existence of Cu-Inhibitor complex gathering in the corroded location. SH-BimH is a good inhibitor. However, oxidation happened on most of the surface, and pitting happened in some locations.

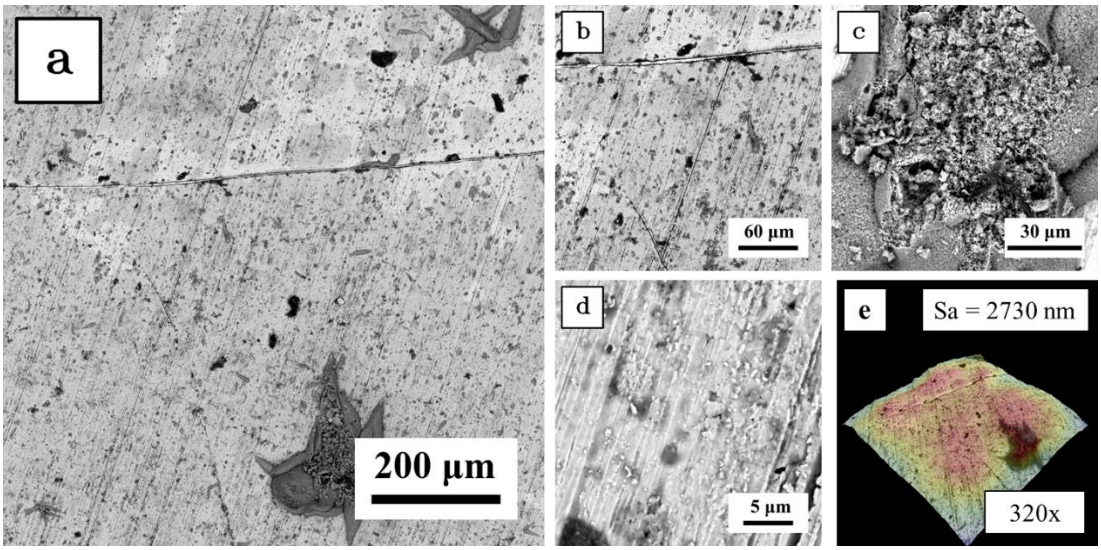

Figure 4.17 Pure Cu immersed in 3 wt.% NaCl aqueous solution with added 1mM SH-BimH solution for 60 days (a) surface under 320x magnification with all typical features (b) surface under 1000x magnification (c) dark part of the surface (d) good surface under 10000x magnification (e) 3D topography under 1000x magnification by SEM

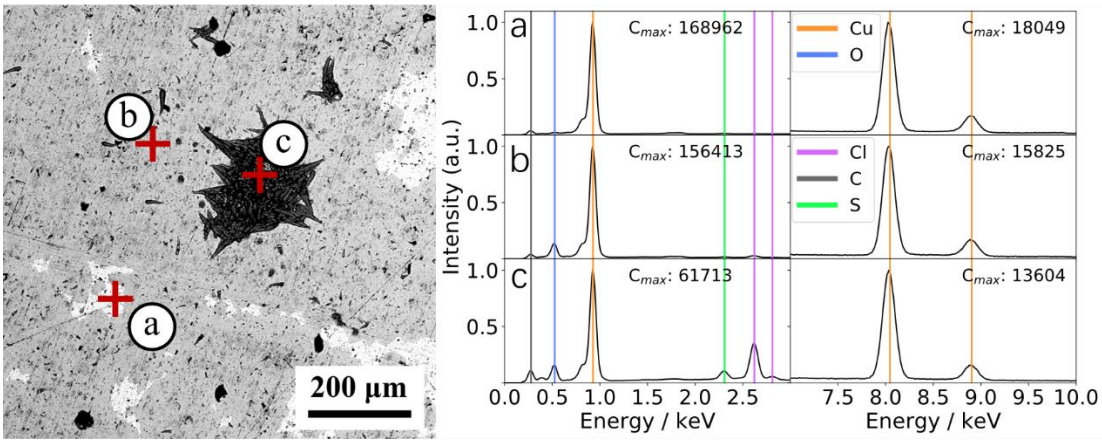

Figure 4.18 EDS elemental point analysis spectrum of Pure Cu immersed in 3 wt.% NaCl aqueous solution with added 1mM SH-BimH for 60 days (a) white flat surface (b) grey flat surface (c) dark part of surface.

Figure 4.19 shows the surface of pure Cu immersed in 3 wt.% NaCl with added Me-S-BimH for 60 days. As shown in (a), most of the surface looks like the bare surface, except

that the surface becomes darker. As shown in **Figure 4.19** (b), (c), (d), the surface shows no obvious pitting corrosion. **Figure 4.19** (e) shows the surface is flat with a roughness Sa of 2.02 µm. **Figure A1.29** shows the distribution of elements. Since S appears on the surface, the inhibitors should gather on the surface and form a thick layer. **Figure 4.20** shows the elemental analysis of three points of the surface. Point (a) is on the white surface, no oxygen is found, and a little peak of S appears. Point (b) shows a higher S peak and no O as well. Point (c) is on the black part of the surface, and high peaks of Si, O, S are also present. This is an interesting result, which indicates that Me-S-BimH shows the same behavior as SH-BimH. The inhibitor probably reacts with the Cu ions to form some kind of complex. This sample immersed in presence of Me-S-BimH shows more inhibitor concentration on the surface; no pitting was found on the surface. The presence of a monolayer cannot be detected by EDX. This inhibitor seems to gather on the Cu surface and form a thick layer which will offer more protection afterwards.

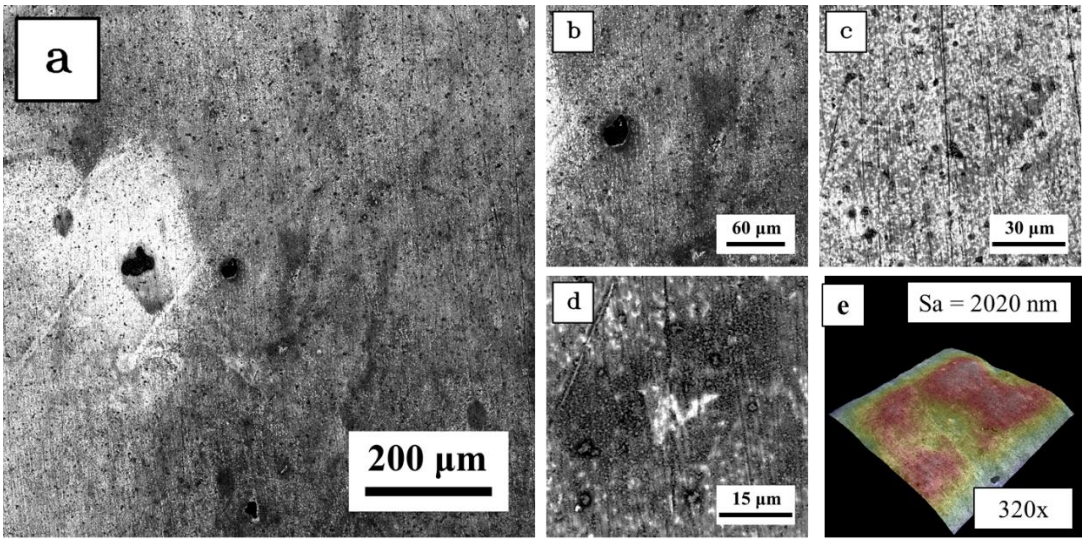

Figure 4.19 Pure Cu immersed in 3 wt.% NaCl with added 1mM Me-S-BimH solution for 60 days (a) surface under 320x magnification with all typical features (b) dark grey part under 1000x magnification (c) white part of the surface under 2500x magnification (d) surface under 10000x magnification (e) 3D topography under 320x magnification by SEM

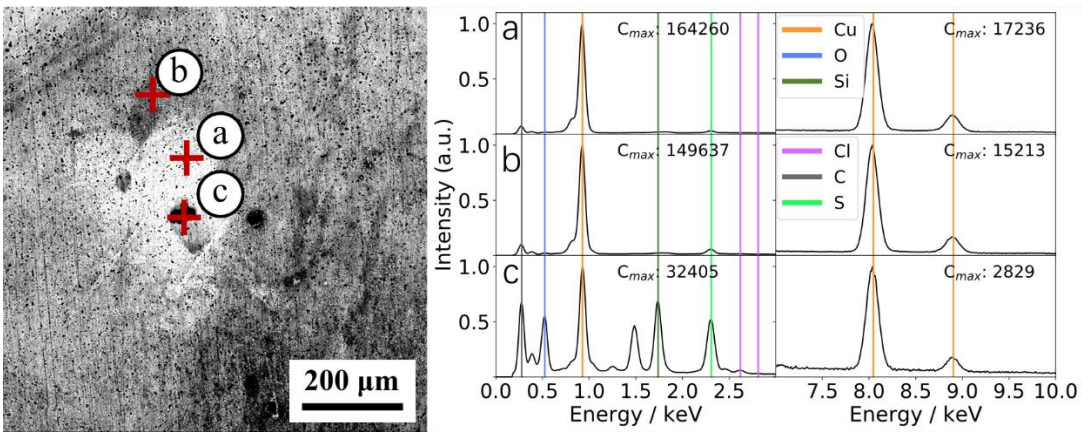

Figure 4.20 EDS elemental point analysis spectrum of pure Cu immersed in 3 wt.% NaCl solution with added 1mM Me-S-BimH for 60 days (a) spectrum of point a, white surface (b) spectrum of point b, dark grey surface (c) spectrum of point c, black part of surface.

Figure 4.21 shows the surface of pure Cu after 60 days' immersion in 3 wt.% NaCl with added SH-BimH-5OMe. (a) shows a global view of the surface, some black parts with light grey surface are presented. As shown in **Figure 4.21** (b) and (d), the black parts are local attacked areas with porous structures. A closer look shows in **Figure 4.21** (c) indicates this kind of local attack appears in a small scale as well as large scale shown in **Figure 4.21** (a). As shown in 3D **Figure 4.21** (e), the black part shows a higher position, which indicates some substance should gather on the local attacked part. Furthermore, consider the exfoliation in bare surface, the look of the surface with SH-BimH-5OMe shows a similar attack. This reveals that SH-BimH-5OMe is sensitive to surface defects. **Figure A1.30** shows the distribution of elements of Cu. O, Cl, S and N, the local attack dissolved some of Cu and forms (Cu, Cl) compounds on the surface. The presence of S on the black part indicates the inhibitor gather on these pits. **Figure 4.22** shows the elemental spectrums on different points of the surface. As shown in point (a), white surface shows little oxygen with Cu, which means SH-BimH-5OMe protect most parts of surface and oxidation happened on the surface, but not severe, Points (b) and (c) are on the black surface, Si appears on both of the spectrums indicates the local attack highly relate to the exfoliations and embedded SiC particles. The high S peaks in these two spectrums conduct the adhesion of Cu-inhibitor complex. SH-BimH-5OMe is an effective inhibitor, but sensitive to defects on the surface. And it can not control the growth of the pits.

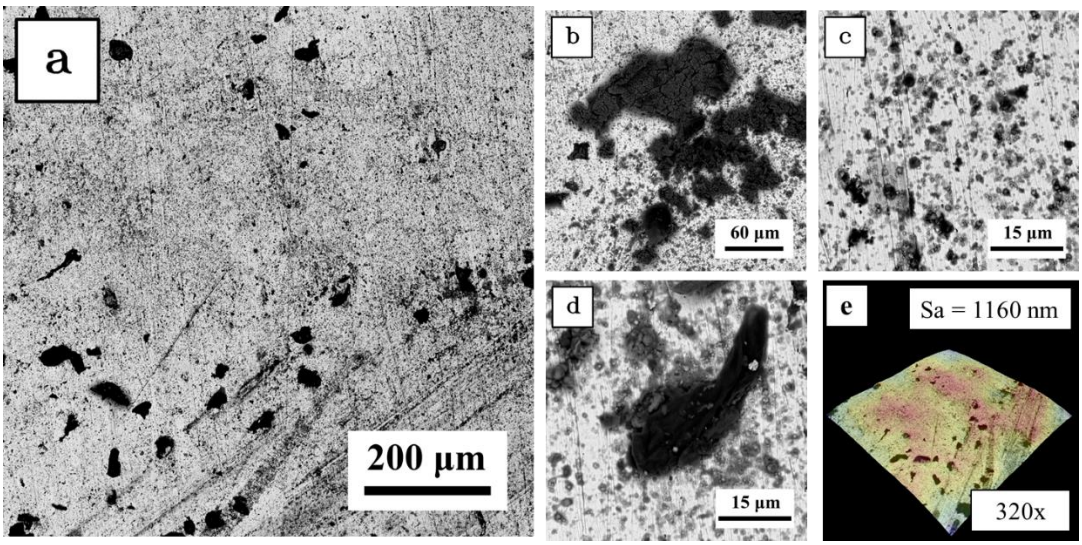

Figure 4.21 Pure Cu immersed in 3 wt.% NaCl with added 1mM SH-BimH-5OMe solution for 60 days (a) surface under 320x magnification with all typical features (b) local attacks on surface under 1000x magnification (c) surface under 5000x magnification (d) local attack (e) 3D topography under 320x magnification by SEM

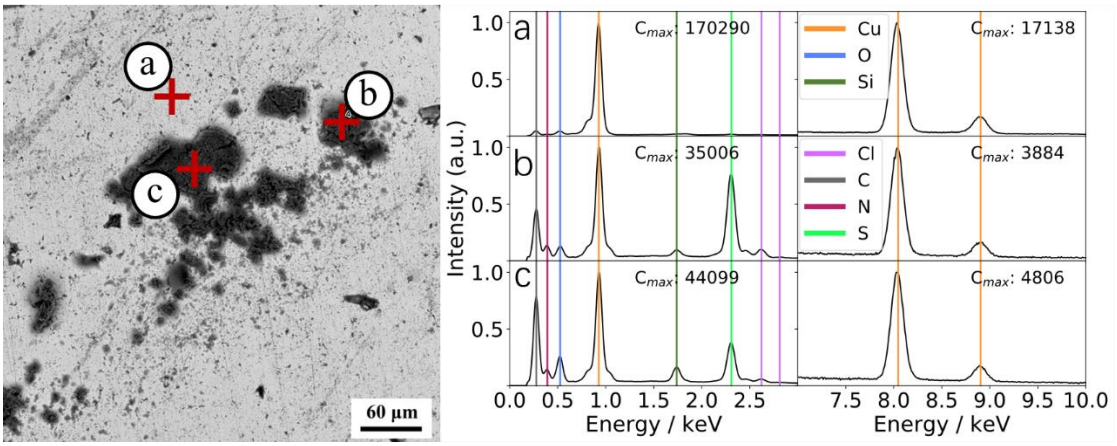

Figure 4.22 EDS elemental point analysis spectrum of pure Cu immersed in 3 wt.% NaCl solution with added 1mM SH-BimH-5OMe for 60 days (a) spectrum of point a, white surface (b) (c) spectrum of point b and c, local attacked part.

As shown in **Figure 4.23**, the surface of immersed pure Cu in 3 wt.% NaCl with added 1 mM SH-ImiH-4Ph is presented. **Figure 4.23** (a) shows an overview of the surface, surface is mostly covered by light grey and dark grey surface under BSE, some black parts appear as well. As shown in **Figure 4.23** (c) and (d), the black parts show local attacks in some locations and dark grey parts are not. (b) shows another local attack in an irregular form on the surface, but not common. **Figure A1.31** shows the distribution of elements of Cu, O, Cl, C on the surface. The dark grey parts show more O than that of light grey. C and Cl concentrated on the black part. **Figure 4.24** shows elemental points analysis on light grey, dark grey and black part of the surface. Point (a) shows the spectrum of light grey surface, only Cu present in the spectrum. As shown in point (b) and (c), small Cl peaks appear, and O appears as well. But the intensities of O and Cl is quite small in point (b). SH-ImiH-4Ph is a good inhibitor for pure Cu which protects the surface and controls the growth of pits. However, there are many slight local attacks on the surface.

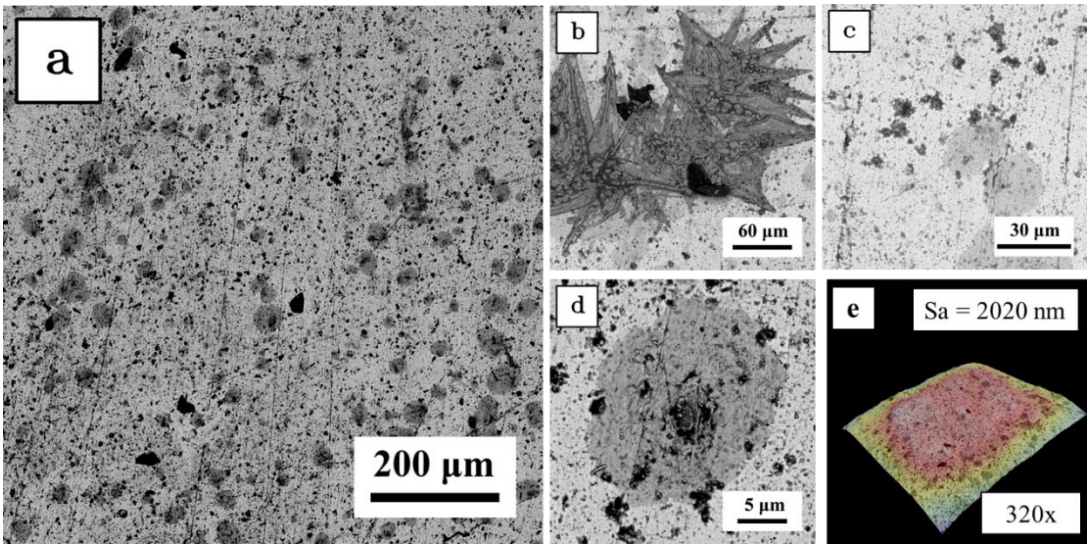

Figure 4.23 Pure Cu immersed in 3 wt.% NaCl with added 1mM SH-ImiH-4Ph solution for 60 days (a) surface under 320x magnification with all typical features (b)

local attack (c) surface under 2500x magnification (d) dark grey part (e) 3D topography under 320x magnification by SEM

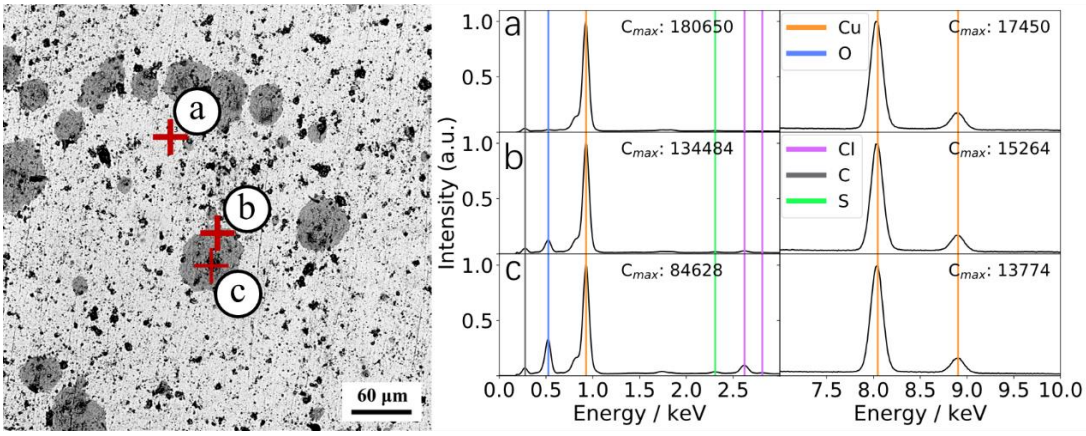

Figure 4.24 EDS elemental point analysis spectrum of pure Cu immersed in 3 wt.% NaCl solution with added 1mM SH-ImiH-4Ph for 60 days (a) spectrum of point a, white surface (b) spectrum of point b, dark grey surface(c) spectrum of point c, black part under BSE.

Figure 4.25 shows the surface of pure Cu immersed in 3 wt.% NaCl with added 1mM OH-Me-BimH for 60 days. There are three typical features present on the surface, light grey surface, dark grey surface and divergent black part. **Figure 4.25** (b) is the divergent black part, there is no evident hole on this part, seems not severe attack. As shown in **Figure 4.25** (c), light grey part inherent the scratches and exfoliations from the polished surface, as well as the dark grey part shown in **Figure 4.25** (d). 3D **Figure 4.25** (e) shows that black parts are small hills on the surface instead of holes. **Figure A1.41** shows the map of elements on the surface. The light grey surface contains little O with Cu, dark grey part contains more O, and black parts are C rich area. **Figure 4.26** shows the point elemental analysis which will offer much precise information. Point (a) is the light grey surface which shows only Cu peak. Point (b) is the dark grey surface, oxidation happened on this part but not so much oxygen is detected. Point (c) on the black part shows little O and much C than that of point (b). Compounds contain C, Cu and O may form on this black part. However, OH-Me-BimH shows a great look of surface, no obvious local attack is found, and this inhibitor with OH-Me function group should be a candidate inhibitor for pure Cu.

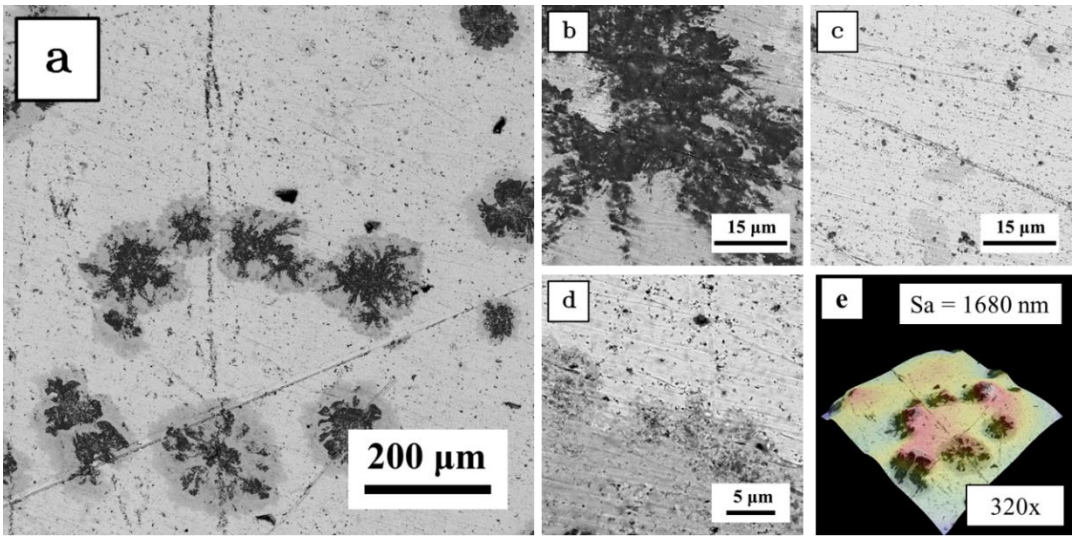

Figure 4.25 Pure Cu immersed in 3 wt.% NaCl with added 1mM OH-Me-BimH solution for 60 days (a) surface under 320x magnification with all typical features (b) black part of the surface (c) light grey surface under 5000x magnification (d) dark grey surface (e) 3D topography under 320x magnification by SEM

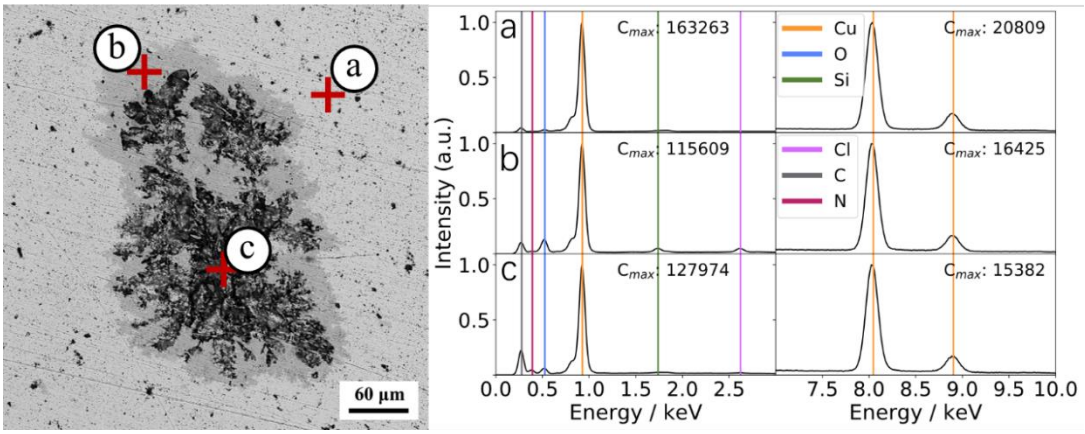

Figure 4.26 EDS elemental point analysis spectrum of Pure Cu immersed in 3 wt.% NaCl solution with added 1mM OH-Me-BimH for 60 days (a) spectrum of point a, light grey surface (b) spectrum of point b, dark grey surface (c) spectrum of point c, black part of the surface.

The SEM-EDX results show corrosion is inhibited by SH-BimH, Me-S-BimH, SH-BimH-5OMe, SH-ImiH-4Ph and OH-Me-BimH. Local attacks appear on all inhibitors but in a different scale. Among all inhibitors, Me-S-BimH shows the smallest pits on the surface. Other bad inhibitors are illustrated in **Appendix 1.1.2**. The adhesion of Cu-inhibitor complex appears on the local attacks, that may reduce the corrosion rate. Identification of this phenomenon will be carried by Raman spectroscopy and the results will be reported in **section 5.3.2**.

4.2 Corrosion Inhibition of Zinc

4.2.1 Short-term electrochemical tests

The anodic and cathodic processes of zinc corrosion in the solution are dissolution of zinc and reduction of oxygen, that is:

$$Zn \rightarrow Zn^{2+} + 2e \text{ and } O_2 + 2H_2O + 4e \rightarrow 4OH^-$$

Then, Zn^{2+} and OH^- will react and form zinc hydroxide, it will deposit on the Zn surface since the solubility is low. And zinc hydroxide on the surface will transfer to zinc oxide and form a passive film [106]:

$$Zn^{2+} + 2OH^- \rightarrow Zn(OH)_2 \rightarrow ZnO + H_2O$$

This film offers protection for corrosion, but addition of NaCl will break down this film by the reaction between the chloride ion and the passive film. A soluble Zn^{2+}−Cl^-−OH^- complex will be produced by this reaction [107]. Thus, local attacks may break the passive film and cause dissolution of Zn afterwards, which means that Zn will suffer pitting corrosion in NaCl solution [108]. Due to the application of Zn as the protective layer for iron, some of the inhibitors were studied to improve the inhibition. However, most of the research was focused on anion inhibitors that can suppress the anodic process by forming deposits at the pit [109–111]. Some organic compounds [112] and natural extracts were studied as well [113]. The aim of the study here is not to explore the inhibition performance of organic inhibitors on pure Zn; on the contrary, all the tests will focus on assisting in understanding corrosion inhibition of CuZn alloys.

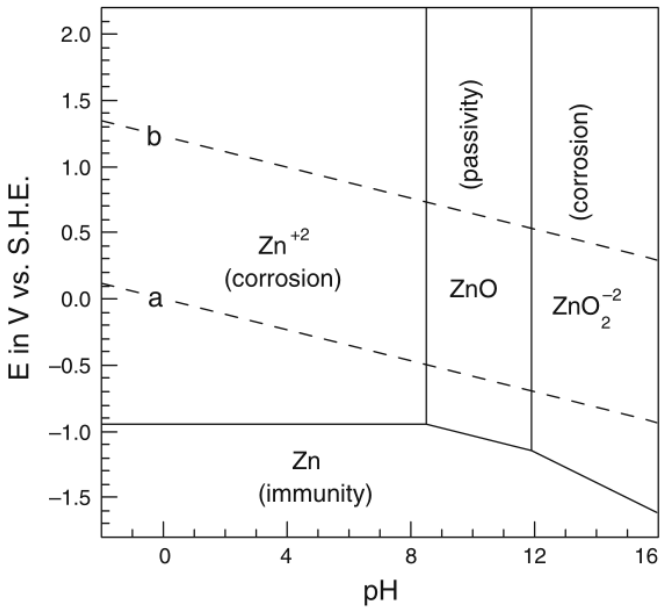

Figure 4.27 Pourbaix diagram for zinc at 25 ◦ C. Drawn from data in [114]

Figure 4.28 displays the linear polarization resistance and low frequency impedance values of pure Zn. It is worth to note that the corrosion resistance of pure Zn is lower than 1 kΩ·cm^2, orders of magnitude lower than that of pure Cu. It is found that SH-BimH, SH-BimH-5OMe and SH-ImiH-4Ph are good inhibitors as for pure Cu. ImiH and SH-BimH-5NH_2, which act as corrosion accelerators for Cu, become now corrosion inhibitors; in particular, SH-BimH-5NH_2 presents the best inhibition effect. On the contrary, SH-ImiMe acts as a corrosion accelerator. As expected, the different chemistry of the metals and the interaction with the different functional groups make it difficult to predict the inhibition efficiency of the studied compounds in different metals.

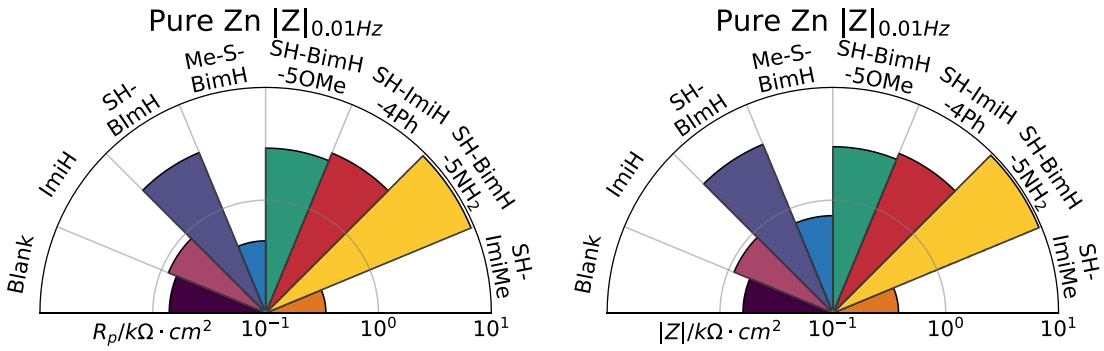

Figure 4.28 Polar graphs of linear polarization resistance (left) and impedance modulus at 0.01 Hz (right) of pure Zn, measured after 1 h immersion in 3 wt.% NaCl aqueous solution (blank) and in the presence of different organic compounds added at 1 mM concentration. Note the logarithmic scale.

The potentiodynamic polarization plots of pure Zn are shown in **Figure 4.29**. The corrosion potential for both pure Zn and in presence of inhibitors is highly negative, reflecting that Zn is prone to fast corrosion. For pure Zn without inhibitor, passivation appears around −1.2 V, but it disappears in the curves corresponding to all inhibitors. All inhibitors shift the corrosion potential to a more positive value, but none of them is able to approach the corrosion potential to neutral. Tafel parameters are shown in **Table 4.2** except for pure Zn, which cannot be calculated due to the appearance of passivation at initial polarization.

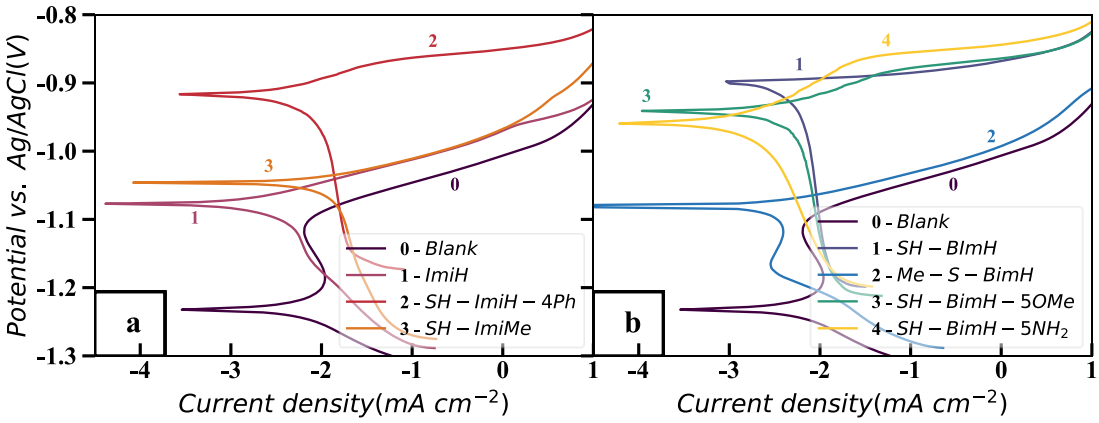

Figure 4.29 Potentiodynamic polarization curves of pure Zn in 3 wt.% NaCl aqueous solution with and without 1 mM of different organic compounds: (top) imidazole derivatives, (middle) mercapto-benzimidazole derivatives, and (bottom) hydroxy-benzimidazole derivatives. Quantitative electrochemical parameters are presented in **Table 4.2**

Table 4.2 Zn Metal Tafel Parameters (cf. **Figure 4.29**).

Solution	E_{corr} (mV) vs. Ag/AgCl	j_{corr} （μA/cm^2）	$-\beta_c$ (mV/dec)	β_a (mV/dec)
3 wt.% NaCl	-	-	-	-
ImiH	-1073	1.647	131	34.5
SH-ImiMe	-1051	11.117	316.6	41.5
SH-ImiH-4Ph	-895	8.646	776.9	38.2
SH-BimH	-923	6.497	949.7	25.4
SH-BimH-5OMe	-930	5.421	737.2	47.1
SH-BimH-5NH_2	-933	1.533	295.8	58.9
Me-S-BimH	-1083	2.949	245.4	33.3

Among imidazole derivatives, SH-ImiH-4Ph is the one that induces a larger change of the corrosion potential, but the corrosion behavior is very similar for all of them. In the group of mercapto-benzimidazole derivatives, SH-BimH, SH-BimH-5OMe and SH-BimH-5NH_2 shift the corrosion potential significantly to less negative values, but fast dissolution seems to happen with SH-BimH. SH-BimH-5NH_2 and ImiH show the smallest corrosion current but only SH-BimH-5NH_2 shows a small current density. The Tafel data of Me-S-BimH may be disturbed by the cathodic curve.

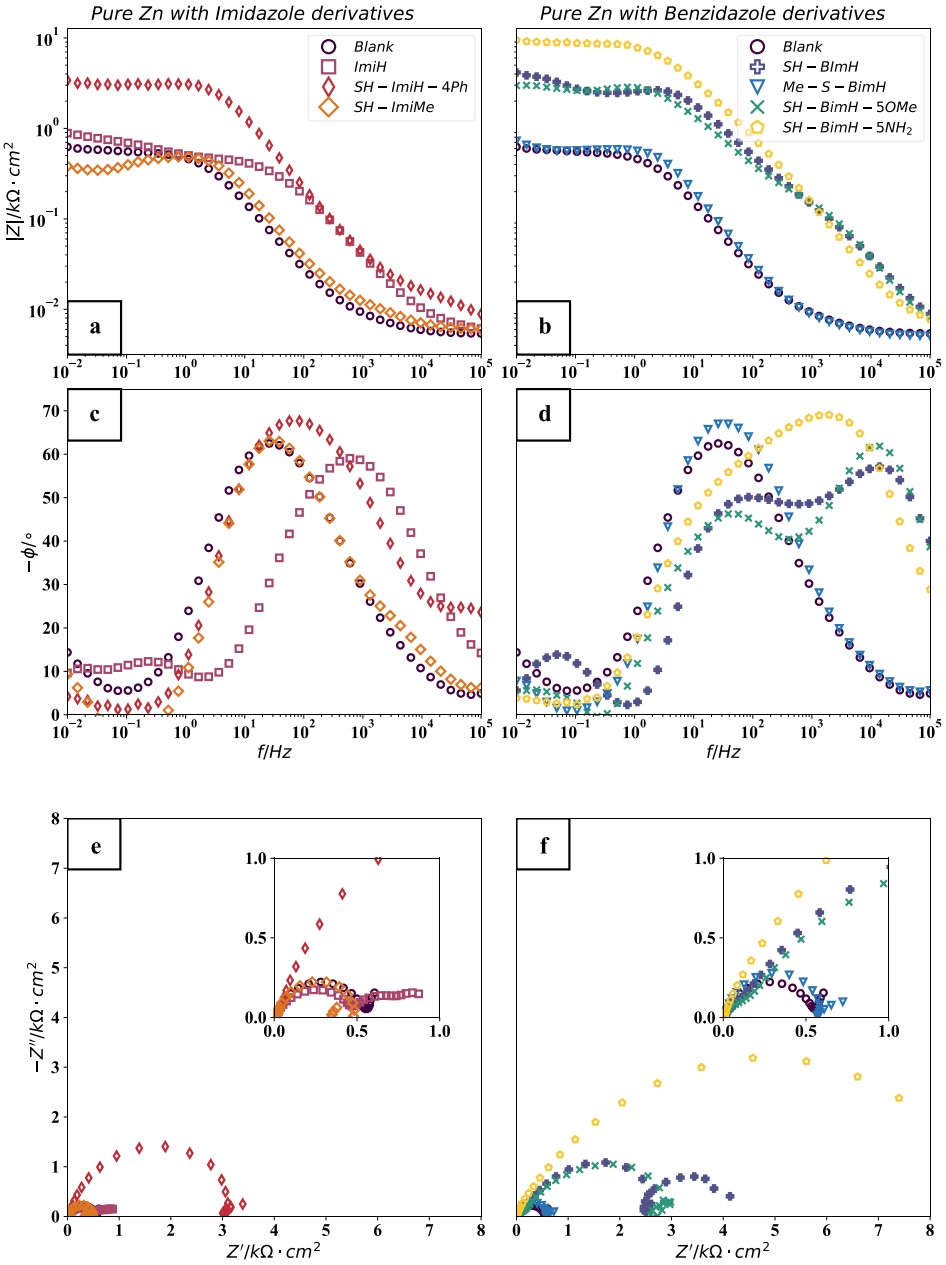

Figure 4.30 Electrochemical impedance spectra of pure Zn in the form of Bode impedance plot, phase angle plot and Nyquist plot with or without addition of 1 mM of different organic compounds in aqueous 3 wt. % NaCl solution: a), c), e) imidazole derivatives and b), d), f) mercapto-benzimidazole derivatives.

The EIS Nyquist and Bode plots in **Figure 4.30** show the inhibition effect on pure Zn, visibly different than that observed on pure Cu. The Nyquist plot of pure Zn in NaCl solution shows a typical semicircle and straight line appearance similar to that of Cu, but the radius is significantly smaller. Phase angle plot shows one time constant with a maximum phase angle of 60°, which indicates that the capacitive behavior is not strong in all the frequency range tested. In imidazole derivatives, only SH-ImiH-4Ph shows a good inhibition, with a maximum phase angle improved from 60° to 70°, and the Nyquist plot shows a large semicircle with a small one. ImiH shows at least two small semicircles

and the radius is not so different from that of the blank curve. SH-ImiMe acts as a corrosion accelerator and the minimum phase angle reaches negative values, which may indicate that inductive behavior appears. For mercapto-benzimidazole derivatives, Me-S-BimH shows almost same EIS plots as those of the blank measurement, while SH-BimH, SH-BimH-5OMe and SH-BimH-5NH_2 show a positive inhibition effect. SH-BimH and SH-BimH-5OMe show a double semicircle in the Nyquist plot, with a similar radius to the first circle. SH-BimH-5OMe introduces two time constants and SH-BimH shows three, which means these two inhibitors induce a complex corrosion reaction on the surface. SH-BimH-5NH_2 seems to have only one time constant, but comparison with the previous two inhibitors suggests that the single wide peak may correspond to the merge of two peaks. Nevertheless, the Nyquist plot shows a significant improvement of radius of a semicircle, indicating that SH-BimH-5NH_2 has the best inhibition performance. The short-term measurements show that the inhibitors with -SH group, SH-ImiH-4Ph, SH-BimH, SH-BimH-5OMe, may inhibit pure Zn in a similar way. However, the -NH_2 group inhibitor – SH-BimH-5NH_2– shows the best inhibition performance of all tested inhibitors. On the contrary, the function group of -CH_3 may activate the corrosion process, and SH-ImiMe and Me-S-BimH. ImiH shows almost no influence on the corrosion process.

4.2.2 Long-term electrochemical tests

Figure 4.31 displays the results of long-term linear polarization resistance and impedance tests. Pure Zn without inhibitors shows a little improvement after 24 hours, attributable to the ZnO passivation film formed on the surface[107], and the subsequent decrease indicates the breakdown effect caused by the presence of the chloride ion[108]. The inhibitors can be divided into three groups, effective inhibitors: SH-BimH, SH-BimH-

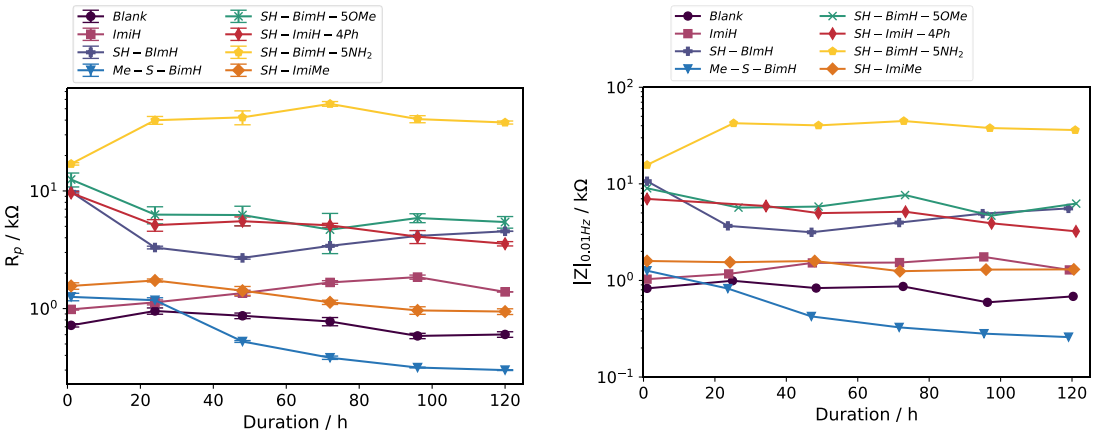

Figure 4.31 Long-term graph of linear polarization resistance (left) and impedance modulus at 0.01 Hz (right) of pure Zn, measured in period of 120 h immersion in 3 wt.% NaCl aqueous solution (blank) and in the presence of different organic compounds added at 1 mM concentration. Note the logarithmic scale.

5OMe, SH-ImiH-4Ph and SH-BimH-5NH_2; no inhibition: SH-ImiMe and ImiH; and corrosion accelerator: Me-S-BimH. In the effective group, SH-BimH, SH-ImiH-4Ph and SH-BimH-5OMe, all of them having a -SH group, show a decreasing inhibition with time. Therefore, the -SH group may initially inhibit corrosion for pure Zn, but the inhibition effect is not stable. Only SH-BimH-5NH_2 shows a stable inhibition effect, and increasing with time, which must be attributed to the presence of -NH_2 group. ImiH shows the no prominent inhibition as short tests.

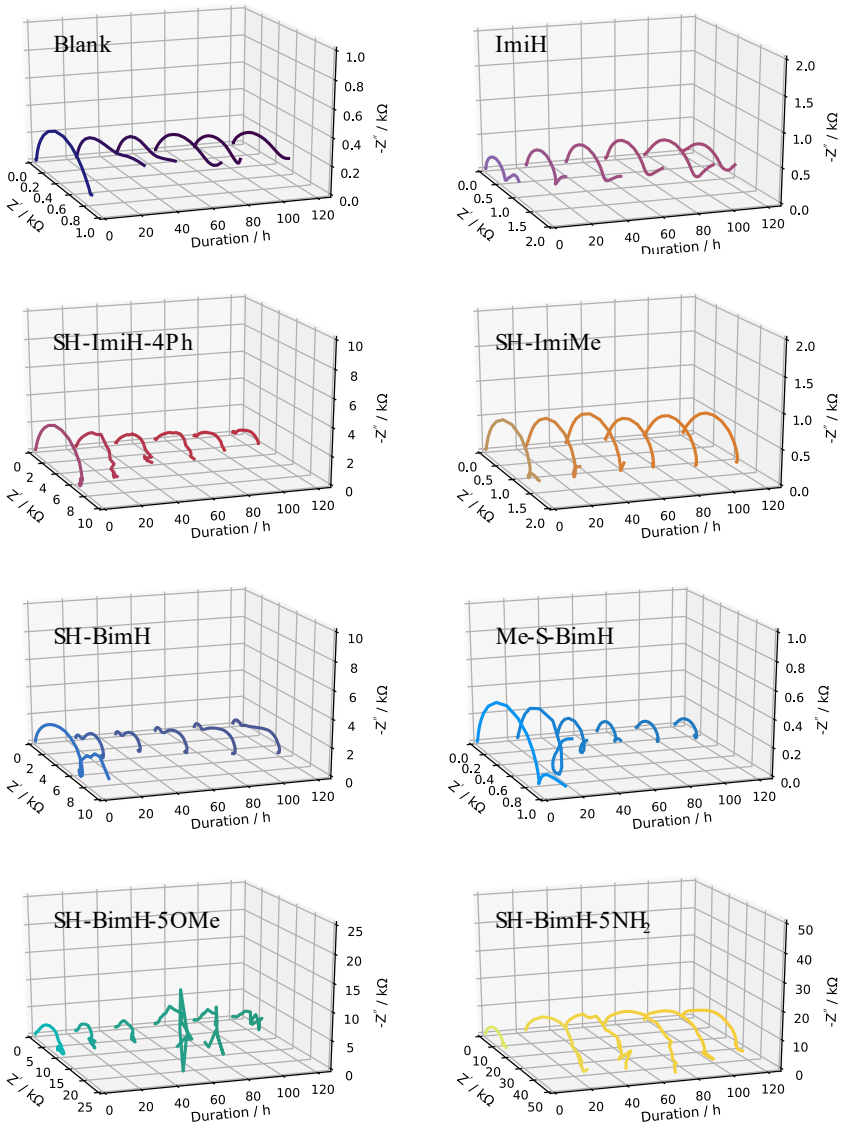

Figure 4.32 Long-term Nyquist plot of pure Zn in NaCl solution without and with 1 mM inhibitor, in period of 120 h.

The dynamic Nyquist plot of pure Zn versus time in NaCl solution without and with inhibitors, displayed in **Figure 4.32**, shows more details. The initial corrosion behavior

of the blank solution is analyzed in short-term test; a double semicircle appears after 24 h, combined with the minimum phase angle increase from ~5° to ~20° (see **Figure A1.12**), reflects that passivation may happen on the surface. The peak of time constant shifts to lower frequencies in the curves corresponding to 24h and 48h immersion time. After 72h, the peak shifts back to higher frequencies, and the maximum phase angle decreases to ~50°; the corrosion resistance worsens. ImiH shows similar behavior in the Nyquist plot (see **Figure 4.32**), but the phase angle plot shows that a new time constant may exist after 96 h. The minimum phase angle is even smaller than in the blank solution. SH-ImiH-4Ph, SH-BimH and SH-BimH-5OMe show similar phase plots (see **Figure A1.14**, **Figure A1.15** and **Figure A1.17**), two time constant appear and the maximum phase angle at low frequency decreases with time. The corrosion behavior shows no change with time. Similar to what was observed in pure Cu, SH-BimH-5OMe shows a chaotic behavior at low frequency as time increases. Therefore, SH-ImiMe is not effective and the corrosion behavior does not improve with time, as shown in the Nyquist and phase angle plot (**Figure A1.19**). SH-BimH-5NH_2 is the best inhibitor, as shown in the Nyquist and phase plot. The time constant peak shifts to high frequency and keeps a phase angle of ~80° (see **Figure A1.18**). The corrosion behavior does not change with time and maintains good impedance and resistance. This may indicate that SH-BimH-5NH_2 can form a layer on the pure Zn surface and hold the bonding stable. This feature should be attributed to the presence of the -NH_2 group.

A summary of the inhibition efficiency and inhibition power of the different inhibitors on pure Zn is shown in **Figure 4.33** and **Figure 4.34**. As in the case of Cu, IP discriminates much more efficiently between good and bad inhibitors, and reflects the much better performance of SH-BimH-5NH_2 among all tested inhibitors.

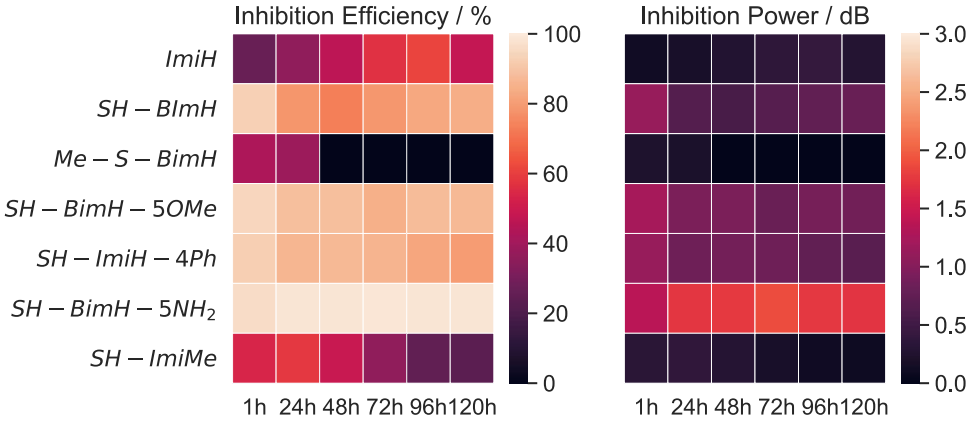

Figure 4.33 Long-term LPR R_p inhibitor efficiency and inhibitor power of pure Zn with different inhibitors in period of 120h

Figure 4.35 shows the statistical analysis of the correlation coefficient during linear regression of LPR measurements. Most of the values are above 0.9 and only SH-BimH-5OMe shows a low coefficient after 24 hours' immersion, similar to what happened in pure Cu; this coincides with the EIS chaotic data at low frequency.

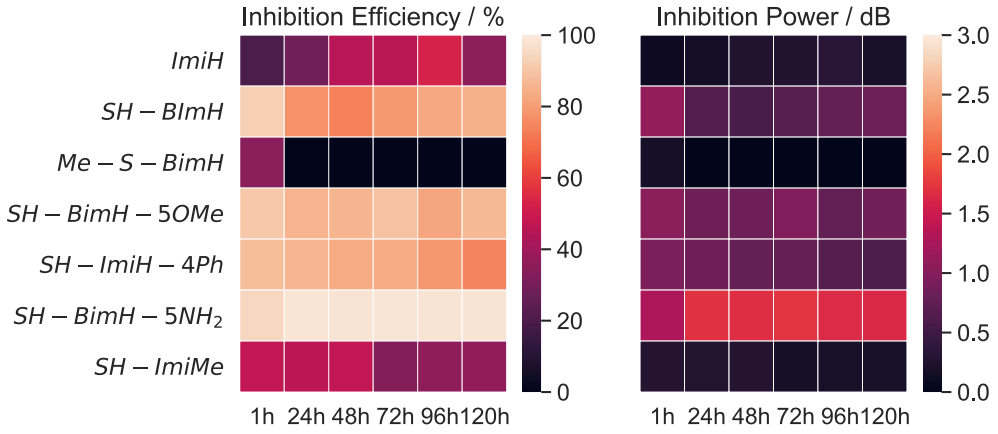

Figure 4.34 Long-term EIS |Z| at 0.01 Hz inhibitor efficiency and inhibitor power of pure Zn with different inhibitors in a period of 120h

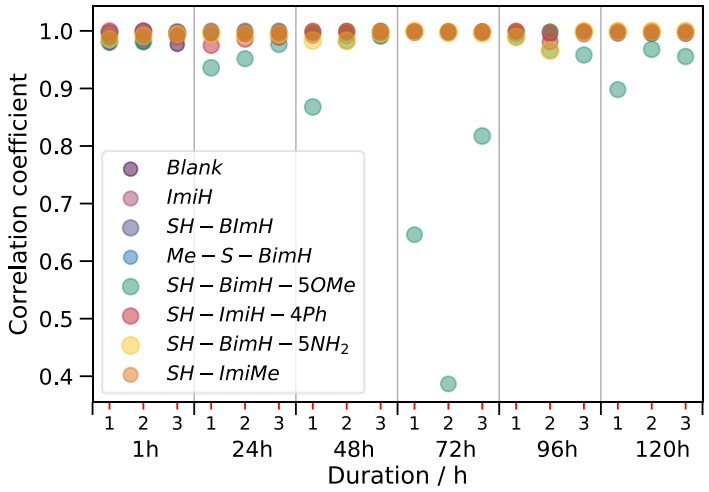

Figure 4.35 Statistic analysis of LPR data based on correlation coefficient in Long-term measurements of pure Zn

4.2.3 Immersion Test

Immersion tests of Zn were performed as support information to analyze corrosion inhibition efficiency of Cu-based alloy. Here, a 12 days' immersion test was performed since the low corrosion resistance of pure Zn. Photographic analysis, SEM-EDX and Raman spectroscopy were used as characterization methods of the specimens.

Photographic analysis

Figure 4.36 shows the appearance of Zn samples after 12 days' immersion. For the samples immersed with inhibitors, a large white floc appears on the surface. This kind of floc is extremely easy to remove by rinsing with DI water. The flocs were suspected to

be the Zn-inhibitor complex and will be characterized by SEM-EDX and Raman spectroscopy. After drying in the vacuum desiccator, the appearance of the zinc surface is similar, dried flocs are still on the surface and partial attack is clear in the blank, ImiH, SH-ImiMe and Me-S-BimH immersion solution samples, which show a dark grey color. The rest of the samples seem covered by an organic film.

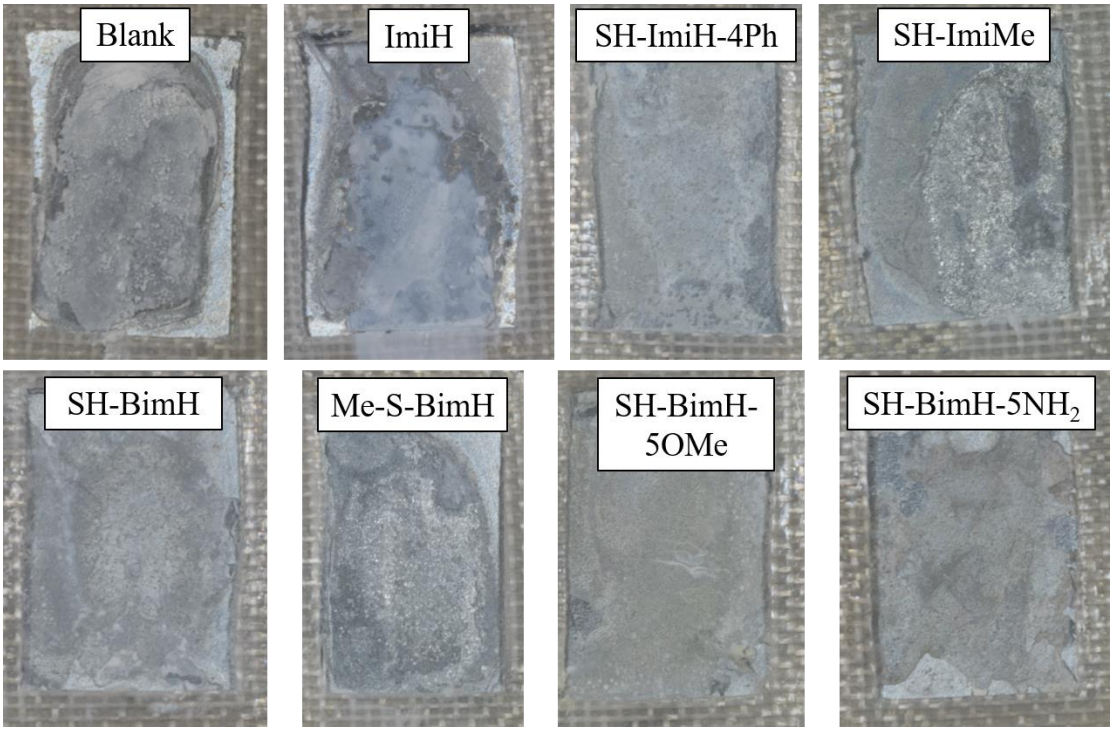

Figure 4.36 Photographies of pure Zn samples after immersion for 12 days with and without presence of 1mM inhibitors in 3wt% NaCl solution sealed in bottle.

SEM-EDX analysis

Figure 4.37 shows the bare surface of pure Zn after polishing with P4000 SiC paper. **Figure 4.37** (a) shows scratches and exfoliations present on the surface. With a closer look in **Figure 4.37** (b) and (d), the scratches and exfoliations are more explicit; these unavoidable defects resulting from polishing may affect the corrosion behavior and inhibition. 3D **Figure 4.37** (e)of the surface shows a good roughness Sa of 0.843 μm. **Figure A1.59** shows the element distribution; only Zn appears and no signal is obtained in the black part. **Figure 4.38** shows the elemental point analysis by EDX. Only the peaks at (~ 8.637 keV) and (~ 9.570 keV) correspond to the Zn $K\alpha_1$ and Zn-$K\beta_1$, respectively, Zn peaks are present in points a, placed on the flat surface. Points b and c are on the black holes, thus the signal is lower than that of point a. Point (b) shows the same profile as that of point (a), and Si and O appear in the spectrum of point (c). This is as same as what happened on pure Cu, some SiC particle could embed in the exfoliations.

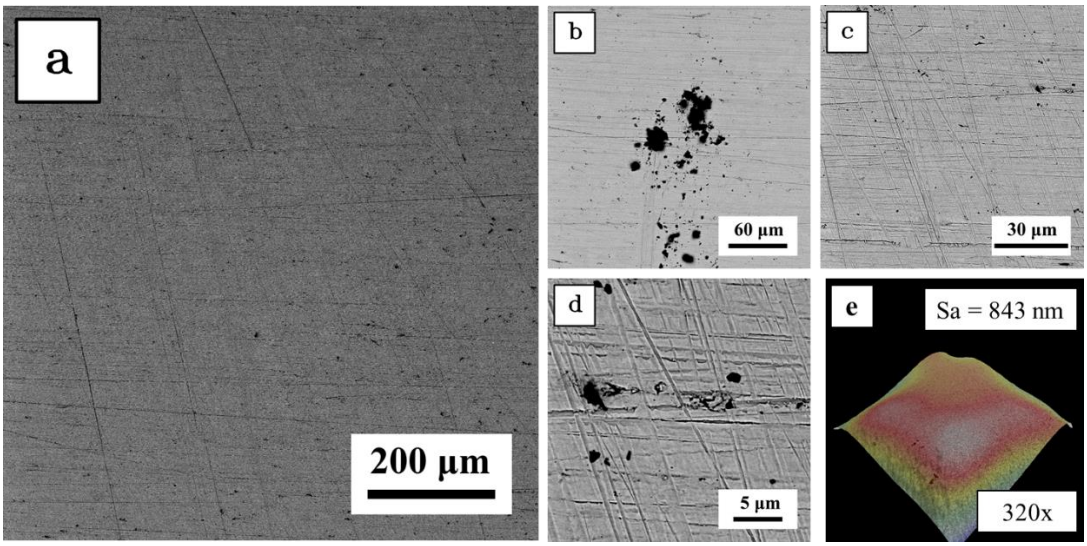

Figure 4.37 Bare surface of Pure Zn after polishing and rinse (a) surface under 320x magnification (b) surface under 1000x magnification (c) flat surface under 1000x magnification (d) detail of the scratches and exfoliations (e) 3D topography under 320x magnification by SEM

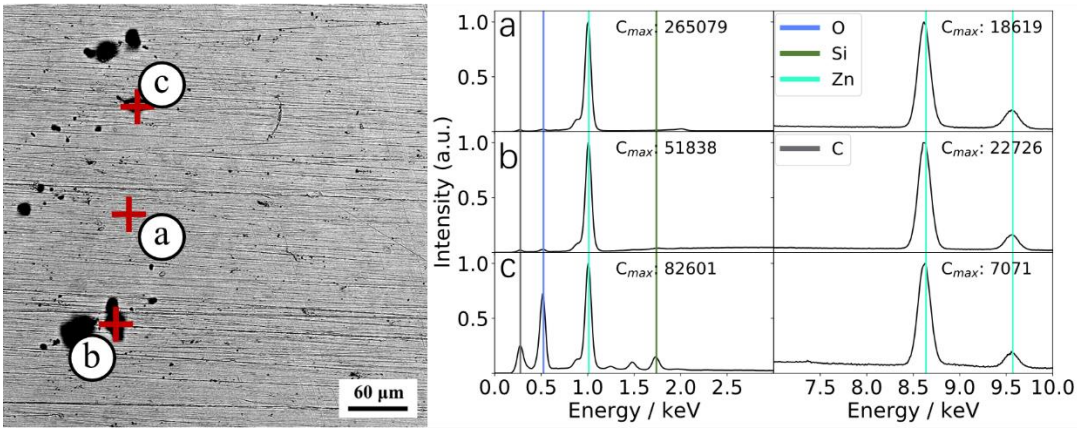

Figure 4.38 EDX elemental point analysis spectrum of bare surface of Pure Zn (a) spectrum of point a, flat surface (b) (c) spectrum of point b and (c), exfoliation holes.

Figure 4.39 shows the surface of pure Zn after immersion for 12 days in 3 wt.% NaCl solution. Surface displays in two typical features, flat surface with some small hills and flower-like substance covered parts, as shown in **Figure 4.39** (a). The flower-like substance with higher magnification in **Figure 4.39** (b) and (d) show that the flowers are composed of lamellar substance. As shown in **Figure 4.39** (c), the flat surface does the same but in small lamellar ones. **Figure 4.39** (e) shows the 3D surface, the flower-like area is higher, and roughness is not lifted so much, Sa is 0.856 µm. **Figure A1.60** is the elemental map of the surface. It shows the major elements of Zn, Cl, O covered the surface. Much more precise point analysis is done and shows in **Figure 4.40**. Point (a), (b) and (c) show the same peaks appear in all three points, the intensity is not the same. Consider the difference of the structure on different locations, this will affect the results of the intensities. The surface should cover by the same substance but with a different scale.

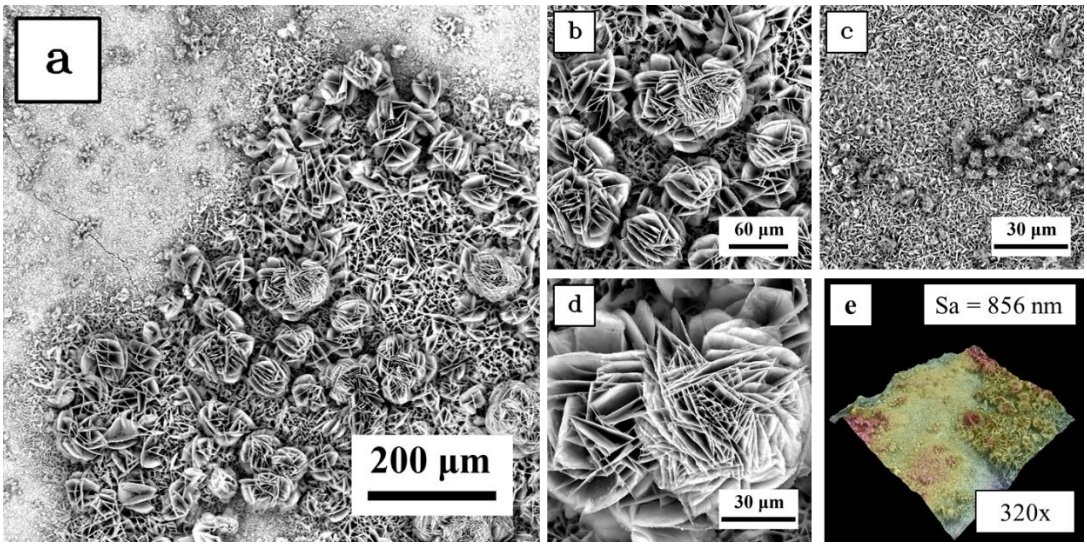

Figure 4.39 Pure Zn immersed in 3 wt.% NaCl solution for 12 days (a) surface under 320x magnification with all typical features (b) flower-like surface under 1000x magnification (c) white surface under 2500x magnification (d) structure of flower-like substance (e) 3D topography under 320x magnification by SEM

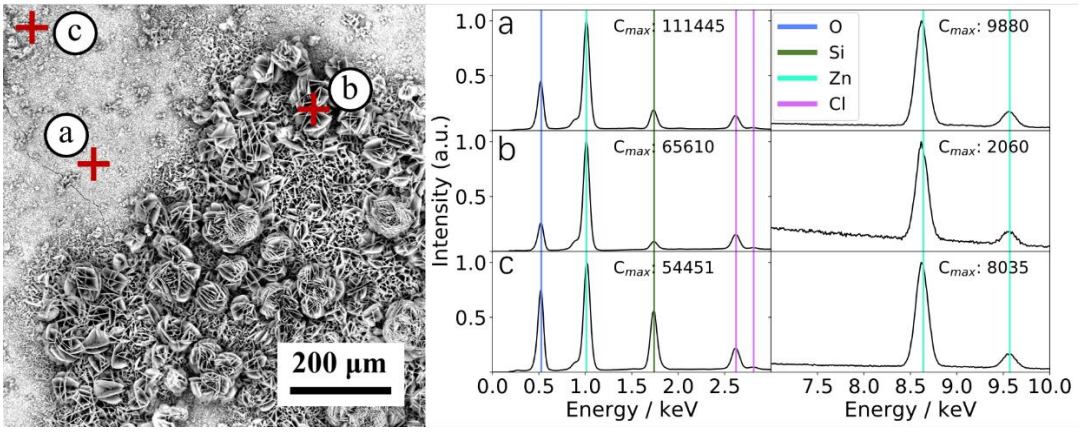

Figure 4.40 EDX elemental point analysis spectrum of Pure Zn immersed in 3 wt.% NaCl solution for 12 days (a) spectrum of point a, white part under BSE detector (b) spectrum of point b, flower-like substance on the surface (c) spectrum of point c, small corrosion products on the surface.

Figure 4.41 shows the surface of pure Zn after immersion in 3 wt.% NaCl with added SH-ImiH-4Ph for 12 days. In **Figure 4.41** (a), cracks and pits appear on the surface, but not as large as in previous inhibitors. **Figure 4.41** (b) and (d) show the locations of pits, combine with the 3d surface in **Figure 4.41** (e), some substances are always adhering on the pits, which suspect to the adhesion of Zn-inhibitor complex. **Figure A1.73** shows distribution of elements by EDX map analysis. S appears on some location, and Zn, O, C covered most of the surface. **Figure 4.42** shows the elemental point analysis, in all three points (a), (b) and (c), the peaks are similar. And Zn oxide exists on the surface with some SiC particles. S peak is too small which indicates it does not always adhere to the pits. SH-ImiH-4Ph shows inhibition on pure Zn, and Zn-inhibitor complex adheres to some location.

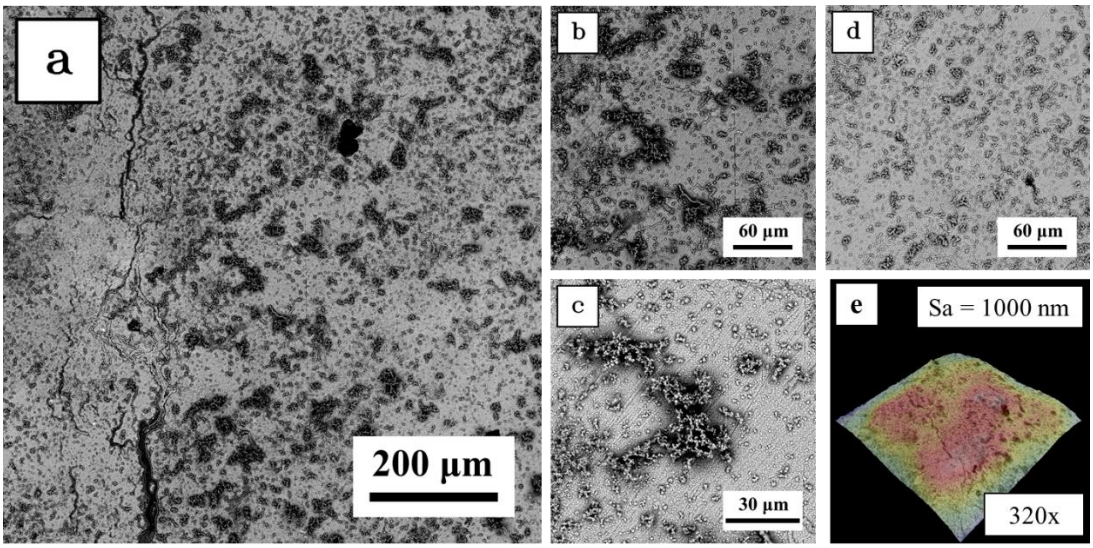

Figure 4.41 Pure Zn immersed in 3 wt.% NaCl with added 1mM SH-ImiH-4Ph solution for 12 days (a) surface under 320x magnification with all typical features (b) local attacks on surface under 1000x magnification (c) good surface under 1000x magnification (d) corrosion product on the surface (e) 3D topography under 320x magnification by SEM

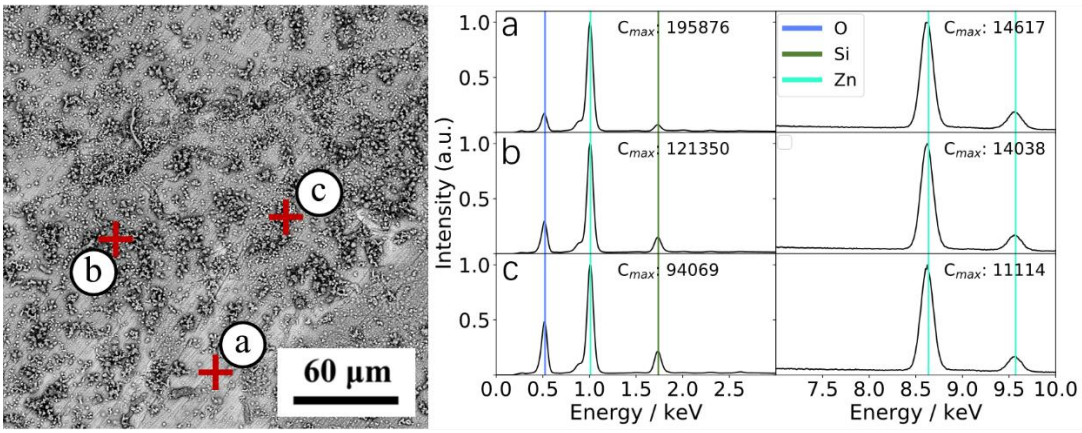

Figure 4.42 EDS elemental point analysis spectrum of Pure Zn immersed in 3 wt.% NaCl solution with added 1mM SH-ImiH-4Ph for 12 days (a) spectrum of point a, white flat surface (b) spectrum of point b and c, corrosion products on the surface.

Figure 4.43 shows the surface of pure Zn immersed in 3 wt.% NaCl with added SH-BimH-5NH_2 for 60 days. As shown in **Figure 4.43** (a), no evident cracks found on the surface, some pits may exist. And surface shows a slightly different contrast. With larger magnification in **Figure 4.43** (b), (c), (d), most of the pits are exceedingly small and scratches from polishing are still clear. **Figure A1.74** shows the distribution of elements. The black part shows a higher concentration of Cl and O than other locations, S, Zn and O covered most of the surface. **Figure 4.44** shows the elemental point analysis. As shown in point (a), the surface is only present little oxidation, and no other reaction happens. Point (b) shows a large peak of Si, Cl, the local attacks should happen on the SiC embedded position. Moreover, S is found in this location to indicate the adhesion of Zn-

inhibitor on the pits. This is quite different from the interaction between SH-BimH-5NH_2 and pure Cu. The small pits in point (c) show presence of Si, S and no Cl, which means the adhesion of inhibitor reduces the pitting process. SH-BimH-5NH_2 is the best inhibitor among all tested inhibitors. And the remarkable difference of inhibition effects between pure Cu and Zn should be noticed.

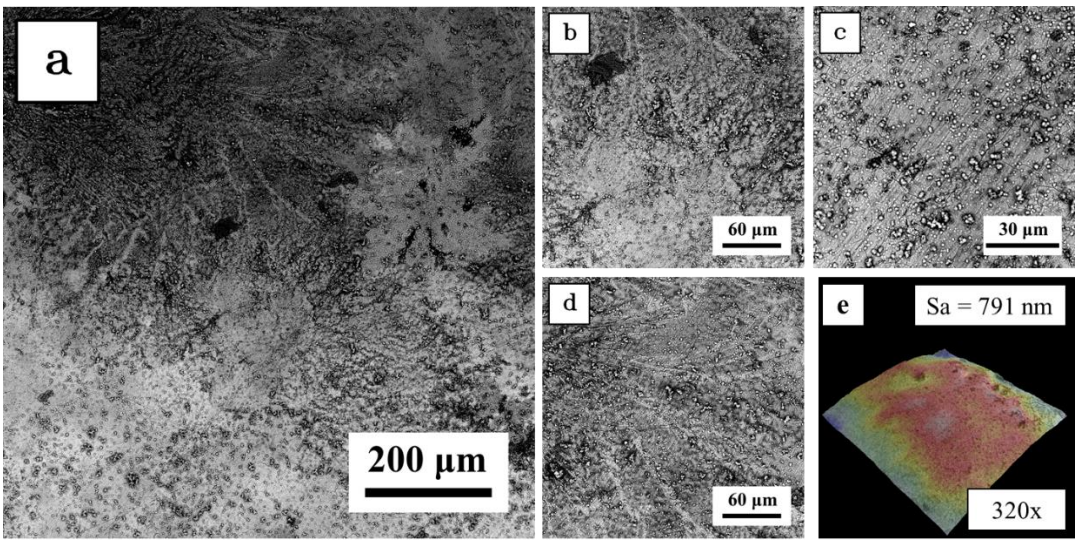

Figure 4.43 Pure Zn immersed in 3 wt.% NaCl with added 1mM SH-BimH-5NH_2 solution for 12 days (a) surface under 320x magnification with all typical features (b) surface under 1000x magnification (c) surface under 2500x magnification (d) surface features in dark part (e) 3D topography under 320x magnification by SEM

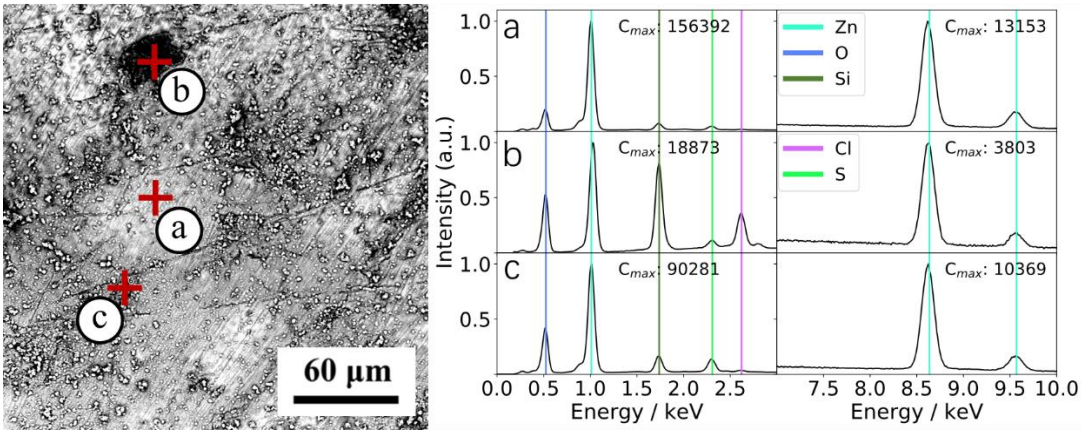

Figure 4.44 EDS elemental point analysis spectrum of Pure Zn immersed in 3 wt.% NaCl solution with added 1mM SH-BimH-5NH_2 for 12 days (a) spectrum of point a, white flat surface (b) spectrum of point b, black corroded surface (c) spectrum of point c, corrosion products on the surface.

Most inhibitors show no evident inhibition for pure Zn. Only SH-ImiH-4Ph and SH-BimH-5NH_2 show inhibition, and SH-BimH-5NH_2 show acceleration on corrosion for pure Cu. This should attribute the -NH_2 group since it is the only one contain this group. Other negative inhibitors' results are shown in Appendix 1.2.2.

4.3 Corrosion Inhibition of Zirconium

4.3.1 Short-term electrochemical tests

Pure Zr shows a quite different interaction with inhibitors. As shown in **Figure 4.45**, left, some of the linear polarization resistance couldn't be calculated as the measurements showed an erratic behavior. **Figure A1.78** shows the line regression curves. Some of the curves gave inconsistent measurements, and some others are not very repeatable. This behavior may be attributed to the formation of ZrO_2 on the surface, with a large dielectric constant, 10 to 23, and huge resistivity, 3.16×10^5 to 3.16×10^{10} Ωm, which provides protection for the material in a corrosive electrolyte. Almost no research focuses on corrosion inhibition of pure Zr due to this effective protective film. The linear polarization is based on the assumption of the existence of a redox reaction in a small overpotential range, but not a passive surface. Considering that the ZrO_2 will allow just an extremely small amount of charge transfer through the film, this film is much more like a real capacitor. A unidirectional current can't pass throw the film and will cause a charging effect at the interface; the theory of linear polarization will not work anymore, and the presence of crystalline boundaries will make the signal ever more complex. Therefore, the linear polarization resistance is not computable when dealing with a dielectric film covered metal surface.

On the contrary, the experiment design of EIS allows it to measure the impedance of a surface covered by a dielectric film. **Figure 4.45**, right, shows that none of the inhibitors induces any improvement on the Zr low frequency impedance. The measured values show negligible changes when compared to the blank solution, as it is noticed under logarithmic scale. SH-BimH, Me-S-BimH and SH-BimH-5NH_2 seem to induce a little increase on the impedance, but these increases are not significant as may be due to the experimental uncertainty due, for example, to the surface topography of the sample.

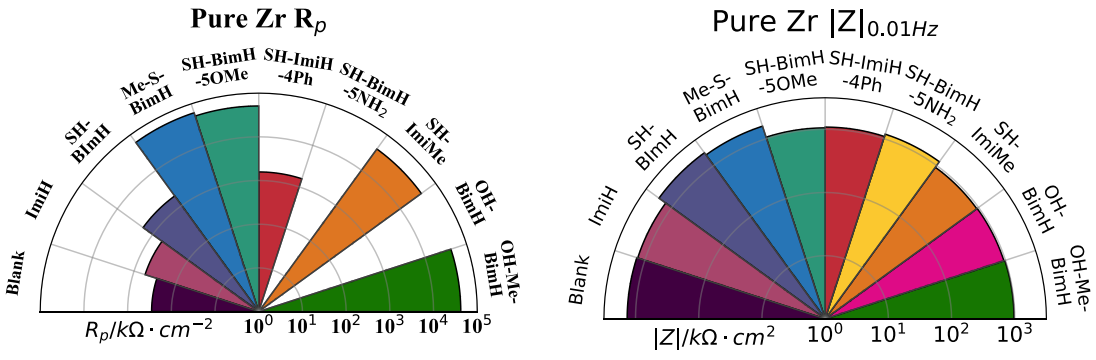

Figure 4.45 Polar graphs of linear polarization resistance (left) and impedance modulus at 0.01 Hz (right) of pure Zr, measured after 1 h immersion in 3 wt.% NaCl aqueous

solution (blank) and in the presence of different organic compounds added at 1 mM concentration. Note the logarithmic scale.

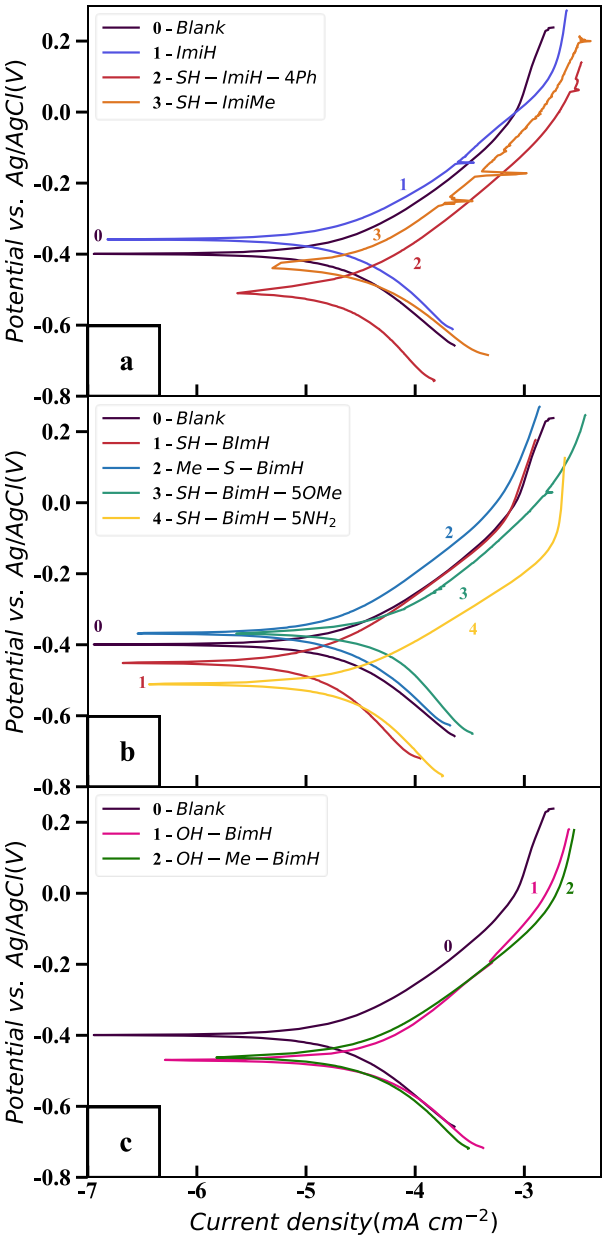

Figure 4.46 Potentiodynamic polarization curves of pure Zr in 3 wt.% NaCl aqueous solution with and without 1 mM of different organic compounds: (top) imidazole derivatives, (middle) mercapto-benzimidazole derivatives, and (bottom) hydroxy-benzimidazole derivatives. Quantitative electrochemical parameters are presented in **Table 4.2**

Potentiodynamic polarization measurements of pure Zr in presence of inhibitors in chloride solution are shown in **Figure 4.46**. Imidazole derivatives showed no inhibition activity. SH-BimH-5NH_2 acted as the most efficient among mercapto-benzimidazoles, causing the largest shift of the E_{corr} to negative values and thus increasing the passive range; however, the j_{corr} was not significantly affected. In contrast to Cu, SH-BimH-5OMe acted as an activator, whilst SH-BimH and Me-S-BimH acted as mild inhibitors. Hydroxy-benzimidazole derivatives also acted as activators. Efficient inhibitors on Zr behave as cathodic type inhibitors. Quantitative electrochemical parameters derived from the polarization curves for Zr presented in **Figure 4.46** are given in **Table 4.3** in the Supplementary material.

EIS plots of pure Zr with and without inhibitors are shown in **Figure 4.47**. The appearance of Nyquist plots and phase angle plots is very similar. Half of a huge semicircle appears in every inhibitor, which indicates that charge transfer dominates the corrosion process. All phase angle plots reach a maximum angle of ~85°, and show a plateau over a large frequency range. Since the 3 wt. % NaCl aqueous solution has a large ion transfer ability and the double-layer at the interface can't introduce such capacitive

behavior, the Zr film must exist on all the surface and dominates the corrosion process.

Therefore, it is observed that corrosion of pure Zr is dominated by the development of a ZrO_2 film and corrosion resistance of Zr itself is quite large. Pure Zr does not need inhibitors to improve corrosion resistance, and ZrO_2 does not interact with any of the tested inhibitors. Since the uselessness of inhibition test on Zr, long-term electrochemical tests were not performed on pure Zr. Only long-term immersion tests were carried out to assess the possible influence of inhibitors on the Zr surface.

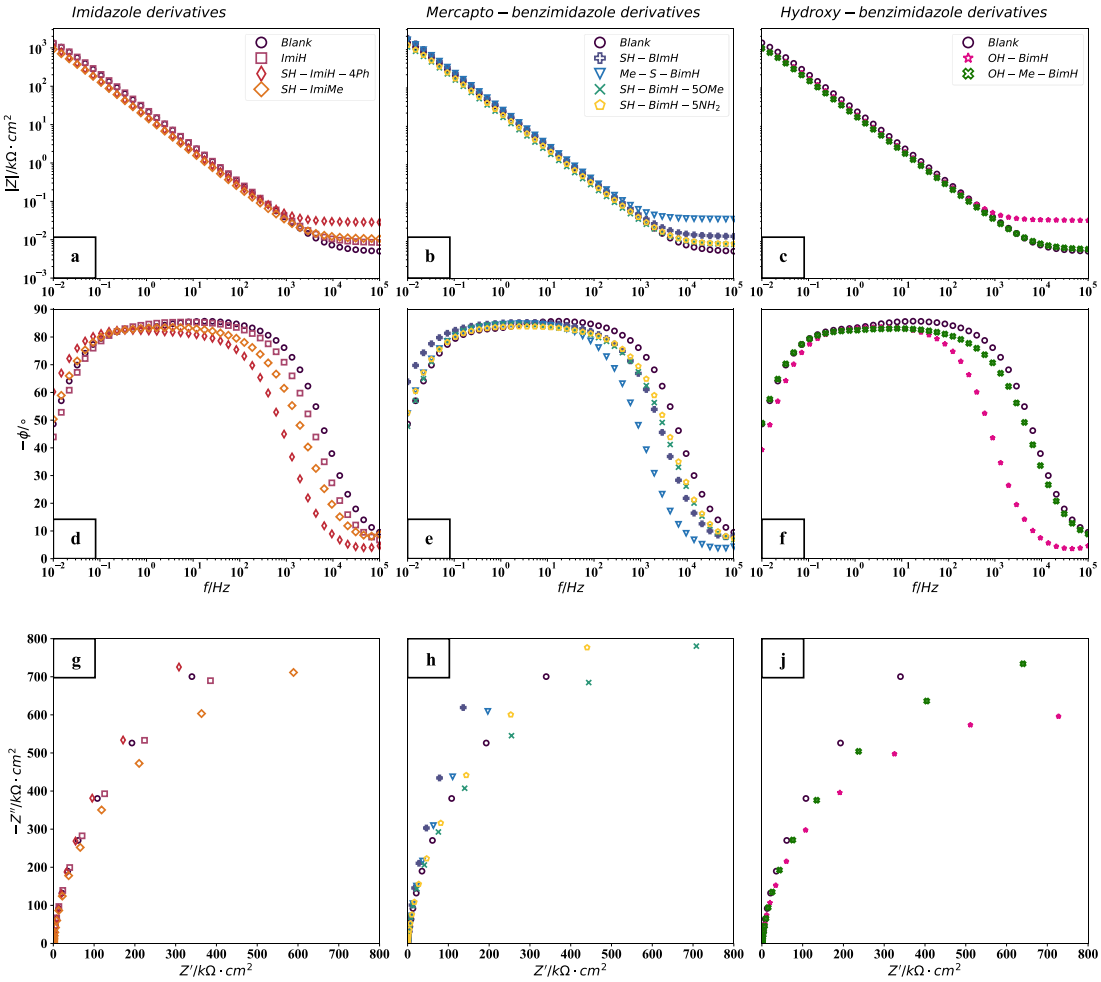

Figure 4.47 Electrochemical impedance spectra of pure Cu alloy in the form of Bode impedance plot, phase angle plot and Nyquist plot with or without addition of 1 mM of different organic compounds in aqueous 3 wt. % NaCl solution: a), c), e) imidazole derivatives and b), d), f) mercapto-benzimidazole derivatives.

Table 4.3 Zr Metal Tafel Parameters (cf. **Figure 4.46**).

Solution	E_{corr} (mV) vs. Ag/AgCl	j_{corr} （μA/cm²）	$-\beta_c$ (mV/dec)	β_a (mV/dec)
3 wt.% NaCl	−398	0.019	195	234
ImiH	−348	0.019	182	247
SH-ImiMe	−417	0.028	186	230

SH-ImiH-4Ph	−501	0.019	198	302
SH-BimH	−449	0.013	195	279
SH-BimH-5OMe	−367	0.041	215	323
SH-BimH-5NH_2	−507	0.022	176	281
Me-S-BimH	−360	0.016	207	240
OH-BimH	−466	0.038	232	246
OH-Me-BimH	−453	0.028	198	254

4.3.2 Immersion Tests

The immersion of pure Zr samples lasted around 1 year due to the high corrosion resistance. The appearance of the samples will be analyzed first by photographic and optical microscopic methods. The observation confirms the results found by short-term electrochemical tests, and for this reason, other measurements were not performed since no effective inhibition on pure Zr was found.

Photographic analysis

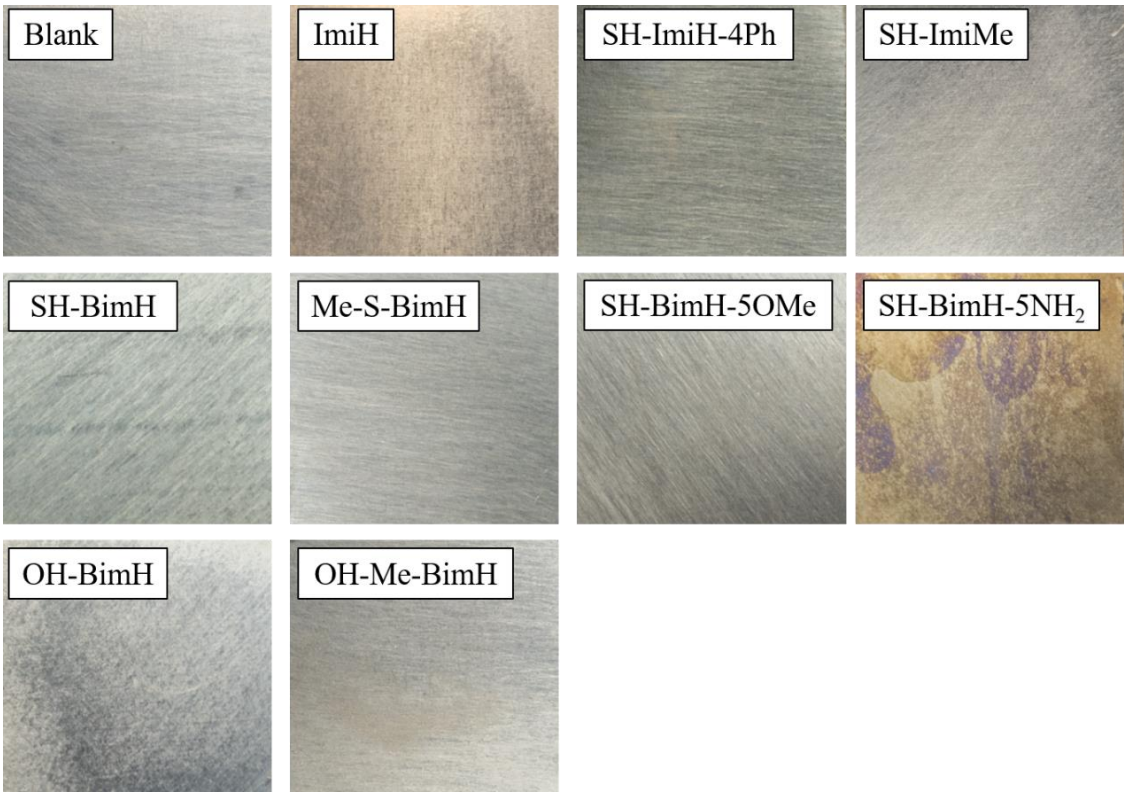

Figure 4.48 Photo of pure Zr samples after immersion for 1 year with and without presence of 1mM inhibitors in 3wt% NaCl solution sealed in bottle.

Figure 4.48 shows the photographs of pure Zr sample immersed in 3wt. % NaCl for 1 year with and without the addition of inhibitors. Most of the samples keep almost the

same appearance as the blank one. The scratches from grinding by P4000 SiC paper are still presented, and no significant corrosion and corrosion products were found. Only SH-BimH-5NH_2 made some change on the appearance of the surface, the surface becomes yellow and the scratches were not clear. This may be attributed to a new film formed on the surface.

Observation of optical microscopy

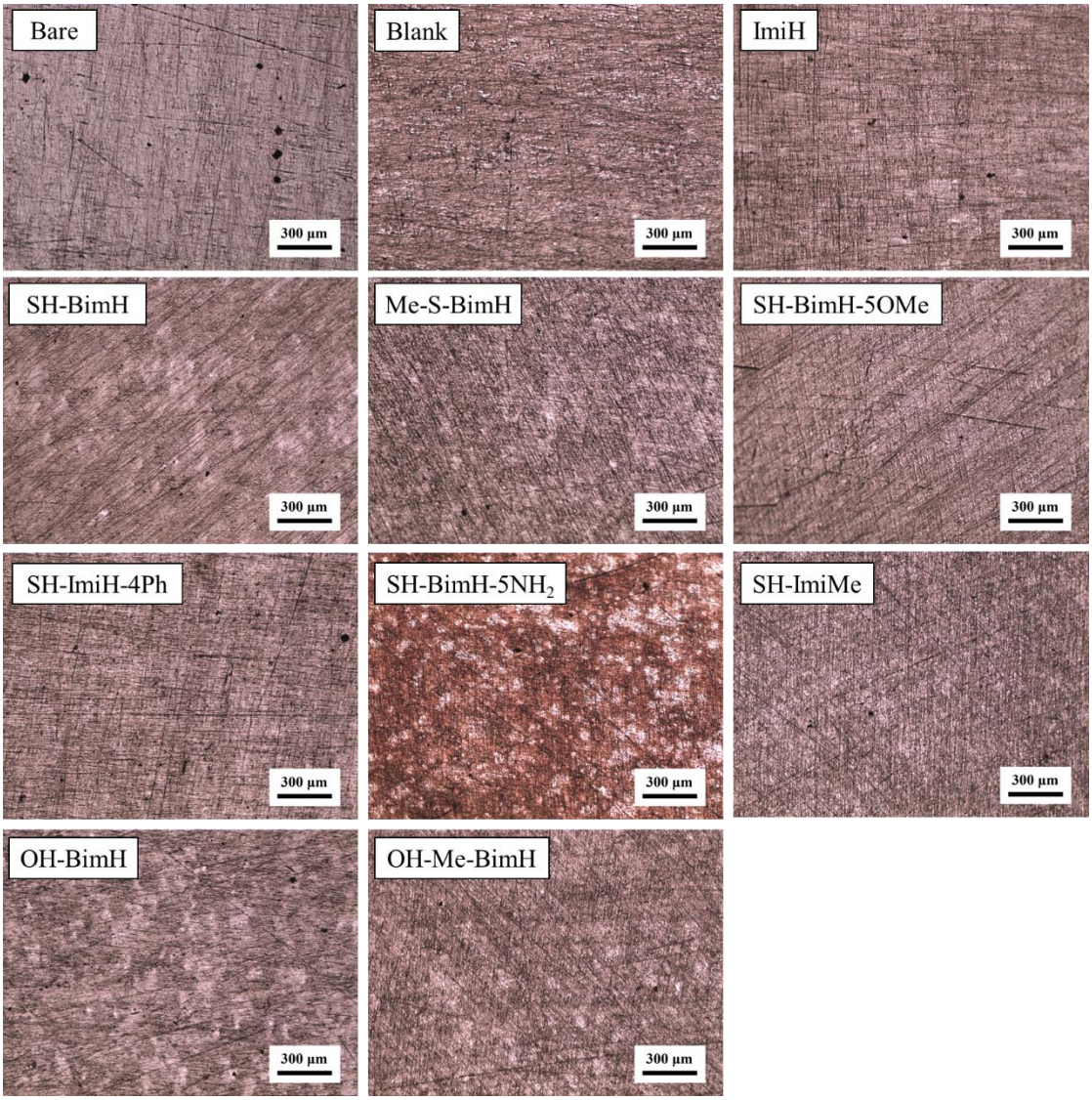

Figure 4.49 Pure Zr immersed in 3 wt. NaCl solution with and without inhibitors for 1 year under optical microscopy at 50x magnification.

As shown in **Figure 4.50**, the sample surface under optical microscopy after immersion in 3 wt.% NaCl for 1 year does not change so much. The bare sample shows some exfoliation due to polishing, and the rest of the samples only follow the surface features as bare surface after immersion. This proved the electrochemical measurements and inhibitors did neither inhibit nor accelerate corrosion on pure Zr.

4.4 Discussion and Conclusion

4.4.1 Discussion

The inhibition of three different derivatives on pure Cu shows the various effect. ImiH and SH-ImiMe from imidazole derivatives could not improve corrosion resistance. However, SH-ImiH-4Ph for the same group shows excellent inhibition; in XPS spectra, only SH-ImiH-4Ph shows a split peak in both 24h immersed and 120h immersed sample. This fact can only be due to the existence of two kinds of chemical bond on the surface, which might be the reason why this compound shows the best inhibition performance. Mercapto-benzimidazole derivatives inhibit pure Cu except for SH-BimH-5NH_2. OH-Me-BimH acts as a suitable inhibitor, but OH-BimH does not work, both from hydroxy-benzimidazole derivatives. Function group is the decisive factor for inhibition; all effective inhibitors contain -SH group except OH-Me-BimH, which is reasonable due to the adsorption between thiol and pure Cu. The accelerated corrosion by SH-BimH-5NH_2 should result from the presence of -NH_2. For the long-term electrochemical measurements, the corrosion resistance of all effective inhibitors increases until 24h, and SH-ImiH-4Ph is the only one that keeps increasing until the end of the test. The immersion tests show that inhibition of OH-BimH can not reach the performance shown in electrochemical measurements, and pits appear in all of the inhibitors. However, the pits' size is different, which indicates the protection of inhibitors is still different when pits appear. Nevertheless, inhibitors perform quite a difference in pure Zn. All inhibitors contain -SH group inhibit pure Zn except Me-S-BimH, and the best inhibitor is SH-BimH-5NH_2, which is the corrosion accelerator for pure Cu. The presence of -NH_2 group should be the contributing group. The long-period tests show the same behavior as pure Cu, the inhibition increasing at first 24h and begin to decrease then. Attribute to the worsen corrosion resistance of Zn, 12 days' immersion measurements, shows that most inhibitor can not keep the surface in good condition except SH-BimH-5NH_2. Besides, SH-ImiH-4Ph also shows a good surface, but with some cracks, this does not follow the results of long-period electrochemical measurements. The interaction between pure Zr and inhibitors conducts the uselessness of inhibitor. Even after immersed for one year, there is no apparent difference between inhibitors. The helpless inhibition of pure Zr should be attributed to the presence of oxide on the surface; ZrO_2 is a stable and inert substance that is always made for ceramics. Compared with Cu_2O, CuO and ZnO, all these three oxides are semiconductors, but ZrO_2 is dielectric; oxide film's conductivity should consider applying a self-assembled monolayer inhibitor.

Moreover, the electrochemical measurements in the short- and long-term show a good correlativity with immersion measurements. However, it should not be the decisive criterion of inhibition, as shown in long-term immersion tests of pure Zn, SH-ImiH-4Ph performs worse than SH-BimH and SH-BimH-5OMe, but the surface tells a different story. The corrosion behavior should be taken care of from immersion tests as well.

Furthermore, the Si element is found in many pits and exfoliation on the bare surface of both Cu and Zn; this embedded SiC from polishing accelerates the corrosion process and create the pits. And the metal-inhibitor complex always appears on these locations. Zn immersion tests result in a floc gathered surface after 12 days' immersion shown in the photo, and a rinse of DI water can easily remove them. However, the flocs on the Cu surface is not distinct; as shown in photos, passivation should happen on the surface. In SEM-EDX tests, the detector can get the characteristic energy of sulfur, which means many organic compounds have adhered to some part of the surface, mostly on pits. The same phenomenon happens on the surface of pure Cu and Zn after long-period immersion, adhesion of metal-inhibitor complex. Moreover, those gathered complexes always locate on the local attacks, which should assist corrosion inhibition. This will be discussed with the result of CuZn alloys afterward.

4.4.2 Conclusion

The effect of the organic compounds on pure metals is diverse. The seven inhibitors affect pure Cu in a complicated way, function groups play a major role on inhibition. -SH group is the basis of all inhibitor for pure Cu, only the -SH group show effective inhibition; -NH_2 group and -CH_3 group apparently reduce inhibition or accelerate corrosion; the main structure of inhibitor also affects the inhibition. SH-BimH-5OMe shows the best performance on pure Cu, this could attribute to two kinds of thiol chemical bond build on the surface. For pure Zn, inhibitors with -SH group also inhibit corrosion for 1 h electrochemical test but decrease fast with time; -CH_3 group highly accelerates corrosion; different from that of pure Cu. -NH_2 shows the best inhibition in Long-term measurements. Imidazole or mercapto-benzimidazole derivatives have almost no inhibition influence on pure Zn. SH-BimH-NH_2 is the best inhibitor for improving the corrosion behavior among all tested inhibitors. No inhibitor works significantly on pure Zr, this may attribute the presence of compact ZrO_2 oxide.

There is no visible film on the surface except local corrosion and part of passivation after 60 days' immersion test for pure Cu. Inhibition comes from the thin monolayer or polymolecular layer adsorbed on the surface. However, local attacks still exists, and passivation happens as well.

Unlike pure Cu, a big number of white flocs appeared on the surface of pure Zn after 12 days' immersion test. This Zn-inhibitor complex shows preference gathering on Zn surface. Inhibition of pure Zn accounts for the formation of the complex, but it is not such strong bonding.

Inhibitors work in different ways on pure Cu and Zn, the influence of these two different kinds of inhibition should be noticed for CuZn alloys. Since no effective inhibition found on Zr, the presence of Cu in CuZr alloy will assist in understanding the influence on inhibition. The relationship between pure metals and alloys is significantly important which could assist the development of new inhibitors for alloys.

Moreover, inhibitors change the corrosion behavior even if no significant Rp and Z different change. Inhibition power shows differences between inhibitors in a much more clear way than inhibition efficiency.

5 Corrosion Inhibition of CuZn alloy

CuZn alloy is one of the most extensively used Cu alloys in the world. Moreover, adequate corrosion resistance made this alloy always applied under corrosive environment. The organic inhibitors maybe one of the best solutions to reduce the corrosion rate since the convenience, applicable and size stability. In chapter 1, a series of inhibitors show different inhibition on pure Cu, and the CuZn alloys contain less than 35% of Zn will present a single α-phase structure. So here, two kinds of alloys will be tested, one is Cu/Zn (70/30) and the other is Cu/Zn (30/70), which is single α-phase and γ- and ε-phase, respectively, phase diagram. This will assist in understanding the inhibition behavior on CuZn alloys, is it only works on single α-phase CuZn alloy, or it is an inhibitor for the materials which contain Cu element.

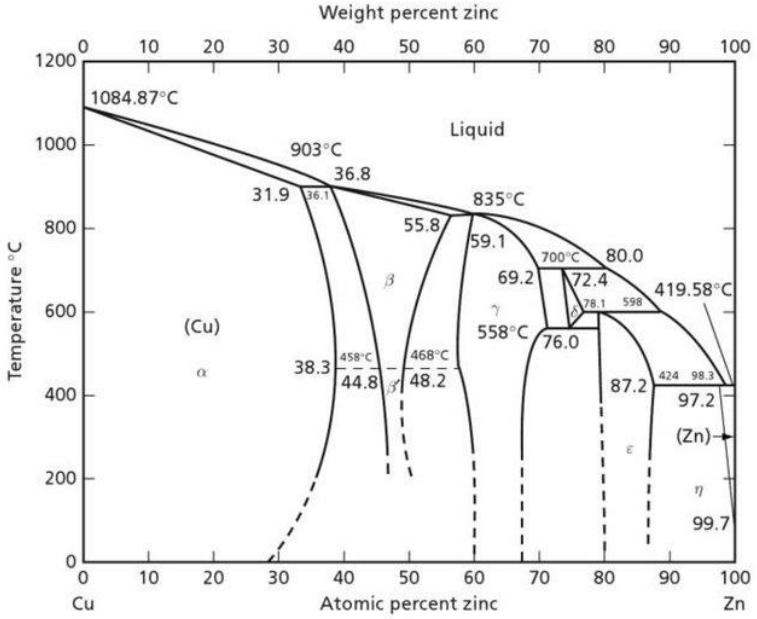

Figure 5.1 CuZn binary phase diagram [115]

5.1 Short-term Electrochemical Measurements

5.1.1 $Cu_{70}Zn_{30}$ alloy

The linear polarization resistance and impedance show in **Figure 5.2**, the effective inhibitor present as the same as pure Cu. The only difference is SH-BimH-5NH_2 improved corrosion resistance of $Cu_{70}Zn_{30}$ alloy slightly but accelerates the process in that of pure Cu. In imidazole derivatives, ImiH act as an accelerator like in pure Cu, SH-ImiMe improves the resistance a little as pure Cu and SH-ImiH-4Ph is one of the best. In mercapto-benzimidazole derivatives, SH-BimH, Me-S-BimH and SH-BimH-5OMe increase the resistance to the level of 10^3. The appearance of LPR and |Z| are almost the

same, these two measurements show a mutual corroboration as in pure metals. Here, the resistance without inhibitors is close to that of pure Cu and the inhibition improved by 2 order of magnitude which means 1 order larger than that of pure Cu. The better performance of inhibitors on $Cu_{70}Zn_{30}$ alloy may indicates addition of Zn improve the interaction between inhibitors and alloy surfaces in some way. The importance of this behavior is how it works and how to select better inhibitors by this effect. However, long-term electrochemical measurements are still needed to prove this effect can last long enough for corrosion protection.

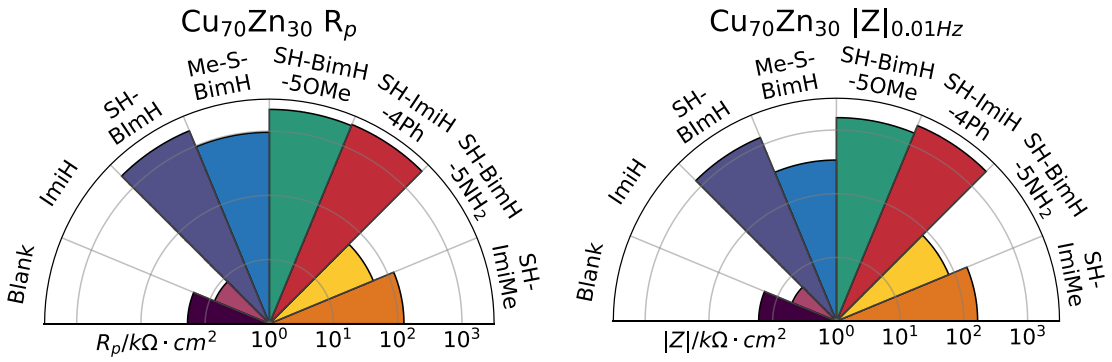

Figure 5.2 Polar graphs of linear polarization resistance (left) and impedance modulus at 0.01 Hz (right) of $Cu_{70}Zn_{30}$ alloy, measured after 1 h immersion in 3 wt.% NaCl aqueous solution (blank) and in the presence of different organic compounds added at 1 mM concentration. Note the logarithmic scale.

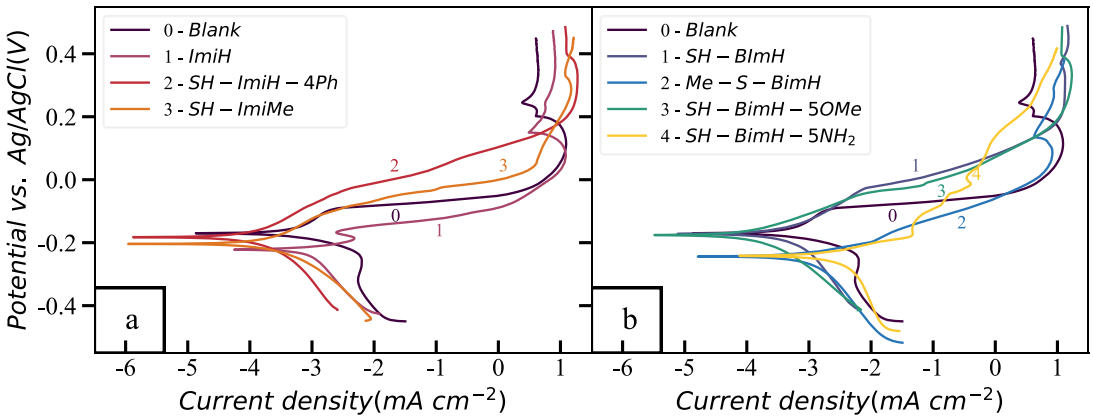

Figure 5.3 Potentiodynamic polarization curves of $Cu_{70}Zn_{30}$ alloy in 3 wt.% NaCl aqueous solution with and without 1 mM of different organic compounds: (top) imidazole derivatives, (middle) mercapto-benzimidazole derivatives, and (bottom) hydroxy-benzimidazole derivatives. Quantitative electrochemical parameters are presented in Table 5.1.

Table 5.1 $Cu_{70}Zn_{30}$ alloy Tafel Parameters (cf. **Figure 5.3**).

Solution	E_{corr} (mV) vs. Ag/AgCl	j_{corr} （μA/cm^2）	$-\beta_c$ (mV/dec)	β_a (mV/dec)
3 wt.% NaCl	-173	0.426	43	117
ImiH	-226	0.836	205	46
SH-ImiMe	-182	0.211	132	87
SH-ImiH-4Ph	-167	0.160	185	115
SH-BimH	-162	0.611	266	122
SH-BimH-5OMe	-163	0.200	165	76
SH-BimH-5NH_2	-221	4.075	441	46
Me-S-BimH	-247	1.391	251	68

Figure 5.3 shows the potentiodynamic polarization curves of $Cu_{70}Zn_{30}$ alloy, the corrosion behavior is different from pure Cu. Small passivation disappears and at around -0.1 V, the corrosion current increasing rapidly, which may be due to the selective dissolution of Zn. As shown in the Pourbaix diagram in **Figure 4.27**, Zn shows a low dissolution potential in Zn- H_2O system. In imidazole derivatives, SH-ImiH-4Ph and SH-ImiMe didn't shift the corrosion potential apparently, ImiH shifts the corrosion potential to more negative. ImiH introduces small passivation at around -0.2 V, it may attribute to oxidation of Cu, and all position of the curve is shifted to more negative position, passivation appears around 0 V as the blank curve. SH-ImiH-4Ph shifts the curve to positive side in anodic polarization part and the initial of passivation is delayed around 0.2 V. This shows there should be a strong bond between SH-ImiH-4Ph and sample surface which can delay the passivation in a large polarization potential. The corrosion current density of SH-ImiMe is half of the blank one and no clear fast increasing of current was found around -0.1 V. In mercapto-benzimidazole derivatives, SH-BimH and SH-BimH-5OMe shift the anodic polarization part to more negative direction and passivation was delayed as well.

Me-S-BimH and SH-BimH-5OMe shift the corrosion potential to more negative value and the current density is also higher than that of blank. However, these two inhibitors both show a higher resistance in LPR and |Z| in **Figure 5.2**. Since linear polarization measurements only scan a narrow range of potential, it reveals the -NH_2 and -Me ground influence the inhibition of mercapto-benzimidazole and the scan from large negative potential may reduce the inhibition effect.

As shown in **Figure 5.4**, imidazole derivatives in left side and mercapto-benzimidazole derivatives in right side. $Cu_{70}Zn_{30}$ alloy without inhibitors shows 1 time constant phase diagram and a semicircle which indicates charge-transfer controlled process and a transfer to diffusion controlled at low frequency. ImiH and SH-ImiH-4Ph improve the maximum phase angle, and all the curves didn't show a new time constant. In **Figure 5.4** c), SH-ImiH-4Ph shows a huge pressed semicircle and no diffusion-controlled part is found. It's clear that SH-ImiH-4Ph inhibits the corrosion process in charge-transfer controlled procedure and it is the resistance for transfer is extremely high.

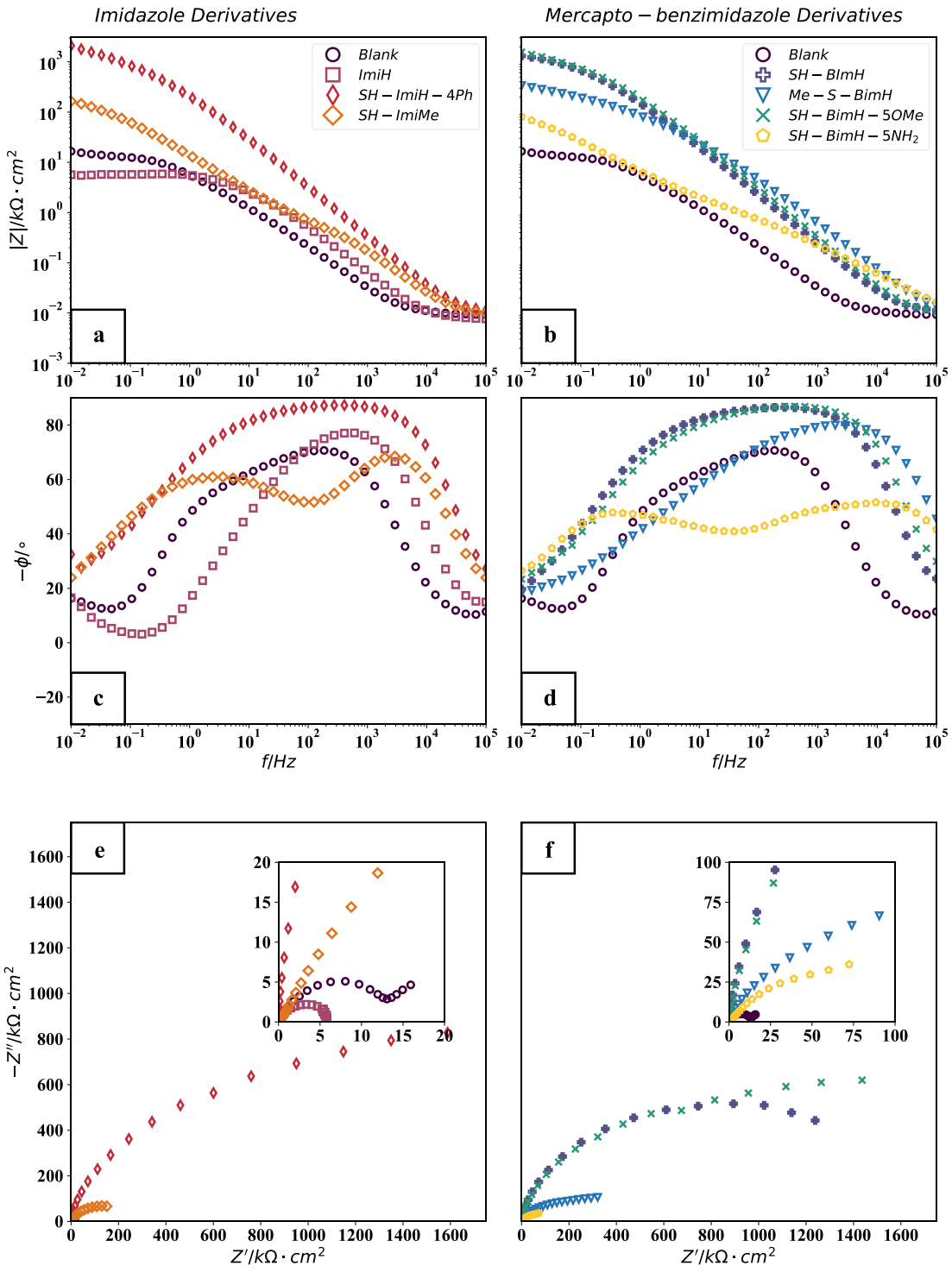

Figure 5.4 Electrochemical impedance spectra of $Cu_{70}Zn_{30}$ alloy in the form of Bode impedance plot, phase angle plot and Nyquist plot with or without addition of 1 mM of different organic compounds in aqueous 3 wt. % NaCl solution: a), c), g) imidazole derivatives and b), d), f) mercapto-benzimidazole derivatives

SH-ImiMe shows the similar behavior as SH-ImiH-4Ph, but with a smaller resistance. However, two clear time constant is found, but all the curves in the figure shows except ImiH show two time constants or a long gentle slope form the maximum phase angle to lower frequency, which may indicate the possibility of merge of two peaks. ImiH improve

the resistance but the stability is low at low frequency. For mercapto-benzimidazole derivatives present the same behavior as SH-ImiH-4Ph, no clear diffusion part and a large pressed semicircle represent high charge transfer resistance. SH-BimH-5NH_2 improved the resistance but maximum phase angle is lower than blank curve and two clear time constants appear.

Short-term electrochemical measurements show that inhibition on single α-phase $Cu_{70}Zn_{30}$ alloy is better than pure Cu, this may indicate the presence of Zn improve the performance of inhibitors. As the huge improvement by SH-ImiH-4Ph, SH-BimH and SH-BimH-5OMe, it is potentially large-scale applications. But the long-term measurements are needed to check the stability of inhibition of this alloy.

5.1.2 $Cu_{30}Zn_{70}$ alloy

The XRD spectra in **Figure 5.5** shows the phase of $Cu_{30}Zn_{70}$ alloy contains γ-brass (Cu5Zn8) and ε-brass (CuZn5). $Cu_{70}Zn_{30}$ alloy shows only one α-phase present. Then the inhibition of $Cu_{30}Zn_{70}$ alloy should depend on the inhibition of these two phases. Moreover, the inhibition of Zn may show a better correlation since the ZnO-rich surface will exist [27,45].

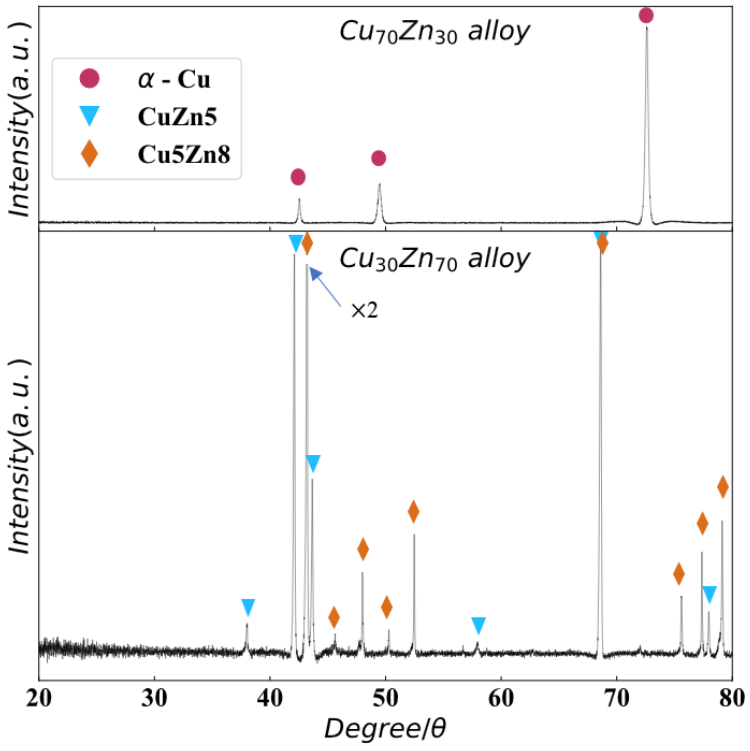

Figure 5.5 X-ray diffraction spectra of $Cu_{70}Zn_{30}$ alloy (up) and $Cu_{30}Zn_{70}$ alloy (down)

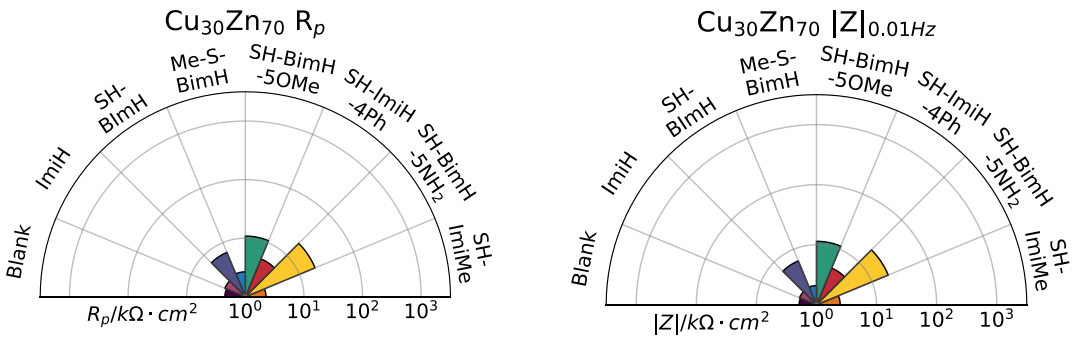

Figure 5.6 Polar graphs of linear polarization resistance (left) and impedance modulus at 0.01 Hz (right) of $Cu_{30}Zn_{70}$ alloy, measured after 1 h immersion in 3 wt.% NaCl aqueous solution (blank) and in the presence of different organic compounds added at 1 mM concentration. Note the logarithmic scale.

The linear polarization resistance and impedance display in **Figure 5.6**. The γ- and ε-phase show an apparent decrease of corrosion resistance, and the LPR and |Z| still show semblable results. In imidazole derivatives, only SH-ImiH-4Ph shows a clear inhibition, ImiH shows a similar value as blank and SH-ImiMe accelerate corrosion process. In mercapto-benzimidazole derivatives, SH-BimH, SH-BimH-5OMe and SH-BimH-5NH_2 present good inhibition and SH-BimH-5NH_2 is the best one. Me-S-BimH shows a similar value as blank sample. Consider the same plot in pure Cu and Zn in **Figure 4.2** and **Figure 4.28**, respectively. The evaluation of inhibition with 1 h immersion tests shows almost the same trend in pure Zn and $Cu_{30}Zn_{70}$ alloy. Which means the appearance of oxide on the surface may determine the inhibition effects.

Figure 5.7 shows the potentiodynamic polarization of $Cu_{30}Zn_{70}$ alloy with and without inhibitors, all of the appearance of curve shapes are similar, and **Table 5.2** shows Tafel parameters. $Cu_{30}Zn_{70}$ alloy without inhibitor shows fast passivation after a small addition of positive potential, and a fast increasing of current density which may indicate dissolution or pitting happens at around -0.4 V. On left side of the figure which is imidazole derivatives, ImiH shows the same curve like the one without inhibitors, neither inhibition nor acceleration should be there. SH-ImiH-4Ph shift the corrosion potential to a more positive value as well as the anodic polarization curve. The fast increase of current density was inhibited to around -0.3 V. SH-ImiMe shows an acceleration when increasing the potential in anodic side. The right side of the figure shows mercapto-benzimidazole derivatives, Me-S-BimH shows a similar behavior like ImiH, the parallel of curves of the blank one. SH-BimH, SH-BimH-5OMe and SH-BimH-5NH_2 all shift the anodic polarization curve to a more positive side. And **Table 5.2** also shows that SH-BimH-5NH_2 presents the lowest corrosion current density among all inhibitors.

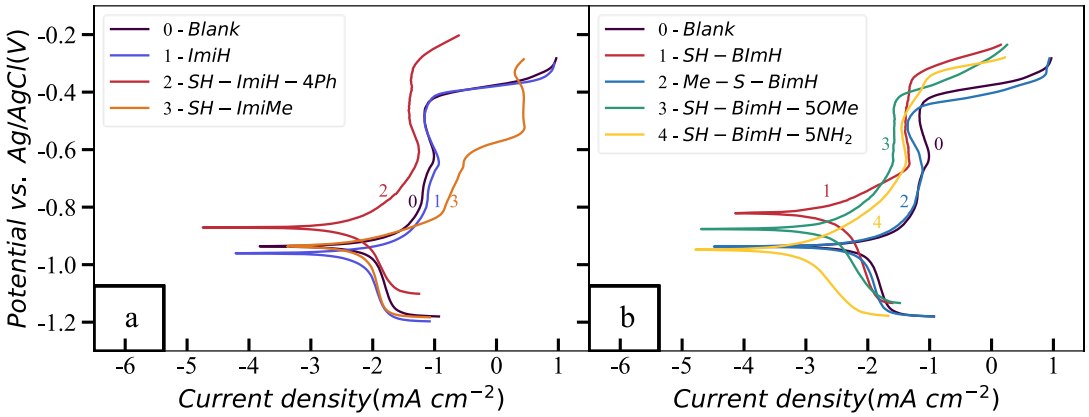

Figure 5.7 Potentiodynamic polarization curves of pure Cu in 3 wt.% NaCl aqueous solution with and without 1 mM of different organic compounds: (top) imidazole derivatives, (middle) mercapto-benzimidazole derivatives, and (bottom) hydroxy-benzimidazole derivatives. Quantitative electrochemical parameters are presented in **Table 5.2**.

Table 5.2 $Cu_{30}Zn_{70}$ alloy Tafel Parameters (cf. **Figure 5.7**).

Solution	E_{corr} (mV) vs. Ag/AgCl	j_{corr} （μA/cm^2）	$-\beta_c$ (mV/dec)	β_a (mV/dec)
3wt%NaCl	-937	9.853	662	125
ImiH	-980	7.493	569	130
SH-ImiMe	-944	8.161	798	97
SH-ImiH-4Ph	-881	6.657	406	243
SH-BimH	-799	3.499	526	120
SH-BimH-5OMe	-892	2.862	342	223
SH-BimH-5NH2	-970	1.044	249	163
Me-S-BimH	-931	7.661	642	106

Figure 5.8 shows EIS spectra of $Cu_{30}Zn_{70}$ alloy in the form of Bode impedance plot, phase angle plot and Nyquist plot with or without inhibitors. The blank curve for phase plot only shows one clear time constant and the maximum phase angle is ~60°, Nyquist plot show a small semicircle followed by a horizontal line. In imidazole derivatives, ImiH follow the same Nyquist plot, phase plot and Bode impedance plot. SH-ImiMe improved the impedance at middle frequency but the impedance is almost same at low frequency. And lower maximum phase angle is presented, only one semicircle appears in Nyquist plot. SH-ImiH-4Ph presents one semicircle and larger radius in Nyquist plot, phase plot isn't change so much. For mercapto-benzimidazole derivatives, Me-S-BimH act as the same as blank curves. SH-BimH shows a larger semicircle in Nyquist plot and two time constant appears in phase plot. SH-BimH-5OMe shows a similar behavior as Me-S-BimH,

but with a larger radius in Nyquist plot and higher maximum phase angle. SH-BimH-5NH_2 shows the largest semicircle in Nyquist plot and maximum phase angle. Even though there is only one peak appears, it may attribute merge of two peaks like SH-BimH and SH-BimH-5OMe. In Figure 4.28, the phase plot of pure Zn of mercapto-benzimidazole derivatives are quite similar as $Cu_{30}Zn_{70}$ alloy.

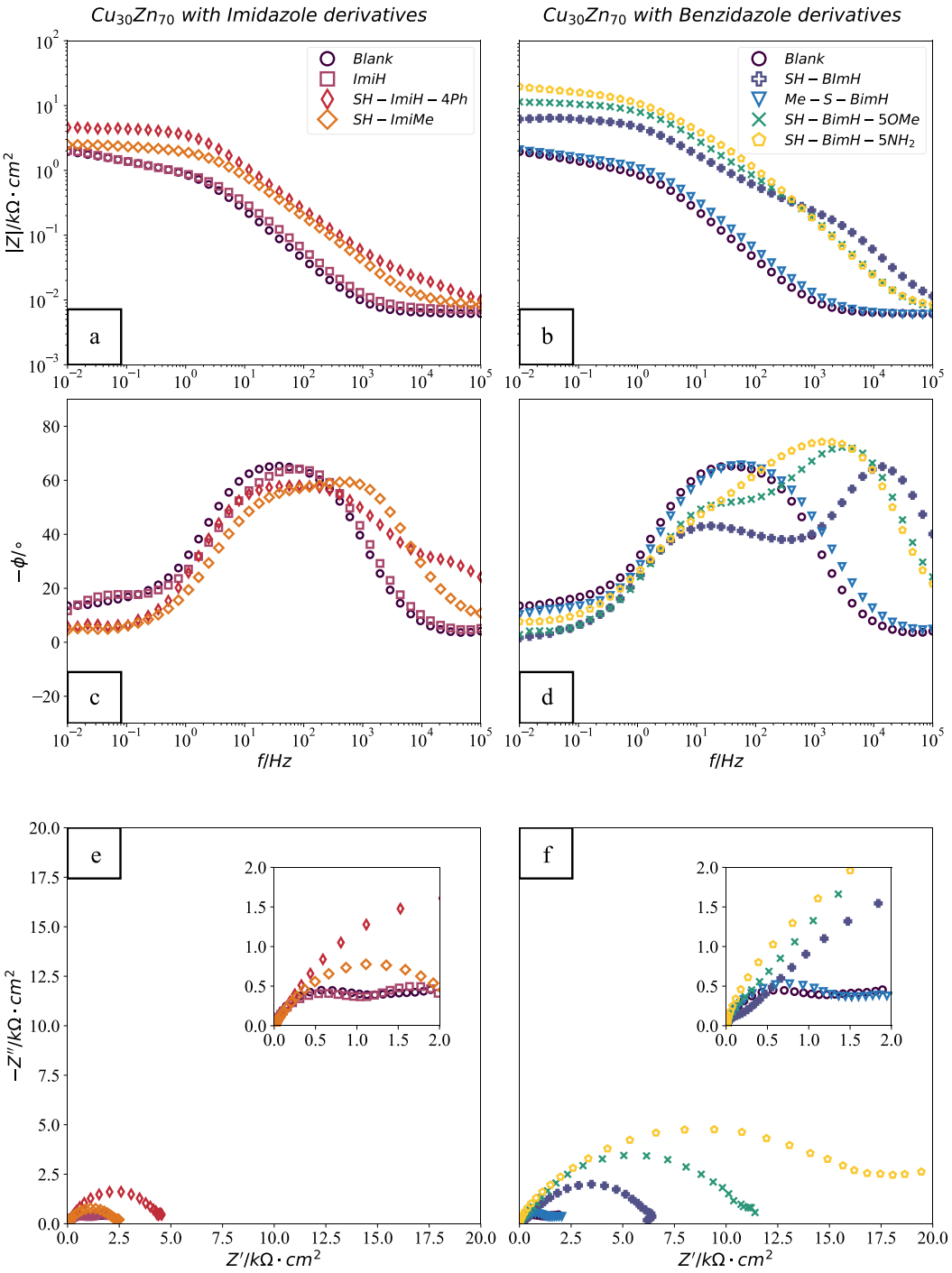

Figure 5.8 Electrochemical impedance spectra of $Cu_{30}Zn_{70}$ alloy in the form of Bode impedance plot, phase angle plot and Nyquist plot with or without addition of 1 mM of different organic compounds in aqueous 3 wt. % NaCl solution: a), c), e) imidazole derivatives and b), d), f) mercapto-benzimidazole derivatives.

Short-term electrochemical measurements show the highly dependency of inhibition behavior and results between pure Zn and $Cu_{30}Zn_{70}$ alloy. The presence of γ- and ε-phase contain high percentage Zn will introduce more Zn oxide and this layer may domain the inhibition behavior for $Cu_{30}Zn_{70}$ alloy.

5.2 Long-term Electrochemical Measurements

Long-term electrochemical measurements are carried out on all inhibitors of $Cu_{70}Zn_{30}$ alloy and selective inhibitors of $Cu_{30}Zn_{70}$ alloy.

5.2.1 $Cu_{70}Zn_{30}$ alloy

In **Figure 5.9**, the curves of LPR (top) and |Z| at 0.01 Hz (middle) in a period of 120h are presented. And a repeat of measurements with SH-BimH-5OMe and SH-ImiH-4Ph in period of ~400 h is presented (bottom), this will show the performance of inhibitors in longer period. The measurements of resistance show the same trend and sample without inhibitor shows an increasing of resistance and impedance at the first a 72 h. Then they begin to decrease. In imidazole derivatives, SH-ImiH-4Ph shows incredible inhibition effects and resistance and impedance keep increasing until the end of measurement. ImiH presents a similar value as blank sample. A drop of resistance and impedance happened after 24 h and then go back to higher value than that of blank for SH-ImiMe. Right side shows the mercapto-benzimidazole derivatives, SH-BimH, Me-S-BimH and SH-BimH-5OMe present good inhibition, but SH-BimH-5OMe meet a large drop of both resistance and impedance after 100 h. All these three inhibitors meet a decreasing after 24h, but then, SH-BimH and Me-S-BimH keep increasing until the end. SH-BimH-5NH_2 shows a slightly improvement but not such effective. Please note that the decreasing of SH-BimH, Me-S-BimH, SH-BimH-5OMe and SH-ImiMe happens at the immersion duration after 24h, the impedance and resistance increased at that moment which may indicate the production of passivation layer. This decrease may be attributed to the formation of this layer. The longer repeat measurements of SH-BimH-5OMe and SH-ImiH-4Ph shows a repeatable trend of change of impedance and resistance. Although the value is not such repeatable, can be different in 1 order of magnitude level, the trend is clear. The impedance and resistance keep a huge value for ~400 h for SH-ImiH-4Ph and SH-BimH-5OMe, decreasing slightly after ~150 h.

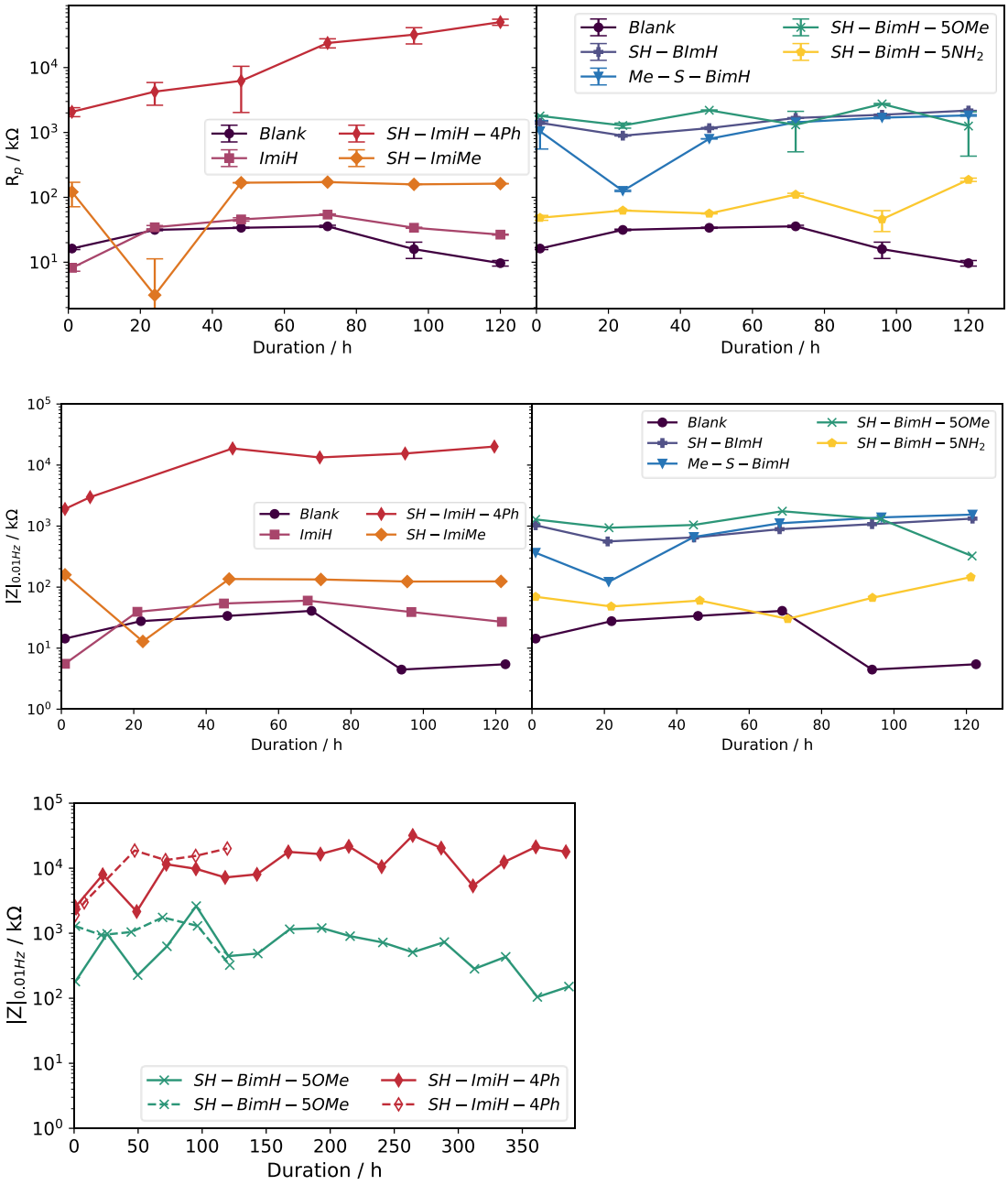

Figure 5.9 Long-term graph of linear polarization resistance (up) and impedance modulus at 0.01 Hz (middle) of $Cu_{70}Zn_{30}$ alloy, measured in period of 120 h immersion in 3 wt.% NaCl aqueous solution (blank) and in the presence of different organic compounds added at 1 mM concentration, measured in period of ~400 h immersion only with presence of SH-BimH-5OMe and SH-ImiH-4Ph (bottom). Note the logarithmic scale.

Figure 5.10 shows the Long-term Nyquist plot of $Cu_{70}Zn_{30}$ alloy in NaCl solution without and with 1 mM inhibitor, in period of 120 h. The Nyquist plot shows a typical charge-transfer controlled and diffusion controlled structure, but the diffusion controlled region disappeared after 1 h immersion and this may attribute to the formation a passivation film mentioned in ref. [27,116], since the ZnO and Cu_2O present a bigger resistance and

semiconductor feature [46], the corrosion process will be controlled in charge-transfer process. However, the curve go back to the charge-transfer controlled and diffusion controlled process with a smaller semicircle after ~72h, this can be attributed to the reaction of the oxide layer to CuCl[47] and $CuCl_2$ [48]. Then the initial dezincification reaction happens as the following process [49][50]:

$$ZnO + OH^- = HZnO_2^-$$
$$CuCl_2 + Zn = ZnCl_2 + Cu$$

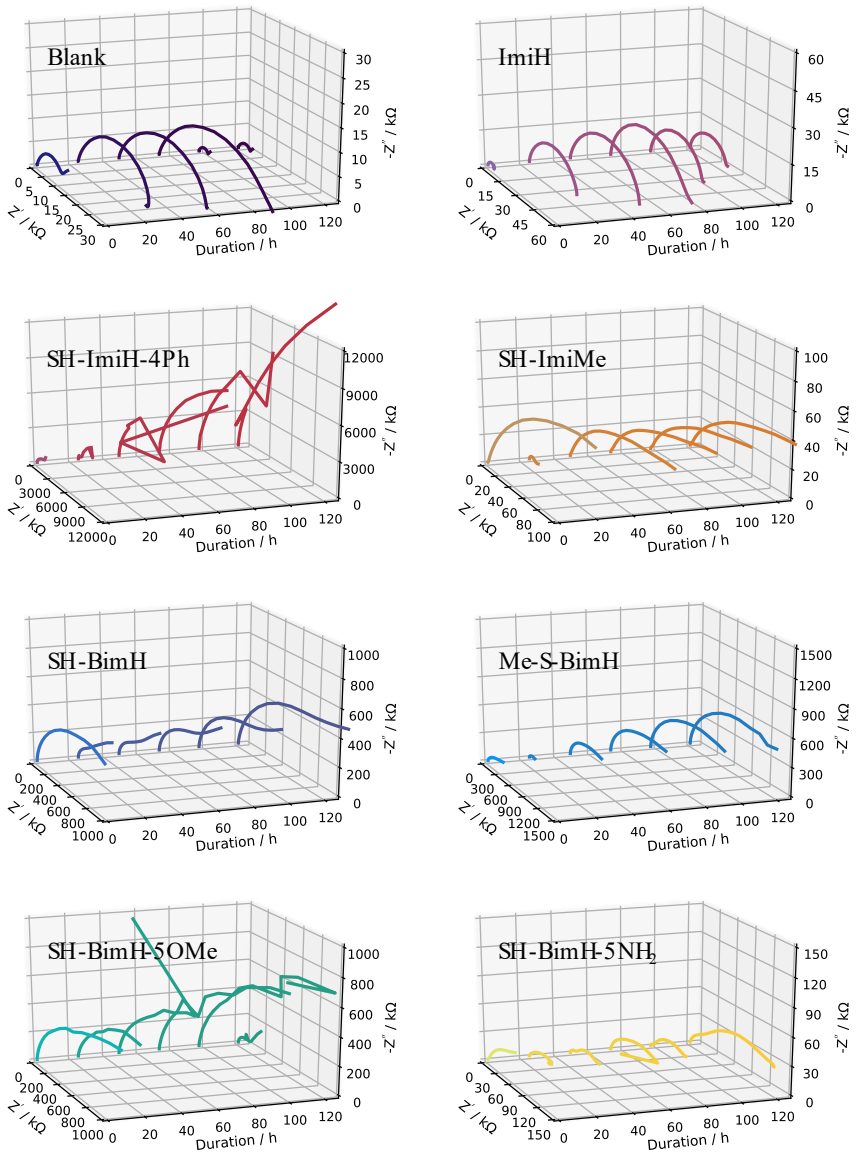

Figure 5.10 Long-term Nyquist plot of $Cu_{70}Zn_{30}$ alloy in NaCl solution without and with 1 mM inhibitor, in period of 120 h.

ImiH shows similar behavior at the first 72 h and then the radius of the semicircle begins to decrease, but diffusion controlled region doesn't appear. It may reveal that ImiH can slightly inhibit the process of dissolution of oxide film. SH-ImiH-4Ph shows the same

shape of Nyquist plot and the radius of semicircle keeps increasing along with the measurements. However, the curve at low frequency show some mess, it may attribute to the stability of inhibitor. When the frequency goes smaller, the inhibitor on the surface may adsorb and desorb on the surface, not in a stable condition. SH-ImiMe shows the same Nyquist plot shape, except the significant decrease at 24 h. However, inhibitor should always on the surface and smaller value of impedance than blank one will not appear, a new kind of film may appear and forms on the surface uniformly. SH-BimH shows a semicircle without a clear diffusion part, but after24 h, a straight line accompanies by a smaller semicircle, which shows a diffusion controlled process appears. However, the semicircle grows up with time and the slope of line decreases. Thus, inhibitor may still work after formation of Cu_2O and ZnO after 24h. Me-S-BimH shows a similar behavior as SH-BimH, but without apparent diffusion controlled region. SH-BimH-5OMe shows great inhibition which is only charge-transfer controlled region with large radius at first 100 h. Nevertheless, the Nyquist plot transferred to a small semicircle with 45° and the impedance decreased sharply. This may indicate the inhibitor is not working at this moment and refer to the longer experiments shown in **Figure 5.9**, the impedance didn't go back to a considerable value again. Nyquist plot of SH-BimH-5NH_2 maintain almost the same shape but the impedance didn't show so much change with time. The inhibition efficiency and inhibition power are presented in **Figure 5.11** and **Figure 5.12**, respectively. For SH-BimH, Me-S-BimH, SH-BimH-5OMe and SH-ImiH-4Ph, they show a great IE from both LPR and impedance view. However, as the previous discussion, IP shows a better hierarchy. The best inhibitor for $Cu_{70}Zn_{30}$ alloy is SH-ImiH-4Ph, and Me-S-BimH, SH-BimH is good inhibitor, SH-BimH-5OMe is good inhibitor for the first 100h but inhibition may keep decreasing.

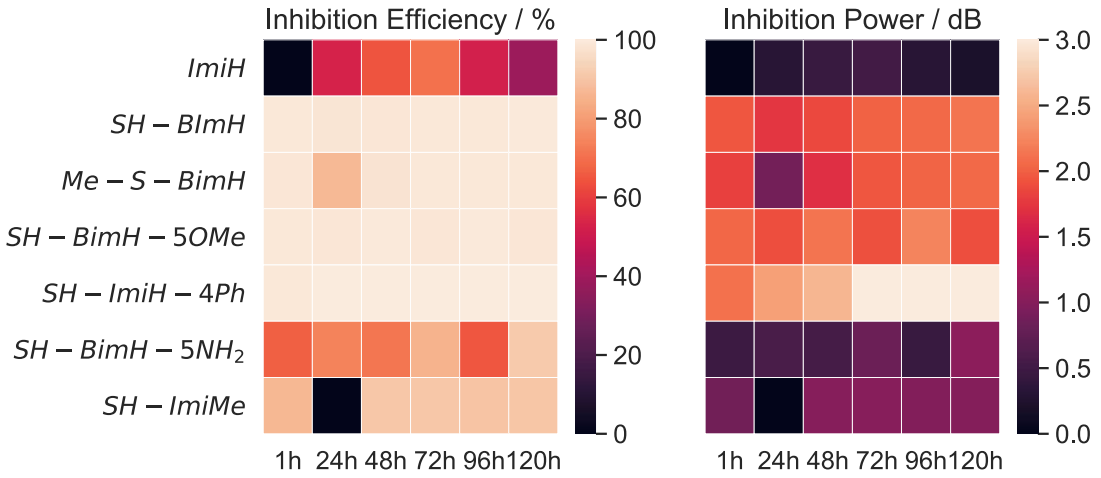

Figure 5.11 Long-term LPR R_p inhibitor efficiency and inhibitor power with different inhibitors in period of 120h

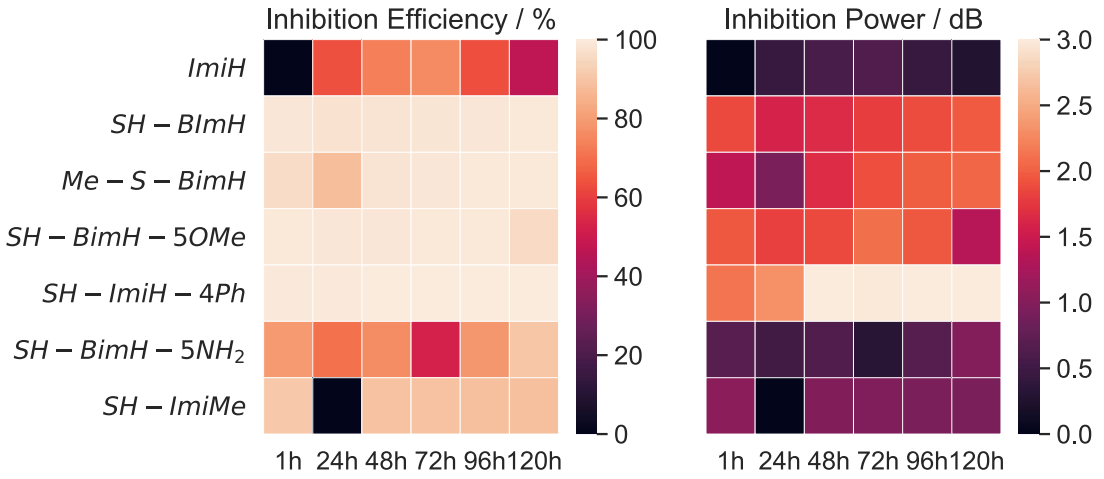

Figure 5.12 Long-term EIS |Z| at 0.01 Hz inhibitor efficiency and inhibitor power with different inhibitors in period of 120h

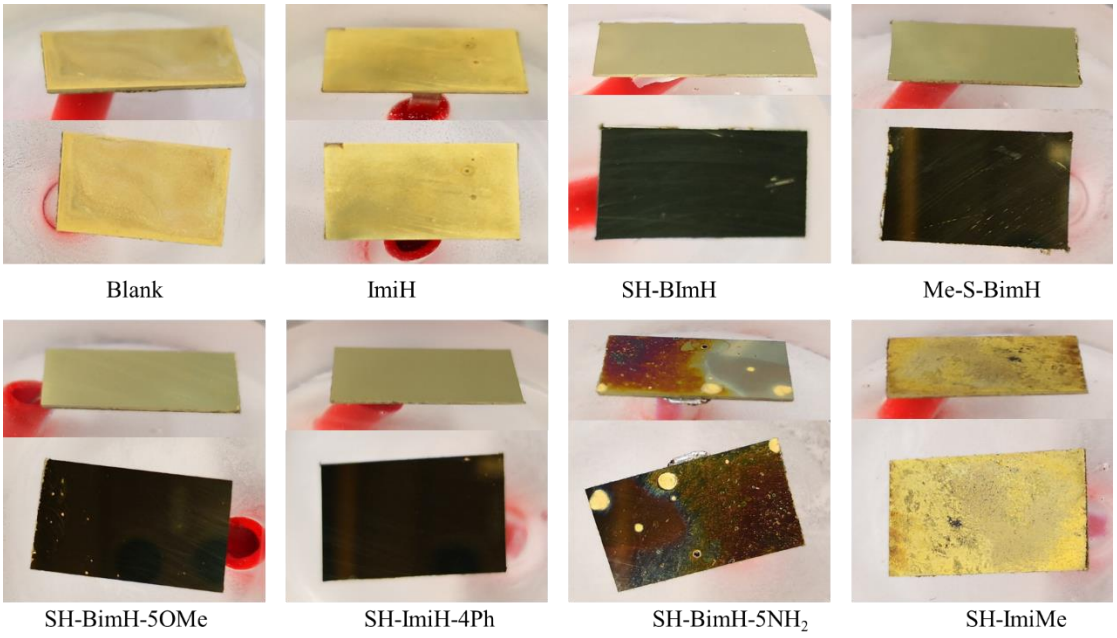

Figure 5.13 Appearance of $Cu_{70}Zn_{30}$ alloy after long-term electrochemical measurements

Figure 5.13 shows the appearance of the sample after long-term LPR and EIS tests. The sample without inhibitor shows a passivated surface without shinning. ImiH shows a similar surface appearance as blank one. SH-BimH, Me-S-BimH, SH-BimH-5OMe and SH-ImiH-4Ph present no-passivated and shinning surface. For SH-BimH-5NH_2, the appearance of surface is not uniform, different appearances present and it may indicate formation of different film on the surface. Passivation happened on sample with SH-ImiMe as well, but the sample is much darker than that of blank sample, the passivation

may be different from blank sample. **Figure 5.14** shows the statistical analysis of LPR tests, the correlation coefficient increasing with time, it can be attribute to the interaction between inhibitor and $Cu_{70}Zn_{30}$ alloy surface was stabilized with time. Besides, the best inhibitor SH-ImiH-4Ph shows a more instability than other inhibitors, this may put down to the great formation of the inhibitor film on the surface. Which is, the high coverage of inhibitor film with a dielectric property will make the surface present more capacitive react with linear polarization, then the measurements will be not such stable. And for the instability of SH-BimH-5NH_2 and SH-ImiMe, it may indicate the formation of the film by inhibitors may affect the measurements of LPR in short-term, stable results will appear after longer duration. Thus, LPR may be not a perfect method for measurement of inhibition, but it is applicable and stable if long-term measurements are applied.

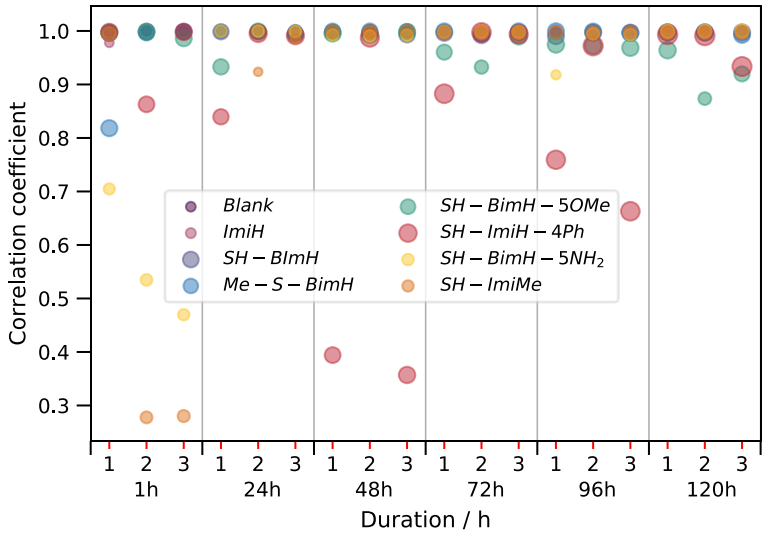

Figure 5.14 Statistical analysis of LPR data based on correlation coefficient in Long-term measurements of pure Cu

The results shown from long-term electrochemical measurements show a great inhibition of SH-ImiH-4Ph and three good inhibitors from mercapto-benzimidazole derivatives, the appearance of samples in **Figure 5.13** shows no clear difference. Immersion tests will be carried afterwards for a better understanding of the experiments.

5.2.2 $Cu_{30}Zn_{70}$ alloy

Selective inhibitors of SH-BimH, SH-BimH-5OMe, SH-ImiH-4Ph and SH-BimH-5NH_2 are tested based on the short-term electrochemical measurements. **Figure 5.15** shows the long-term LPR (left) and impedance modulus (right) plots of $Cu_{30}Zn_{70}$ alloy in period of 120 h. The performance of inhibitors is less effective than that of $Cu_{70}Zn_{30}$ alloy. The powerful SH-ImiH-4Ph is not working on this γ- and ϵ-phase brass, so as other inhibitors. SH-BimH, Me-S-BimH and SH-BimH-5OMe which are good inhibitors for $Cu_{70}Zn_{30}$ alloy present better inhibition after 1 h but keep decreasing then. The only inhibitor without reduction of LPR and impedance with time is SH-BimH-5NH_2, which is also

perform the same for pure Zn (see **Figure 4.31**). This may prove the suggestion that the oxidation film will be the key factor which influence inhibition. Since the high percentage of Zn, the oxide film is ZnO rich, and the interaction between ZnO and inhibitors may domain the process.

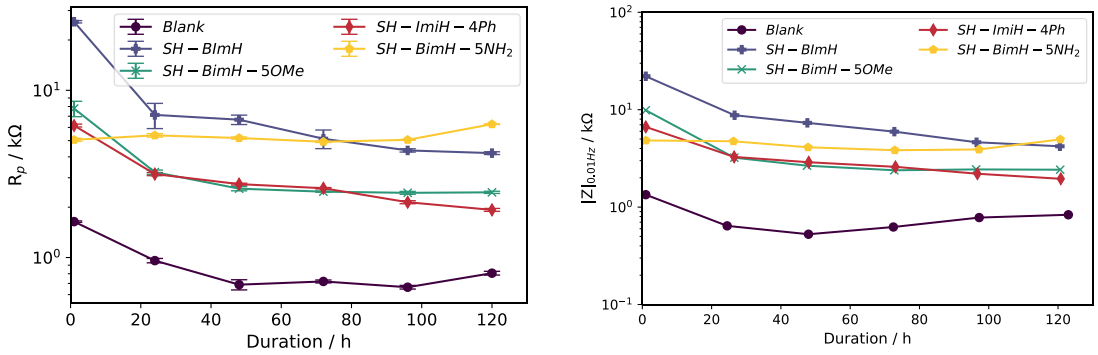

Figure 5.15 Long-term graph of linear polarization resistance (left) and impedance modulus at 0.01 Hz (right) of $Cu_{30}Zn_{70}$ alloy, measured in period of 120 h immersion in 3 wt.% NaCl aqueous solution (blank) and in the presence of different organic compounds added at 1 mM concentration. Note the logarithmic scale.

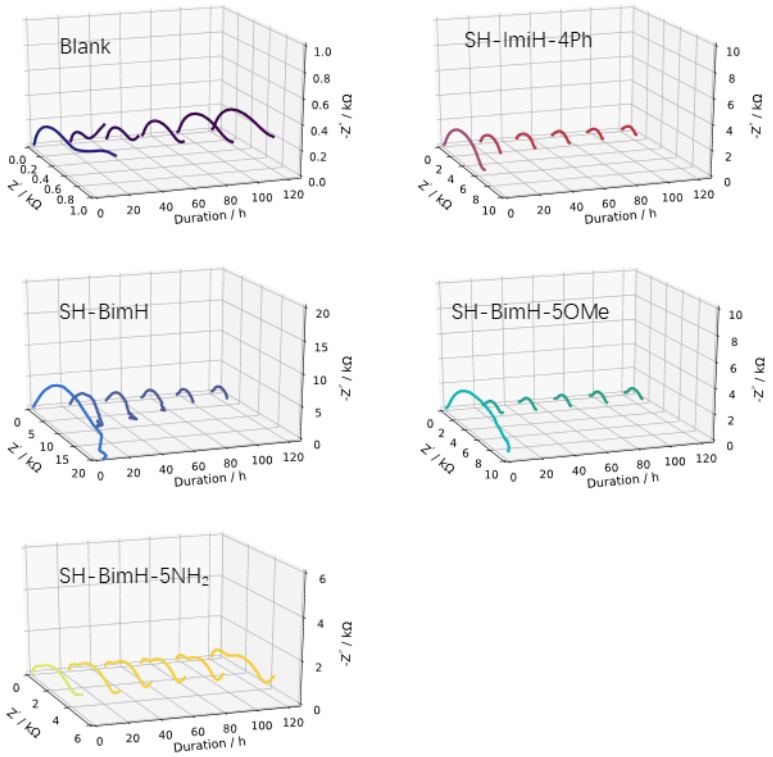

Figure 5.16 Long-term Nyquist plot of $Cu_{30}Zn_{70}$ alloy in NaCl solution without and with 1 mM selective inhibitor, in period of 120 h.

Figure 5.16 shows the dynamic Nyquist plot of $Cu_{30}Zn_{70}$ alloy in period of 120h with selective inhibitors. The curve without inhibitor shows the impedance and shape of the curve is close to that of pure Zn, it may indicate the corrosion process of Zn-rich γ- and ε-brass have is close to pure Zn. As discussed in Chapter 4, the ZnO improves the corrosion resistance but existence of NaCl will break down this film by produce a soluble Zn^{2+}−Cl−OH^- complex [94]. Thus, local attacks may cause break the passive film and dissolution of Zn afterwards [95]. Besides, during the experiments, a lot of white floc appear on the surface for all samples. There are much more flocs on the ones with inhibitors than that of the blank one. As the same as what appears on the pure Zn. The floc on blank sample should be the Zn^{2+}−Cl−OH^- complex, for the rest, it should be the Zn^{2+}-inhibitor complex. As shown in SH-BimH, SH-ImiH-4Ph, SH-BimH-5OMe, Nyquist plot show no clear new type of corrosion process happens on the sample, the only change is the reducing radius of semicircle. This can prove these three inhibitors cannot form a compact layer on the surface for protection and Zn^{2+}-inhibitor complex can not stay on the surface of $Cu_{30}Zn_{70}$ alloy to offer sufficient protection. SH-BimH-5NH_2 shows a similar performance as for pure Zn. However, the improvement is worse than that of pure Zn, this may attribute to the existence of Cu element, which is an accelerator for pure Cu.

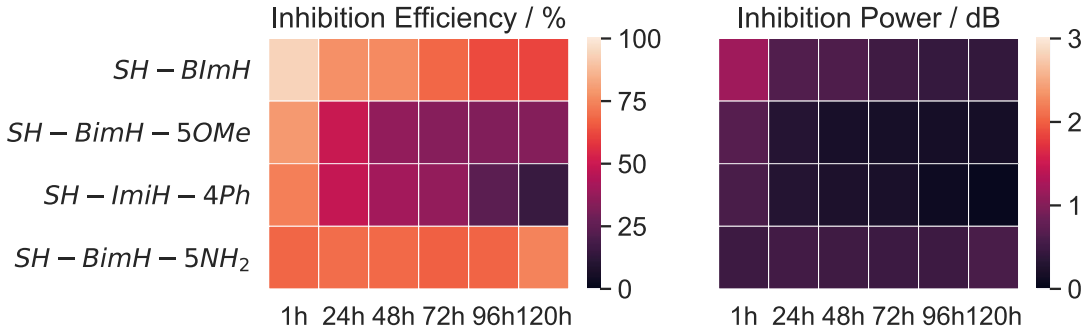

Figure 5.17 Long-term LPR R_p inhibitor efficiency and inhibitor power with different inhibitors in period of 120h

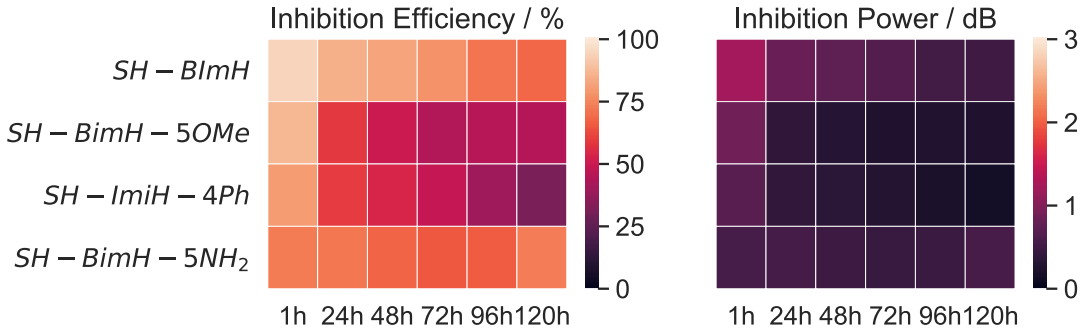

Figure 5.18 Long-term EIS |Z| at 0.01 Hz inhibitor efficiency and inhibitor power with different inhibitors in period of 120h

The inhibitor efficiency and inhibitor power show clear the performance with time for $Cu_{30}Zn_{70}$ alloy, see **Figure 5.17** and **Figure 5.18**. The improvement is extremely low for $Cu_{30}Zn_{70}$ alloy, compare with pure Zn, it is even worse. The presence of Cu seems to reduce the inhibition of SH-BimH, SH-BimH-5OMe, SH-ImiH-4Ph and SH-BimH-5NH_2 (see **Figure 4.33** and **Figure 4.34**). However, SH-BimH, SH-BimH-5OMe and SH-ImiH-4Ph are effective inhibitors for pure Cu, it may attribute the different effect of inhibitors on Zn and Cu. Besides, compare the result of $Cu_{70}Zn_{30}$ alloy which the inhibition improved by adding Zn element, this is quite interesting topic to analyze what kind of interaction happens on the surface and how it works. The statistical analysis of linear polarization of $Cu_{30}Zn_{70}$ alloy in **Figure 5.19** shows the measurements is massive stable than the previous results, the less effective inhibition may has less interrupt at the interface. Thus, a stable result will be presented.

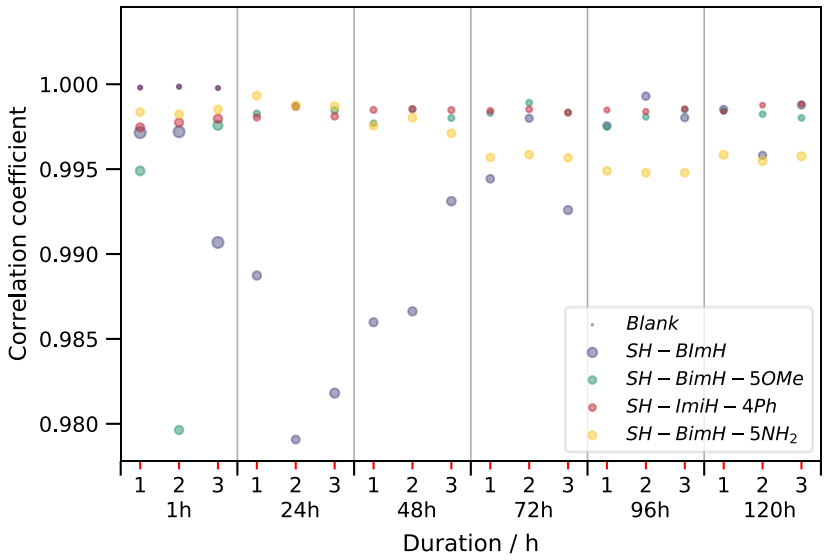

Figure 5.19 Statistical analysis of LPR data based on correlation coefficient in Long-term measurements of pure Cu

5.3 Immersion Test

The interaction between inhibitors and surface is particularly important, XPS will assist in understanding this effect. However, the analysis area of XPS is in several micrometer diameters, which can't be a global view of all samples. Furthermore, long-term electrochemical measurements show fruitful results, but the interference is still existing, and 5 days' test is not enough to evaluate the corrosion resistance for application in years. Thus, 60 days' immersion test was applied on $Cu_{70}Zn_{30}$ alloy and 12 days' immersion for $Cu_{30}Zn_{70}$ alloy due to the worse corrosion resistance. All the samples were immersed in the sealed bottles as described in Chapter 3.

5.3.1 Short-term immersion test characterized by XPS

As for pure Cu, four effective inhibitors were selected for 24 h and 120 h immersion tests of $Cu_{70}Zn_{30}$, and further analyzed by XPS. The selected inhibitors are SH-BimH, Me-S-BimH, SH-BimH-5OMe and SH-ImiH-4Ph. The survey XPS spectra of $Cu_{70}Zn_{30}$ alloy bare surface and surface immersion after 24h and 120h are shown in **Figure A2.17**; the different dash lines are guides to the eye to show the presence of different chemical compounds. The spectra of bare surface shows presence of Cu, Zn, C, O and Si. As in pure Cu, Si appears in all spectra as a consequence of SiC particles embedded on the surface during polishing, as well as some C of undetermined origin. Polishing also induces slight oxidation and corrosion, proved by the presence of O. S and N signal the presence of inhibitors on the surface. The intensity of both Cu and Zn peaks decreases apparently in samples immersed with inhibitors. The Zn peaks almost disappeared after 24h immersion, but is reappear in 120h immersion tests. On the contrary, Cu peaks almost disappear in presence of inhibitors after 120h immersion. Considering the white film that appears on the surface of some samples after 120h electrochemical measurements, this may indicate that the inhibitor reacts with Zn and forms a layer on the surface.

Figure 5.20 shows the normalized high-resolution XPS spectrums of Cu 2p, Cu LMM, O 1s and Cl 2p from the surface of $Cu_{70}Zn_{30}$ alloy after polishing, pickling and subsequent 24h (up) and 120h (down) immersion in 3wt.% NaCl with and without added inhibitors. In **Figure 5.20** (a), weak satellite features appear in bare sample, which indicates the presence of Cu_2O. The blank sample presents a big CuO satellite peak in both 24h and 120h immersed samples, and Cu 2p main peaks are matched as well. Samples with inhibitors show no clear features at these energies; the interaction between inhibitor and Cu_2O is attributed to this observation. However, the intensity after 120h immersion decreases significantly; in SH-ImiH-4Ph, there is almost no signal, indicating the presence of a thick film with little Cu on the surface of samples immersed in presence of all tested inhibitors. Since no CuO features appear, there should not be a large peak of CuO in Cu LMM spectra. As shown in **Figure 5.20** (b), Cu LMM peaks show presence of Cu_2O and CuO in bare sample. However, in samples immersed with inhibitors Cu LMM peaks show a shift to higher binding energy, which should account for the combination between inhibitor and Cu/ Cu_2O; this shift was also observed in the literature [102]. And a puzzling shift of Cu LMM peak of blank sample appears, which is difficult to explain. The O 1s peaks are shown in **Figure 5.20** (c). The bare surface shows a wide peak around the three binding energies of O^{2-}, OH^-, H_2O. After 24h and 120h immersion the peaks of blank sample shift to an energy larger than that of reference H_2O. This can be attributed to further corrosion. All inhibitor treated samples' O 1s peaks shift to the peak around H_2O after 24h immersion, same as in pure Cu. This is difficult to explain since the organic compounds may interact with O. However, in SH-BimH-5OMe and SH-BimH, a shoulder appears at binding energy around O^{2-}, which indicates that oxide should present on the surface. This appears on Me-S-BimH and SH-ImiH-4Ph after 120h immersion as well. In **Figure 5.20** (d), Cl 2p appears only in blank sample after 24h

immersion, and in SH-BimH-5OMe and blank sample after 120h immersion; this result agrees with the result of long-term electrochemical measurements, which shows a big decrease at 120h. Compared to the peak of blank sample, all the rest peaks are smaller.

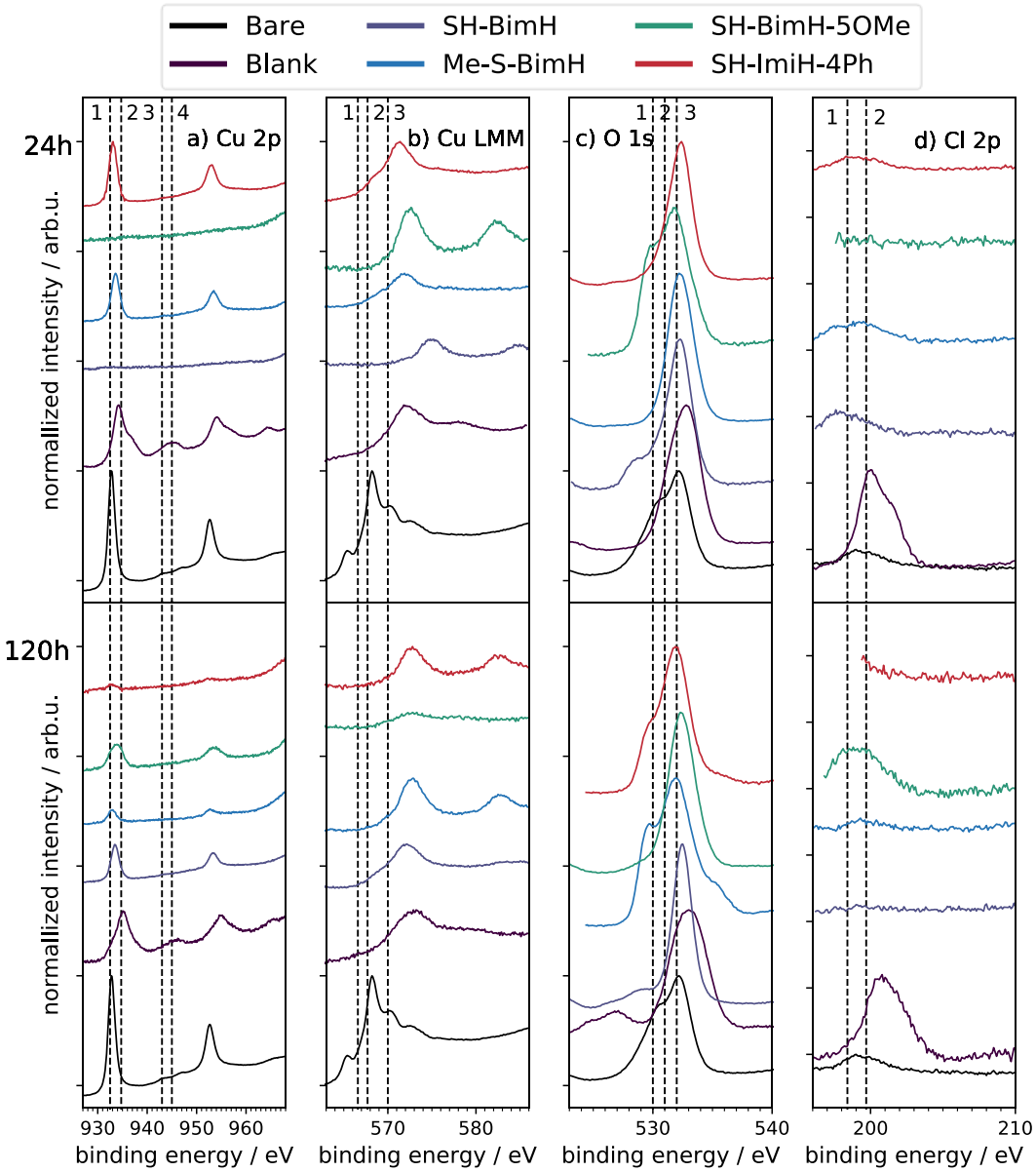

Figure 5.20 Normalized high-resolution XPS spectrums for the surface of $Cu_{70}Zn_{30}$ alloy after polishing and pickling and after immersion in 3wt.% NaCl with and without added of SH-BimH, Me-S-BimH, SH-BimH-5OMe and SH-ImiH-4Ph. Dash lines represent the position of peaks of reference compounds: (a) 1: Cu/Cu_2O, 2: $Cu(OH)_2$, 3: Cu(II) satellite peak, 4: Cu(I) satellite peak, (b) 1: Cu, 2: CuO, 3: Cu_2O, (c) 1: O^{2-}, 2: OH^-, 3: H_2O, (d) 1: Cl $2p_{3/2}$, 2: Cl $2p_{1/2}$. Upper: Immersion for 24h. Down: Immersion for 120h.

Figure 5.21 shows the normalized high-resolution XPS spectrums of C 1s, N 1s and S 2p of the surface of $Cu_{70}Zn_{30}$ alloy after polishing, pickling and subsequent immersion in

3wt.% NaCl with and without added inhibitors. As shown in **Figure 5.21** (a), carbon peaks appear in all spectra, and the intensity of peaks on the bare sample is lower than of

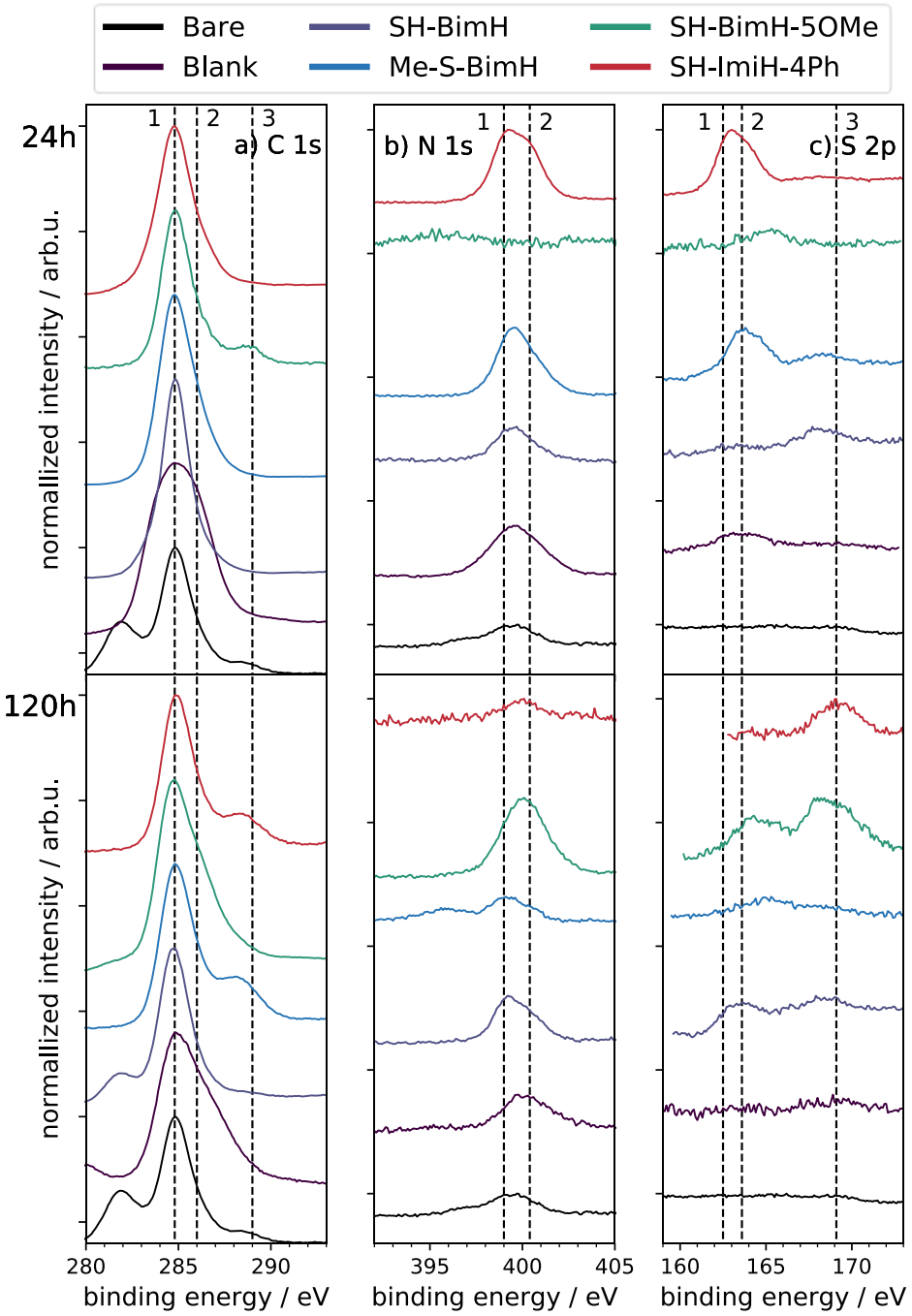

Figure 5.21 Normalized high-resolution XPS spectrums for the surface of $Cu_{70}Zn_{30}$ alloy after polishing and pickling and after immersion in 3wt.% NaCl with and without added of SH-BimH, Me-S-BimH, SH-BimH-5OMe and SH-ImiH-4Ph. Dash lines represent the position of peaks of reference compounds: (a) 1: C–C,C–H, 2: C–O, 3: C=O, (b) 1: - C=N-C, 2: C-NH-C, (c) 1: S $2p_{3/2}$, 2: S $2p_{1/2}$. Upper: Immersion for 24h. Down: Immersion for 120h.

those with inhibitors. The peak width of blank and inhibited samples is wider as well, which proves the presence of more kinds of carbon bond to other elements, i.e. nitrogen,

oxygen and sulfur. In the case of N 1s peaks in (b), two reference binding energy are indicated by dash lines [66], C-N (400.4 eV) and C=N (399.0 eV). There is almost no signal of these two peaks in the bare samples. Wide peaks appear in SH-ImiH-4Ph, Me-SH-BimH and SH-BimH, but no peak appears in SH-BimH-5OMe. There is no nitrogen signal in SH-BimH-5OMe immersed sample, which indicates the sample is not fully covered. But the signal decreased significantly after 120h. Besides, all inhibitors show a decrease of nitrogen intensity with time except SH-BimH-5OMe and SH-BimH. A new kind of film appears after 120h immersion due to the presence of Zn. As discussed before, the thione tautomer is important to show the formation of the film. However, since there is no good signal on the surface and a new film appears, it is difficult to identify the interface between $Cu_{70}Zn_{30}$ alloy and the inhibitors. In S 2p spectra, shown in **Figure 5.21** (b), SH-ImiH-4Ph and Me-S-BimH show wide peaks located between 162.2eV and 164.4eV after immersion for 24h. For the rest spectra after immersion for 24h and 120h, there is no clear signal. However, a wide peak appears around 169 eV in the samples immersed with SH-ImiH-4Ph, SH-BimH-5OMe and SH-BimH, which is attributed to the formation of sulfate or sulfide [117]. Nevertheless, the weak signal of N 1s, S 1s, Cu 2p and Cu LMM indicate that a film different from inhibitor compounds appears on the surface. This film may provide external protection or be just corrosion products. Further, longer immersion experiments will help to explain the surface evolution and the different interaction of $Cu_{70}Zn_{30}$ alloy and pure Cu with inhibitors.

5.3.2 Long-term immersion test

The long-term immersion test in period of 60 days for $Cu_{70}Zn_{30}$ alloy was analyzed by photography, SEM-EDX and Raman spectroscopy.

Photographic analysis

Photo of $Cu_{70}Zn_{30}$ alloy after 60 days' immersion

Figure 5.22 shows the image after rinsing with DI water and positioned in the DI water. The sample without inhibitor shows a rough surface with part of green particle covered area, part of brown area and some yellow parts like bare sample. The green parts are typical basic copper carbonate which is the corrosion products of copper in presence of CO_2, O_2, and H_2O. Brown parts may indicate the passivation layer and the yellow parts should be less passivated layer. In imidazole derivatives, ImiH shows a little darker green which may indicate the presence of $CuCl_2 \cdot 2H_2O$, this will be checked by XRD and SEM-EDX. SH-ImiH-4Ph shows a good surface and a little white film covered part of the surface. The rest of surface is kept yellow or a little brown. This appearance may indicate inhibitor or Cu/Zn-inhibitor complex gathered on the surface and form a stable layer on the surface which may provide resistance to corrosion. For SH-ImiMe, a uniform blue film presented on the surface which suspect to $Cu_3(CO_3)_2(OH)_2$ (Azurite), this will be analyzed by XRD. Mercapto-benzimidazole derivatives show a thicker white film than

that of SH-ImiH-4Ph. There are no apparent corrosion products exist on the surface. SH-BimH-5NH_2 produce different films on the surface, black part which is easy to remove and a red copper color appears the black film, and a white film cover rest of the surface. It's very difficult to explain what may happen with SH-BimH-5NH_2 added sample, SEM-EDX will show more details.

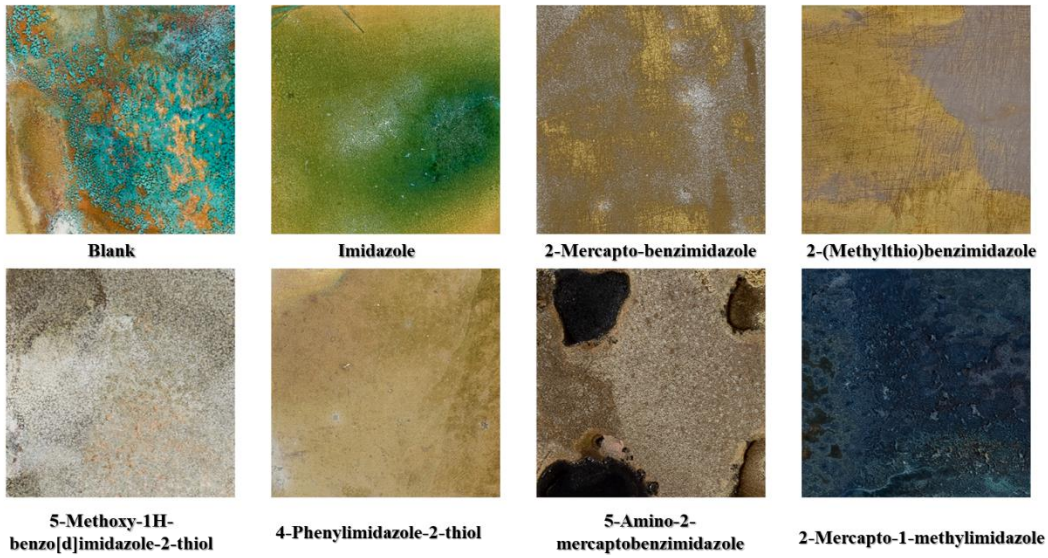

Figure 5.22 Photo of pure Zn samples after immersion for 12 days with and without presence of 1mM inhibitors in 3wt% NaCl solution sealed in bottle.

Photo of $Cu_{30}Zn_{70}$ alloy after 12 days' immersion

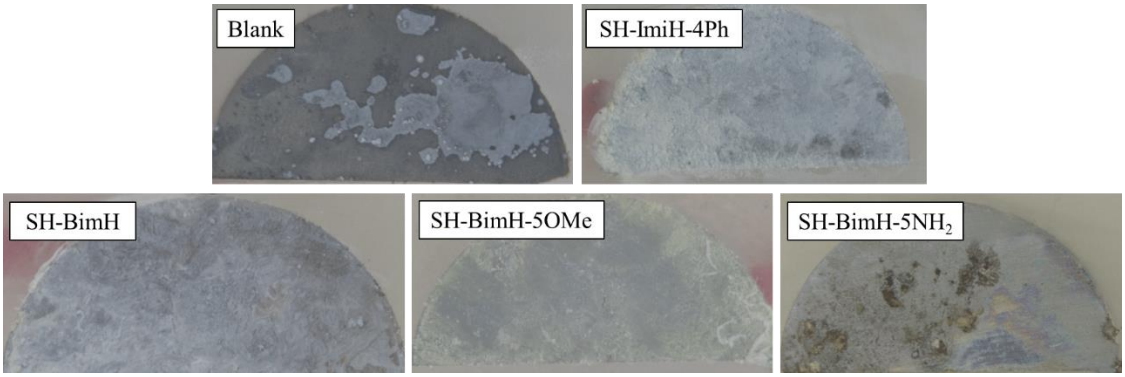

Figure 5.23 Photo of Cu30Zn70 alloy immersed in 3 wt.% NaCl with and without selected inhibitors for 12 days

Figure 5.23 shows the photo of $Cu_{30}Zn_{70}$ alloy after immersion in 3 wt.% NaCl with and without 1mM selected inhibitors for 12 days. The sample without inhibitor shows some white film on part of the surface, this is similar to the surface of pure Zn after 12 days' immersion without inhibitor. The rest part is dark and no shining. All the samples with inhibitor show slightly different color films on the surface. SH-ImiH-4Ph and Me-S-

BimH show thicker film and the surface under film is almost invisible. The sample surface of added SH-BimH shows thinner film, and the surface under the film is not shining. This indicates even film formed on the surface, reaction still carries on. The sample surface with SH-BimH-5NH_2 shows some naked part and it is not dark grey, still show some shining appearance. Since the thick film on SH-BimH-5OMe and Me-S-BimH sample surface, we can not get clear result by photos. The following SEM-EDX measurements will cooperate with the photos here and show more information.

SEM-EDX analysis

$Cu_{70}Zn_{30}$ alloy

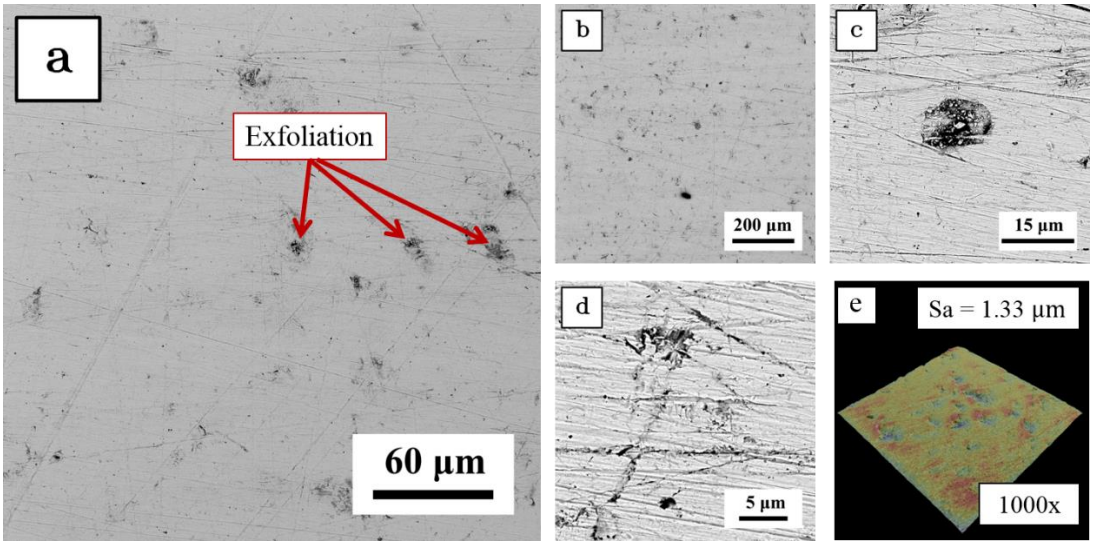

Figure 5.24 Bare surface of $Cu_{70}Zn_{30}$ alloy after polishing and rinse (a) surface under 1000x magnification (b) surface under 320x magnification (c) detail of the exfoliation (d) detail of the scratch (e) 3D topography under 1000x magnification by SEM

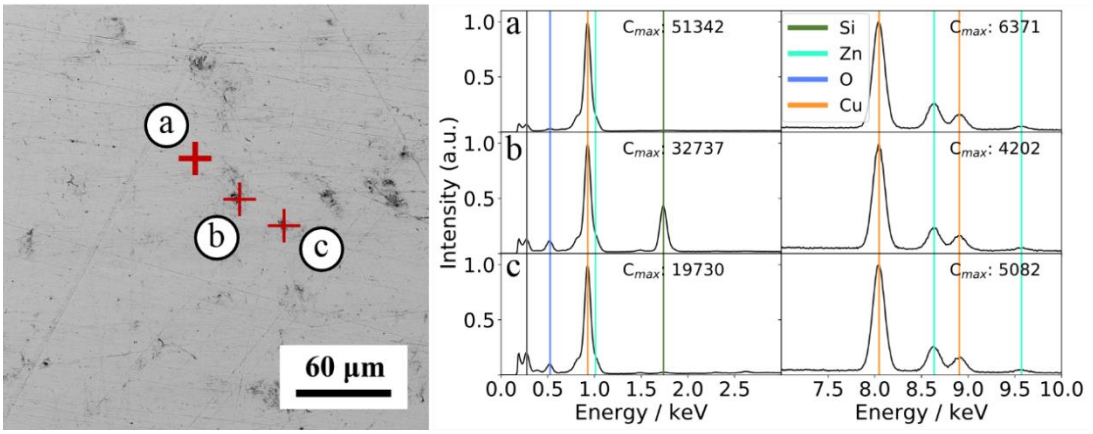

Figure 5.25 EDX elemental point analysis spectrum of bare surface of $Cu_{70}Zn_{30}$ alloy (a) spectrum of point a, flat surface (b) spectrum of point b, exfoliation hole (c) spectrum of point c, exfoliation hole

Figure 5.24 shows the bare surface of $Cu_{70}Zn_{30}$ alloy of the backscattered electron image (BSE). **Figure 5.24** (a) shows grey lines and black particles on the surface after polishing and pickling. As shown in the 3D **Figure 5.24** (e), it is clear that the black parts are the exfoliations, and grey lines are scratches on the surface, and it gives a surface roughness Sa (arithmetical mean height) of 1.33 μm. Those defects can not be avoided and ignored during the experiments. A homogeneous surface was presented except those defects observed under 320x magnification, as shown in **Figure 5.24** (b). **Figure 5.24** (c) and (d) show a close-up view of the exfoliation and scratches. In exfoliation, part of the material is removed and contains small particles, and it shows the same contrast with the sample surface, most exfoliation is around 5 – 15 μm. The scratches are produced by polishing of SiC paper on the surface, around 1 μm width.

Figure A2.18 shows the EDS elements map of Cu and Zn (resolution: 123x128 pixels). Except for the exfoliations, the distribution of the elements is uniform. The heterogeneity of the EDS map may result from a tilted and deeper surface, which will reduce the characteristic X-ray emission.

Figure 5.25 shows several EDS elemental points analysis spectrums of the material. Points (b) and (c) are the dark part display by BSE detector, and they are the exfoliations caused by polishing. In both points, there is a peak around 0.6 keV due to O (K_α ~ 0.525 keV); comparing with the same position in the spectrum (a) it is much more significant. The structure of exfoliation may accelerate oxidation and reduce the pickling effect. The difference between (b) and (c) is a new peak appeared around 1.6 keV, which matched the Si peak. The presence of Si may come from the SiC polishing paper, which embeds into the exfoliation. Both ultrasonic bath and pickling cannot remove this kind of mechanical bond. For the peaks in the right plot, the intensities are close to the ones in the spectrum (a). This silicon signal may also appear due to the application of the dead layer of SDD (Silicon Drift Detector), and the Si signal will be magnified when it exists. The quantification of EDS points on the flat surface shows a result of Cu (74.77 at. %) and Zn (25.23 at. %), the higher concentration of Cu may be attributed to the fluorescence of Cu-Kα x-ray generated by the Kα x-ray of the Zn existing in the brass sample. In 70Cu-30Zn alloy, more than expected Cu K α and less than anticipated Zn K α x-rays will be generated due to the fluorescence effect. In this way, Cu will be overrepresented, and Zn will be underreported unless corrections are made to the calculations.

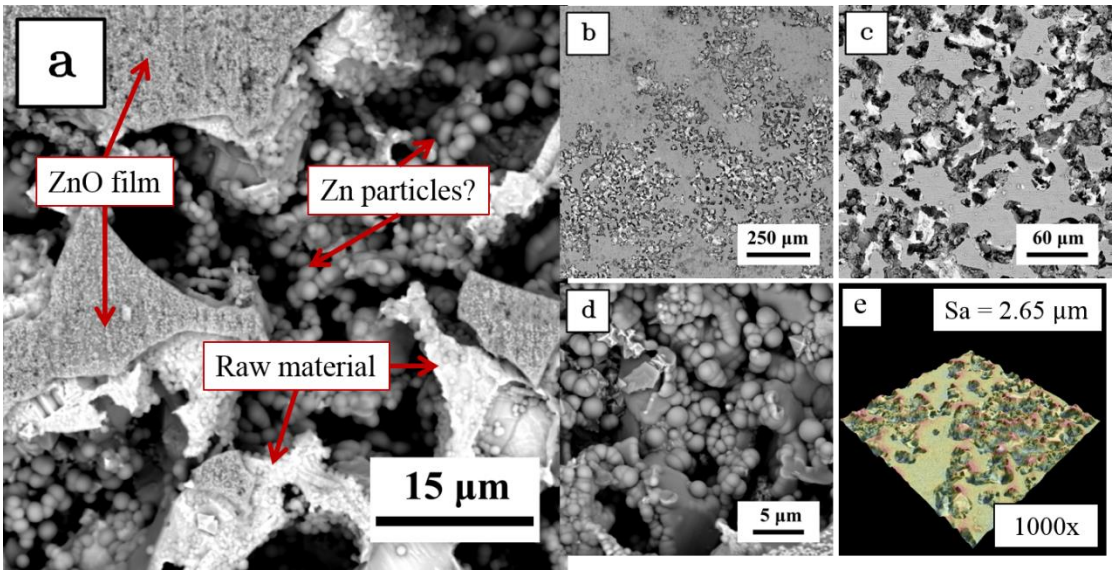

Figure 5.26 $Cu_{70}Zn_{30}$ alloy immersed in 3 wt.% NaCl solution for 60 days (a) surface under 5000x magnification with all typical features (b) surface under 320x magnification (c) surface under 1000x magnification (d) surface features in the porous (e) 3D topography under 1000x magnification by SEM

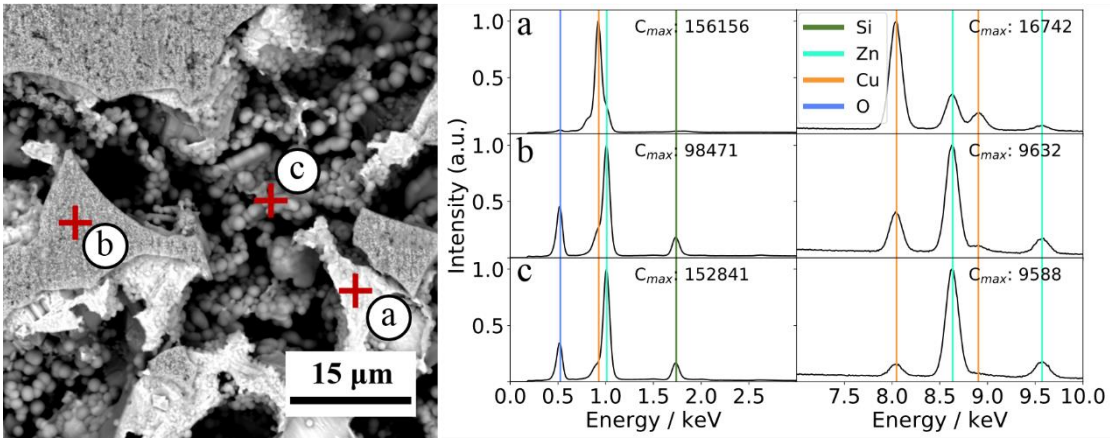

Figure 5.27 EDX elemental point analysis spectrum of $Cu_{70}Zn_{30}$ alloy immersed in 3 wt.% NaCl solution for 60 days (a) spectrum of point a, white part under BSE detector (b) spectrum of point b, grey film on the surface (c) spectrum of point c, particles in porous

Figure 5.26 shows the BSE images of the $Cu_{70}Zn_{30}$ alloy immersed in 3 wt.% NaCl aqueous solution for 60 days. **Figure 5.26** (a) seems to show a porous structure, part of the flat grey film on the surface, some particles in the holes, and some white pieces under the grey film. **Figure 5.26** (e) confirmed the porous structure and showed a surface roughness Sa of 2.65 µm. The overlook of the surface shows a lot of porous on the surface, and the rest of the areas are a flat grey surface and some small parts of white, as shown in **Figure 5.26** (b) and (c). The scratches from polishing appear on the grey parts. Besides, the holes are around 20 µm in width. **Figure 5.26** (d) is a close-up observation into the hole, and the ball particles around 1 - 2 µm are in contact with each other.

Figure A2.19 shows the EDS elemental map analysis of the immersed sample. Zn is present on most of the surface. The distribution of Zn and O is significantly overlapping. The grey film is probably a Zinc oxide. Cu and Zn coincide in the areas lacking O. Point elemental analysis was conducted as well.

Figure 5.27 shows several EDS elemental points spectrums, namely (a) white piece, (b) grey film, and (c) grey particles. Spectrum (a) is almost the same as the spectrum in **Figure 5.27** (a). The white pieces in the figure should be the remaining raw materials, and the quantification result shows a Zn/Cu ratio of 0.46/1 ($Cu_{70}Zn_{30}$ alloy: 0.43/1). Spectrum (b) and (c) show a familiar Cu and Zn peak in the Kα energy range, and the O peak is quite high as well. The quantification results were transferred to a ratio of different elements in **Table 5.3**. The grey surface seems to be the ZnO oxide on the surface formed during immersion. The particles in the holes are much close to pure Zn with little oxide content on the surface, and they may result from the redeposited Zn after dissolving into solution.

Table 5.3 Atomic ratio of different elements

Spectrum	Zn/O	Zn/Cu	CuZn/O
a	-	0.46/1	-
b	0.74/1	3.86/1	0.93/1
c	4.41/1	14.33/1	4.71/1

Furthermore, the maximum of measured depth can be calculated based on the Castaing's formula:

$$z_m = 0.033(E_0^{1.7} - E_c^{1.7})\frac{A}{\rho Z}$$

Where E_0 is accelerating voltage (kV), E_c is minimum emission voltage (keV), A is atomic mass, ρ is the density (kg/m^3), and Z is the atomic number. With the acceleration voltage of 15kV, maximum analytical depth of Cu-Lα is ~0.8 μm, Zn-Lα ~1 μm. The depth of the ZnO layer can be estimated to be at most ~0.8 μm. The $Cu_{70}Zn_{30}$ alloy immersed in the 3wt. % NaCl aqueous solution in a sealed bottle shows an unambiguous plug-type dezincification. The ZnO oxide layer covered part of the surface, and some holes and raw materials under the oxide layer. Other parts show a porous structure with some redeposited Zn particles and remaining materials in the gap. The alloy with efficient inhibitors should show a porous free surface with less oxide layer.

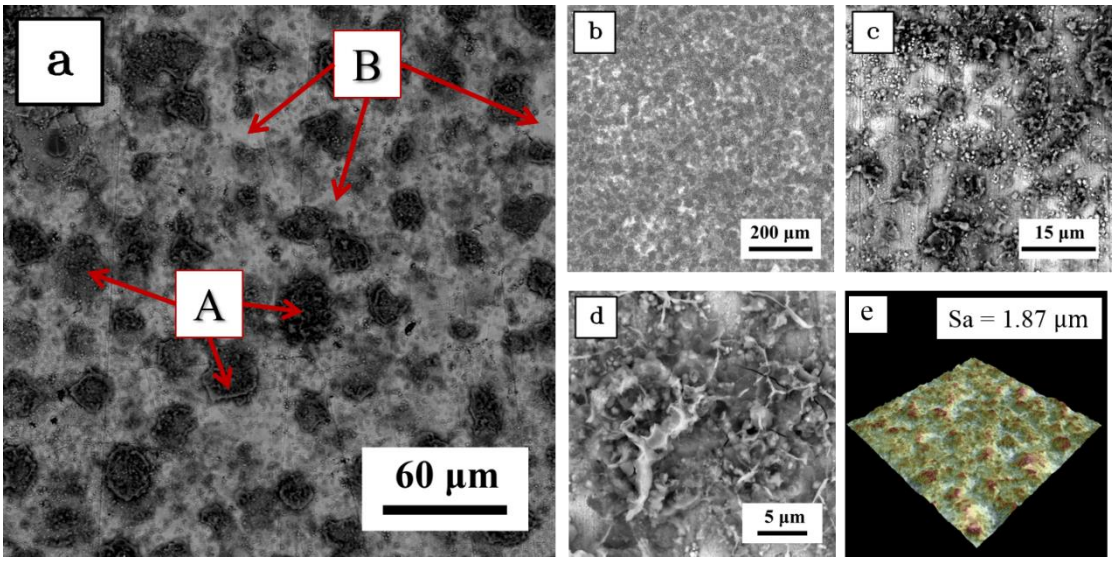

Figure 5.28 $Cu_{70}Zn_{30}$ alloy immersed in 3 wt.% NaCl with added 1mM SH-BimH solution for 60 days (a) surface under 2500x magnification with all typical features (b) surface under 320x magnification (c) surface under 1000x magnification (d) surface features in the valley (e) 3D topography under 1000x magnification by SEM

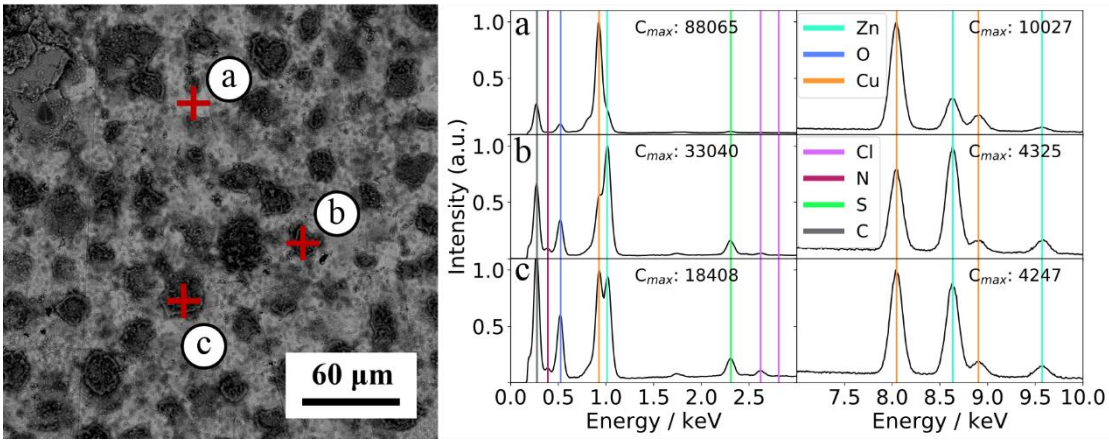

Figure 5.29 EDS elemental point analysis spectrum of $Cu_{70}Zn_{30}$ alloy immersed in 3 wt.% NaCl solution with added 1mM SH-BimH for 60 days (a) spectrum of point a, white part under BSE detector (b) spectrum of point b, grey film on the surface (c) spectrum of point c, particles in porous

Figure 5.28 shows the BSE images of $Cu_{70}Zn_{30}$ alloy immersed in 3 wt.% NaCl with added 1mM SH-BimH for 60 days. **Figure 5.28** (a) shows two typical features, which are better identified in conjunction with **Figure 5.28** (e). (A) are black irregular low hills, around 15 – 30 µm. The black in BSE image always refers to the heavy elements, but here it may attribute to less conductivity of the surface caused by the dielectric organic film; it may also introduce fewer counts in EDS measurements. (B) shows a white grid around the hills. Moreover, the roughness Sa is 1.87 µm. Magnification of 320x – **Figure 5.28** (b) – shows an overview of the surface covers by the hill and grid structure with uniform size. As shown in **Figure 5.28** (c), the scratches inherited from polishing are still visible

on the white grid, which means this kind of surface is not severely corroded. The close-up **Figure 5.28** (d) shows the detail of the black hill, which seems to be a kind of organic compound on the top and some cracks under it.

Figure A2.24shows the EDS elemental map of Cu, Zn, O, C and S. It is clear that the black parts are C and S rich, showing almost no Cu. Zn is present in part of the black hills, overlapping with O. The white parts are covered by Cu, Zn, O, and maybe some C and S. **Figure 5.29** is the EDS point spectrum of the features, (a) on the white grid part, (b) and (c) on the black part. Spectrum (a) shows the presence of C, O, S. The photograph in **Figure 5.22** after immersion shows the white layer on the surface, which may be an organic film. Assuming that the film did not substantially affect the x-ray emission, the Cu/Zn ratio can identify the alloy under this film. The quantification shows a Zn/Cu ratio of 0.423/1, close to the ratio of raw materials. This indicates surface oxidation, covered by a thick inhibitor film. The inhibitors protect the surface not just by a monolayer but as a film over time. The inhibitors in solution may combine with those on the surface and form a thick film on the surface as in **ref.** [118]. Spectrum (b) and (c) show that the concentration of Zn is higher than that of Cu, and the ratio varies with the position. This proves that corrosion happened in these black regions. The peaks of sulfur and chlorine are bigger, which indicates that a higher amount of inhibitors accumulate in these regions. The removed Cu may react with inhibitors during the corrosion reactions and form the flocculent precipitation in the solution. The crystal orientation may be responsible of the different bond strength of inhibitors, which will result in the differential corrosion of different crystalline surfaces.

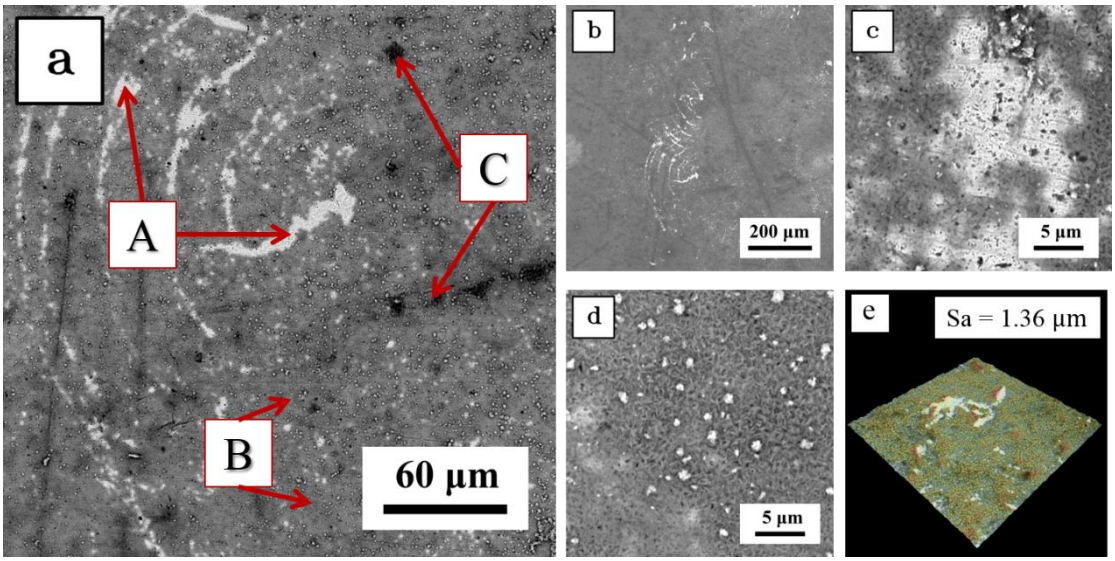

Figure 5.30 $Cu_{70}Zn_{30}$ alloy immersed in 3 wt.% NaCl with added 1mM Me-S-BimH solution for 60 days (a) surface under 2500x magnification with all typical features (b) surface under 320x magnification (c) surface under 1000x magnification (d) surface features in the valley (e) 3D topography under 1000x magnification by SEM

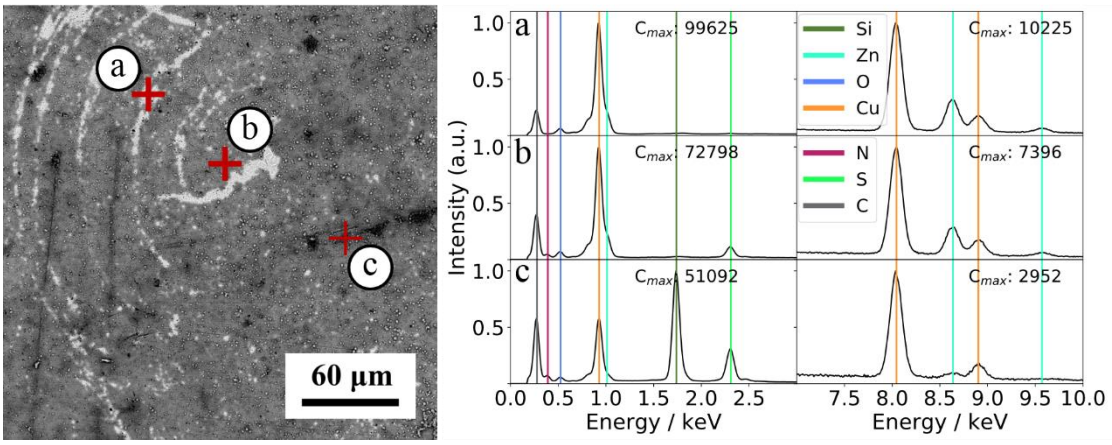

Figure 5.31 EDS elemental point analysis spectrum of $Cu_{70}Zn_{30}$ alloy immersed in 3 wt.% NaCl solution with added 1mM Me-S-BimH for 60 days (a) spectrum of point a, white part under BSE detector (b) spectrum of point b, grey film on the surface (c) spectrum of point c, particles in porous

Figure 5.30 shows the BSE images of $Cu_{70}Zn_{30}$ alloy immersed in 3 wt.% NaCl aqueous solution with added 1mM Me-S-BimH for 60 days. According to subfigure (a) and (e), there are three features on the surface, (A): white plane lower than other features, present on some parts of the surface, (B): grey organic film higher than the white plane, covering most of the surface, as shown in subfigure (b), (C): black small organic hills on the top. The measured roughness Sa is 1.36 µm. In subfigure (c), scratches are still present on the white parts and under the grey films. There are some small black spots on the surface, maybe holes or organic compounds. There are some white particles on the grey film, and the grey film seems made of grey fibers, as shown in subfigure (d). **Figure A2.24** shows the EDS elemental map of Cu, Zn, O, C and S. Most of the C and S are distributed on the grey and some black parts. The white plane shows the presence of some C and S, and the major elements are Cu and Zn; there is also some oxygen around the border. Moreover, the black spots on the white plane do not show S- or C-rich spots, which means that they are holes. On the top left of the figure, there is a genuine black part, showing none of the elements. The white particles on the grey films only show the presence of Zn and O, which should correspond to ZnO particles. **Figure 5.31** shows the EDS point spectrum of the features, (a) on the white plane, (b) on the grey film, and (c) on the black hill. Spectrum (a) shows that there is a few O and C on the surface, and no clear S peak. Spectrum (b) shows the presence of S, a higher C peak, and almost the same O peak than (a), the right spectrum is very similar to that of (a). The quantification results give a Zn/Cu ratio of 0.42/1 on point (a) and 0.37/1 on point (b), which may indicate that the inhibitor protects the surface. Spectrum (c) shows a high Si peak, and although the concentration is only 8 at. %, by comparing with the Cu Lα peak, it is clear the S and C peaks are quite higher than those in point (b). Nevertheless, Zn concentration is quite low in this position, which may be a sign of dezincification. Me-S-BimH shows efficient inhibition ability, as not significant porous structure is observed. Moreover, inhibitors covered most of the surface.

The only noticeable issue is the small holes of less than 1 µm which appear in some locations.

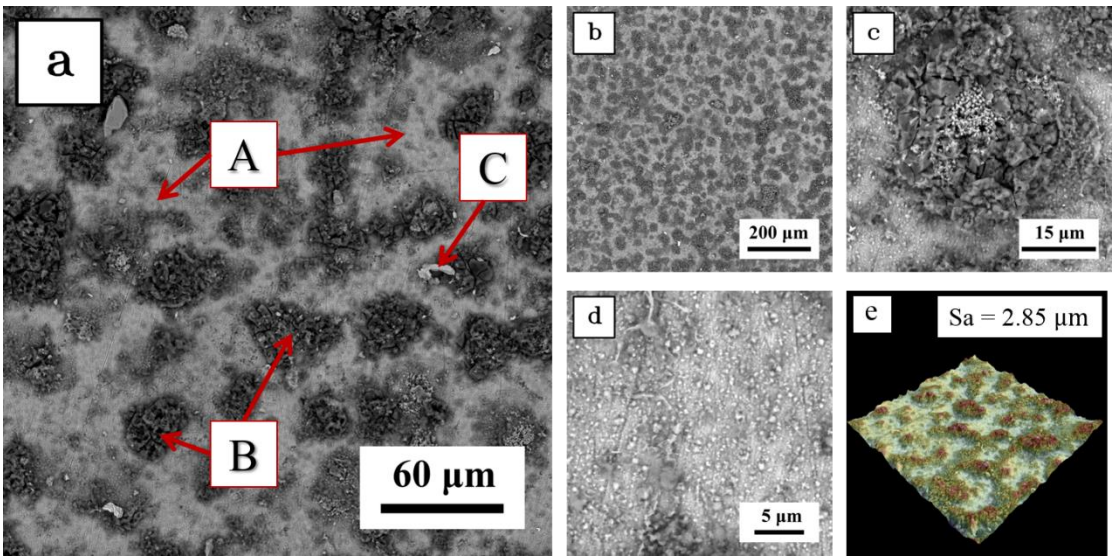

Figure 5.32 $Cu_{70}Zn_{30}$ alloy immersed in 3 wt.% NaCl with added 1mM SH-BimH-5OMe solution for 60 days (a) surface under 2500x magnification with all typical features (b) surface under 320x magnification (c) surface under 1000x magnification (d) surface features in the valley (e) 3D topography under 1000x magnification by SEM

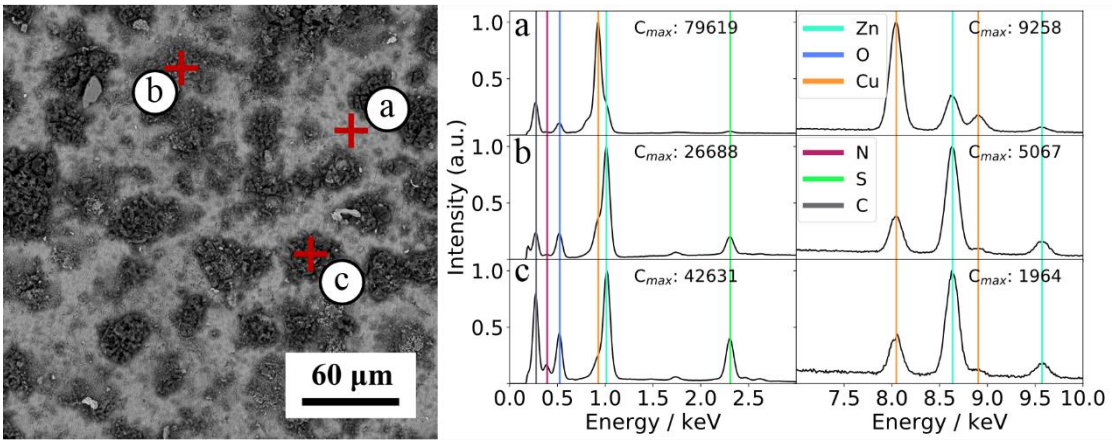

Figure 5.33 EDS elemental point analysis spectrum of $Cu_{70}Zn_{30}$ alloy immersed in 3 wt.% NaCl solution with added 1mM SH-BimH-5OMe for 60 days (a) spectrum of point a, white part under BSE detector (b) spectrum of point b, grey film on the surface (c) spectrum of point c, particles in porous

Figure 5.32 shows the BSE images of the $Cu_{70}Zn_{30}$ alloy immersed in 3 wt.% NaCl aqueous solution with added 1mM SH-BimH-5OMe for 60 days. Subfigure (a) and (e) show three typical features, a flat grey surface (A), small cluster hills (B), and white bars or particles (C).

The appearance is similar to the sample of SH-BimH, they all show a cluster and grid structure on the surface, and the cluster size is around 30 – 60 µm. However, the

roughness is higher than for SH-BimH-5OMe, with a Sa value of 2.85 μm. Subfigure (b) shows that the same features cover the whole surface in the image. The cracks under the clusters may include partial dissolution of one element, shown in subfigure (c). On the flat grey surface, the scratches of polishing are still observable, and some small particles are on the surface, which may arise due to the redeposition. **Figure A2.25** shows the EDS elemental map of Cu, Zn, O, C and S. Cu is observed out of the clusters, which means there is very little Cu in clusters, and there is a dark orange bar on the center-right. Zn covers most of the surface except some edges of the clusters. Some parts of the clusters show dark blue, which means a high concentration of Zn. The distribution of O is very similar to that of Zn, especially the dark part. Moreover, in the position of the dark orange bar, there are no O and Zn. Therefore, the white bar on the center-right should be pure Cu, and the thickness is larger than 0.8 μm. There are signs of ZnO particles in the clusters. The distribution of C and S shows that organic compounds cover the clusters and some of the flat surface as well. **Figure 5.33** shows the EDS point spectrum of the features, (a) on the light grey grid part, (b) and (c) on the black clusters. In spectrum (a), the concentration of the Cu and Zn is similar to that of the raw material, but the C and O peaks are higher, which indicates oxidation and absorption of organic compounds. The sulfur peak is not so clear, which means that the organic film is thin. Furthermore, the quantification result shows a Zn/Cu ratio of 0.459/1. Spectrum (b) and (c) show higher peaks of C, O and S; thus, there are more organic compounds on the clusters. The concentration of Cu is shallow, and the Cu peaks are quite small compared with the raw material. The dissolution of Cu may occur because of the inhibitor bond with the Cu ions on the surface where corrosion may happen through the reaction

$$Cu^{+}/Cu^{2+} + \text{SH-BimH-5OMe} \rightarrow Cu(\text{SH-BimH-5OMe})$$

The electrochemical results show that the inhibition of SH-BimH-5OMe decreases rapidly after 5 days' immersion, which is due to the partial dissolution in the black part. Then, the resistance and impedance begin to drop; this kind of island distribution may be consequence of crystal orientation, like with SH-BimH.

Figure 5.34 shows the BSE images of $Cu_{70}Zn_{30}$ alloy immersed in 3 wt.% NaCl aqueous solution with added 1mM SH-ImiH-4Ph for 60 days. From subfigure (a) and (e), it is clear this sample has a much flatter surface than the other inhibited samples considered before. The black parts are higher parts with less conductivity. Moreover, the black parts distribute on the scratches and maybe exfoliations. The roughness is a Sa value of 1.13 μm, even lower than that of the raw materials. This may be attributed to the accumulation of organic compounds on the scratches and exfoliations, which can reduce the roughness. The overview of the surface under 320x magnification shows a similar image than that of raw materials. The only difference is the darken of scratches and exfoliations. Subfigure (c) and (d) are the close-up image of a dark part, there are just some small particles around, and the size of these features is small, also showing a reduced contrast.

Figure A2.26 shows the EDS elemental map of Cu, Zn and O. C is not included as the significant C concentration may hide the information of Cu and Zn. The distribution of Cu, Zn and O almost uniform. **Figure 5.35** is the EDS point spectrum of the features, (a) normal surface, (b) and (c) on the black particles. All three spectrums show a significant peak of C, and the maximum counts in the range 0.5 – 3 keV and 7 – 10 keV are much lower than in the previous samples with the same scanning duration (1.5 minutes).

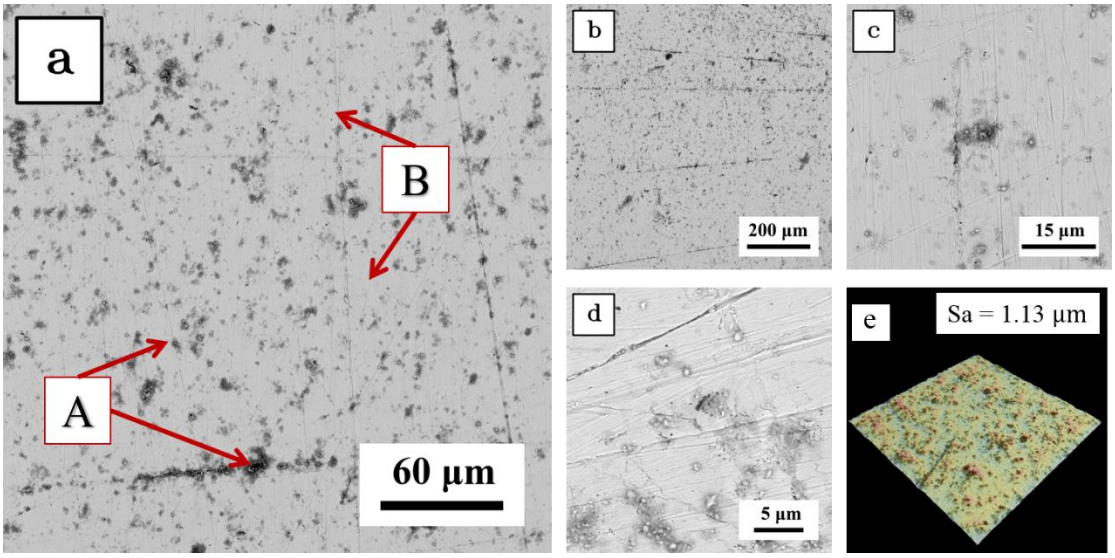

Figure 5.34 $Cu_{70}Zn_{30}$ alloy immersed in 3 wt.% NaCl with added 1mM SH-ImiH-4Ph solution for 60 days (a) surface under 2500x magnification with all typical features (b) surface under 320x magnification (c) surface under 1000x magnification (d) surface features in the valley (e) 3D topography under 1000x magnification by SEM

Furthermore, there is a massive peak in the range of 0.2 – 0.3 keV, which cannot be measured on this detector. This may be due to the absorption and fluorescence of the characteristic x-ray of the organic film. In the spectrum (a), the O peak is tiny. The general surface is covered by the organic films and shows a Zn/Cu ratio of 0.408/1, and the oxide film is also very thin. Spectrum (b) and (c) show similar peaks of Cu and Zn, the Zn peak being slightly more intense than that of spectrum (a). O and S peaks are also more significant, which indicates the presence of more oxides and organic compounds in these positions. As shown in **Figure 5.24** (c) and (d), the scratches and exfoliations show the presence of some particles of raw materials and maybe SiC particles. These spots are preferential locations for corrosion, inducing the production of Cu ions which, in turn, attract inhibitor molecules which eventually accumulate over them. This kind of accumulation may adhere to the surface and protect the position from further corrosion; this process is observed in solutions containing SH-BimH, SH-BimH-5OMe and SH-ImiH-4Ph. Moreover, cracks and selective dissolution developed under the organic compounds. However, SH-ImiH-4Ph is found only in the positions of defects. According to the EDS results, selective dissolution may develop in those accumulation locations, but SH-ImiH-4Ph did not show a distinct selective dissolution. Compare to Me-S-BimH, which presents some holes of size less than 1 µm on the surface, there are no apparent holes or new features appear on the surface. This inhibitor shows a significant inhibition

during 60 days' immersion and should be a competitive inhibitor for convenient applications.

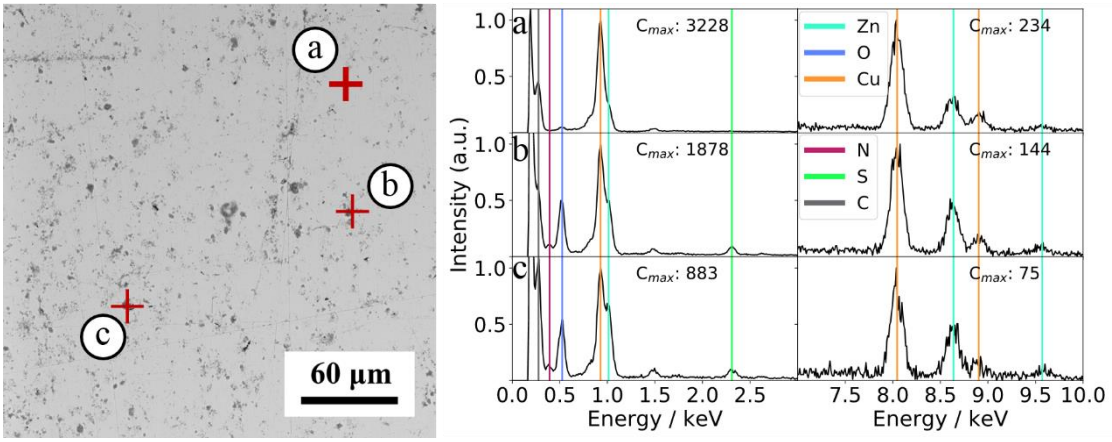

Figure 5.35 EDS elemental point analysis spectrum of $Cu_{70}Zn_{30}$ alloy immersed in 3 wt.% NaCl solution with added 1mM SH-ImiH-4Ph for 60 days (a) spectrum of point a, white part under BSE detector (b) spectrum of point b, grey film on the surface (c) spectrum of point c, particles in porous

$Cu_{30}Zn_{70}$ alloy

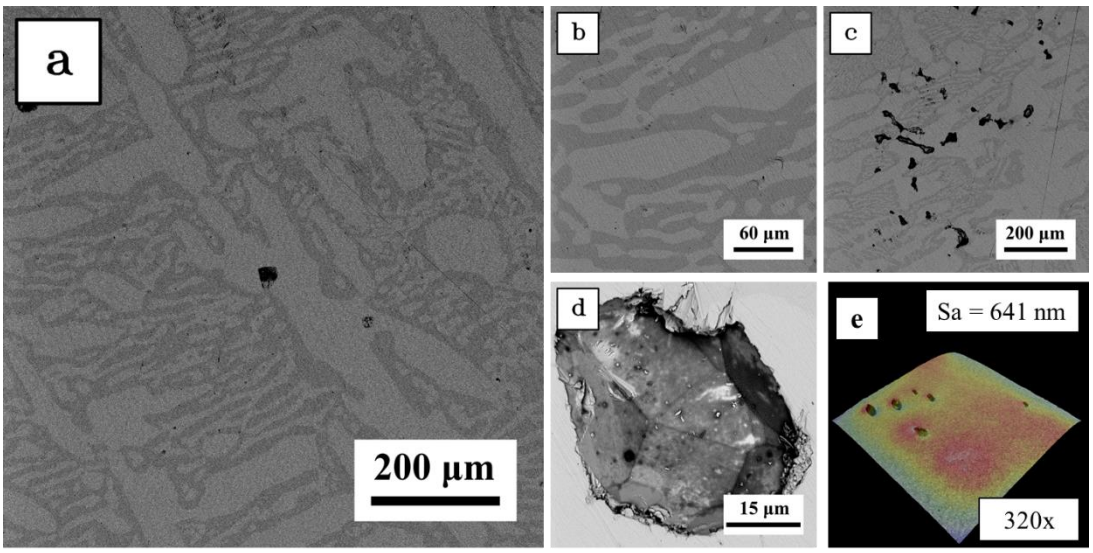

Figure 5.36 Bare surface of $Cu_{30}Zn_{70}$ alloy after polishing and rinse (a) surface under 320x magnification (b) surface under 1000x magnification (c) casting pin holes (d) detail of the hole (e) 3D topography under 1000x magnification by SEM

Figure 5.36 shows the bare surface of $Cu_{30}Zn_{70}$ alloy. (a) shows two different contrast regions, which should correspond to the different phases as characterized by XRD in section 5.1.2. **Figure 5.36** (c) shows some black parts on the surface, corresponding to casting pin holes instead of polishing introduced exfoliations. The surface is very flat after polishing, as shown in **Figure 5.36** (b) and (e). **Figure 5.36** (d) shows the structure inside

the hole. **Figure A2.33** shows the map of elemental analysis. Darker parts show much more Zn than Cu. **Figure 5.37** shows the elemental point analysis. Points (a) and (b) show different Cu/Zn ratio on dark and light surface areas. Point (c) is on the hole which shows no Si peaks.

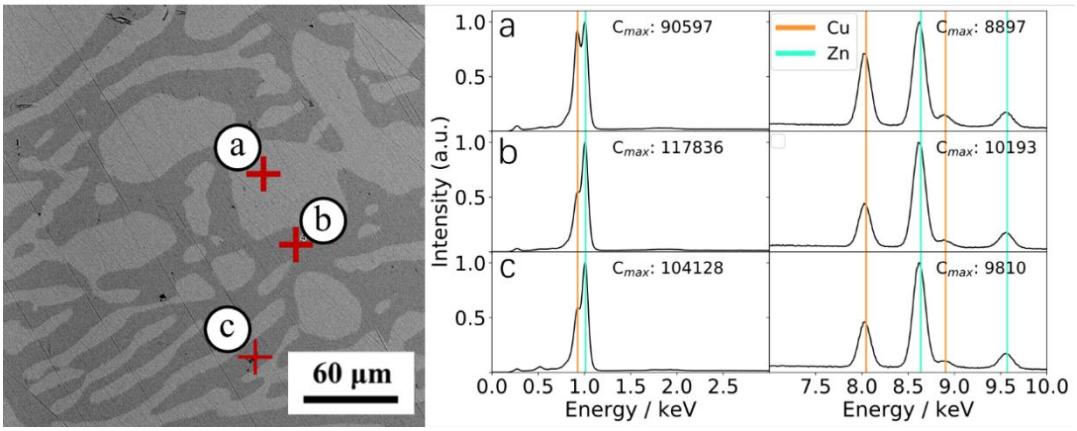

Figure 5.37 EDX elemental point analysis spectrum of bare surface of $Cu_{30}Zn_{70}$ alloy (a) spectrum of point a, light grey part (b) spectrum of point b, dark grey part (c) spectrum of point c, hole

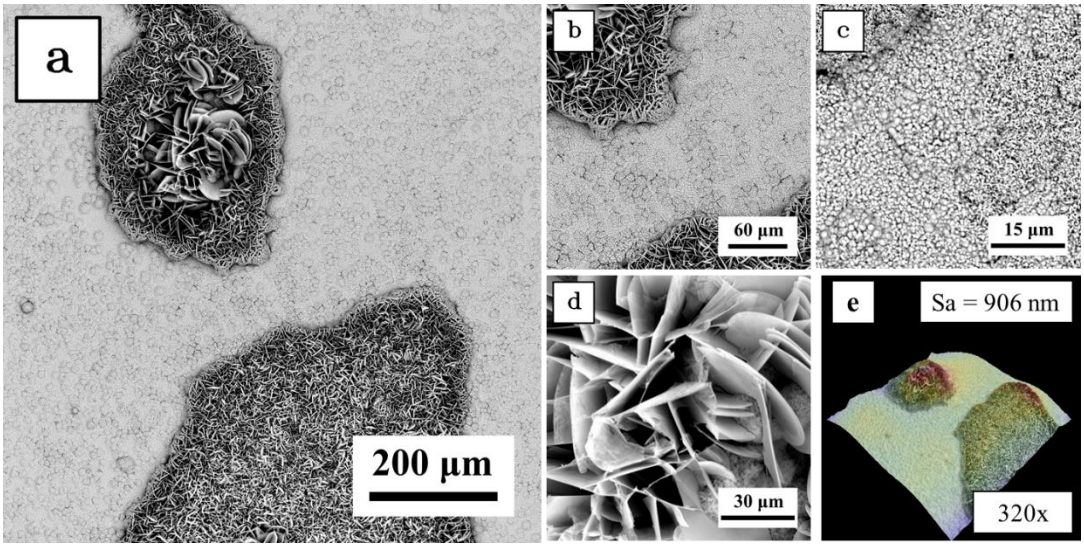

Figure 5.38 Cu30Zn70 alloy immersed in 3 wt.% NaCl solution for 12 days (a) surface under 320x magnification with all typical features (b) surface under 1000x magnification (c) surface under 5000x magnification (d) structure of flower-like substance (e) 3D topography under 320x magnification by SEM

Figure 5.38 shows the surface of $Cu_{30}Zn_{70}$ alloy immersed in 3 wt.% NaCl for 12 days. The look of the surface is close to the pure Zn surface in same condition, as shown in **Figure 5.38** (a). A closer look in **Figure 5.38** (b) and (c) show the flat surface is composed of porous structure. **Figure 5.38** (d) shows the flower-like substance is made of lamellar substance. **Figure A2.34** shows the elemental map of the surface, Cu, Zn, Cl, O appear on the surface and distribute at the same position. **Figure 5.39** shows the elemental point

analysis of the surface. All three points show similar peaks and intensities, which indicates $Cu_{30}Zn_{70}$ alloy corroded and (Zn, O, Cl) complex covered the surface. Cu was removed from the surface.

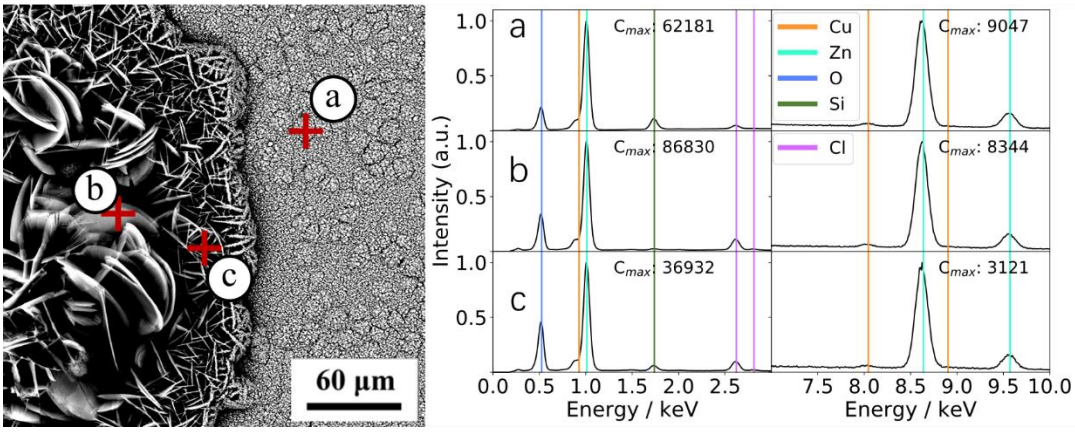

Figure 5.39 EDX elemental point analysis spectrum of $Cu_{30}Zn_{70}$ alloy immersed in 3 wt.% NaCl solution for 12 days (a) spectrum of point a, small porous surface (b) spectrum of point b and c, flower-like substance.

Figure 5.40 shows the surface of $Cu_{30}Zn_{70}$ alloy immersion in 3 wt.% NaCl with added SH-BimH-5NH_2 for 60 days. (a) shows there is major their features on the surface, black part with particles, some white particles, and white surface. As shown in **Figure 5.40** (b), white particles on the surface are close to the contrast of uncorroded flat surface shown in **Figure 5.40** (c). In **Figure 5.40** (d), the black part shows the cracked film, and scratches appear on the film indicate this part is not severely corroded. **Figure A2.44** is the elemental map of the surface, the presence of Cu, Zn, Cl, S, O, C indicates the inhibitor adhere to the surface. Elemental point analysis in **Figure 5.41** shows much precise elemental concentration. Point (a) on the flat white surface show Cu and Zn peaks close to bare surface, and small S and C appear to show the presence of inhibitor. Point (b) is on the darker surface, the peaks of Cu and Zn are the same, but higher peaks of C and S are found, there should be more inhibitor on this part. Black corroded surface shown in point (c) display remarkable S peak and a small Cl peak, and Cu peaks are negligible. Which means corrosion happened on this location and inhibitor complex adhere on the local attacks. SH-BimH-5NH_2 is the best inhibitor for $Cu_{30}Zn_{70}$ alloy as same as for pure Zn.

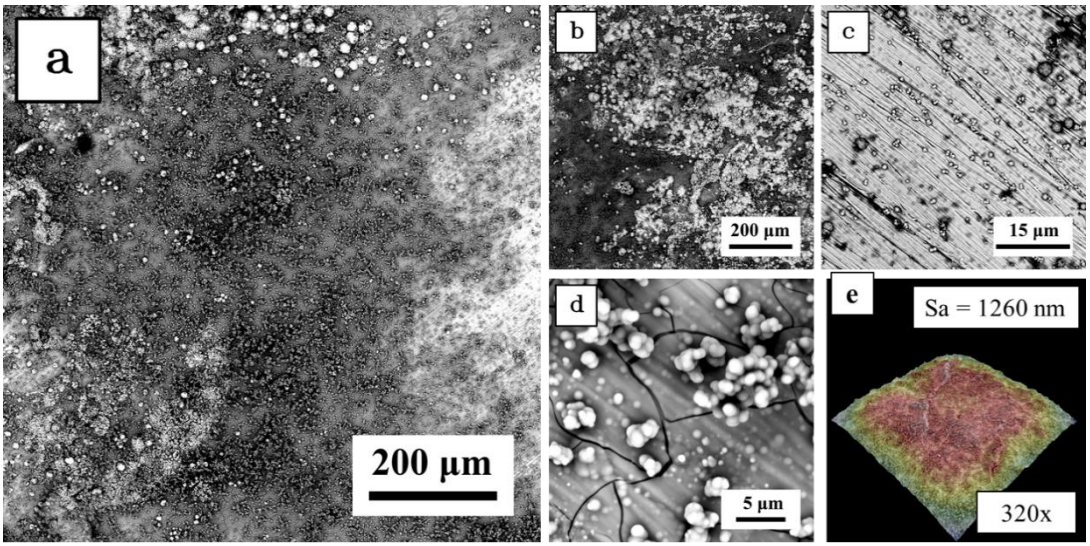

Figure 5.40 $Cu_{30}Zn_{70}$ alloy immersed in 3 wt.% NaCl with added 1mM SH-BimH-$5NH_2$ solution for 12 days (a) surface under 320x magnification with all typical features (b) surface under 320x magnification with white particles (c) surface under 5000x magnification (d) dark surface under 10000x magnification (e) 3D topography under 320x magnification by SEM

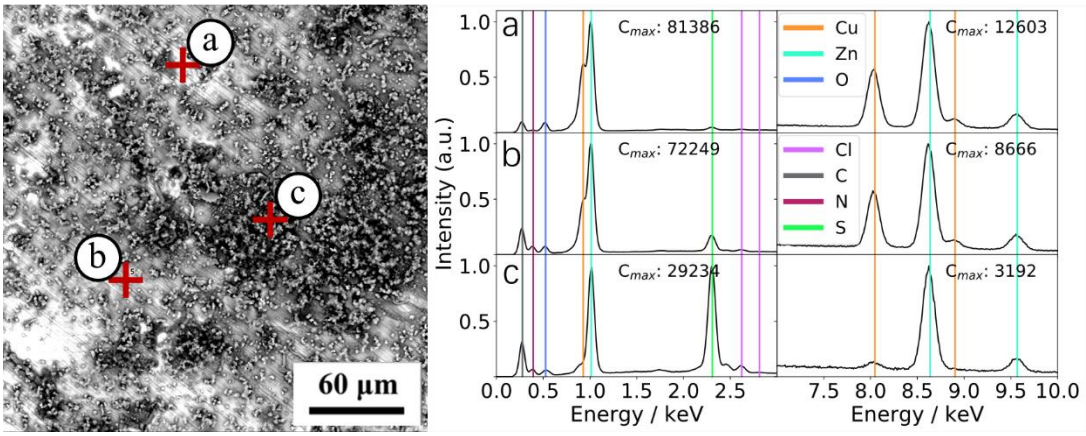

Figure 5.41 EDS elemental point analysis spectrum of $Cu_{30}Zn_{70}$ alloy immersed in 3 wt.% NaCl solution with added 1mM SH-BimH-$5NH_2$ for 12 days (a) spectrum of point a, white flat surface (b) spectrum of point b, darker flat surface (c) spectrum of point c, black corroded surface.

SH-BimH-$5NH_2$ is the only effective inhibitor among all selected ones, this result shows that the corrosion inhibition has a strong correlation with major elements in CuZn alloy. And rest introduction of inhibition is shown in Appendix 2.3.2.

Raman spectroscopic analysis

Raman spectroscopy is a convenient characterization method for surface analysis, especially for organic compounds. Even though it can not detect the monolayer on the sample surface, the adhesion film on the surface should be an adequate target for this technology. As shown in **Figure 5.42**, the spectrums of inhibitor, adhesion substance after immersion of Cu and $Cu_{70}Zn_{30}$ alloy are present in the same plot. For SH-BimH and Me-S-BimH, the spectrum of Cu and $Cu_{70}Zn_{30}$ alloy are close. The position of peaks compare with inhibitor are almost the same, only two spectrums with materials show different intensity. This should attribute to the enhance effect due to the presence of Cu combine with the inhibitors [119], this phenomenon shows that in most of effective inhibitors, Cu-inhibitor complex adheres to the surface. This kind of adhesion should reduce the corrosion rate at the local attacked surface (shown in SEM-EDX part). The complex gathers to the pits, thus acts as a patch to repair the leakage of the surface. However, this repair-effect is different on different inhibitors. The best inhibitor for $Cu_{70}Zn_{30}$ alloy shows very small patch on the surface, on the contrary, SH-BimH and SH-BimH-5OMe show big patch that indicates the pits are growing.

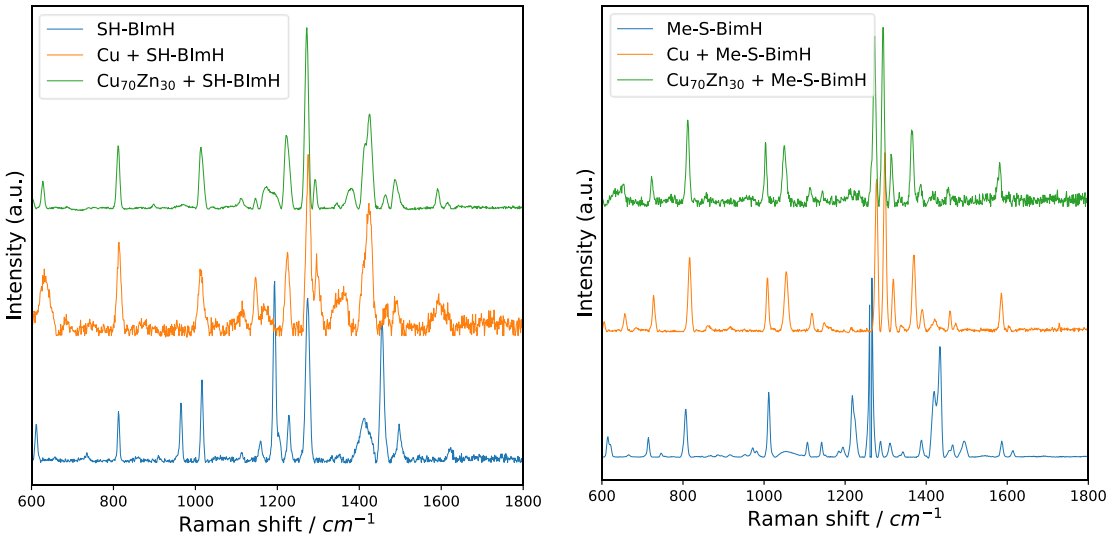

Figure 5.42 Raman spectrum of SH-BimH (left) and Me-S-BimH (right), inhibitor powder (bottom), pure Cu surface after 60 days' immersion with added 1mM inhibitor (middle) and $Cu_{70}Zn_{30}$ alloy surface after 60 days' immersion with added 1mM inhibitor (top).

Figure 5.42 shows another two inhibitors of SH-BimH-5OMe and SH-ImiH-4Ph, they both present on the surface and the intensity of the peaks are changed as well. **Figure A2.45** Raman spectrum of OH-Me-BimH powder (bottom), pure Cu surface after 60 days' immersion with added 1mM OH-Me-BimH (top). shows the peaks of inhibitor and substance on the immersed sample surface of OH-Me-BimH with Cu, the same effect is found.

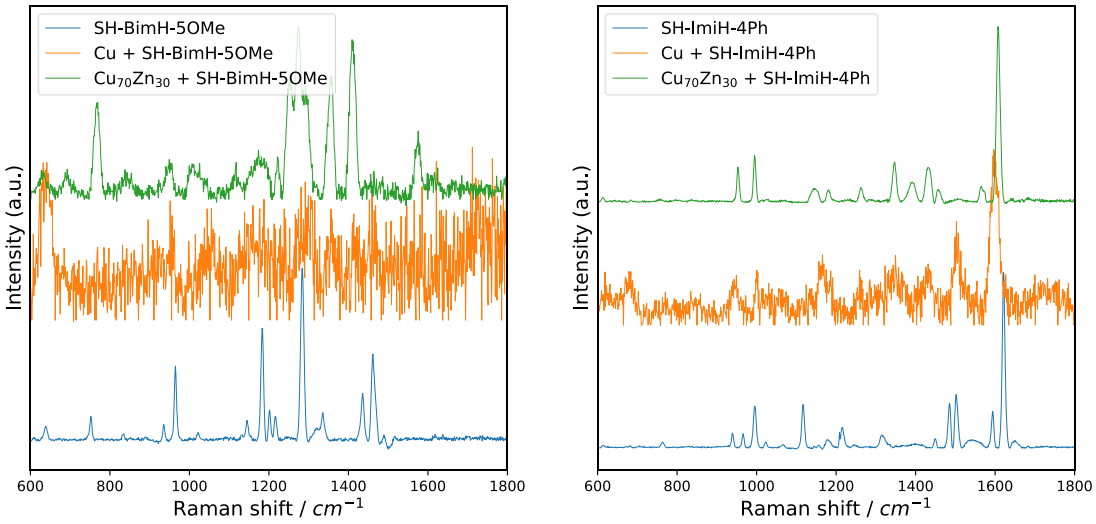

Figure 5.43 Raman spectrum of inhibitor SH-BimH-5OMe (right) and SH-ImiH-4Ph (left), inhibitor powder (bottom), pure Cu surface after 60 days' immersion with added 1mM inhibitor (middle) and $Cu_{70}Zn_{30}$ alloy surface after 60 days' immersion with added 1mM inhibitor (top).

5.4 Discussion and Conclusion

5.4.1 Discussion

Typical plug dezincification happens on $Cu_{70}Zn_{30}$ alloy, and ZnO covered most of the surface. Inhibition on $Cu_{70}Zn_{30}$ alloy is more efficient than the rest of the materials. SH-ImiH-4Ph shows excellent improvement not only in electrochemical measurements but also after 60 days' immersion tests. All inhibitors display better performance for $Cu_{70}Zn_{30}$ alloy than pure Cu, but the effective inhibitors are the same. The correlation of this parallel improvement should attribute to the same α-Cu phase on the surface. However, the better performance of inhibitors on alloy than that of pure material is complicated. As we illustrated in the introduction part, Cu_2O and ZnO will form on the surface, and the inhibition increases even the ZnO present on the surface. However, the inhibition of pure Zn shows no noticeable improvement after long immersion duration. These two results opposite conclusion in this view. The adhesion of metal-inhibitor compounds is exceptionally stable on $Cu_{70}Zn_{30}$ alloy; even after 3 minutes' rinse with ethanol in the ultrasonic base, the EDX detector can get sulfur's characteristic energy. Thus, the flocs appear on the surface of Zn, Cu and $Cu_{70}Zn_{30}$ alloy should be taken into consideration. The stable film of the metal-inhibitor complex on the surface attached to the surface, this complex is a mixture of different complexes, which show a better adhesion. As shown in SEM-EDX and Raman spectrums, the presence of S always appears on the local attacks

for both pure Cu and $Cu_{70}Zn_{30}$ alloy; the Raman spectrum confirmed the presence of inhibitor complexes on the surface. The local attacks will dissolve Cu and Zn; then, the ions will react with inhibitor close to them, the formation of the complexes will gather on the local attacks and patch the pits. This healing effect makes the inhibitors form monolayer to protect the surface and patch the pits to slow down the local attacks.

The corrosion behavior of $Cu_{30}Zn_{70}$ alloy is similar to that of pure Zn, and inhibition is slightly different. SH-BimH-5NH_2 still shows the best performance on $Cu_{30}Zn_{70}$ alloy, as same as pure Zn. However, the inhibitor power shows the improvement is decreasing. The presence of -SH group will conduct the adsorption on Cu; this is why this organic is selected. The Cu ions around the surface will react with Cu and remove it from the surface. This effect will decrease the protective effect from -NH_2 group. SH-ImiH-4Ph shows flower-like as same as the blank sample surface; this should attribute to stronger adsorption with Cu; it will react will Cu ions, which will assist the dissolution of Cu and leave Zn. This also proves that the Cu-inhibitor complex will not prefer to adhere to the Zn surface for protection; thus, the $Cu_{30}Zn_{70}$ alloy will be corroded like pure Zn. Besides, there are more flocs $Cu_{30}Zn_{70}$ alloy than that of $Cu_{70}Zn_{30}$ alloy.

The short- and long-term electrochemical measurements on $Cu_{70}Zn_{30}$ alloy, $Cu_{30}Zn_{70}$ alloy and the pure metals show remarkable correlations with immersion tests. In these experiments, both linear polarization resistance and impedance are conducted, the intercomparison assists in improving the stability of results. Significantly, the impedance always shows a similar result of linear polarization resistance; this shows the feasibility of LPR on inhibition measurements. The short-term tests should be the pre-select method for inhibition measurement, and long-term electrochemical tests will show the sustainability of the inhibition. With these two steps, most of the real effective inhibitors will be selected. Since some inhibitors will decrease resistance after five days, the measurements may last more than this duration. The immersion tests are valuable since electrochemical tests will not show the surface condition after a long period. This will assist in understanding the behavior of inhibitor, which can guide the further design of inhibitor.

5.4.2 Conclusion

The performance of inhibitors decreases in a sequence such as: $Cu_{70}Zn_{30}$ alloy > pure Cu > pure Zn > $Cu_{30}Zn_{70}$ alloy. $Cu_{70}Zn_{30}$ alloy shows a better interaction with inhibitors than that of pure Cu with one order of magnitude improvement of resistance and impedance. Moreover, the inhibition shows two groups of correlation: $Cu_{70}Zn_{30}$ alloy and pure Cu; $Cu_{30}Zn_{70}$ alloy and pure Zn. The inhibitors which work well on Cu have similar behavior on $Cu_{70}Zn_{30}$ alloy, and the inhibition power sequence is the same as well. Contrarily, SH-BimH-5NH_2 shows the best performance in both pure Zn and $Cu_{30}Zn_{70}$ alloy.

SH-ImiH-4Ph shows excellent inhibition for $Cu_{70}Zn_{30}$ alloy, there is almost no obvious corrosion injury during 60 days' immersion test. This should be a competitive inhibitor

for $Cu_{70}Zn_{30}$ alloy. SH-BimH, Me-S-BimH and SH-BimH-5OMe show a good inhibition as well.

SH-BimH-5NH_2 shows best inhibition on pure Zn and $Cu_{30}Zn_{70}$ alloy, this should be attributed to the presence of -NH_2 group which may interact with ZnO or Zn. The effect of the -NH_2 group on Zn and its alloys deserves further study.

The look of $Cu_{70}Zn_{30}$ alloy after immersion is different from that of pure Cu, a strong bonded white film appears on most of the sample immersed with the effective inhibitors. The complex bonds strongly on the sample surface and protects the surface as in pure Zn. This should be one of the reasons why the $Cu_{70}Zn_{30}$ alloy shows a better inhibition than pure Cu.

The analysis by SEM-EDX shows that the inhibitor complex gathered in some locations that had been attacked. Dezincification causes dissolution of Zn and offers Zn^{2+} ions to form a Zn-inhibitor complex which results in the gathering at the same location. A kind of repair-effect appears that eventually stops the local attack and improves the inhibition.

The previous two effects of inhibitors on $Cu_{70}Zn_{30}$ alloy are significant as they bring new ideas for exploring inhibitors. The synergistic effect between major elements on the surface and minor elements on the inhibitor could improve the inhibition effect on the alloys. For the case of $Cu_{70}Zn_{30}$ alloy, the major elements build the single α-brass structure and interact with inhibitors by forming a monolayer or polymolecular layers; this makes the major inhibition. Zn interaction with minor elements on the inhibitor resulting in the formation of a Zn-inhibitor complex, which bonds strongly on the surface strongly and gathers at the dezincification locations.

Chapter 6 Corrosion Inhibition of CuZr alloy – Influence of Structure

6.1 Characterization of alloys and electrochemical measurements in NaCl solution

6.1.1 Characterization of CuZr alloys

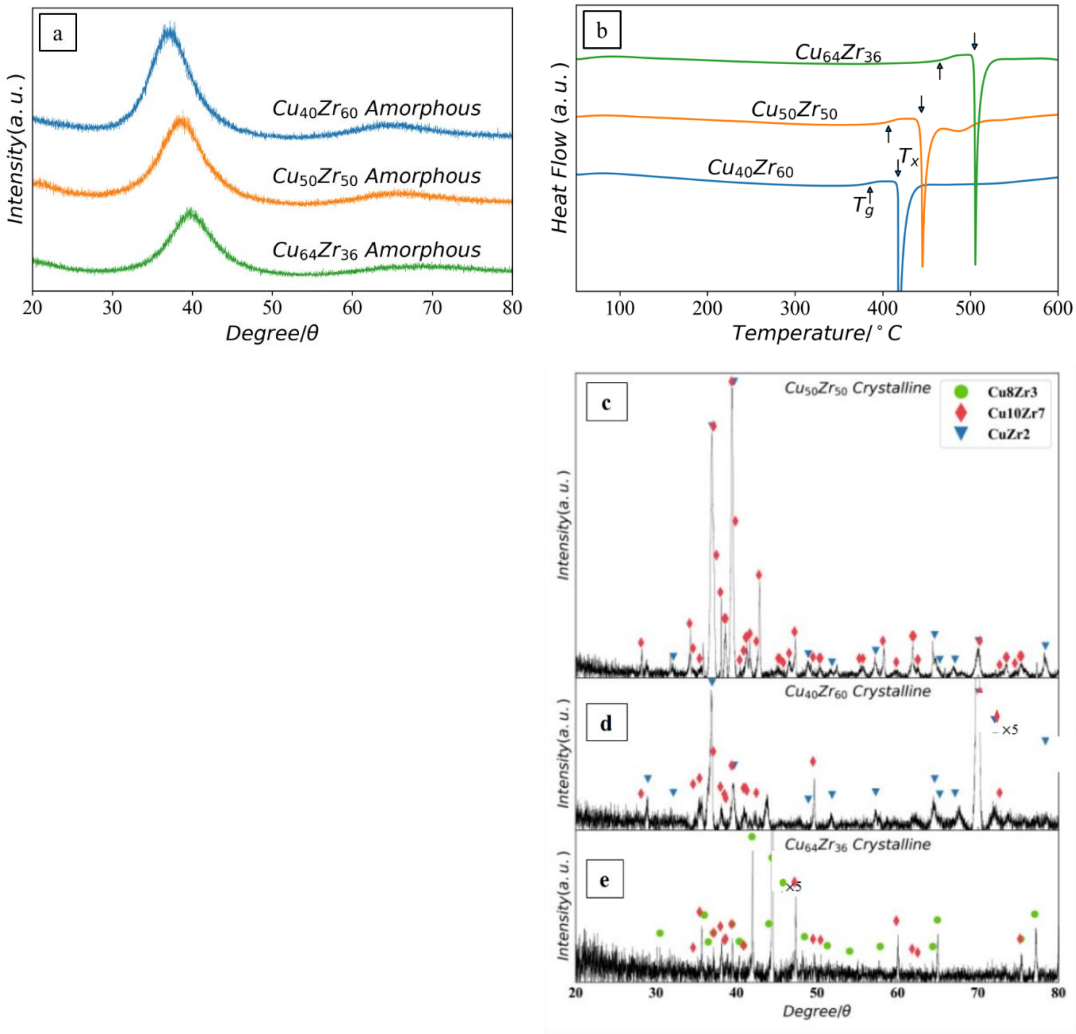

Figure 6.1 (a) X-ray diffraction spectra, (b) DSC curves of amorphous CuZr alloys and XRD spectra of (c) $Cu_{40}Zr_{60}$, (d) $Cu_{50}Zr_{50}$ and (e) $Cu_{64}Zr_{36}$ crystalline alloys.

Figure 6.1a shows the X-ray diffraction (XRD) patterns of the as-cast melt-spun amorphous samples with different Cu/Zr ratio. The three melt-spun alloys are amorphous as indicated by a typical broad amorphous peak and the absence of any detectable

crystalline peaks. **Figure 6.1**b shows the DSC curves of the amorphous CuZr alloys. The glass transition T_g and crystallization T_x temperatures increase with the Cu content. The temperature range of the supercooled liquid ($\Delta T = T_x - T_g$) is a signature of the glass-forming ability of the alloys, and it is similar in all compositions.

Figure 6.1 c-e show the XRD patterns of the as-cast crystalline samples with different Cu/Zr ratio. The main crystalline phase in $Cu_{40}Zr_{60}$ is identified to be $CuZr_2$, although it may also contain traces of $Cu_{10}Zr_7$. $Cu_{50}Zr_{50}$ is composed of $CuZr_2$ and $Cu_{10}Zr_7$, while $Cu_{10}Zr_7$ and Cu_8Zr_3 are identified in $Cu_{64}Zr_{36}$. All the identified phases are coherent with the phase diagram [120] provided in **Figure 6.2**. Furthermore, the phase diagram shows that even for a small addition of Zr the alloy will not be a single α-Cu phase; new CuZr phases are present. Considering that the α-Cu phase showed a quite effective inhibition, the corrosion inhibition on the crystalline alloys will highly depend on the interaction between the CuZr phases and inhibitors.

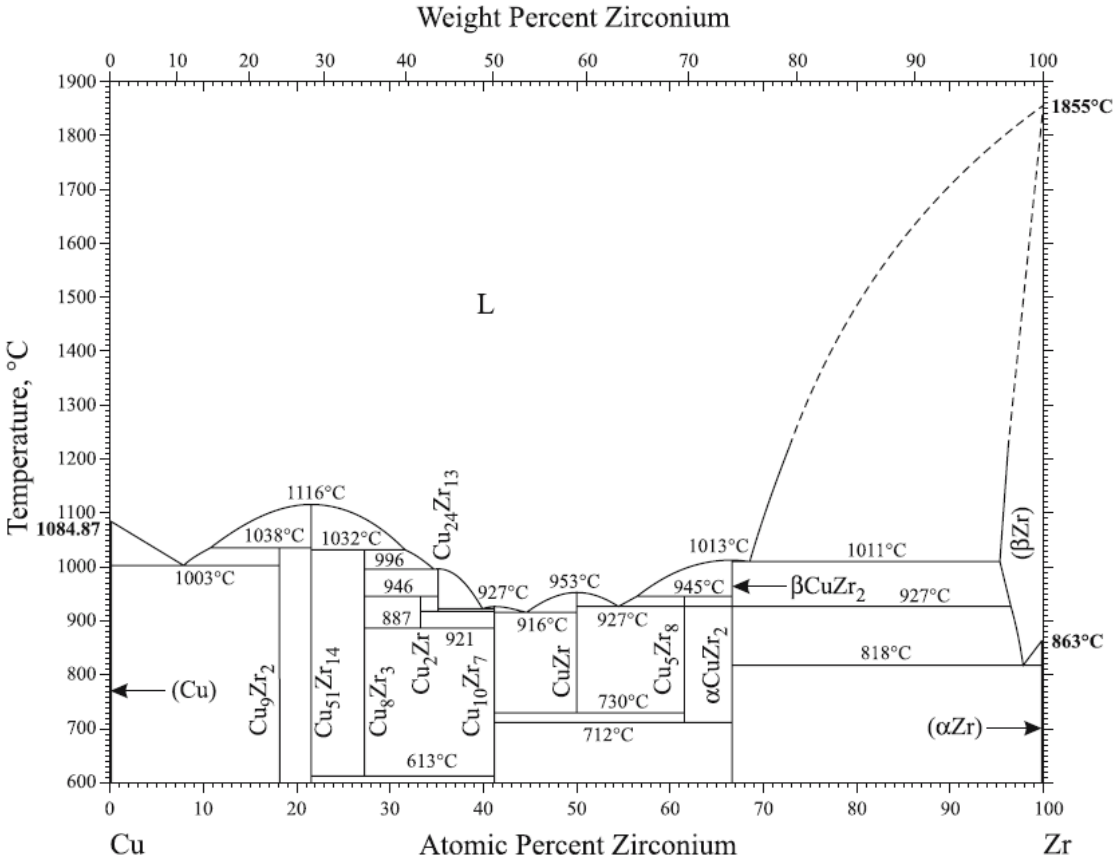

Figure 6.2 CuZr phase diagram, reproduced from Ref. [120].

6.1.2 Electrochemical measurements in NaCl solution

Figure 6.3 schematically shows the interface structure between electrode and electrolyte, based on the model postulated by Xu et al. [83]. The native oxide passive layer of the CuZr amorphous turns out to be ZrO_2 oxide, developed over a Cu-rich region above the amorphous matrix. The thickness of the ZrO_2 layer increases with the concentration of Zr and the formation of Cu-rich region is caused by the diffusion of Zr to the surface. Due to the ultrafast initial oxidation process, the ZrO_2 ultrathin passive film becomes the interface between sample surface and electrolyte. Additionally, ZrO_2 has a large dielectric constant, 10 to 23, and huge resistivity, 3.16×10^5 to 3.16×10^{10} Ωm, which provides protection for the material in a corrosive electrolyte. Introduction of inhibitors in the electrolyte is expected to induce a rapid physisorption and may result in eventual chemisorption on the surface. But this ultrathin film may need to be considered.

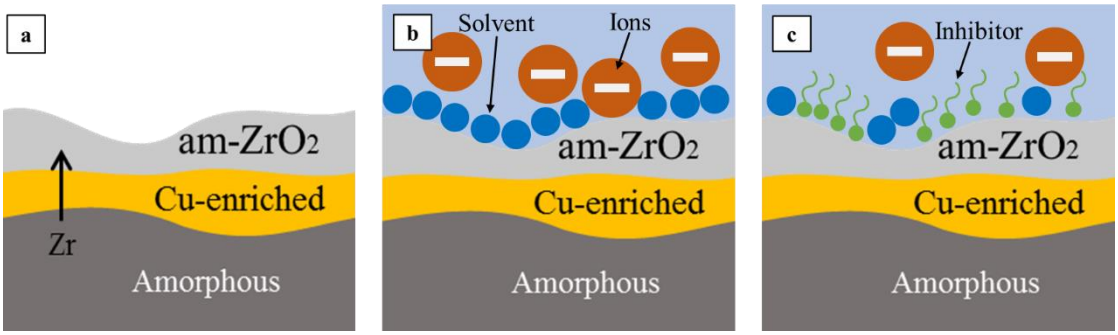

Figure 6.3 Schematic of interface structure between electrode and electrolyte. (a) Native oxide layer of CuZr amorphous alloy. (b-c) Simple model for the interface between CuZr amorphous and electrolyte (b) without and (c) with inhibitor in solution.

The developed dielectric film is inhomogeneous, as indicated in **Figure 6.3**a. This anodic oxide layer is well described by Young's model [121–123], which assumes that the nonstoichiometry of the oxide film generates an exponential variation of the conductivity with respect to the normal distance to the electrode. In this model, the measured impedance ($Z_{Y,oxide}$) is given by:

$$Z_{Y,oxide} = \frac{\lambda}{j\omega\varepsilon\varepsilon_0}\ln\left(\frac{1+j\omega\rho_0\varepsilon\varepsilon_0}{1+j\omega\rho_0\varepsilon\varepsilon_0\exp(-\delta/\lambda)}\right) \quad (1)$$

where $j=\sqrt{-1}$, ω is the angular frequency, ε is the dielectric constant of the oxide film, ε_0 is permittivity of vacuum, δ is the film thickness, ρ_0 is the resistivity at a position of spatial coordinate perpendicular to the electrode surface equal to 0, and λ is a material dependent parameter. According to Eq. (1), the Nyquist plot of a dielectric passive film shows a depressed semicircle, and for decreasing frequencies the impedance depends essentially on the resistivity of the film (**Figure 6.3**b). After adsorption of inhibitors, the impedance of the layer will increase, due to their dielectric nature (Figure 6.3c). Thus, the impedance modulus at 0.01 Hz, labelled as $|Z|_{0.01\ Hz}$, will be used as a reference value to

reflect the initial inhibition performance of the organic compounds. This initial performance allows us to select the most promising organic compounds and assess their performance on long-term tests.

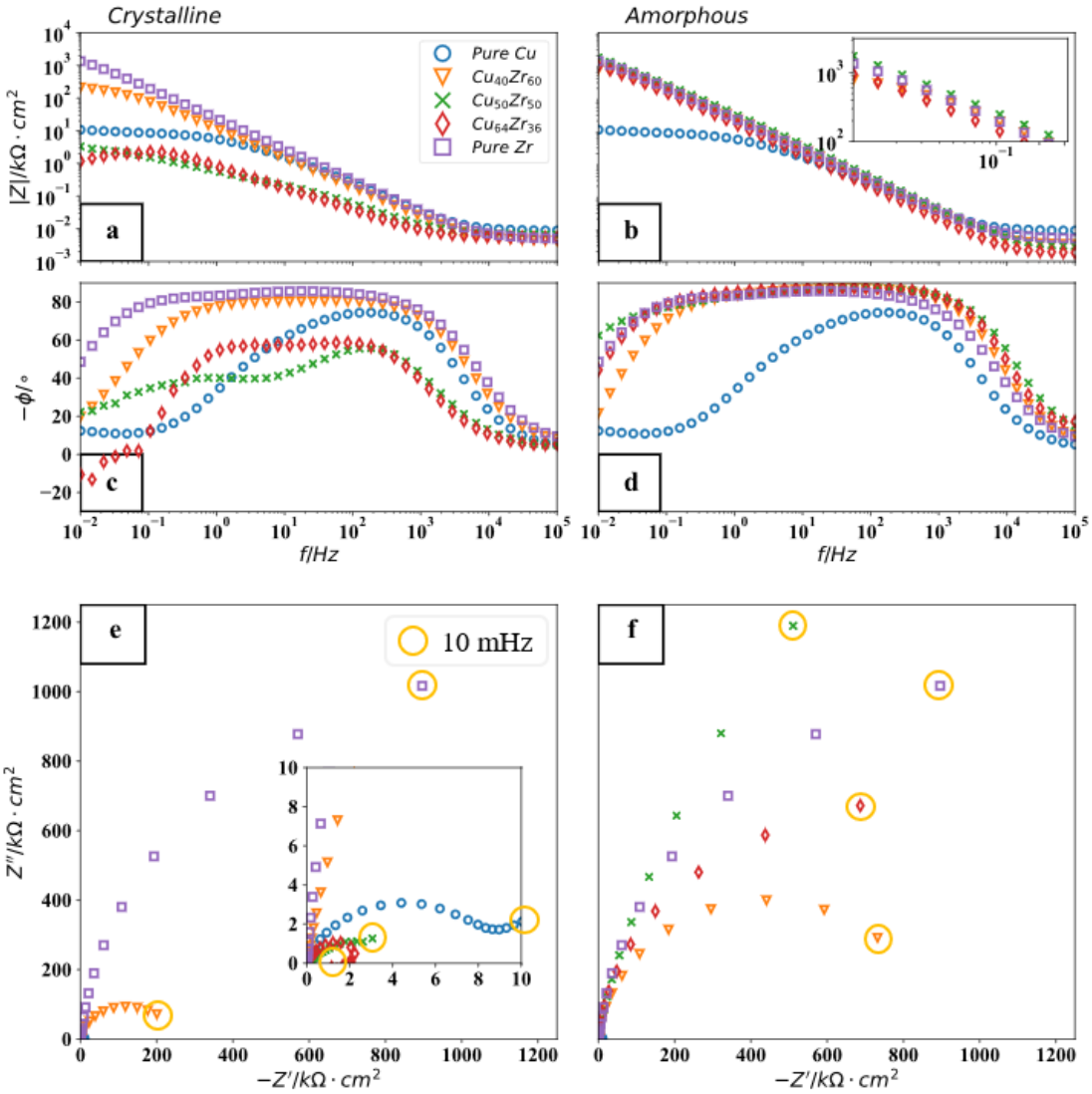

Figure 6.4 Electrochemical impedance spectra in the form of (a, b) Bode impedance magnitude plot, (c, d) phase angle plot, and (e, f) Nyquist plot recorded for crystalline (left) and amorphous (right) alloys as well as Cu and Zr metals in aqueous 3 wt.% NaCl solution after 1 h at the open circuit conditions.

Figure 6.4 shows the Bode and Nyquist plots of CuZr alloys as well as of Cu and Zr pure metals. Zr metal exhibits better protective characteristics than Cu metal, as evidenced by (i) a broad range of linear increase of impedance modulus with frequency and larger impedance values over the whole frequency range (**Figure 6.4**a); (ii) a broad range of frequency where phase angle is constant at values of about −80° indicating strong capacitive behavior (**Figure 6.4**c); and (iii) much larger diameter of the Nyquist plot

indicating much larger overall resistance (**Figure 6.4**e) [123]. Crystalline alloys, considered in **Figure 6.4**a, show reduced values of low frequency impedance as the Zr content decreases. $Cu_{40}Zr_{60}$ shows an impedance behavior close to that of pure Zr, but both $Cu_{50}Zr_{50}$ and $Cu_{64}Zr_{36}$ have impedances even lower than that of pure Cu. Analogously, the phase angle plots of $Cu_{50}Zr_{50}$ and $Cu_{64}Zr_{36}$ crystalline alloys reached a maximum at middle frequency range and then decreased to *ca.* −20° indicating the initiation of corrosion process (**Figure 6.4**c). This behaviour is attributed to the different crystalline phases present in these alloys (**Figure 6.1**c), with different corrosion resistance, as well as to the existence of preferential corrosion sites at grain boundaries. In contrast, the corrosion behaviour of the amorphous alloys (**Figure 6.4**b,d,f) is similar to that of pure Zr, showing strong capacitive behaviour (**Figure 6.4**b,d) and large semicircle (**Figure 6.4**f) as expected for the aforementioned Young's model.

Interestingly, the low frequency impedance of amorphous $Cu_{50}Zr_{50}$ is somewhat larger than that of pure Zr (inset of **Figure 6.4**b), while those of $Cu_{40}Zr_{60}$ and $Cu_{64}Zr_{36}$ are lower than that of pure Zr. According to the model presented in **Figure 6.3**, a larger Zr concentration should stimulate the development of the protective amorphous ZrO_2 dielectric layer. The fact that the equiatomic alloy shows the larger low frequency impedance after one hour seems to indicate that not only the Zr concentration is important for the creation of the ZrO_2 film, but also the atomic mobilities of Cu, Zr and O play an important role [88]. Given its smaller atomic size, Cu is known to have a large diffusivity in metallic glasses [124]. Thus, the development of the amorphous ZrO_2 layers in the Zr-rich amorphous alloys is probably delayed by the lower atomic mobility.

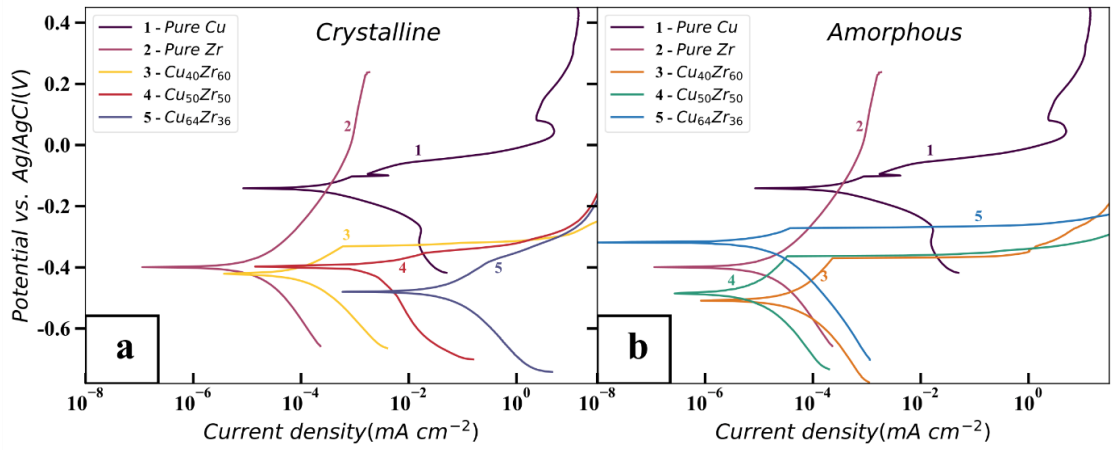

Figure 6.5 Potentiodynamic curves for Cu, Zr, and crystalline and amorphous Cu_xZr_{100-x} alloys in 3 wt.% NaCl. Quantitative electrochemical parameters are presented in **Table A3.1** to **Table A3.2**.

Figure 6.5 shows the potentiodynamic polarization curves of Cu and Zr in NaCl. In chloride solution copper shows a well-known curve with cathodic reaction related to reduction of oxygen and anodic reaction related to dissolution of copper as cuprous Cu(I)

species [64]. Current density increased starting from corrosion potential at −0.14 V up to an anodic peak at ~0 V when the formation of CuCl occurred [125,126]. At more positive potentials, the current density shortly decreased but then it increased again due to the formation of soluble cupric complexes [125,126]. In contrast, for Zr metal a rather broad passive range was established; following the E_{corr} at −0.40 V, passive range extended up to potentials above 0.2 V. **Table 4.1** and **Table 4.3** in the Supplementary material provide more data on the quantitative electrochemical parameters derived from the polarization curves.

All three crystalline alloys exhibit worse corrosion resistance than Zr metal and the curves resemble more to that of Cu. Regarding the alloy composition, the corrosion parameters deteriorate with decreasing Zr content, as evidenced by the increasing corrosion current density (**Table A3.7** and **Table A3.12**). The position of E_{corr} values is closer to that of Zr metal than that of Cu. However, compared to Zr metal, which shows a broad passive region, all crystalline and amorphous alloys show much narrower range between E_{corr} and abrupt increase in current density at more positive potentials. Amorphous alloys exhibit better performance than crystalline counterparts and smaller differences depending on Cu content than crystalline alloys (**Figure 6.5**, **Table A3.7** and **Table A3.12**).

6.2 Electrochemical and microscopy measurements in NaCl solution with added organic compounds - Short-term electrochemical results

6.2.1 $Cu_{40}Zr_{60}$

Polarization curves and quantitative electrochemical parameters derived from the polarization curves for $Cu_{40}Zr_{60}$ alloys are presented in **Figure 6.6** and **Table A3.7Table A3.8** in Appendix 3, respectively. The inhibition performance of all inhibitors is poor in the $Cu_{40}Zr_{60}$ crystalline phase, as dissolution initiates in the anodic branch at a similar potential, regardless the inhibitor. A more diverse behavior is observed in the amorphous samples, where several of them act as cathodic inhibitors as in the case of pure Zr.

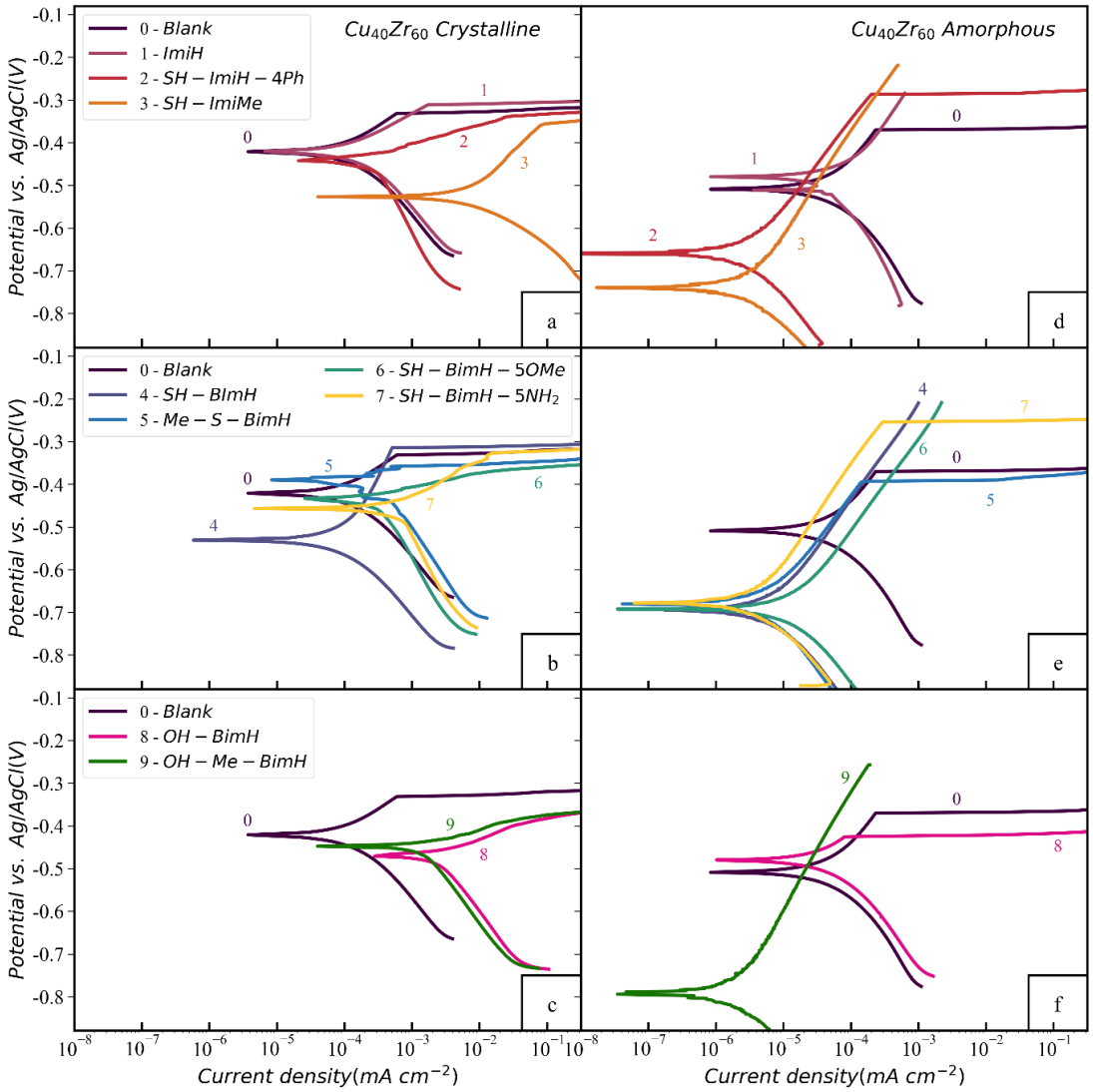

Figure 6.6 Potentiodynamic polarization curves of crystalline (left) and amorphous (right) $Cu_{40}Zr_{60}$ in 3 wt.% NaCl aqueous solution with and without 1 mM of different organic compounds: (top) imidazole derivatives, (middle) mercapto-benzimidazole derivatives, and (bottom) hydroxy-benzimidazole derivatives. Quantitative electrochemical parameters are presented in **Table A3.3 and Table A3.4**.

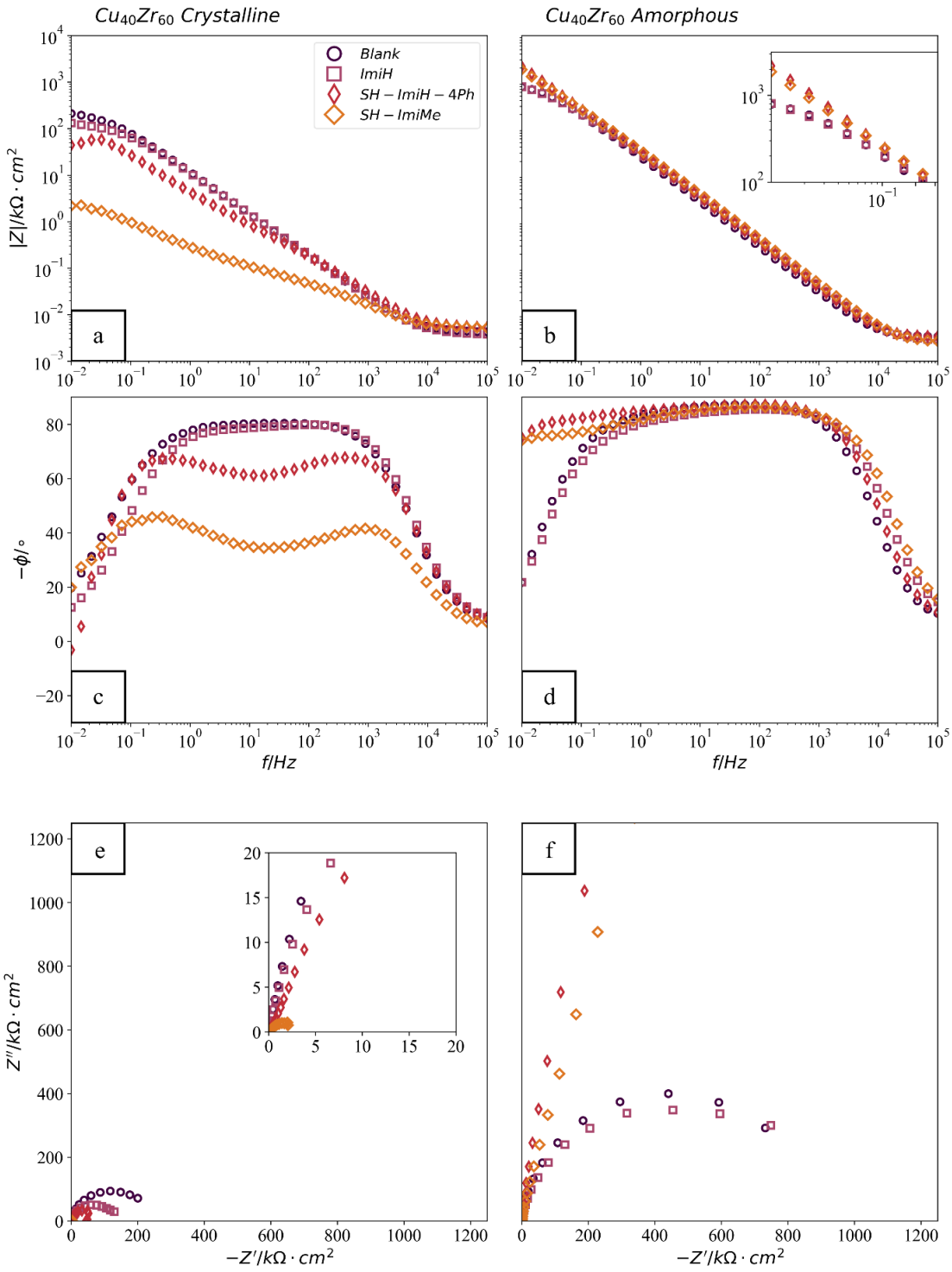

Figure 6.7. Electrochemical impedance spectra of $Cu_{40}Zr_{60}$ alloy in the form of Bode impedance plot, phase angle plot and Nyquist plot recorded for a), c), e) crystalline and b), d), f) amorphous alloys with or without addition of imidazole derivatives in aqueous 3 wt. % NaCl solution after 1 h at the open circuit conditions.

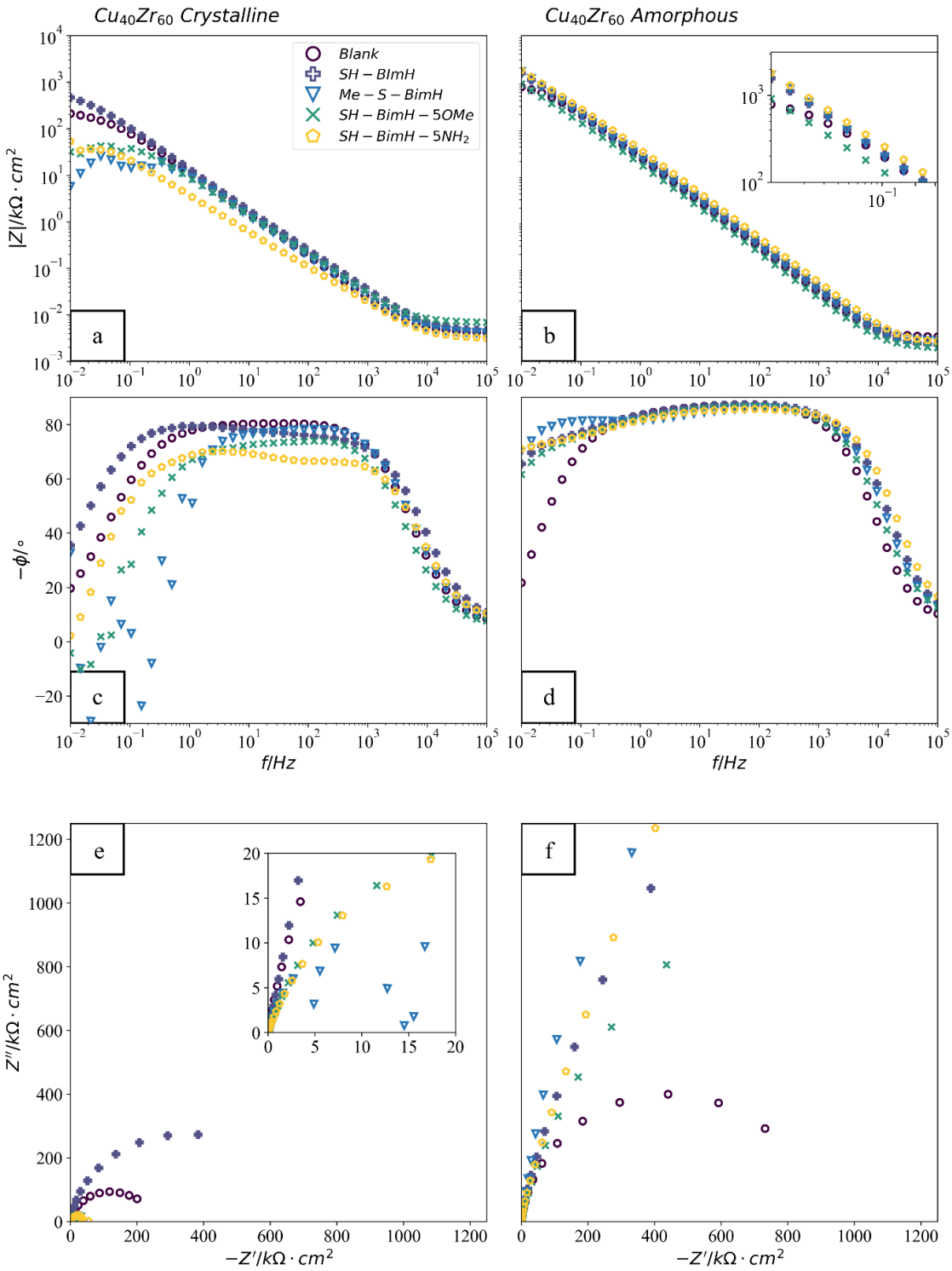

Figure 6.8. Electrochemical impedance spectra of $Cu_{40}Zr_{60}$ alloy in the form of Bode impedance plot, phase angle plot and Nyquist plot recorded for a), c), e) crystalline and b), d), f) amorphous alloys with or without addition of mercapto-benzimidazole derivatives in aqueous 3 wt. % NaCl solution after 1 h at the open circuit conditions.

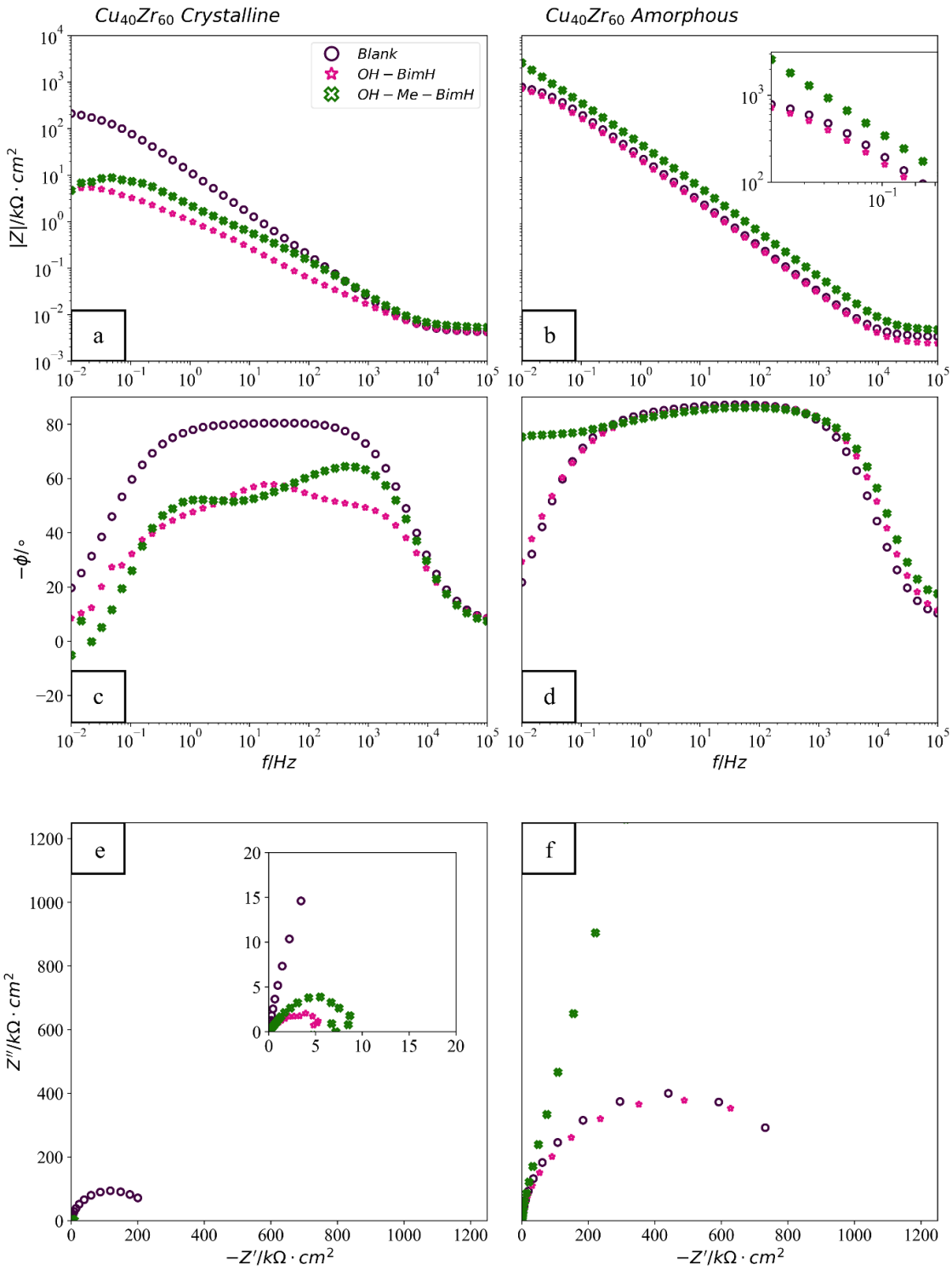

Figure 6.9. Electrochemical impedance spectra of $Cu_{40}Zr_{60}$ alloy in the form of Bode impedance plot, phase angle plot and Nyquist plot recorded for a), c), e) crystalline and b), d), f) amorphous alloys with or without addition of hydroxy-benzimidazole derivatives in aqueous 3 wt. % NaCl solution after 1 h at the open circuit conditions.

EIS spectra recorded for $Cu_{40}Zr_{60}$ crystalline and amorphous alloys after 1 h immersion in NaCl containing organic compounds are presented in **Figure 6.7** to **Figure 6.9**. The

comparison of $|Z|_{0.01Hz}$ again shows much larger impact of inhibitors on crystalline alloys than on amorphous alloys which show better corrosion performance (**Figure 6.10**).

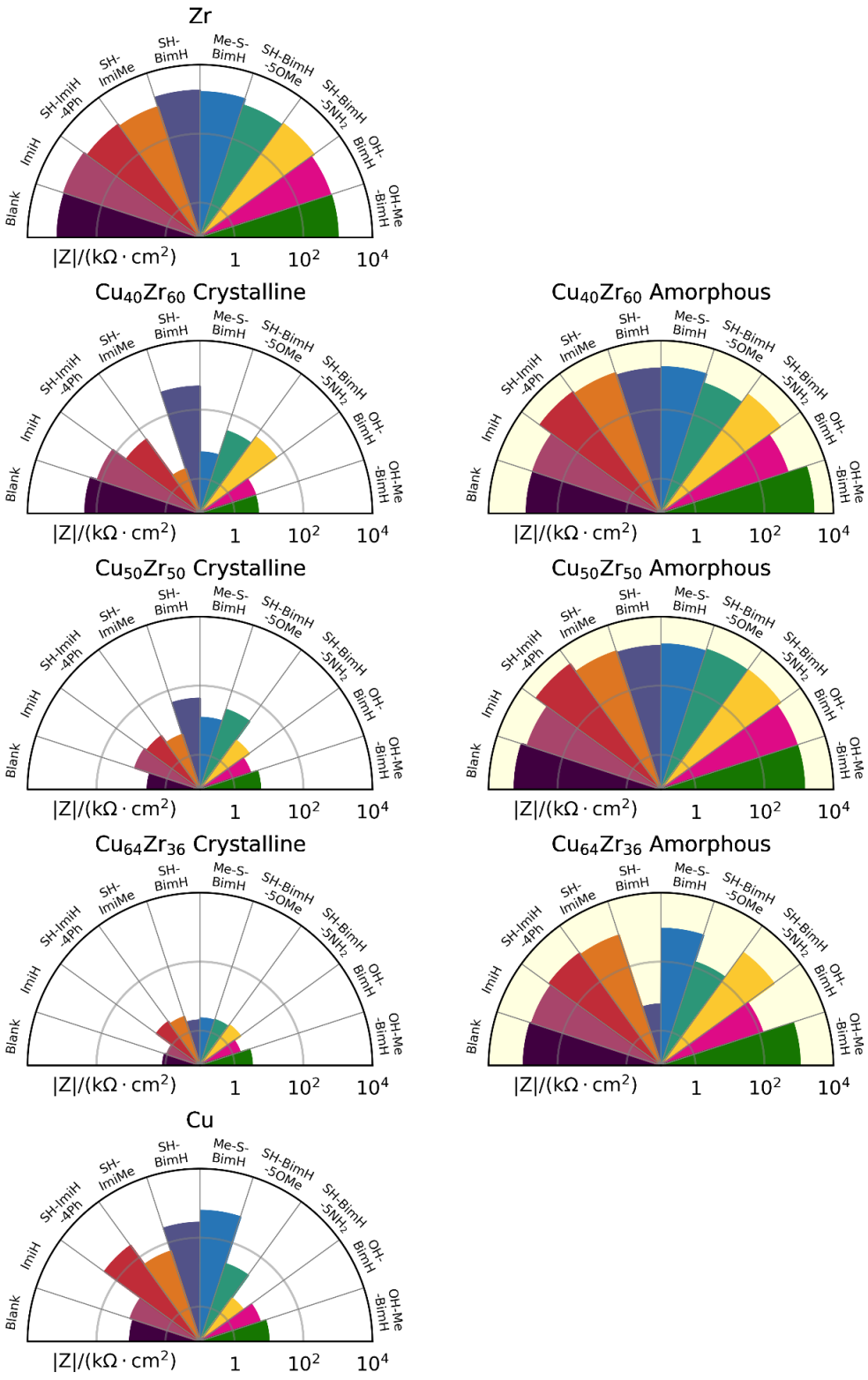

Figure 6.10 Polar graphs of impedance modulus at 0.01 Hz, measured after 1 h immersion, for Zr (top) and Cu (bottom) metals and crystalline (left) and amorphous (right) Cu_xZr_{100-x} alloys in 3 wt.% NaCl aqueous solution (blank) and in the presence

of different organic compounds added at 1 mM concentration. Note the logarithmic scale.

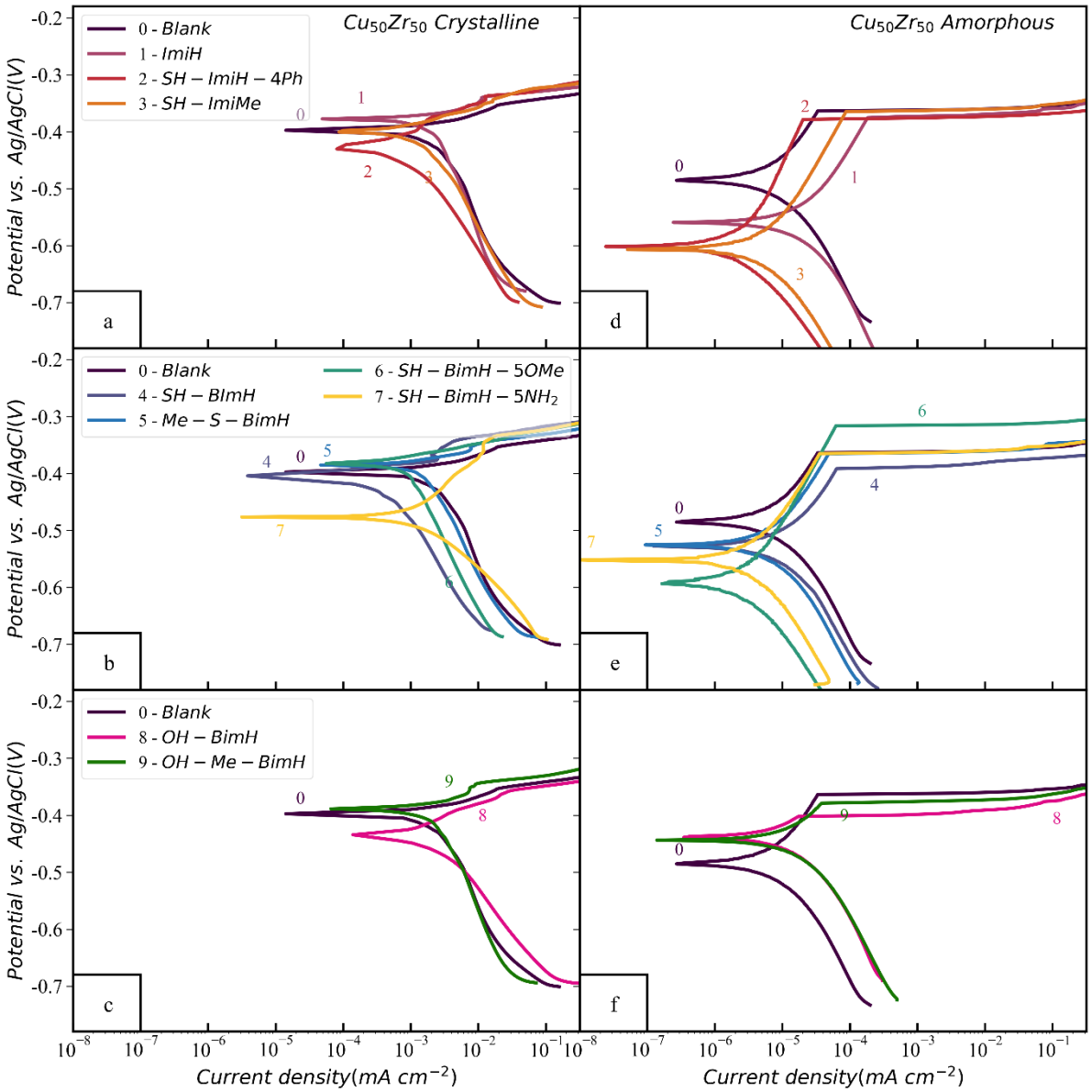

Figure 6.11. Potentiodynamic polarization curves of crystalline (left) and amorphous (right) $Cu_{50}Zr_{50}$ in 3 wt.% NaCl aqueous solution with and without 1 mM of different organic compounds: (top) imidazole derivatives, (middle) mercapto-benzimidazole derivatives, and (bottom) hydroxy-benzimidazole derivatives. Quantitative electrochemical parameters are presented in **Table A3.5** and **Table A3.6**.

6.2.2. $Cu_{50}Zr_{50}$

None among compounds tested shows any inhibition properties on crystalline $Cu_{50}Zr_{50}$ alloy. The potentiodynamic polarization curves are quite similar for solutions with and without organic inhibitors as shown in **Figure 6.11**. With inhibitors added, in the cathodic range the current density is slightly decreased but in the anodic range a fast dissolution of the alloy takes place, similar as in the absence of inhibitor. Amorphous $Cu_{50}Zr_{50}$ shows slightly better performance than the crystalline alloy. A passive range is induced on the sample, both in the non-inhibited and inhibited solutions. When adding imidazole-based derivatives, SH-ImiH-4Ph showed the best performance, shifting the E_{corr} more negative and decreasing the cathodic current density. Even more, pronounced inhibitive behaviour was observed for mercapto-benzimidazole derivatives, with SH-BimH-5OMe being the most efficient (**Figure 6.11**e) as it increased the pitting potential slightly. Both hydroxy-derivatives acted as corrosion activators (**Figure 6.11**f). Quantitative electrochemical parameters derived from the polarization curves for $Cu_{40}Zr_{60}$ alloys are presented in **Table A3.9**Table A3.10 in the Appendix 3.

EIS spectra recorded for $Cu_{50}Zr_{50}$ crystalline and amorphous alloys after 1 h immersion in NaCl containing organic compounds are presented in **Figure 6.12** to **Figure 6.14**. The comparison of short term EIS behaviour is given in **Figure 6.10**.

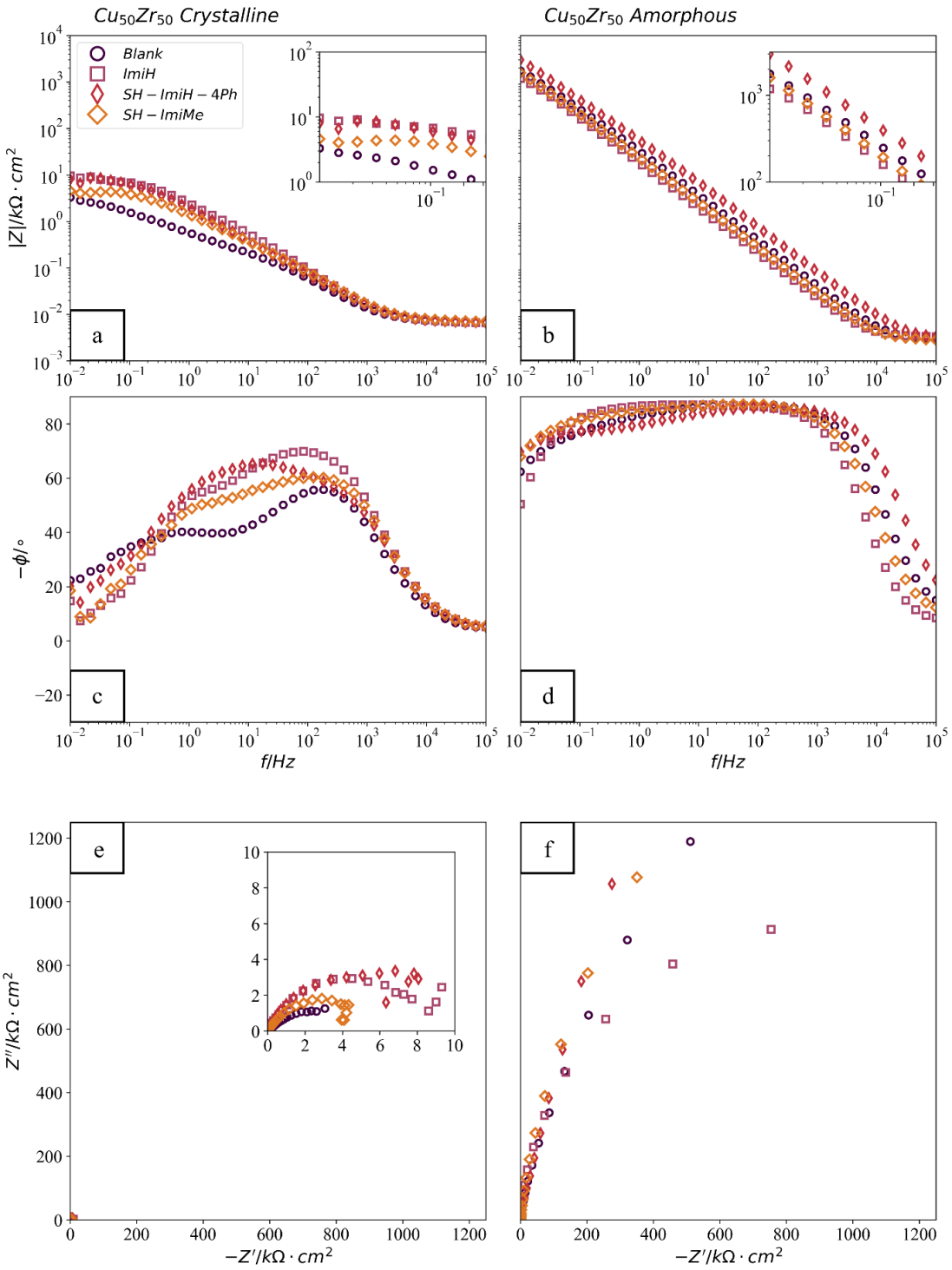

Figure 6.12. Electrochemical impedance spectra of $Cu_{50}Zr_{50}$ alloy in the form of Bode impedance plot, phase angle plot and Nyquist plot recorded for a), c), e) crystalline and b), d), f) amorphous alloys with or without addition of imidazole derivatives in aqueous 3 wt. % NaCl solution after 1 h at the open circuit conditions.

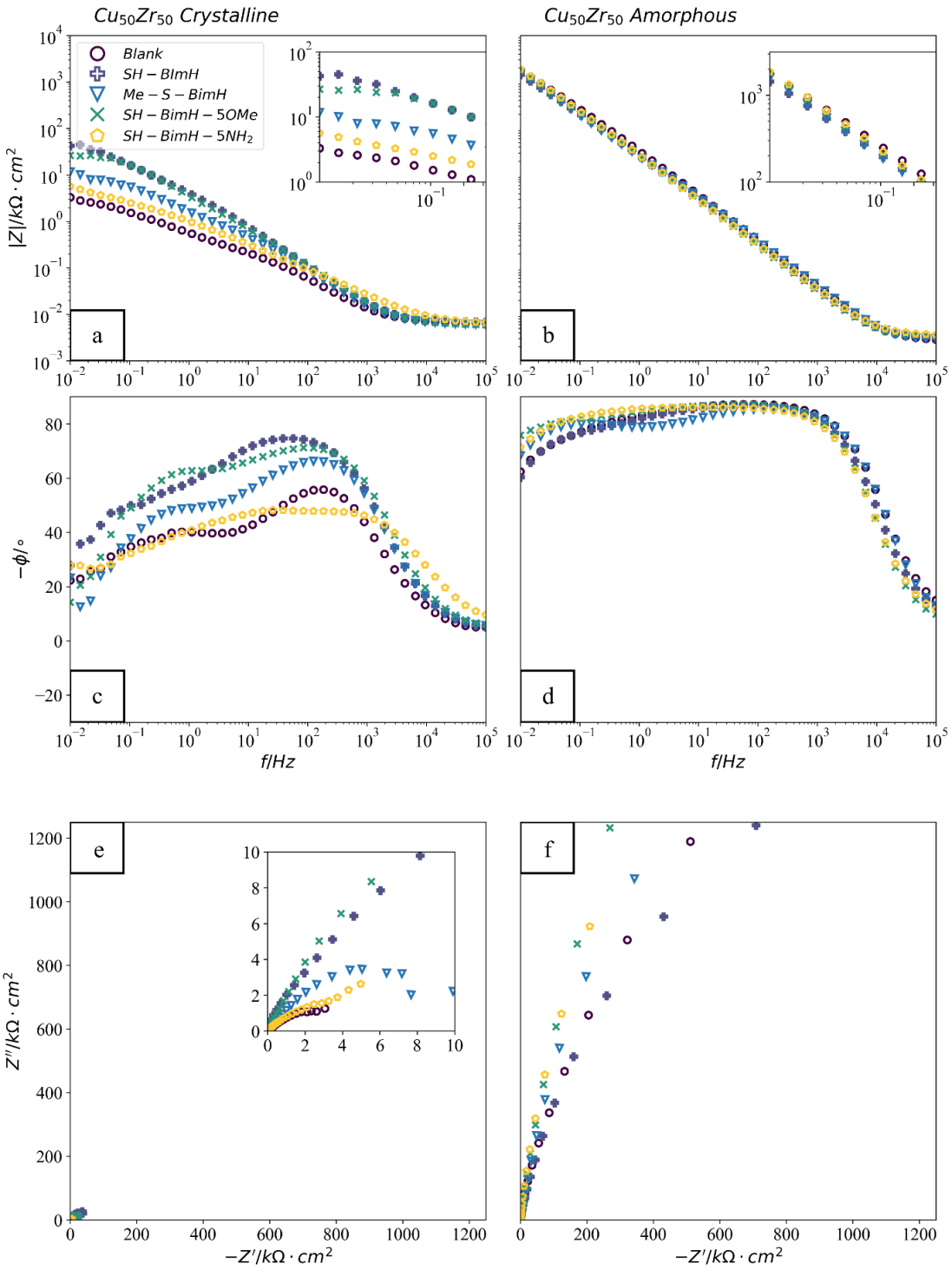

Figure 6.13. Electrochemical impedance spectra of $Cu_{50}Zr_{50}$ alloy in the form of Bode impedance plot, phase angle plot and Nyquist plot recorded for a), c), e) crystalline and b), d), f) amorphous alloys with or without addition of mercapto-benzimidazole derivatives in aqueous 3 wt. % NaCl solution after 1 h at the open circuit conditions.

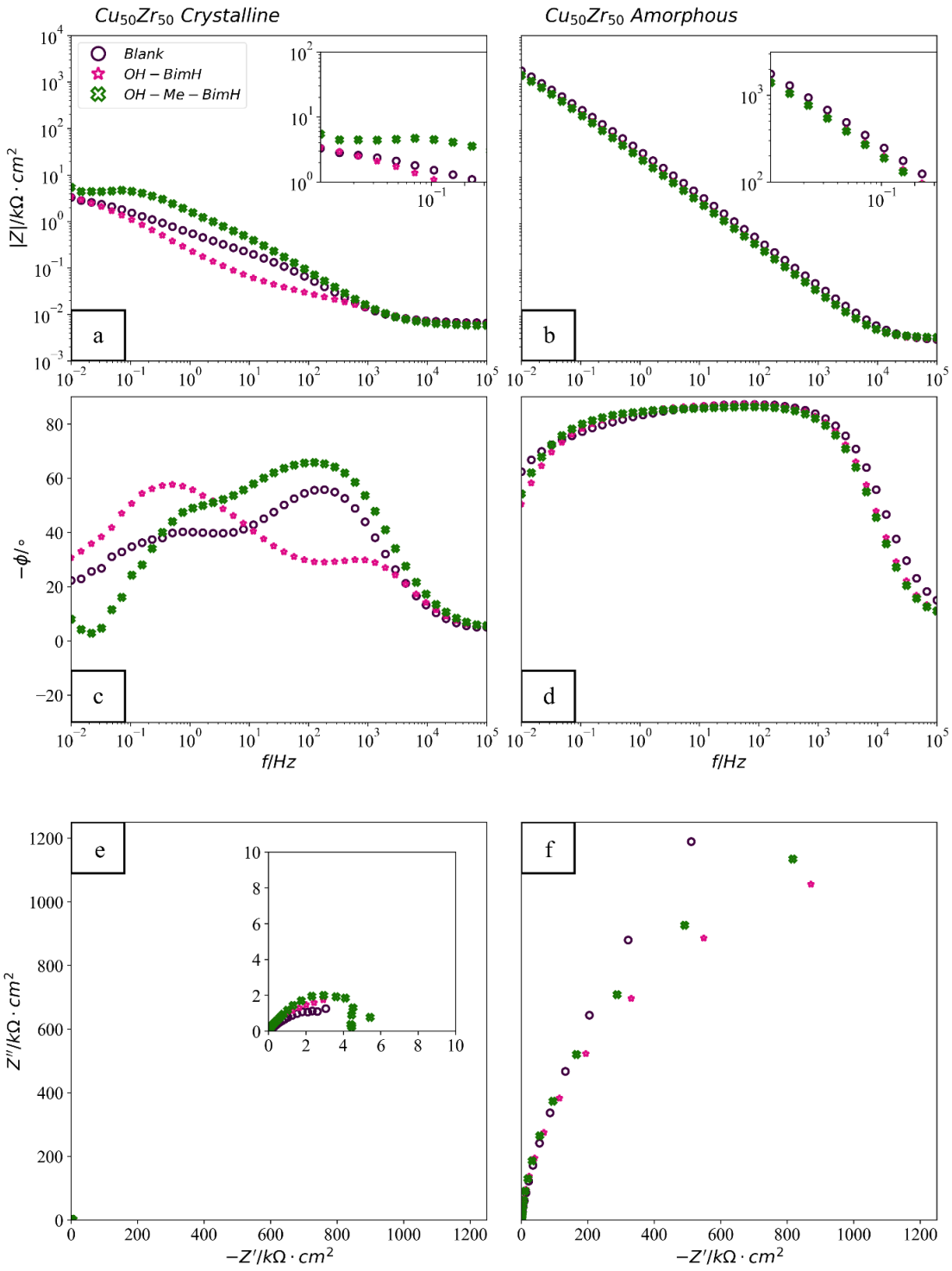

Figure 6.14. Electrochemical impedance spectra of $Cu_{50}Zr_{50}$ alloy in the form of Bode impedance plot, phase angle plot and Nyquist plot recorded for a), c), e) crystalline and b), d), f) amorphous alloys with or without addition of hydroxy-benzimidazole derivatives in aqueous 3 wt. % NaCl solution after 1 h at the open circuit conditions.

6.2.3. $Cu_{64}Zr_{36}$

Almost no inhibition effect was achieved with any of the compounds for crystalline or amorphous samples of $Cu_{64}Zr_{36}$ in 3 wt.% NaCl aqueous solution in the presence of the organic compounds studied, as shown in **Figure 6.15Figure 6.15Figure 6.15**. Quantitative electrochemical parameters derived from the polarization curves for $Cu_{40}Zr_{60}$ crystalline and amorphous alloys are presented in **Table A3.11**Table A3.12 in the Appendix 3. Due to the fast dissolution of materials, the Tafel parameters could not be determined for crystalline $Cu_{64}Zr_{36}$.

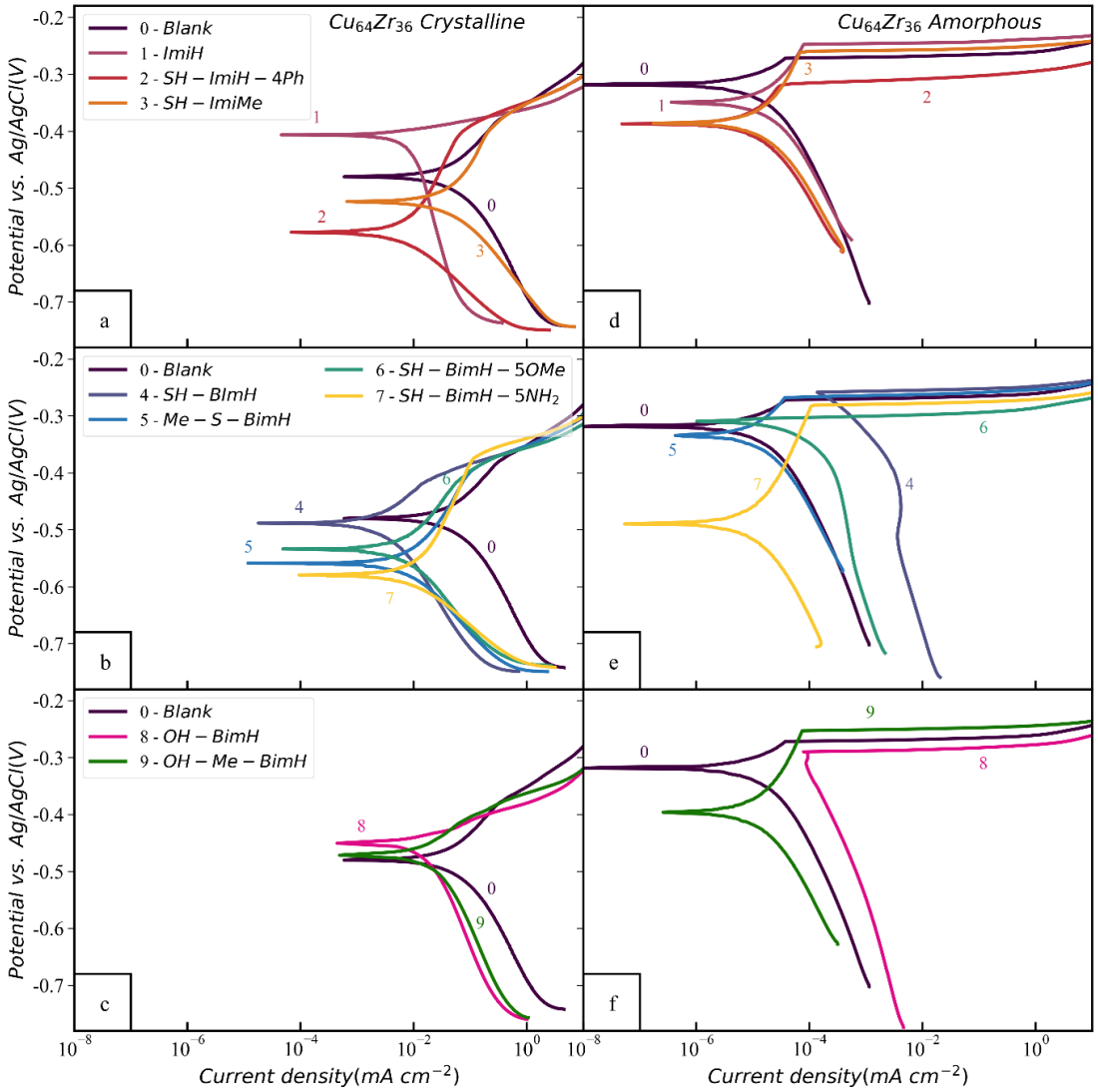

Figure 6.15. Potentiodynamic polarization curves of crystalline (left) and amorphous (right) $Cu_{64}Zr_{36}$ in 3 wt.% NaCl aqueous solution with or without added 1 mM concentration of different organic compounds: (top) imidazole derivatives, (middle) mercapto-benzimidazole derivatives, and (bottom) hydroxy-benzimidazole derivatives. Quantitative electrochemical parameters are presented in **Table A3.11**Table A3.12.

EIS spectra recorded for $Cu_{50}Zr_{50}$ crystalline and amorphous alloys after 1 h immersion in NaCl containing organic compounds are presented in **Figure 6.16** to **Figure 6.17**. The comparison of short term EIS behaviour is given in **Figure 6.10**.

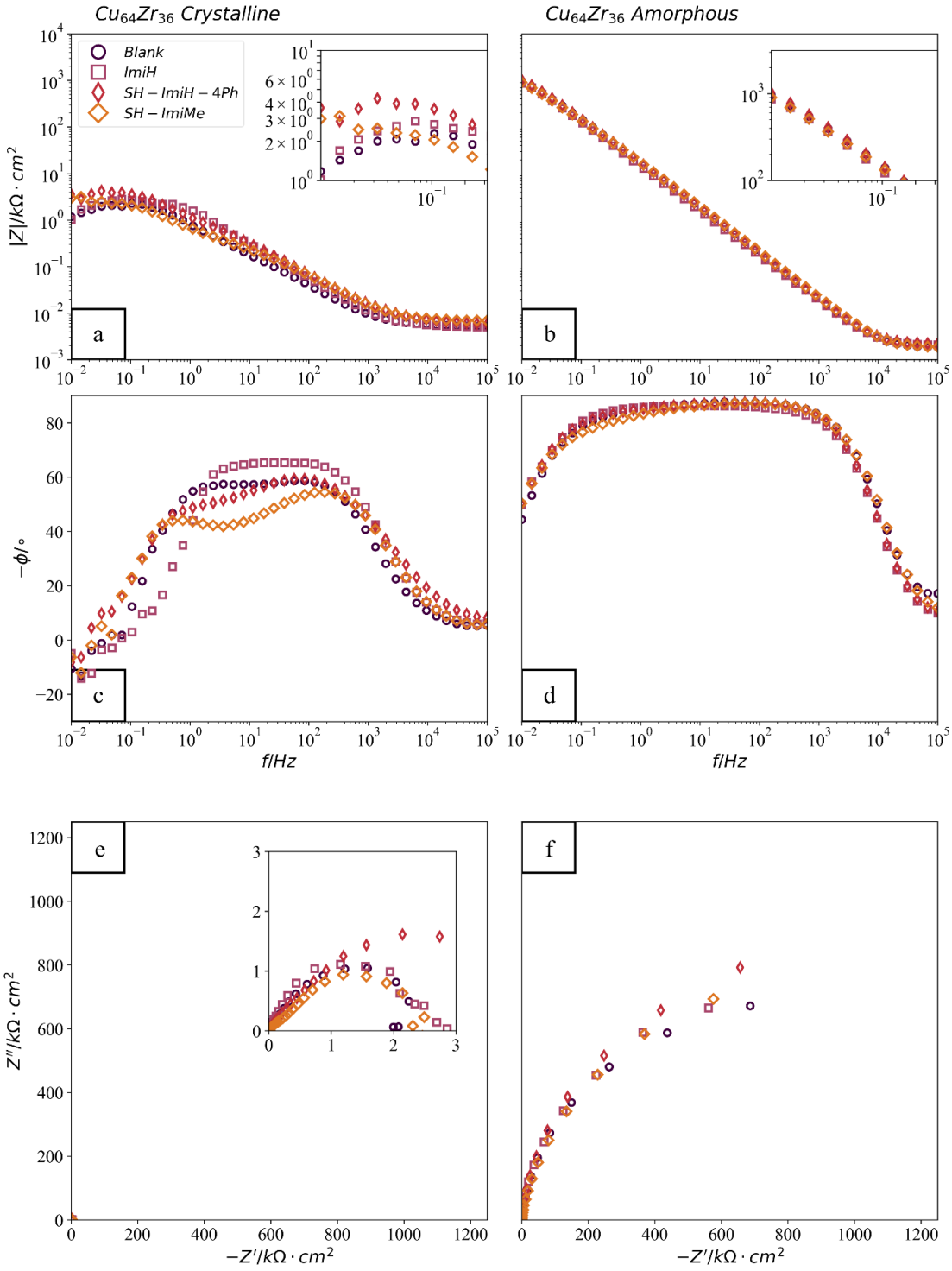

Figure 6.18 Electrochemical impedance spectra of $Cu_{64}Zr_{36}$ alloy in the form of Bode impedance plot, phase angle plot and Nyquist plot recorded for a), c), e) crystalline and b), d), f) amorphous alloys with or without addition of imidazole derivatives in aqueous 3 wt. % NaCl solution after 1 h at the open circuit conditions.

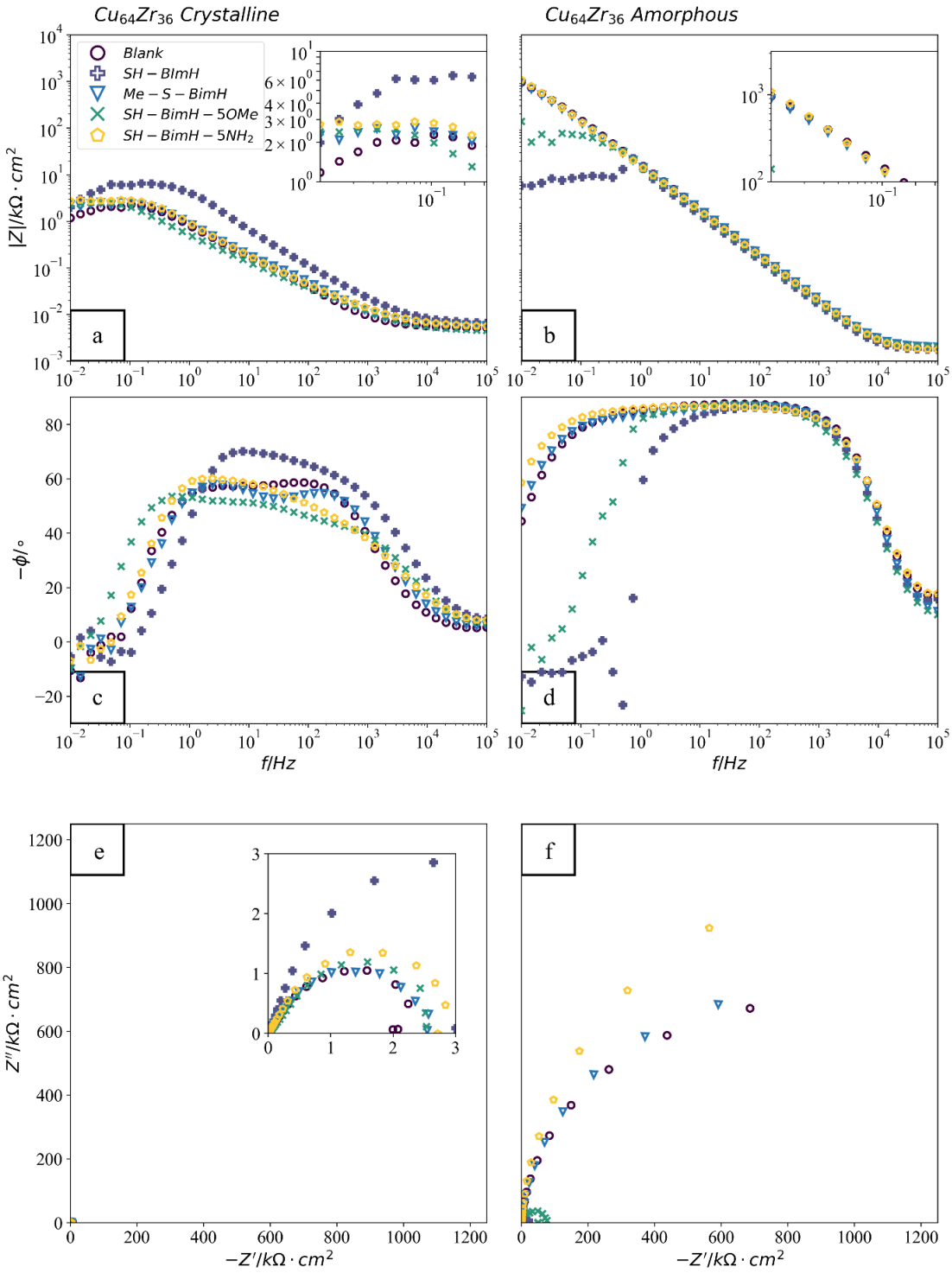

Figure 6.19 Electrochemical impedance spectra of $Cu_{64}Zr_{36}$ alloy in the form of Bode impedance plot, phase angle plot and Nyquist plot recorded for a), c), e) crystalline and b), d), f) amorphous alloys with or without addition of mercapto-benzimidazole derivatives in aqueous 3 wt.% NaCl solution after 1 h at the open circuit conditions.

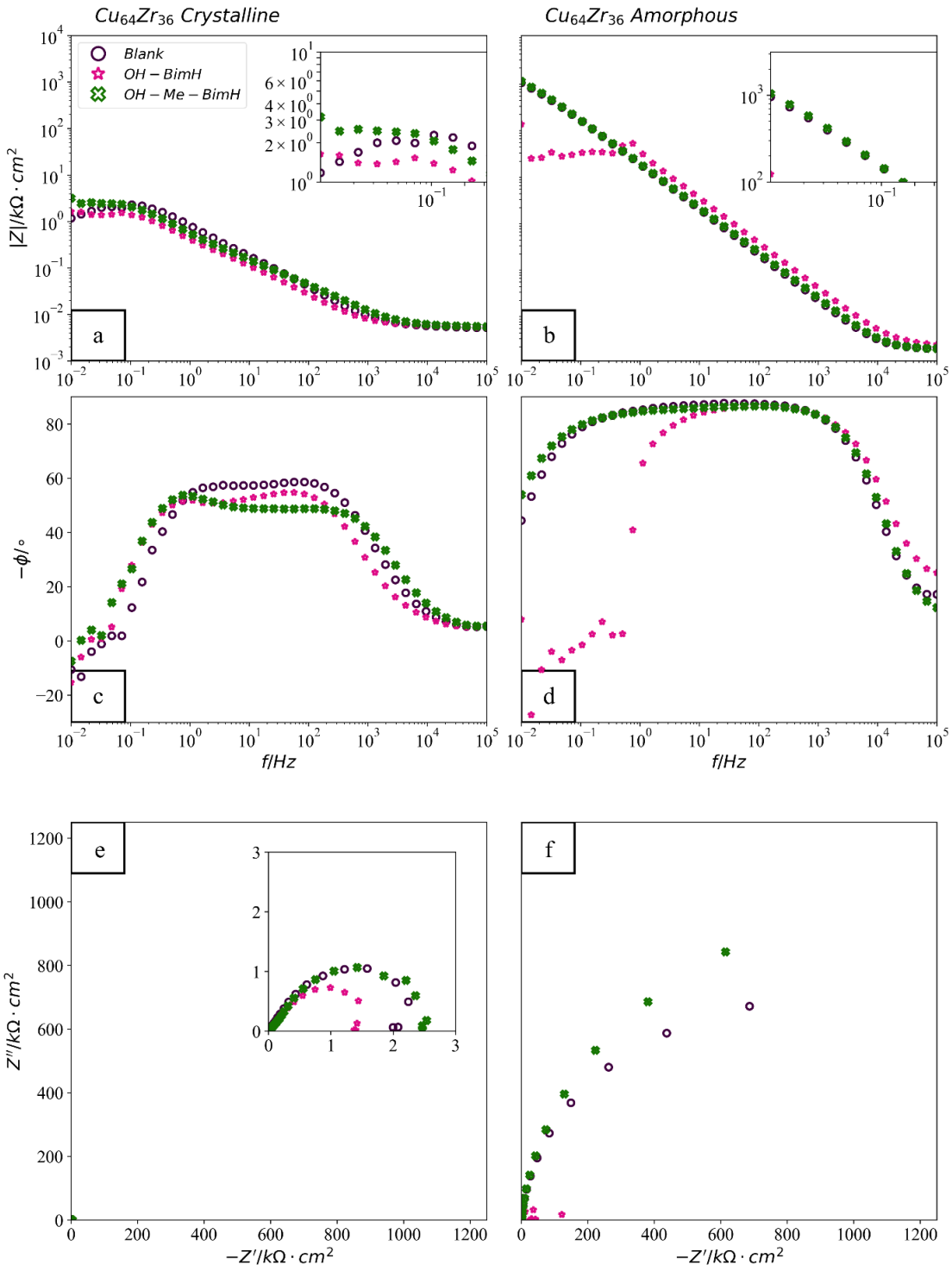

Figure 6.20 Electrochemical impedance spectra of $Cu_{64}Zr_{36}$ alloy in the form of Bode impedance plot, phase angle plot and Nyquist plot recorded for a), c), e) crystalline and b), d), f) amorphous alloys with or without addition of hydroxy-benzimidazole derivatives in aqueous 3 wt.% NaCl solution after 1 h at the open circuit conditions.

6.3 Electrochemical and microscopy measurements in NaCl solution with added organic compounds - Long-term electrochemical results

Time-resolved performance of the studied inhibitors was determined by measuring the EIS spectra of the crystalline and amorphous alloys over an immersion time of 120 h in the presence of the most promising inhibitors, chosen from the results of potentiodynamic polarization measurements (**Figure 6.6**, **Figure 6.11** and **Figure 6.15**). **Figure 6.21** displays in a compact way the long-term EIS behaviour of the alloys in blank NaCl and with added inhibitors selected for each alloy.

The $|Z|_{0.01Hz}$ of the amorphous $Cu_{40}Zr_{60}$ alloy in chloride solution was about two orders of magnitude larger than that of the crystalline alloy. In contrast, in the presence of SH-Imi-Me, SH-ImiH-4Ph and SH-BimH-5NH_2 the low frequency impedance values remained two orders of magnitude higher than those of the crystalline samples, and even showed a small but steady increase with time which may correspond to the formation of a passive film. The EIS findings are confirmed by direct observation of the samples after 5 days immersion tests. **Figure 6.22** shows the SEM images of the $Cu_{40}Zr_{60}$ samples in the presence of several inhibitors. The most protected surface was the one corresponding to the immersion in the presence of SH-ImiMe (Fig. **Figure 6.22**e). Other samples showed some corrosion damage.

The initial $|Z|_{0.01Hz}$ values in NaCl for crystalline $Cu_{50}Zr_{50}$ were smaller than those for $Cu_{40}Zr_{60}$, whereas for amorphous alloys were similar. However, amorphous $Cu_{50}Zr_{50}$ alloy deteriorated noticeably with time (**Figure 6.21**). The best inhibition effect was shown by SH-BimH-5NH_2, which kept a high and quite stable impedance in all measurements. The performance of SH-BimH-5OMe and SH-ImiH-4Ph decreased as a consequence of an incipient pitting process. **Figure 6.23** confirms that only the sample immersed in NaCl with added SH-BimH-5NH_2 (**Figure 6.23**e) was able to remain without apparent pitting after immersion over 5 days. Some inhibitors were not able to protect the alloys (SH-BimH-5OMe, SH-ImiH-4Ph, OH-Me-BimH) and after 60 h a sudden decrease is observed for blank (NaCl) and OH-Me-BimH samples (**Figure 6.21**). Following the breakdown, either the sample was partially dissolved or the surface was covered by corrosion products, and EIS measurements were no longer trustable.

The long-term EIS measurements confirmed a low corrosion resistance of $Cu_{64}Zr_{36}$ alloys, which quickly deteriorate with time (**Figure 6.21**), as evidences also by SEM images (**Figure 6.23**).

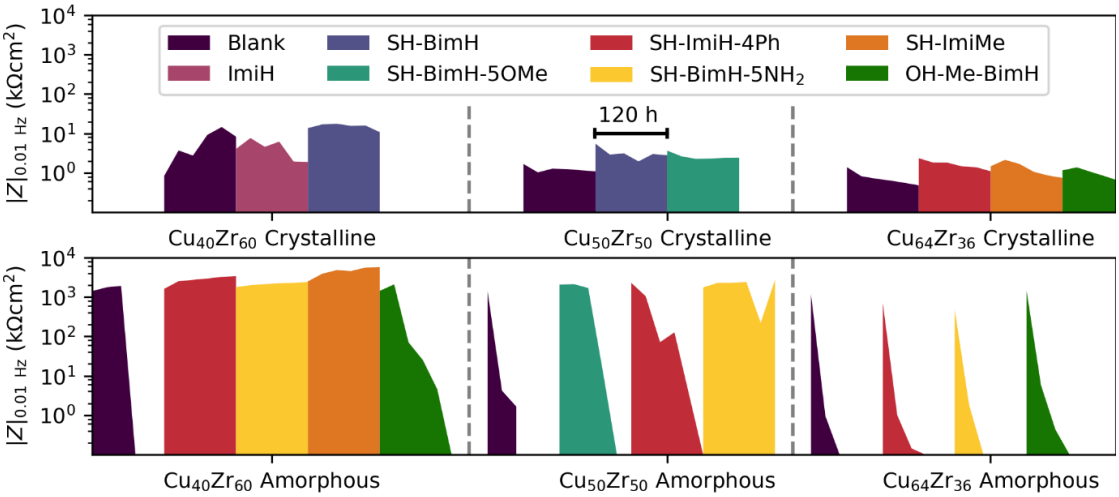

Figure 6.21. Long-term tests of the impedance modulus at 0.01 Hz in the presence of selected inhibitors. Each bar corresponds to the 120h period of testing of the alloy in the presence of the inhibitor in the 3 wt.% NaCl aqueous solution.

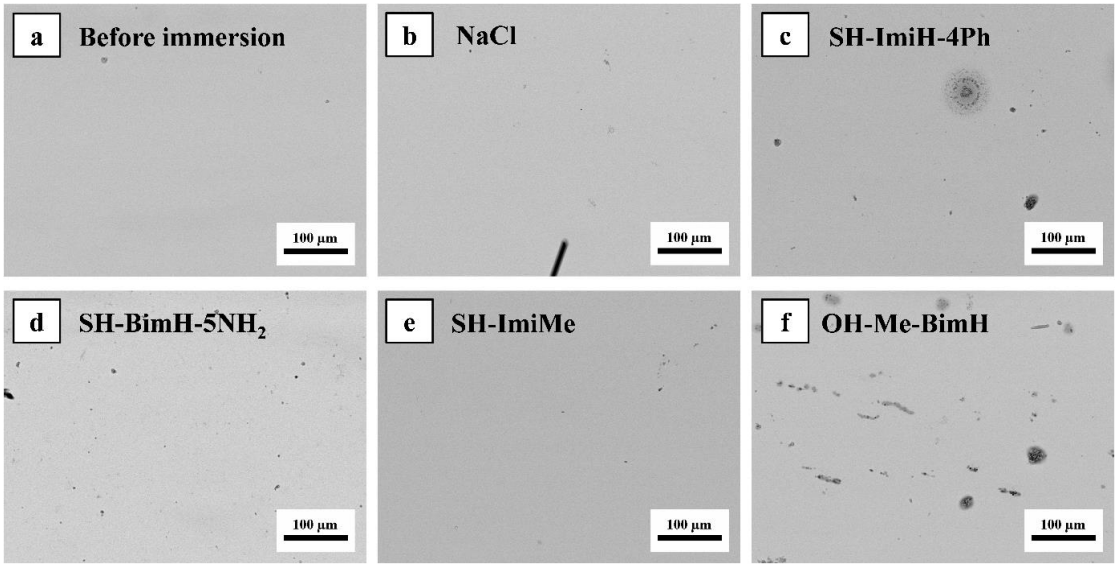

Figure 6.22. SEM images of $Cu_{40}Zr_{60}$ amorphous alloy (a) prior to immersion and after 5 days immersion in (b) 3 wt.% NaCl with added (c) SH-ImiH-4Ph, (d) SH-BimH-5NH_2, (e) SH-ImiMe, and (f) OH-Me-BimH.

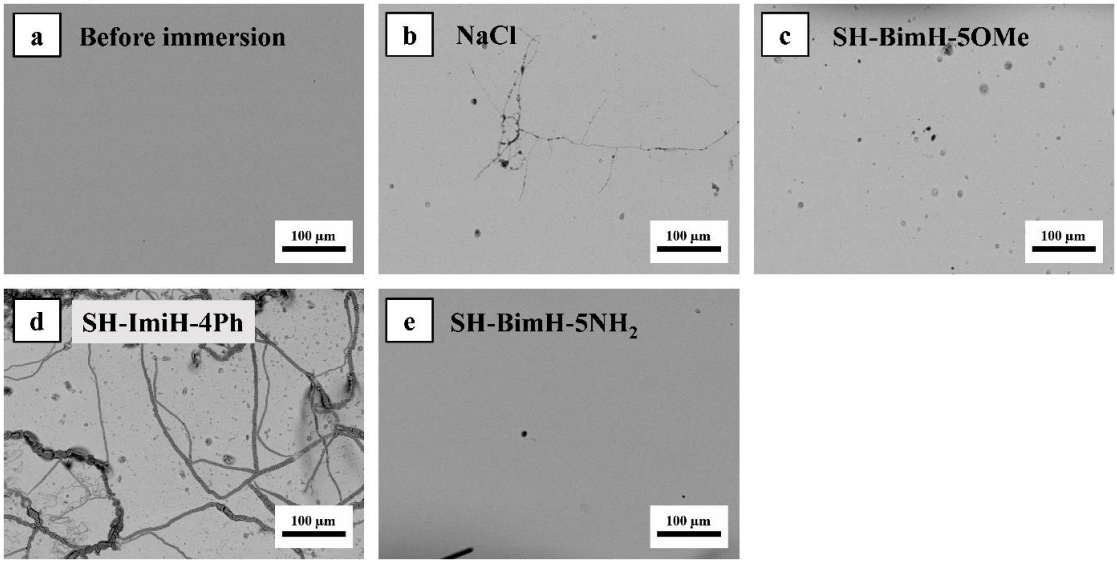

Figure 6.23. SEM images of $Cu_{50}Zr_{50}$ amorphous alloy (a) prior to immersion and after 5 days immersion in (b) 3 wt.% NaCl, and with added (c) SH-BimH-5OMe, (d) SH-ImiH-4Ph, and (e) SH-BimH-5NH_2.

6.4 Discussion and Conclusion

6.4.1 Discussion

The summarized comparison of impedance modulus at 0.01 Hz ($|Z|_{0.01\ Hz}$) of Cu and Zr metals as well as of all the tested crystalline and amorphous alloys after immersion for 1 h in 3 wt.% NaCl aqueous solution is shown in **Figure 6.10**; note the logarithmic scale. Some of the inhibitors appear beneficial for Cu, particularly the mercapto compounds Me-S-BimH, SH-BimH, SH-ImiH-4Ph and SH-ImiMe, as they increase the low frequency impedance by a factor of 10 or more compared to that in blank NaCl solution. Contrarily, the low frequency impedance of Zr in the presence of all tested inhibitors is very similar to that of blank Zr. It is therefore clear that the inhibition efficiency of the selected inhibitors on Cu is much higher than on Zr.

As for the crystalline alloys, the inhibition performance, deduced either from reduced current density or impedance modulus, of all the inhibitors is rather limited. Even the best case is not able to reach the low frequency impedance of non-inhibited Zr. The corrosion resistance of Zr is rapidly degraded by the addition of Cu. The corrosion resistance of all crystalline alloys in the presence of any organic compound is lower than that of bare Zr. As an example, the inhibition performance of Me-S-BimH, which is the best inhibitor for Cu and almost neutral for Zr, is clearly lower for all the crystalline alloys. This is attributed to the presence of different crystalline phases, and especially the corresponding grain boundaries which may become preferential sites for accelerated corrosion.

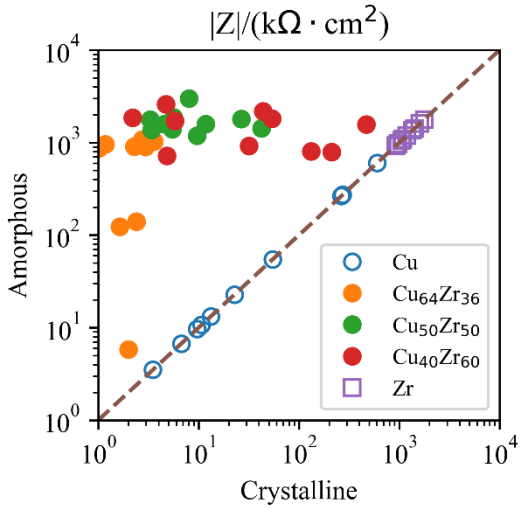

Figure 6.24. Impedance modulus at 0.01 Hz, measured after 1 h immersion, of the alloys in the presence of the organic compounds, tested as corrosion inhibitors for the studied alloys (●). For comparison, also the values for bare Zr (□) and bare Cu (○) are plotted on the dashed diagonal line.

Amorphous alloys, on the contrary, show a different behaviour (**Figure 6.10**). All three amorphous alloys show an intrinsic corrosion resistance similar to that of bare Zr. The performance of all tested compounds for amorphous $Cu_{40}Zr_{60}$ and $Cu_{50}Zr_{50}$ is similar. In both cases, SH-ImiH-4Ph increases substantially the low frequency impedance. SH-BimH, Me-S-BimH, SH-BimH-5NH_2, SH-ImiMe and OH-Me-BimH are also protective for $Cu_{40}Zr_{60}$. However, all organic compounds are neutral or even accelerate corrosion for $Cu_{64}Zr_{36}$. It is worth to mention that the phase diagram (**Figure 6.2**) shows that the stable phase for this composition is a solid solution of Cu_8Zr_3 and $Cu_{10}Zr_7$, present in the crystalline alloy (**Figure 6.1**e) [120]. Because the chemical composition of the CuZr amorphous alloy varies continuously, the atomic environments are changing and the intrinsic topology changes with them. According to the solute centred cluster model [127], slight changes in the atomic composition affect significantly the packing efficiency [128] and inhibitor−surface interaction responds to these changes, which is presumably critical for the corrosion resistance. Furthermore, by changing the Cu/Zr atomic ratio, the solute/solvent role of the atoms becomes inverted and both the glass structure and the atomic diffusivities must inevitably be different. These facts in turn affect the formation of the ZrO_2 rich layer on top of the amorphous surface (**Figure 6.3**). Zr-rich amorphous alloys may show lower diffusivities which initially may hinder the formation of the amorphous ZrO_2 film, but in the long term they eventually develop passivation layers that in combination with the proper inhibitors prevent localized corrosion. As the concentration of Zr is decreased, the ZrO_2 layer may be defective in Zr thus resulting in a mixed (CuZr)-oxide layer, which probably allows the removal of metallic ions. Thus, a Zr content equal or above 50% is needed for an adequate inhibition performance.

The comparison of the initial performance, measured after 1 h immersion, of the tested inhibitors for the crystalline and amorphous phases is summarized in **Figure 6.24**. The inhibitor performances for bare Cu and Zr metals are shown on the diagonal, because bare metals lack the amorphous phase. It is clearly evident that (1) all the tested amorphous alloys show a much better corrosion resistance than their crystalline counterparts in the presence of inhibitors and that (2) amorphous $Cu_{40}Zr_{60}$ and $Cu_{50}Zr_{50}$ perform better than amorphous $Cu_{64}Zr_{36}$, in line with the aforementioned argument of the importance of the

high content of Zr in alloys for corrosion resistance. In view of the saturation of the low frequency impedance for all the considered inhibitors it is therefore reasonable to conclude that the main factor controlling the corrosion resistance of the alloys is the Zr-rich (or at least equiatomic) amorphous structure, the effect of the inhibitor being secondary.

It is also worth to mention that the initial performance of the inhibitors is not sufficient to predict the long-term behaviour of the corrosion rate for the alloys. **Figure 6.21** shows that the long-term corrosion resistance degrades in all amorphous alloys except in $Cu_{40}Zr_{60}$ in the presence of SH-ImiH-4Ph, SH-BimH-5NH_2 and SH-ImiMe, and in $Cu_{50}Zr_{50}$ in the presence of SH-BimH-5NH_2. SH-BimH-5NH_2 is, thus, the most effective inhibitor, provided the Zr concentration is high enough (≥ 50%). Of all the tested compounds, this was the single one containing the amino group. It is noteworthy that SH-BimH-5NH_2 does not perform well for bare Cu, although it was computed that interaction between the amino group and Cu is stronger than with Au and Ag [129]. Besides, there is evidence of formation of $ZrNH_3$ on annealing [130], which suggests some affinity of Zr for the amino group. This suggests that the good performance on Zr-rich alloys is consequence of the interaction of the amino group with Zr atoms.

6.4.2 Conclusions

The inhibition performance of imidazole, mercapto-benzimidazole and hydroxy-benzimidazole derivatives on CuZr crystalline and amorphous alloys was studied. We used the impedance modulus at 0.01 Hz, measured after 1 h immersion, as a measure of the initial inhibitor performance. On the basis of this initial evaluation we selected the promising compounds for long-term tests. Amorphous alloys showed always a higher corrosion resistance than their crystalline counterparts.

The corrosion resistance of crystalline alloys is substantially lower than that of bare Zr. It is also much lower than that of Cu in the presence of efficient inhibitors, such as 2-(methylthio)benzimidazole (Me-S-BimH), 2-mercaptobenzimidazole (SH-BimH) or 2-mercapto-4-phenylimidazole (SH-ImiH-4Ph). This fact is attributed to the coexistence of several intermetallic phases with different corrosion resistance and/or the reduced corrosion resistance of dislocations and grain boundaries in the studied alloys. The addition of corrosion inhibitors did not improve the corrosion resistance of the crystalline CuZr alloys, even those which showed a protective effect in bare Cu.

Amorphous alloys showed a good initial corrosion resistance even without inhibitors, similar to that of bare Zr. In alloys with high Zr content (equal or above 50 at.%), the corrosion resistance is increased by the two tested mercapto-imidazole based inhibitors and all tested mercapto-benzimidazole based inhibitors. These data show that the homogeneous surface structure of amorphous alloys is much less prone to corrosion, and

the tested corrosion inhibitors even improve it to some extent. However, the increase of the low frequency impedance modulus due to the presence of inhibitors tends to saturate regardless the organic compound in solution, showing that the determinant factor in the corrosion resistance is the smooth surface topology of amorphous alloys and the stability of the oxide layer. Furthermore, the long-term corrosion resistance degrades except in $Cu_{40}Zr_{60}$ in the presence of SH-ImiH-4Ph, SH-BimH-5NH_2 and SH-ImiMe, and in $Cu_{50}Zr_{50}$ in the presence of SH-BimH-5NH_2. Therefore, 5-amino-2-mercaptobenzimidazole is the most promising corrosion inhibitor in CuZr amorphous alloys. This result advises to deepen the study of the surface interaction of the amino group with these materials.

Chapter 7 Conclusion

The determination of the performance of corrosion inhibitors on materials is a complex problem due to the mixed influence of surface condition, inhibitor-surface interaction and environmental conditions. The conducted research offers some understanding on the corrosion mechanism and resistance after inhibitor application. Imidazole derivatives were chosen as a potential inhibitor for copper alloys due to its diverse performance on pure Cu. Previous surface oxidation, defects on the surface, and inhibitor functional group are found to be the most significant factors that influence inhibition. A kind of healing effect is also found.

The inhibition of the studied molecules on pure Cu and $Cu_{70}Zn_{30}$ alloy shows similar behavior. SH-ImiH-4Ph performs as the best inhibitor, while ImiH and SH-ImiMe from imidazole derivatives could not improve corrosion resistance. Mercapto-benzimidazole derivatives inhibit pure Cu except for SH-BimH-5NH_2. Since α-Cu is the phase of these two materials, this indicates that the presence of the same inhibitor should result in similar inhibition effects on same metallic phase. However, all inhibitors display better performance on $Cu_{70}Zn_{30}$ alloy than pure Cu. The healing effect appears with some inhibitors on pure Cu, Zn and CuZn alloys. This effect will assist in slowing down the local attack on the surface. Even though the real complexes were not fully characterized, these patches on the pits offer the new sight of the inhibitors' design. Surface defects commonly exist, and are the accelerated locations for corrosion. All polished samples in this research showed the presence of Si from SiC polish paper, and these locations always show a worse condition than other areas after a long period of immersion. So, the inhibitor's performance on these defects is essential; a suitable inhibitor should conquer these defects.

Amorphous alloys always showed a higher corrosion resistance than their crystalline counterparts. The corrosion resistance of crystalline CuZr alloys is substantially lower than that of bare Zr. It is also much lower than that of Cu in the presence of efficient inhibitors, such as Me-S-BimH, SH-BimH or SH-ImiH-4Ph. This fact is attributed to the coexistence of several intermetallic phases with different corrosion resistance and/or the reduced corrosion resistance of dislocations and grain boundaries in the studied alloys. The addition of corrosion inhibitors did not improve the corrosion resistance of the crystalline CuZr alloys, even those which showed a protective effect in bare Cu. In amorphous alloys with high Zr content (equal or above 50 at.%), the corrosion resistance is increased by the two tested mercapto-imidazole based inhibitors and all tested mercapto-benzimidazole based inhibitors. These data show that the homogeneous surface structure of amorphous alloys is much less prone to corrosion, and the tested corrosion inhibitors even improve it to some extent. Furthermore, the long-term corrosion resistance degrades except in $Cu_{40}Zr_{60}$ in the presence of SH-ImiH-4Ph, SH-BimH-5NH_2 and SH-ImiMe, and in $Cu_{50}Zr_{50}$ in the presence of SH-BimH-5NH_2. Therefore, SH-BimH-5NH_2

is the most promising corrosion inhibitor in CuZr amorphous alloys. This result advises to deepen the study of the surface interaction of the amino group with these materials. Oxidation is inevitable; for most materials, the ultrathin oxides form in milliseconds after the preparation. If the organic inhibitors can not adsorb on this oxide layer, they will not work on the metals which possess a uniform layer of this oxide. CuZr amorphous alloy and pure Zr shows this behavior due to the formation of ZrO_2 on the surface. On the contrary, for pure Cu and $Cu_{70}Zn_{30}$ alloy, even knowing that oxidation proceeds on the surface, inhibitors still can protect the surface.

SH-BimH-5NH_2 inhibits corrosion on Zn, $Cu_{30}Zn_{70}$ alloy and Zr-rich CuZr alloys. This was the only inhibitor containing the -NH_2 group, and this fact advises to pursuit the research on the interaction between the -NH_2 group and these alloys. SH-ImiH-4Ph is an excellent inhibitor on Cu and $Cu_{70}Zn_{30}$ alloy; it shows the potential to become a competitive commercial inhibitor. Moreover, the design of more effective inhibitors for Cu and its alloys based on this compound is also a promising choice.

The short- and long-term electrochemical measurements show remarkable correlations with immersion tests. In these experiments, both linear polarization resistance and impedance are conducted, the intercomparison assists in improving the stability of results. Significantly, the correlation between low frequency impedance data and linear polarization resistance measurements; this shows the feasibility of LPR on inhibition measurements. However, LPR can not be applied when a uniform dielectric layer appears on the surface, such as in CuZr amorphous alloy and pure Zr. Accordingly, short-term tests should be the primary method for inhibition measurement, and long-term electrochemical tests will confirm the sustainability of the inhibition. With these two steps, most of the effective inhibitors will be properly selected. Immersion tests are valuable since electrochemical tests will not show the surface condition after a long period. This will assist in understanding the behavior of the inhibitor, which can guide the further design of efficient inhibitors.

Chapter 8 Perspective

Based on the previous research, some potential research directions might be:

Research on a potential enhanced α-Cu inhibitor based on SH-ImiH-4Ph compounds. Since this compound displays the best performance on pure Cu and $Cu_{70}Zn_{30}$ alloy, higher inhibition could be expected.

The -NH_2 containing inhibitor shows good inhibition on pure Zn, $Cu_{30}Zn_{70}$ alloy and CuZr amorphous alloy. Inhibitors with amino group are candidates for protection of Zn-based alloys and Zr-based amorphous alloys.

Inhibitor mixing is a fully unexplored path. The pair SH-ImiH-4Ph / SH-BimH-5NH_2 may become effective for the whole range of CuZn and CuZr alloys.

Since the oxidation and oxide stability highly influence the corrosion of amorphous alloys, controlled oxidation of Cu-Zr alloys with addition of minor elements should assist the understanding of corrosion on amorphous alloys.

The healing effect happens on Cu and its alloy shows another factor which should be considered for selecting of inhibitor: interaction between materials and metal-inhibitor complex. The mechanism of healing effect can be object of further study.

Reference

1. M. E. Schlesinger, K. C. Sole, and W. G. Davenport, *Extractive Metallurgy of Copper* (Elsevier, 2011).

2. T. E. Graedel, M. Bertram, K. Fuse, R. B. Gordon, R. Lifset, H. Rechberger, and S. Spatari, Ecol. Econ. **42**, (2002) 9.

3. M. Bertram, T. E. Graedel, K. Fuse, R. Gordon, R. Lifset, H. Rechberger, and S. Spatari, Reg. Environ. Chang. **3**, (2003) 119.

4. A. Elshkaki, T. E. Graedel, L. Ciacci, and B. Reck, Glob. Environ. Chang. **39**, (2016) 305.

5. B. Hou, X. Li, X. Ma, C. Du, D. Zhang, M. Zheng, W. Xu, D. Lu, and F. Ma, Npj Mater. Degrad. **1**, (2017) 1.

6. C. on C. of C. in Japan, Zairyo-to-Kankyo **50**, (2001) 490.

7. G. H. Koch, M. P. H. Brongers, N. G. Thompson, Y. P. Virmani, and J. H. Payer, in *Handb. Environ. Degrad. Mater.* (Elsevier Inc., 2005), pp. 3–24.

8. F. Al-Kharafi, (1996).

9. B. Cherry and B. Skerry, (1983).

10. Proc. R. Soc. London. A. Math. Phys. Sci. **348**, (1976) 1.

11. R. W. Revie, *Uhlig's Corrosion Handbook* (John Wiley & Sons, 2011).

12. R. (Engineer) Francis, *The Corrosion of Copper and Its Alloys : A Practical Guide for Engineers* (NACE International, 2010).

13. J. M. Heras and E. V. Albano, Appl. Surf. Sci. **17**, (1983) 207.

14. J. M. Heras and E. V. Albano, Appl. Surf. Sci. **17**, (1983) 220.

15. N. Cabrera and N. F. Mott, Reports Prog. Phys. **12**, (1948) 163.

16. P. Marcus, *Corrosion Mechanisms in Theory and Practice*, 3rd ed. (CRC Press, Boca Raton, 2012).

17. F. P. Fehlner and N. F. Mott, Oxid. Met. **2**, (1970) 59.

18. J. C. Yang, M. Yeadon, B. Kolasa, and J. M. Gibson, Appl. Phys. Lett. **70**, (1997) 3522.

19. J. C. Yang, M. Yeadon, B. Kolasa, and J. M. Gibson, Scr. Mater. **38**, (1998) 1237.

20. J. C. Yang, B. Kolasa, J. M. Gibson, and M. Yeadon, Appl. Phys. Lett. **73**, (1998) 2841.

21. R. Guan, H. Hashimoto, and T. Yoshida, Acta Crystallogr. Sect. B Struct. Sci. **40**, (1984) 109.

22. R. Guan, H. Hashimoto, K. H. Kuo, and T. Yoshida, Acta Crystallogr. Sect. B Struct. Sci. **43**, (1987) 343.

23. R. Guan, H. Hashimoto, and K. H. Kuo, Acta Crystallogr. Sect. B Struct. Sci. **40**, (1984) 560.

24. R. Guan, H. Hashimoto, and K. H. Kuo, Acta Crystallogr. Sect. B Struct. Sci. **41**, (1985) 219.

25. U. R. Evans, *An Introduction to Metallic Corrosion* (1963).

26. W. J. Van Ooij, Surf. Technol. **6**, (1977) 1.

27. S. Maroie, G. Haemers, and J. J. Verbist, Appl. Surf. Sci. **17**, (1984) 463.

28. S. Maroie, R. Caudano, and J. Verbist, Surf. Sci. **100**, (1980) 1.

29. P. Qiu and C. Leygraf, Appl. Surf. Sci. **258**, (2011) 1235.

30. J. Kruger, J. Electrochem. Soc. **106**, (1959) 847.

31. J. Kruger, J. Electrochem. Soc. **108**, (1961) 503.

32. D. J. G. Ives and A. E. Rawson, J. Electrochem. Soc. **109**, (1962) 447.

33. D. J. G. Ives and A. E. Rawson, J. Electrochem. Soc. **109**, (1962) 452.

34. D. J. G. Ives and A. E. Rawson, J. Electrochem. Soc. **109**, (1962) 458.

35. D. J. G. Ives and A. E. Rawson, J. Electrochem. Soc. **109**, (1962) 462.

36. F. M. Reinhart, *Corrosion of Materials in Hydrospace Part 4-Copper and Copper Alloys* (NAVAL CIVIL ENGINEERING LAB PORT HUENEME CA, 1968).

37. R. F. North and M. J. Pryor, Corros. Sci. **10**, (1970) 297.

38. G. Bianchi and P. Longhi, Corros. Sci. **13**, (1973) 853.

39. G. Bianchi and P. Longhi, Corros. Sci. **13**, (1973) 853.

40. H. S. Campbell, J. Inst. Met. **77**, (1950) 345.

41. J. G. N. Thomas and A. K. Tiller, Br. Corros. J. **7**, (1972) 256.

42. F. M. Al-Kharafi, H. M. Shalaby, and V. K. Gouda, Br. Corros. J. **24**, (1989) 284.

43. F. J. Cornwell, G. Wildsmith, and P. T. Gilbert, Br. Corros. J. **8**, (1973) 1.

44. V. F. Lucey, Br. Corros. J. **1**, (1965) 9.

45. C. W. Stillwell and E. S. Turnipseed, Ind. Eng. Chem. **26**, (1934) 740.

46. T. L. Barr and J. J. Hackenberg, J. Am. Chem. Soc. **104**, (1982) 5390.

47. A. A. EL WARRAKY, Br. Corros. J. **32**, (1997) 57.

48. V. F. Lucey, Br. Corros. J. **2**, (1967) 175.

49. C. H. Bonfiglio, H. C. Albaya, and O. A. Cobo, Corros. Sci. **13**, (1973) 717.

50. R. S. Cooper and J. H. Bartlett, J. Electrochem. Soc. **105**, (1958) 109.

51. M. Pourbaix, J. Electrochem. Soc. **123**, (1976) 25C.

52. W. J. Schwerdtfeger, IEEE Trans. Ind. Gen. Appl. **IGA-3**, (1967) 66.

53. G. Bianchi, G. Fiori, P. Longhi, and F. Mazza, Corrosion **34**, (1978) 396.

54. R. F. North and M. J. Pryor, Corros. Sci. **8**, (1968) 149.

55. V. F. Lucey, Br. Corros. J. **1**, (1965) 53.

56. N. S. Iegemund, H. Aktiengesellschaft, F. Republic, F. R. E. D. B. Ehr, M. Mining, M. Company, and S. Paul, *Ullmann's Encyclopedia of Industrial Chemistry: Fluorine Compounds, Organic* (Wiley, 2000).

57. W. C. Bigelow, D. L. Pickett, and W. A. Zisman, J. Colloid Sci. **1**, (1946) 513.

58. C. D. Bain, E. B. Troughton, Y. T. Tao, J. Evall, G. M. Whitesides, and R. G. Nuzzo, J. Am. Chem. Soc. **111**, (1989) 321.

59. R. W. Revie, *Uhlig's Corrosion Handbook: Third Edition* (2011).

60. J. B. Cotton and I. R. Scholes, Br. Corros. J. **2**, (1967) 1.

61. I. Dugdale and J. B. Cotton, Corros. Sci. **3**, (1963) 69.

62. M. M. Antonijević, S. M. Milić, and M. B. Petrović, Corros. Sci. **51**, (2009) 1228.

63. Y. I. Kuznetsov and L. P. Kazansky, Russ. Chem. Rev. **77**, (2008) 219.

64. M. Finšgar and I. Milošev, Corros. Sci. **52**, (2010) 2737.

65. A. M. Abdullah, F. M. Al-Kharafi, and B. G. Ateya, Scr. Mater. **54**, (2006) 1673.

66. I. Milošev, N. Kovačević, J. Kovač, and A. Kokalj, Corros. Sci. **98**, (2015) 107.

67. N. Kovačević, I. Milošev, and A. Kokalj, Corros. Sci. **98**, (2015) 457.

68. E. M. Sherif and S. M. Park, Electrochim. Acta **51**, (2006) 4665.

69. E. M. Sherif and S.-M. Park, J. Electrochem. Soc. **152**, (2005) B428.

70. T. M. H. Saber and A. A. El Warraky, Br. Corros. J. **26**, (1991) 279.

71. Y. S. Tan, M. P. Srinivasan, S. O. Pehkonen, and S. Y. M. Chooi, Corros. Sci. **48**, (2006) 840.

72. H. Baba, T. Kodama, K. Mori, and H. Hirahara, Corros. Sci. **39**, (1997) 555.

73. J. B. Matos, L. P. Pereira, S. M. L. Agostinho, O. E. Barcia, G. G. O. Cordeiro, and E. D'Elia, J. Electroanal. Chem. **570**, (2004) 91.

74. M. Edwards, L. Hidmi, and D. Gladwell, Corros. Sci. **44**, (2002) 1057.

75. J. H. Henríquez-Román, L. Padilla-Campos, M. A. Páez, J. H. Zagal, M. A. Rubio, C. M. Rangel, J. Costamagna, and G. Cárdenas-Jirón, J. Mol. Struct. THEOCHEM **757**, (2005) 1.

76. E. Stupnišek-Lisac, A. L. Božić, and I. Cafuk, Corrosion **54**, (1998) 713.

77. E. Stupnišek-Lisac, A. Gazivoda, and M. Madžarac, Electrochim. Acta **47**, (2002) 4189.

78. W. Klement, R. H. Willens, and P. Duwez, Nature **187**, (1960) 869.

79. R. Ray, B. C. Giessen, and N. J. Grant, Scr. Met. **2**, (1968) 359.

80. M. Naka, K. Hashimoto, and T. Masumoto, J. Non. Cryst. Solids **30**, (1978) 29.

81. A. Gebert, K. Buchholz, A. Leonhard, K. Mummert, J. Eckert, and L. Schultz, Mater. Sci. Eng. A **267**, (1999) 294.

82. P. Sen, D. D. Sarma, R. C. Budham, K. L. Chopra, and C. N. R. Rao, J. Phys. F Met. Phys. **14**, (1984) 565.

83. Y. Xu, X. Liu, L. Gu, J. Wang, P. Schützendübe, Y. Huang, Y. Liu, and Z. Wang, Appl. Surf. Sci. **457**, (2018) 396.

84. S. H. Park, K. R. Lim, M. Y. Na, K. C. Kim, W. T. Kim, and D. H. Kim, Corros. Sci. **99**, (2015) 304.

85. L. Liu and K. C. Chan, Appl. Phys. A Mater. Sci. Process. **80**, (2005) 1737.

86. S. K. Sharma, T. Strunskus, H. Ladebusch, V. Zaporojtchenko, and F. Faupel, J. Mater. Sci. **43**, (2008) 5495.

87. C. Y. Tam and C. H. Shek, J. Mater. Res. **20**, (2005) 1396.

88. Y. Xu, L. P. H. Jeurgens, P. Schützendübe, S. Zhu, Y. Huang, Y. Liu, and Z. Wang, J. Mater. Sci. Technol. **40**, (2020) 128.

89. D. Zander and U. Köster, Mater. Sci. Eng. A **375**–**377**, (2004) 53.

90. A. Gebert, P. F. Gostin, and L. Schultz, Corros. Sci. **52**, (2010) 1711.

91. A. Kawashima, K. Ohmura, Y. Yokoyama, and A. Inoue, Corros. Sci. **53**, (2011) 2778.

92. M. Naka, K. Hashimoto, and T. Masumoto, J. Non. Cryst. Solids **30**, (1978) 29.

93. J. C. Turn and R. M. Latanision, Corrosion **39**, (1983) 271.

94. D. Zander and U. Köster, Mater. Sci. Eng. A **375**–**377**, (2004) 53.

95. J. Kruger, J. Electrochem. Soc. **106**, (1959) 847.

96. L. R. F. Allen J. Bard, *Electrochemical Methods: Fundamentals and Applications, 2nd Edition | Wiley*, 2nd. Edition (2001).

97. A. Kokalj, M. Lozinšsek, B. Kapun, P. Taheri, S. Neupane, P. Losada-Pérez, C. Xie, S. Stavber, D. Crespo, F. U. Renner, A. Mol, and I. Milošev, Corros. Sci. (2020) 108856.

98. H. D. Speckmann, S. Haupt, and H.-H. Strehblow, Surf. Interface Anal. **11**, (1988) 148.

99. U. Collisi and H. H. Strehblow, J. Electroanal. Chem. **284**, (1990) 385.

100. B. Timmermans, F. Reniers, A. Hubin, and C. Buess-Herman, Appl. Surf. Sci. **144**–**145**, (1999) 54.

101. I. Milošev and H.-H. Strehblow, J. Electrochem. Soc. **150**, (2003) B517.

102. D. Chadwick and T. Hashemi, Surf. Sci. **89**, (1979) 649.

103. O. Benali, L. Larabi, M. Traisnel, L. Gengembre, and Y. Harek, Appl. Surf. Sci. **253**, (2007) 6130.

104. P. Kalimuthu and S. A. John, Electrochem. Commun. **11**, (2009) 367.

105. B. Wrzosek and J. Bukowska, J. Phys. Chem. C **111**, (2007) 17397.

106. C. V. D'Alkaine, J. Electrochem. Soc. **144**, (1997) 3331.

107. S. Peulon and D. Lincot, J. Electrochem. Soc. **145**, (2019) 864.

108. R. Guo, F. Weinberg, and D. Tromans, CORROSION **51**, (1995) 356.

109. A. A. Aghzzaf, B. Rhouta, E. Rocca, A. Khalil, and J. Steinmetz, Corros. Sci. **80**, (2014) 46.

110. K. Aramaki, Corros. Sci. **43**, (2001) 591.

111. A. C. Bastos, M. G. S. Ferreira, and A. M. Simões, in *Prog. Org. Coatings* (Elsevier, 2005), pp. 339–350.

112. K. Aramaki, Corros. Sci. **43**, (2001) 1985.

113. F. Suedile, F. Robert, C. Roos, and M. Lebrini, Electrochim. Acta **133**, (2014) 631.

114. M. Pourbaix, *Atlas of Electrochemical Equilibria in Aqueous Solutions* (National Association of Corrosion Engineers, Houston, Tex, 1974).

115. T. Massalski, J. Murray, L. Bennett, H. B.-V. I, and undefined 1987, *Binary Alloy Phase Diagrams (American Society for Metals, Metals Park, Ohio, 1986)* (n.d.).

116. B. S. Kim, T. Piao, S. N. Hoier, and S. M. Park, Corros. Sci. **37**, (1995) 557.

117. L. Qiu, K. Zou, and G. Xu, Appl. Surf. Sci. **266**, (2013) 230.

118. R. Naderi, M. Mahdavian, and M. M. Attar, Electrochim. Acta **54**, (2009) 6892.

119. B. H. Loo, Y. Tse, K. Parsons, C. Adelman, A. El-Hage, and Y. G. Lee, J. Raman Spectrosc. **37**, (2006) 299.

120. H. Okamoto, J. Phase Equilibria Diffus. **29**, (2008) 204.

121. L. Young, Trans. Faraday Soc. **51**, (1955) 1250.

122. L. Young, *Anodic Oxide Films* (Academic Press, London ;;New York (N.Y.), 1961).

123. B. Tribollet, V. Vivier, and M. E. Orazem, in *Encycl. Interfacial Chem.* (Elsevier, 2018), pp. 93–107.

124. A. Masuhr, T. A. Waniuk, R. Busch, and W. L. Johnson, Phys. Rev. Lett. **82**, (1999) 2290.

125. G. D. Bengough and R. May, J. Inst. Met. **32**, (1924) 90.

126. G. D. Bengough, G. Jones, and R. Pirret, J. Inst. Met. **23**, (1920) 65.

127. D. B. Miracle, Acta Mater. **54**, (2006) 4317.

128. Y. Yang, J. F. Zeng, A. Volland, J. J. Blandin, S. Gravier, and C. T. Liu, Acta Mater. **60**, (2012) 5260.

129. A. Martínez, J. Braz. Chem. Soc. **16**, (2005) 337.

130. M. Zhou, M. Chen, L. Zhang, and H. Lu, J. Phys. Chem. A **106**, (2002) 9017.

Appendix 1: Corrosion on pure metals. Supplemental information.

A1.1 Corrosion Inhibition of Copper

A1.1.1 Short-term and long-term electrochemical tests

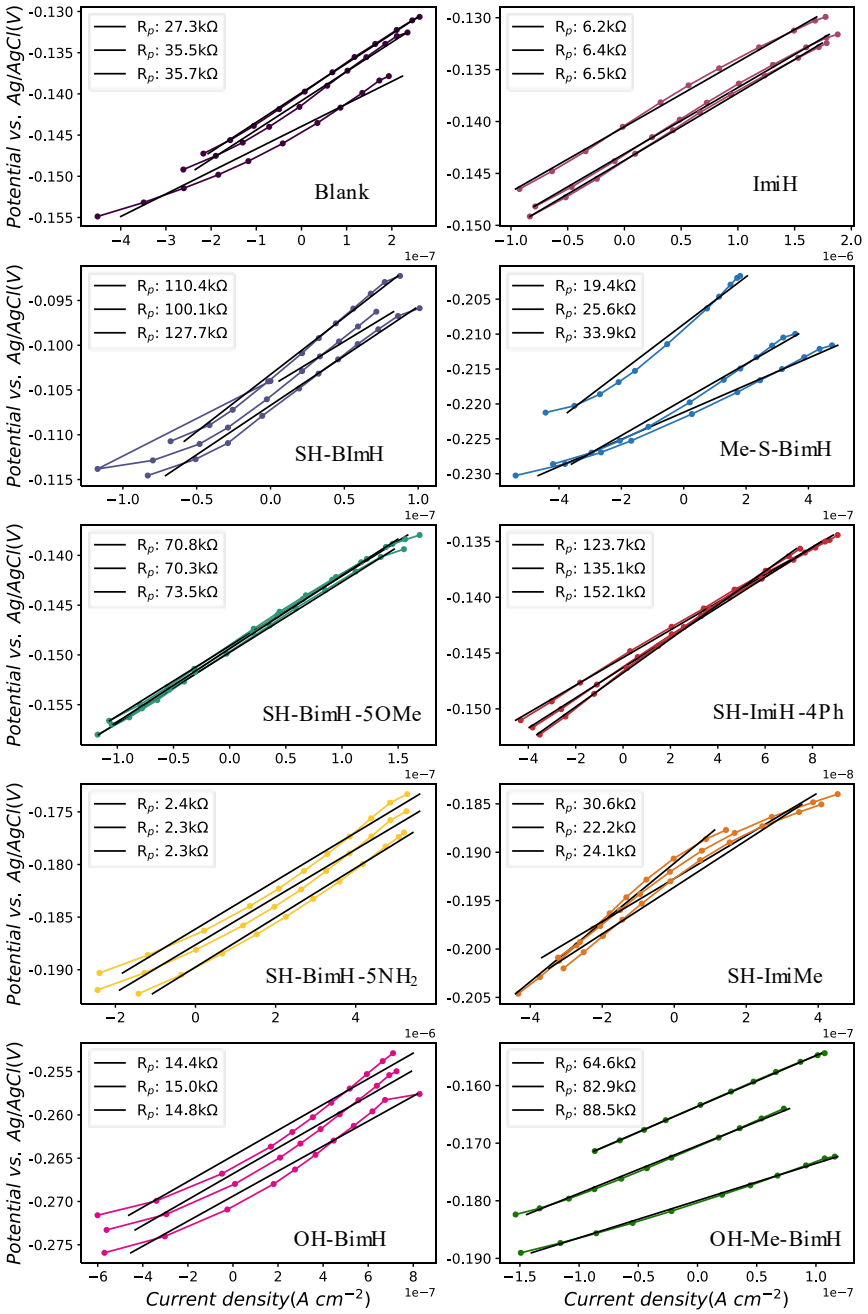

Figure A1.1 All linear polarization resistance curves of pure copper with and without inhibitors

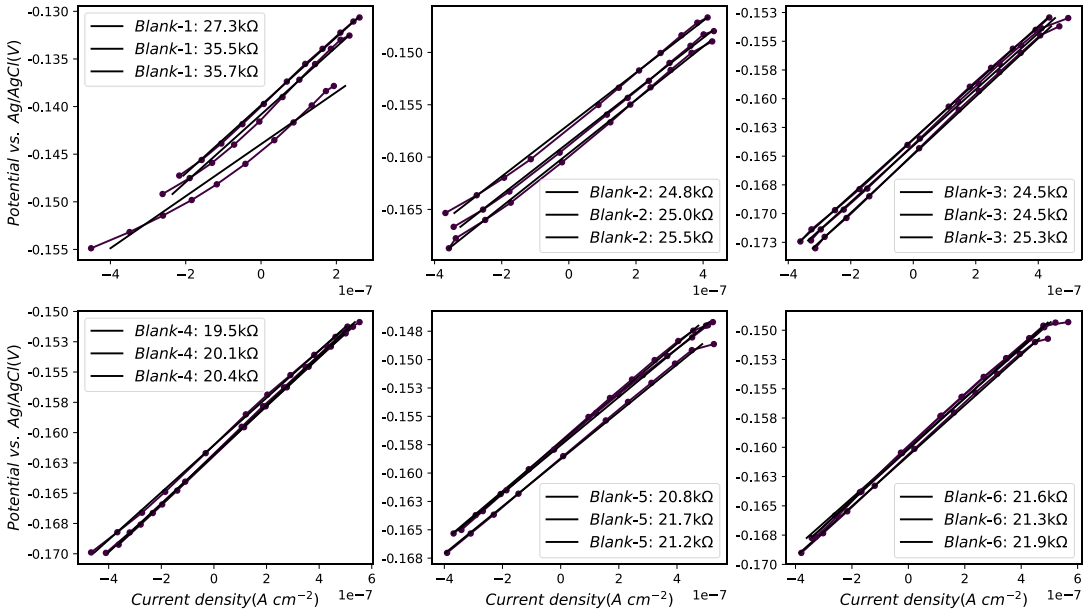

Figure A1.2 Long-term linear polarization curves of pure Cu under the 120h period of testing of the alloy in the presence of the inhibitor in the 3 wt.% NaCl aqueous solution without inhibitors

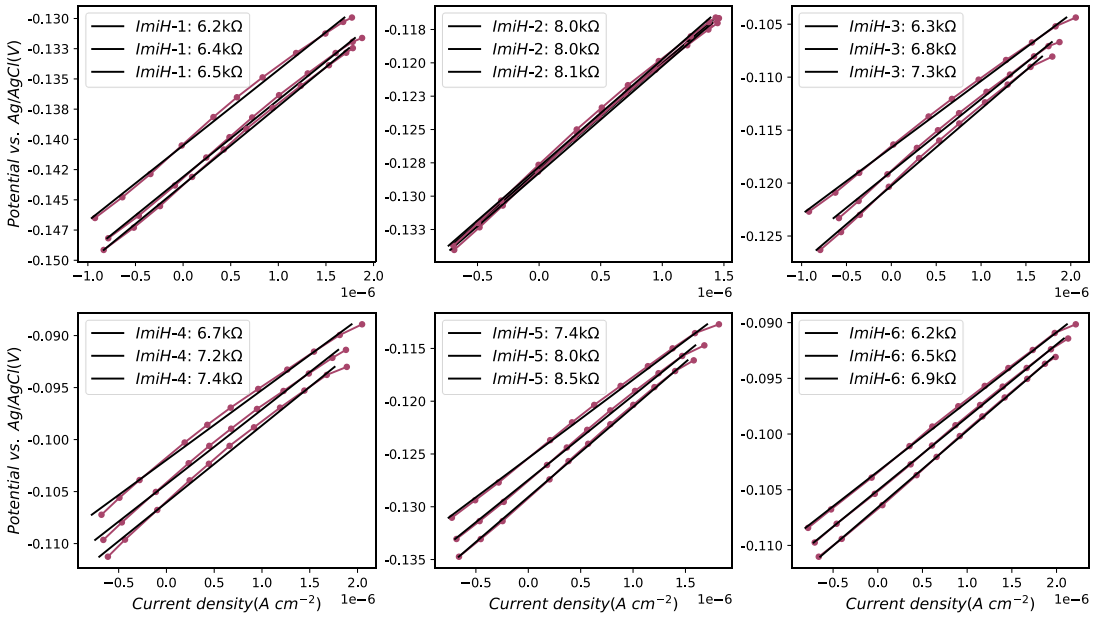

Figure A1.3 Long-term linear polarization curves of pure Cu under the 120h period of testing of the alloy in the presence of the inhibitor in the 3 wt.% NaCl aqueous solution with ImiH

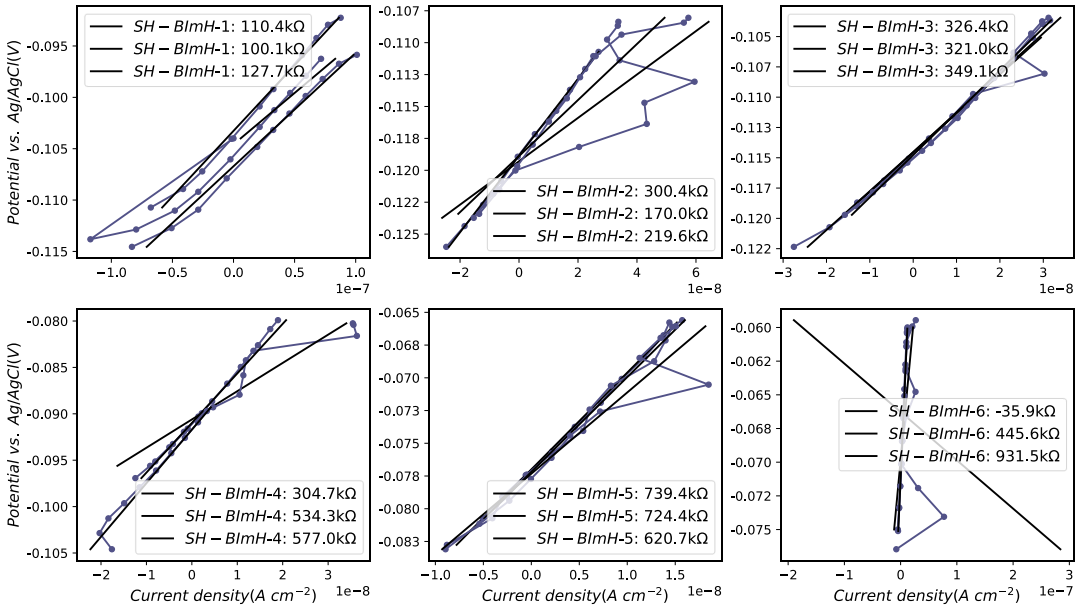

Figure A1.4 Long-term linear polarization curves of pure Cu under the 120h period of testing of the alloy in the presence of the inhibitor in the 3 wt.% NaCl aqueous solution with SH-BimH

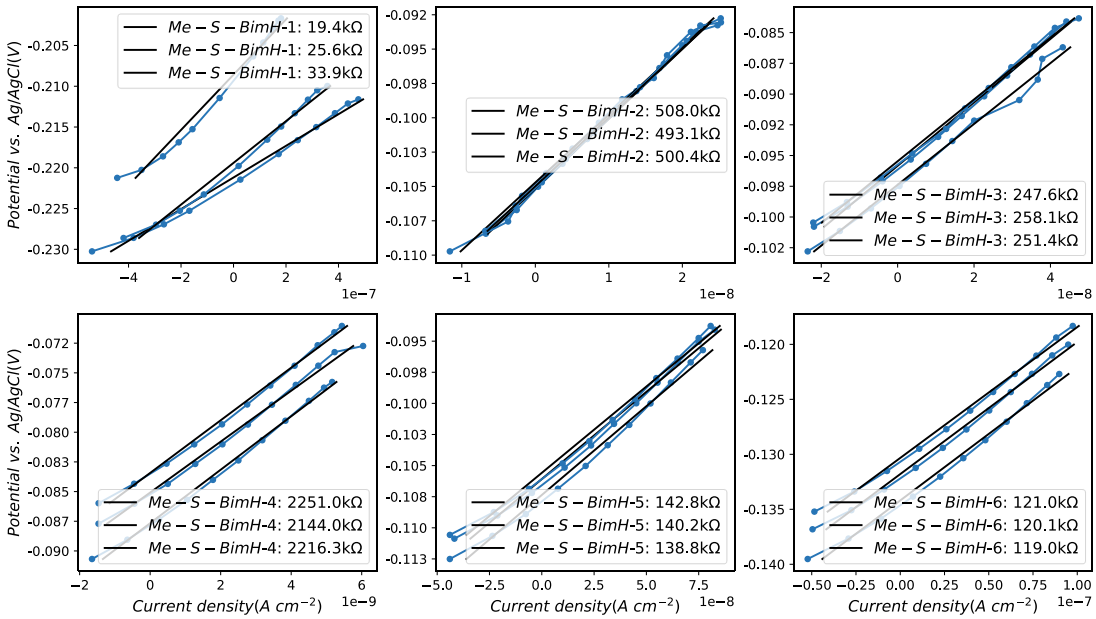

Figure A1.5 Long-term linear polarization curves of pure Cu under the 120h period of testing of the alloy in the presence of the inhibitor in the 3 wt.% NaCl aqueous solution with Me-S-BimH

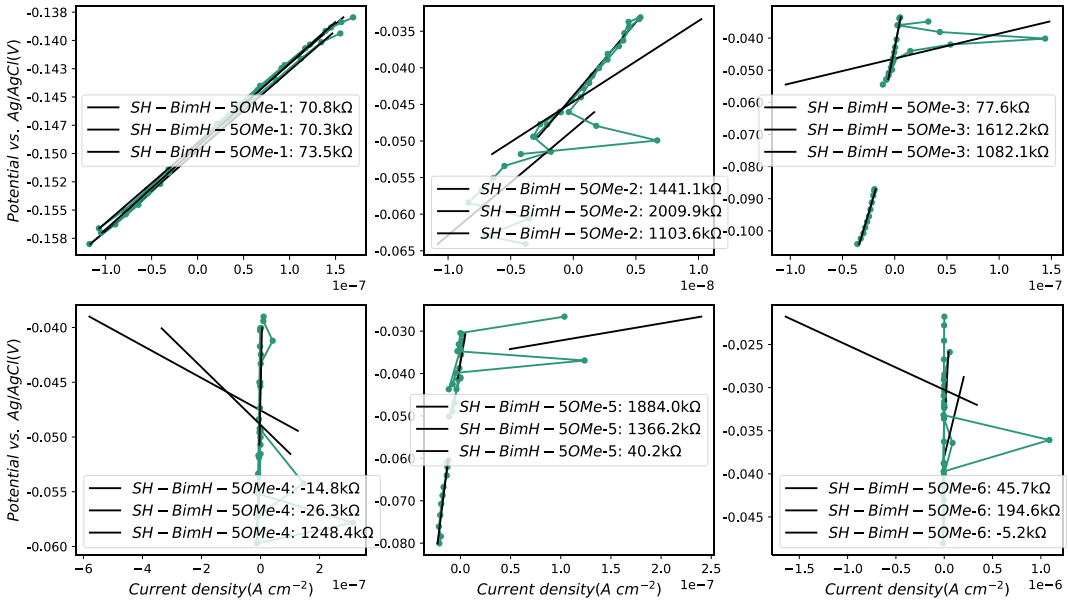

Figure A1.6 Long-term linear polarization curves of pure Cu under the 120h period of testing of the alloy in the presence of the inhibitor in the 3 wt.% NaCl aqueous solution with SH-BimH-5OMe

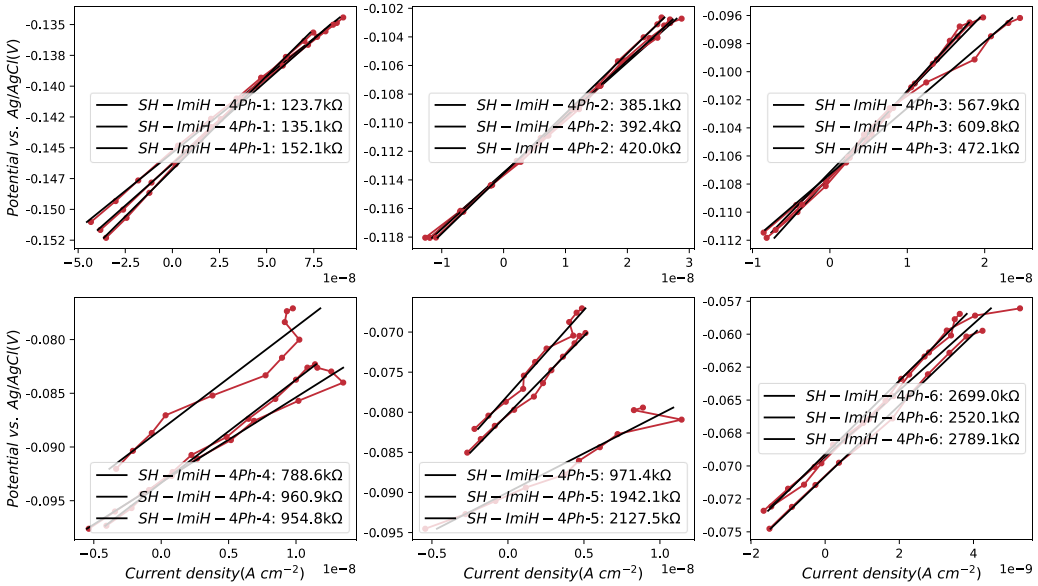

Figure A1.7 Long-term linear polarization curves of pure Cu under the 120h period of testing of the alloy in the presence of the inhibitor in the 3 wt.% NaCl aqueous solution with SH-ImiH-4Ph

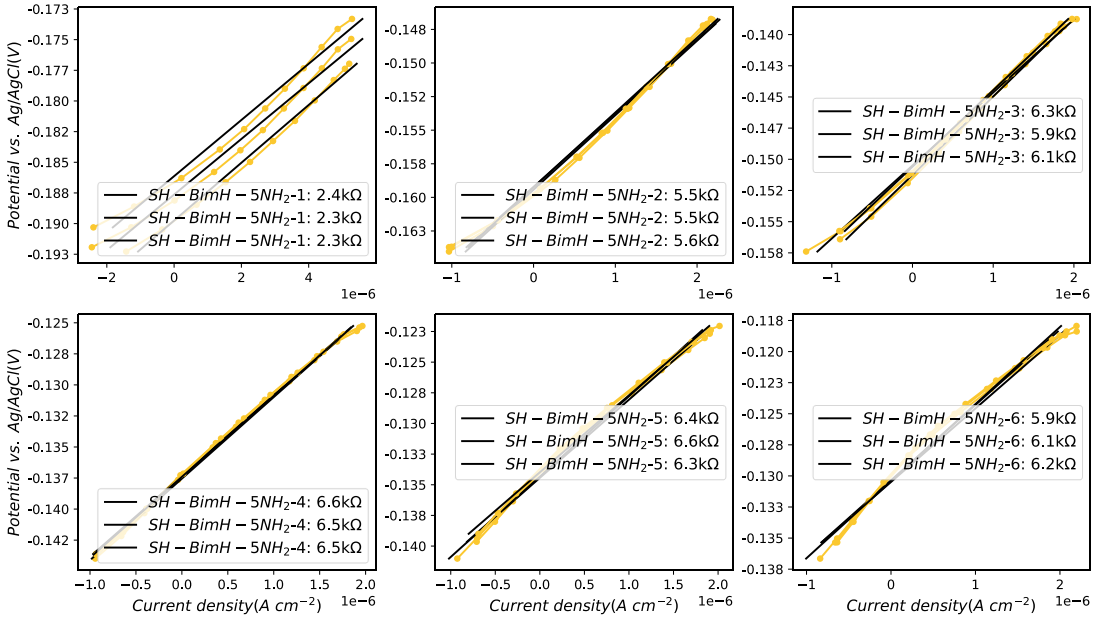

Figure A1.8 Long-term linear polarization curves of pure Cu under the 120h period of testing of the alloy in the presence of the inhibitor in the 3 wt.% NaCl aqueous solution with SH-BimH-5NH$_2$

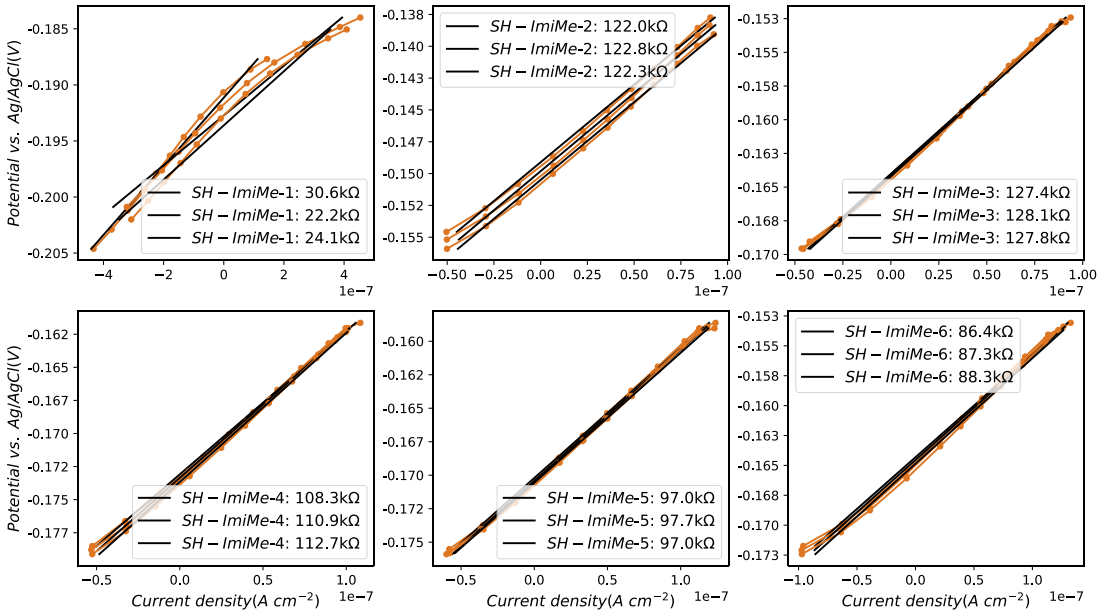

Figure A1.9 Long-term linear polarization curves of pure Cu under the 120h period of testing of the alloy in the presence of the inhibitor in the 3 wt.% NaCl aqueous solution with SH-ImiMe

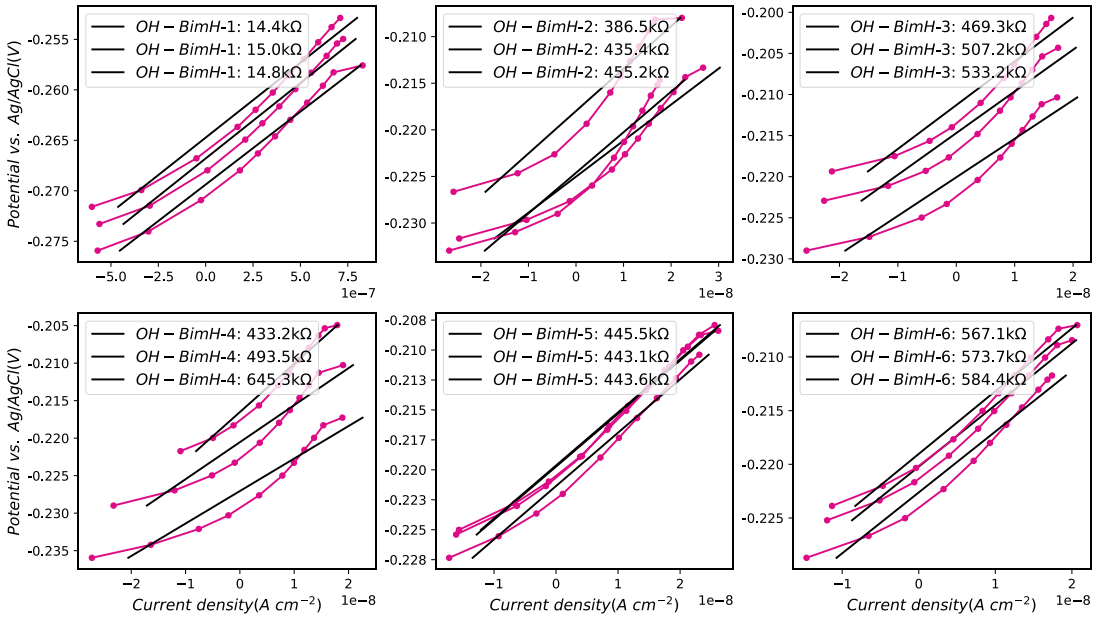

Figure A1.10 Long-term linear polarization curves of pure Cu under the 120h period of testing of the alloy in the presence of the inhibitor in the 3 wt.% NaCl aqueous solution with OH-BimH

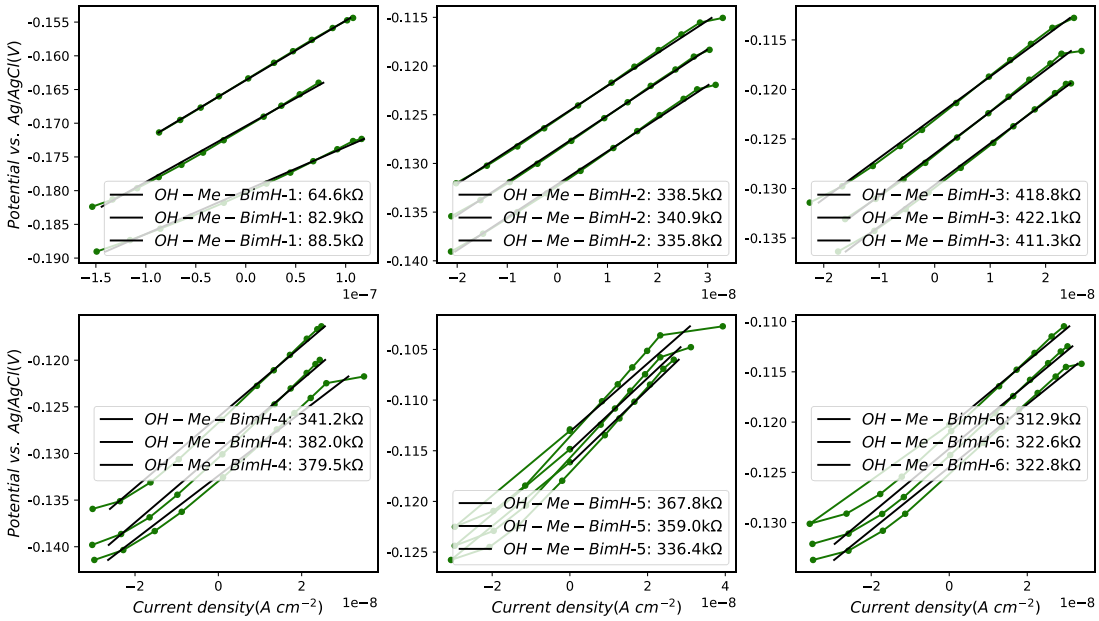

Figure A1.11 Long-term linear polarization curves of pure Cu under the 120h period of testing of the alloy in the presence of the inhibitor in the 3 wt.% NaCl aqueous solution with OH-Me-BimH

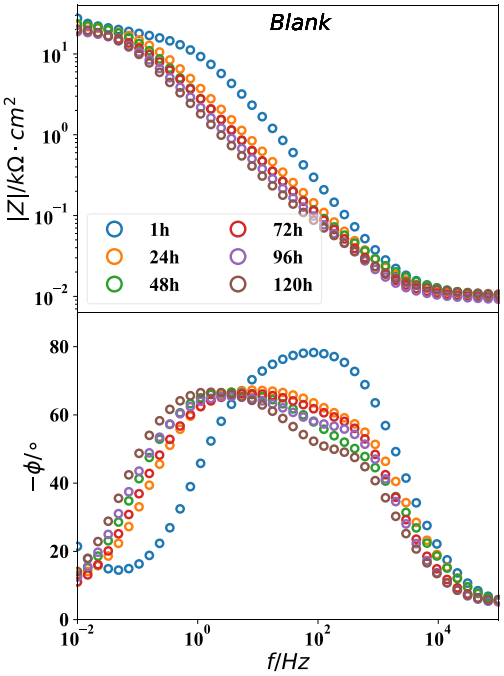

Figure A1.12 Long-term EIS impedance and phase diagram of pure Cu in NaCl, in period of 120h without inhibitor

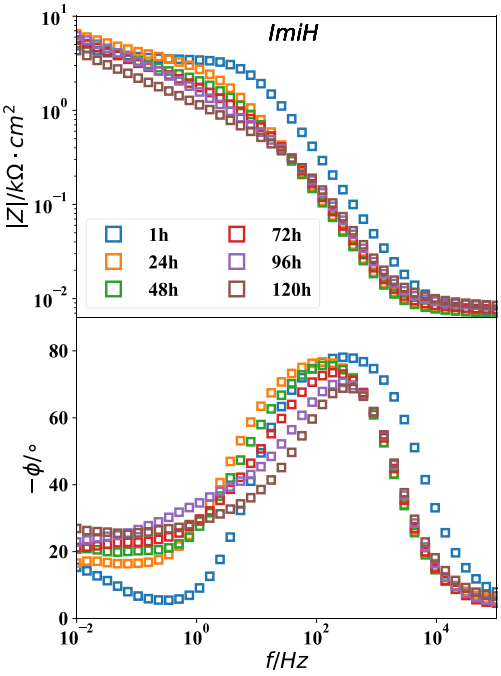

Figure A1.13 Long-term EIS impedance and phase diagram of pure Cu in NaCl, in period of 120h with ImiH

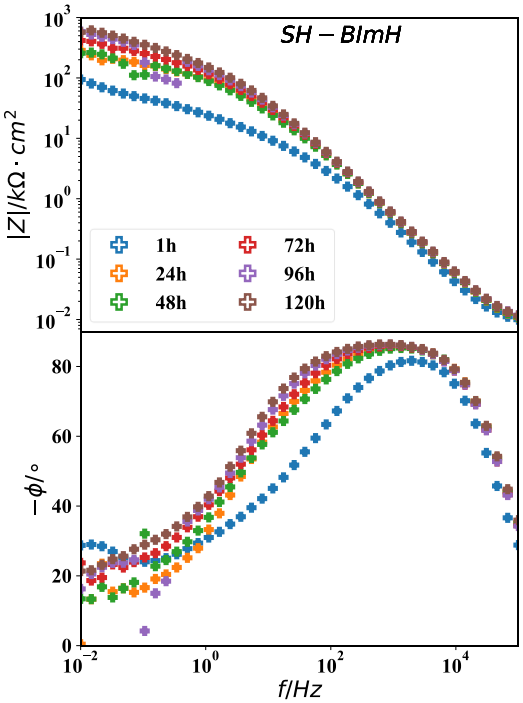

Figure A1.14 Long-term EIS impedance and phase diagram of pure Cu in NaCl, in period of 120h with SH-BimH

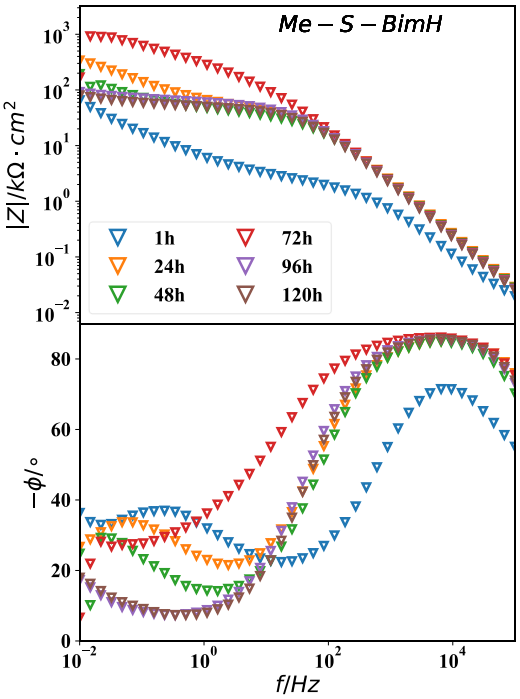

Figure A1.15 Long-term EIS impedance and phase diagram of pure Cu in NaCl, in period of 120h with Me-S-BimH

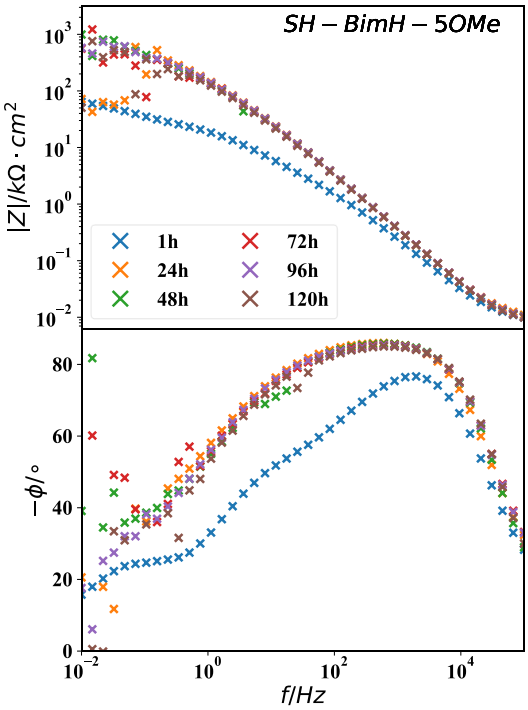

Figure A1.16 Long-term EIS impedance and phase diagram of pure Cu in NaCl, in period of 120h with SH-BimH-5OMe

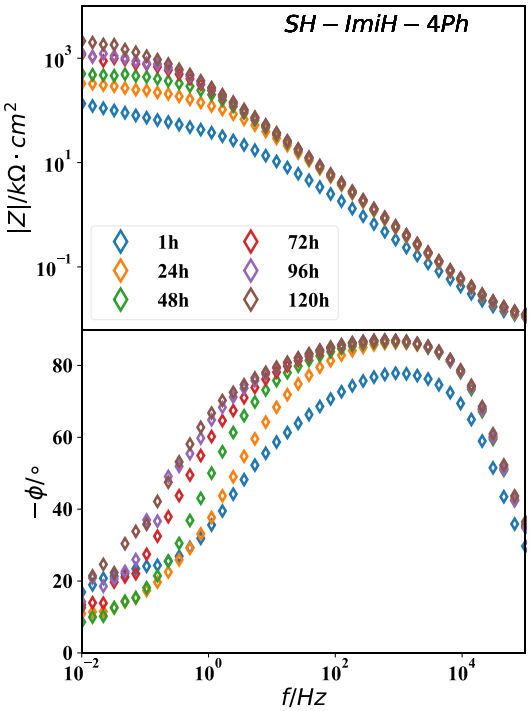

Figure A1.17 Long-term EIS impedance and phase diagram of pure Cu in NaCl, in period of 120h with SH-ImiH-4Ph

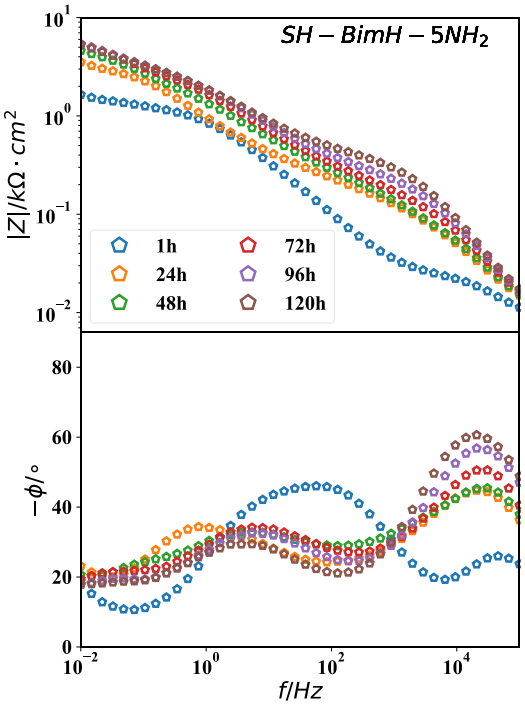

Figure A1.18 Long-term EIS impedance and phase diagram of pure Cu in NaCl, in period of 120h without SH-BimH-5NH_2

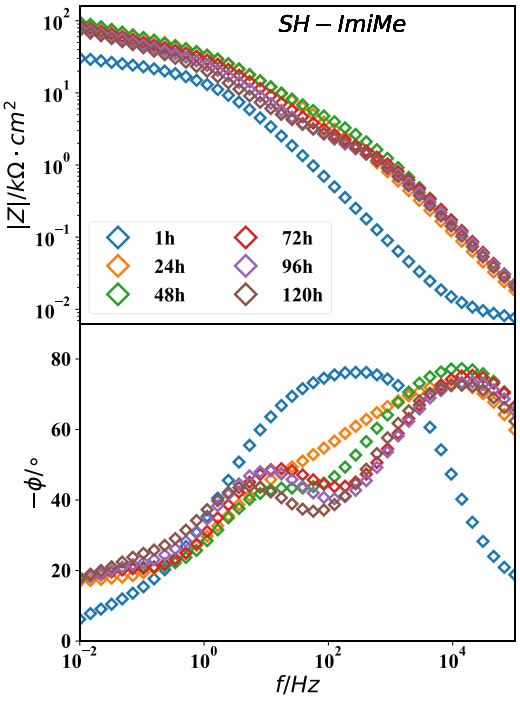

Figure A1.19 Long-term EIS impedance and phase diagram of pure Cu in NaCl, in period of 120h with SH-ImiMe

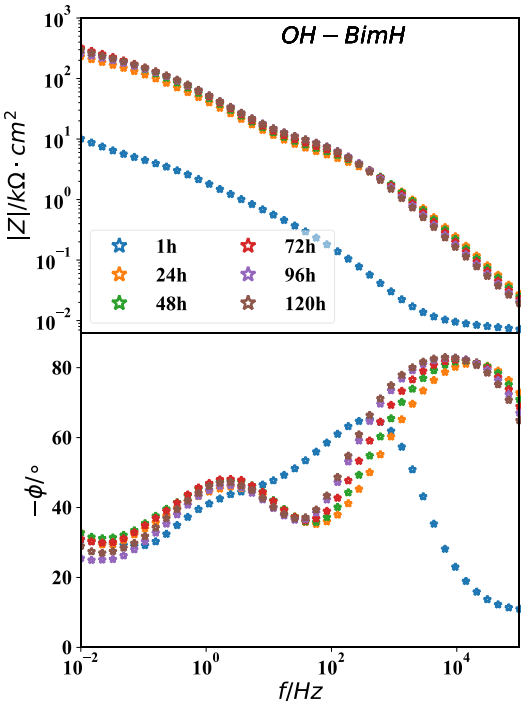

Figure A1.20 Long-term EIS impedance and phase diagram of pure Cu in NaCl, in period of 120h with OH-BimH

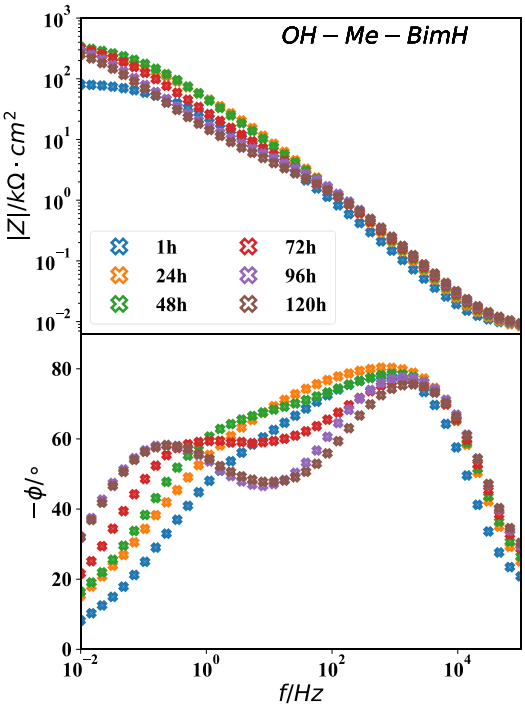

Figure A1.21 Long-term EIS impedance and phase diagram of pure Cu in NaCl, in period of 120h with OH-Me-BimH

A1.1.2 Immersion test of pure Cu

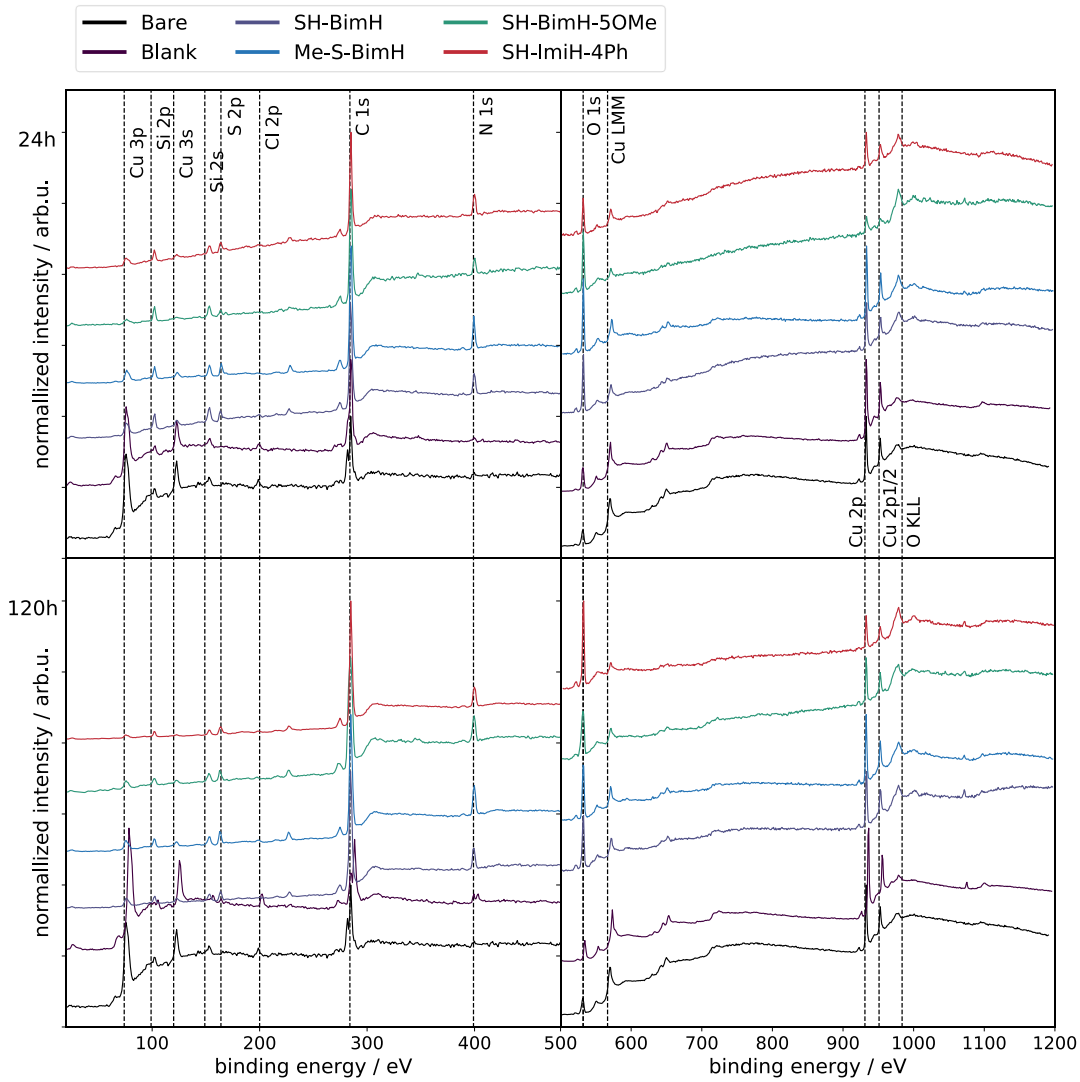

Figure A1.22 Normalized survey XPS spectrums for the surface of pure Cu after polishing and pickling, and after immersion in 3wt.% NaCl with and without added of SH-BimH, Me-S-BimH, SH-BimH-5OMe and SH-ImiH-4Ph. Dash lines represent the position of peaks of reference compounds. Upper: Immersion for 24h. Down: Immersion for 120h.

Table A1.1 Characteristic X-ray Energies (keV) of related elements in experiments of immersion test

Element	$K\alpha_1$	$K\beta_1$	$L\alpha_1$	$L\beta_1$
C	0.277			
N	0.392			
O	0.525			
Si	1.740	1.837		
S	2.309	2.465		
Cl	2.622	2.812		
Cu	8.046	8.904	0.928	0.947

Zn	8.637	9.570	1.012	1.035

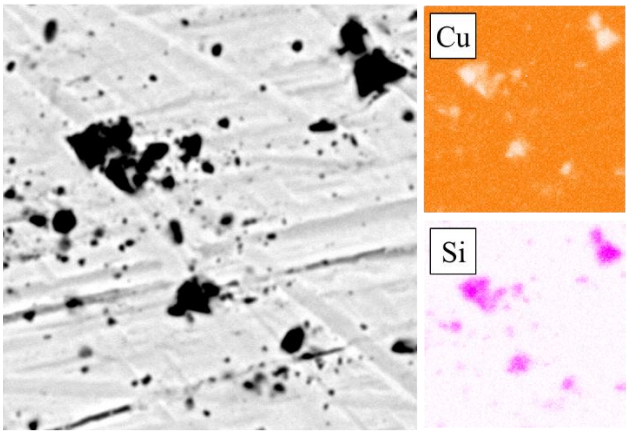

Figure A1.23 EDX elemental map analysis of the bare pure Cu sample under 10000x magnification

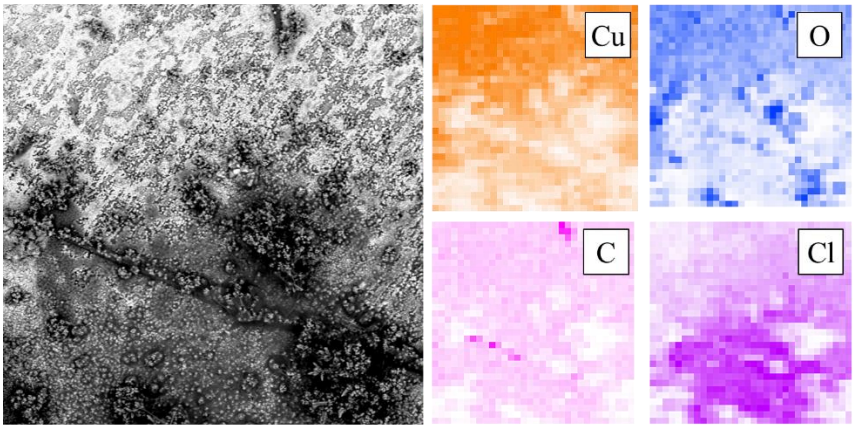

Figure A1.24 EDX elemental map analysis of pure Cu immersed in 3 wt.% NaCl solution for 60 day

Figure A1.25 shows the surface of pure Cu after immersion in 3 wt.% NaCl solution with added 1mM ImiH for 60 days. In **Figure A1.25** (a) and (b), the surface show more homogeneous look than that of surface without inhibitor. Some black part appears in **Figure A1.25** (a) and the closer look in **Figure A1.25** (b) shows it is some cracks on the surface. Under 5000x magnification in **Figure A1.25** (c) and (d), the surface is composed of uniform islands different from the ones in blank sample. As shown in (b), this is a layer of compounds on the surface. In 3D image **Figure A1.25** (e), the surface roughness increases to 3.03 μm. **Figure A1.26** shows the distribution of elements on the surface. Cu, O and Cl are uniformly existing on the surface. **Figure A1.27** is points analysis of elements by EDX on uniform surface (point (a)) and cracks (point (b) and (c)). All three spectrums show the same elemental distribution. This indicates the added ImiH assist the formation of compounds contain of Cu, Cl and O. And this kind of inhibitor is not work for pure Cu.

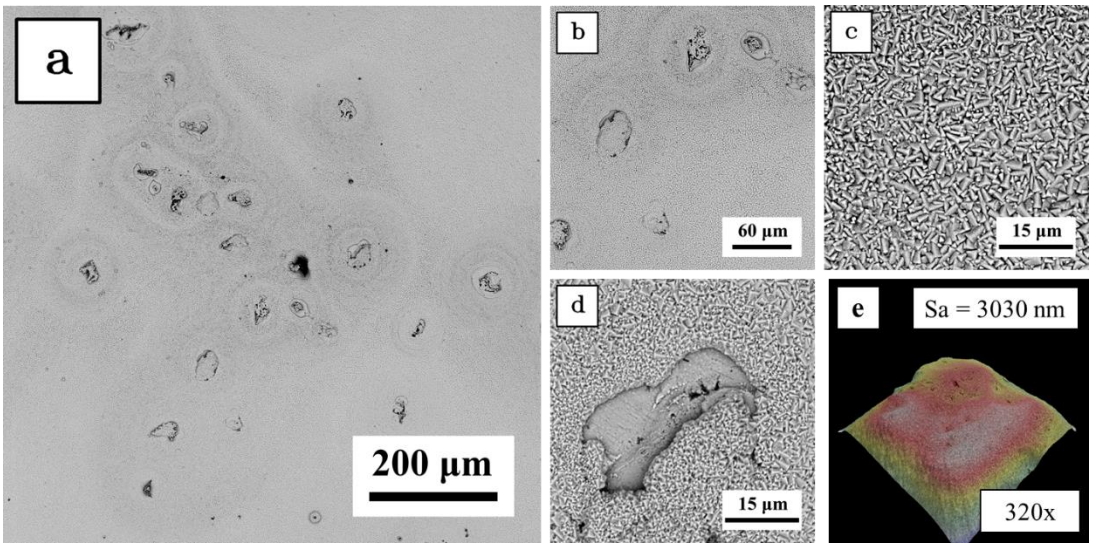

Figure A1.25 Pure Cu immersed in 3 wt.% NaCl with added 1mM ImiH solution for 60 days (a) surface under 320x magnification with all typical features (b) surface under 1000x magnification (c) surface under 5000x magnification (d) surface features in black part (e) 3D topography under 320x magnification by SEM

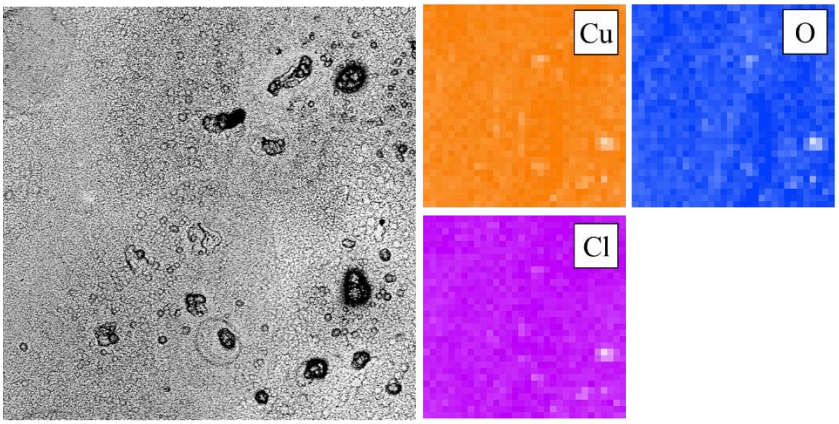

Figure A1.26 EDS elemental map analysis of Pure Cu immersed in 3 wt.% NaCl solution with added 1mM ImiH for 60 days

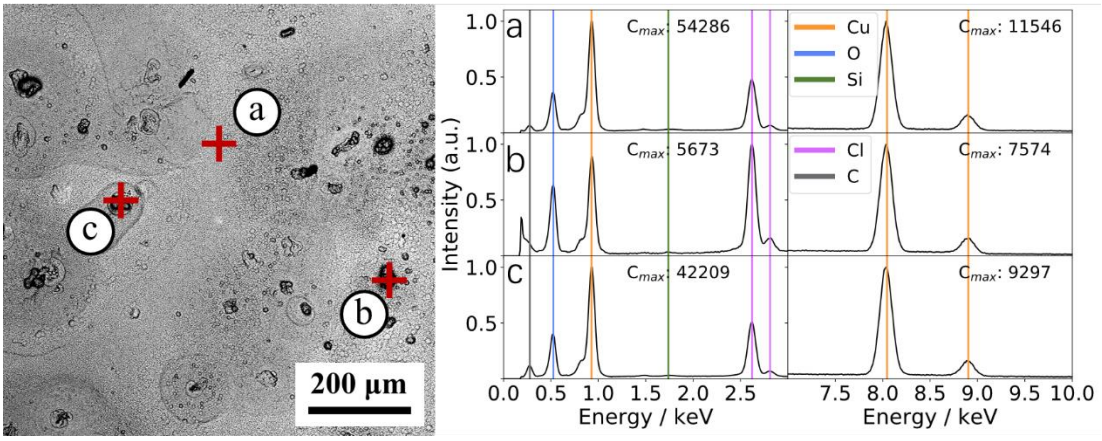

Figure A1.27 EDS elemental point analysis spectrum of Pure Cu immersed in 3 wt.% NaCl solution with added 1mM ImiH for 60 days (a) spectrum of point a, flat homogenous surface (b) (c) spectrum of point b and c, black part on the surface.

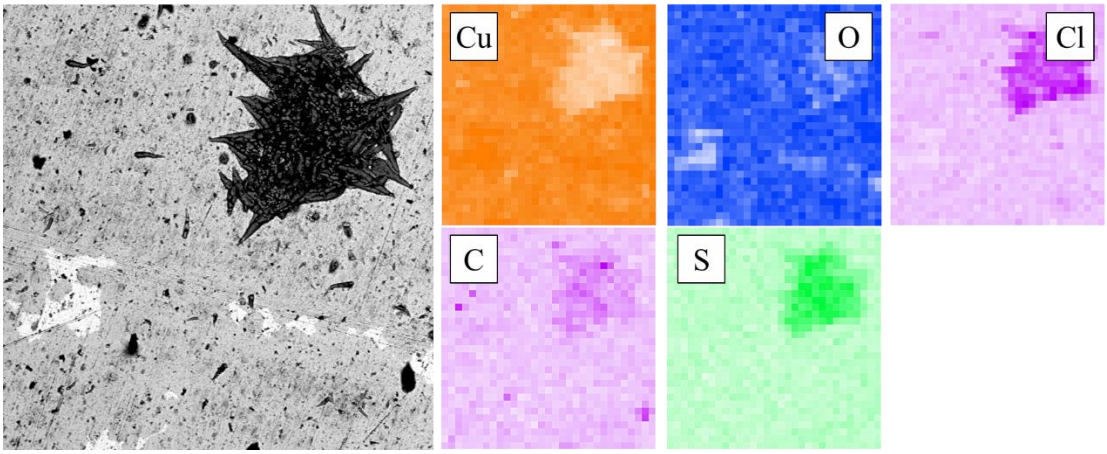

Figure A1.28 EDS elemental map analysis of Pure Cu immersed in 3 wt.% NaCl solution with added 1mM SH-BimH for 60 days

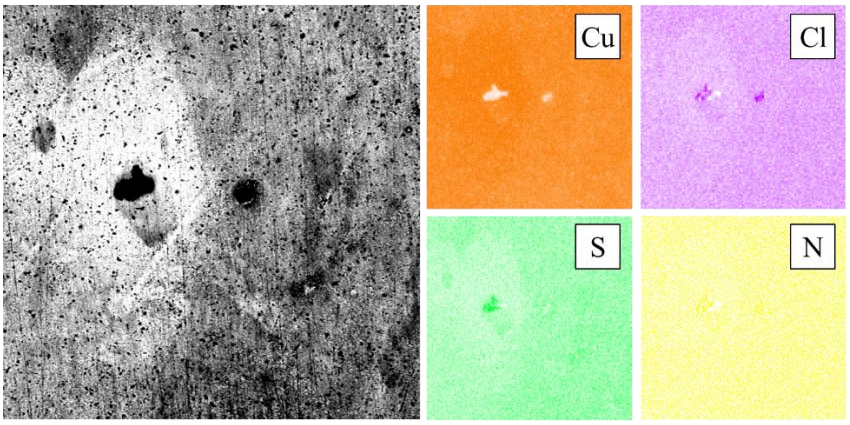

Figure A1.29 EDS elemental map analysis of pure Cu immersed in 3 wt.% NaCl solution with added 1mM Me-S-BimH for 60 days

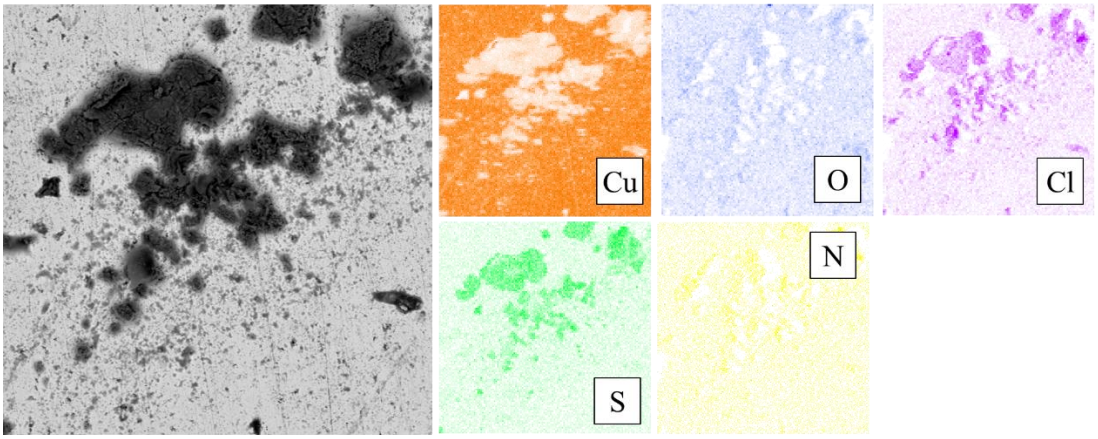

Figure A1.30 EDS elemental map analysis of pure Cu immersed in 3 wt.% NaCl solution with added 1mM SH-BimH-5OMe for 60 days

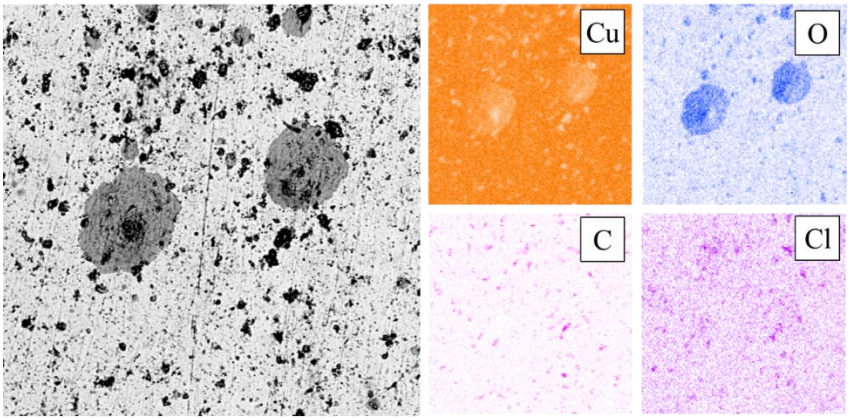

Figure A1.31 EDS elemental map analysis of pure Cu immersed in 3 wt.% NaCl solution with added 1mM SH-ImiH-4Ph for 60 days

Figure A1.32 shows the surface of pure Cu after immersion in 3wt.%NaCl with added SH-BimH-5NH_2 for 60 days. **Figure A1.32** (a) and (b) show the global view of the surface, the surface is totally destroyed, and different kind of features present on the surface. Some parts are covered by light grey cracked surface, some parts are cover by net black film, some parts are covered by black film. **Figure A1.32** (c) shows the net black film and the light grey surface seems under the film. As shown in **Figure A1.32** (d). there are some particles on the black film as well. As shown in **Figure A1.33**, the distribution of elemental map by EDX detects presence of O, Cl, S on the Cu surface, the black film is Cl and S rich. Figure A1.34 shows the point elemental analysis of different features. Point (a) shows that light grey surface is pure Cu. The black film shows presence of Cl and S as shown in point (b) and (c). SH-BimH-5NH_2 introduces new reaction on the surface, and the surface was destroyed. It can not be an inhibitor for pure Cu.

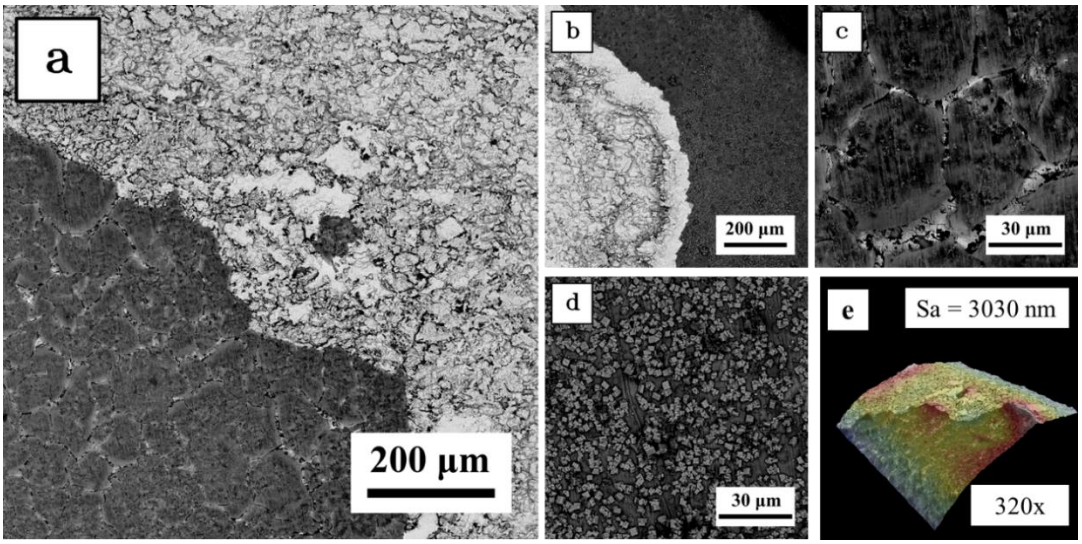

Figure A1.32 Pure Cu immersed in 3 wt.% NaCl with added 1mM SH-BimH-5NH_2 solution for 60 days (a) surface under 320x magnification (b) surface under 320x magnification (c) surface of black part in figure (a) (d) surface of black part in figure (b) (e) 3D topography under 320x magnification by SEM

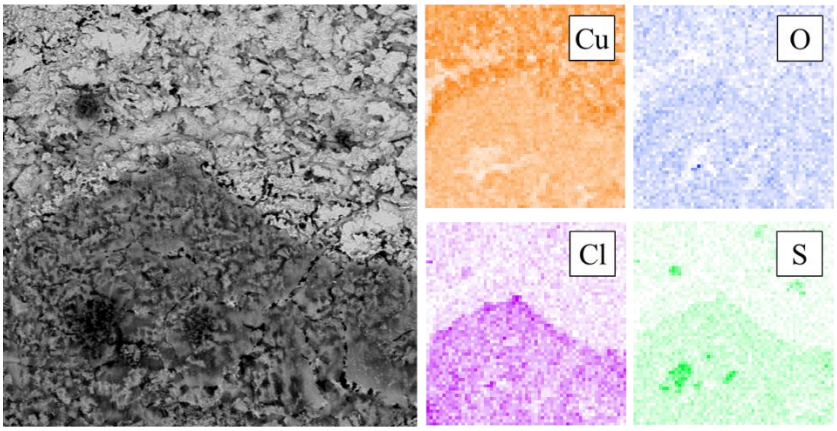

Figure A1.33 EDS elemental map analysis of pure Cu immersed in 3 wt.% NaCl solution with added 1mM SH-BimH-5NH_2 for 60 days

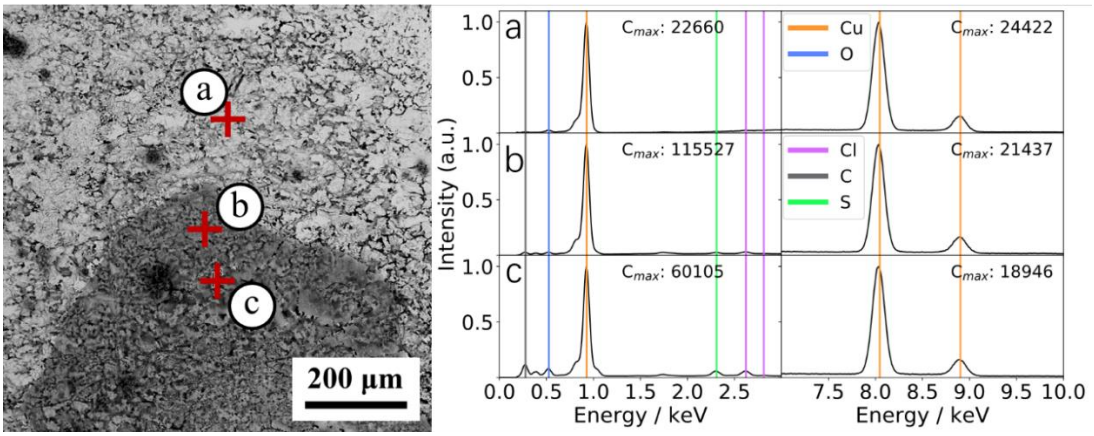

Figure A1.34 EDS elemental point analysis spectrum of pure Cu immersed in 3 wt.% NaCl solution with added 1mM SH-BimH-5NH_2 for 60 days (a) spectrum of point a, white surface (b) (c) spectrum of point b and c, black film on the surface.

Figure A1.35 shows the surface of pure Cu after immersion in 3 wt.% NaCl with added 1mM SH-ImiMe for 60 days. **Figure A1.35** (a) and (b) show the surface is covered by the same feature, a kind of dendritic substance, which is similar to part of the surface of pure Cu immersed in 3wt. NaCl. **Figure A1.35** (c) shows a bulk appears, and **Figure A1.35** (d) is a closer look of the dendritic structure. **Figure A1.36** shows the elemental map of surface and most part of the surface is not detectable. The dendritic substance is composed of Cu, Cl and O. **Figure A1.37** shows the point elemental analysis of the surface. Point (a) and (b) is on the dendritic substance which shows the similar result as elemental map. As shown in point (c), C_{max} in 0-3 KeV range is so small, and this part is not detectable by this method. Nevertheless, all results conduct that SH-ImiMe is not effective inhibitor and it will assist Cu to form a uniform (Cu, Cl, O) compounds surface after immersion for long period.

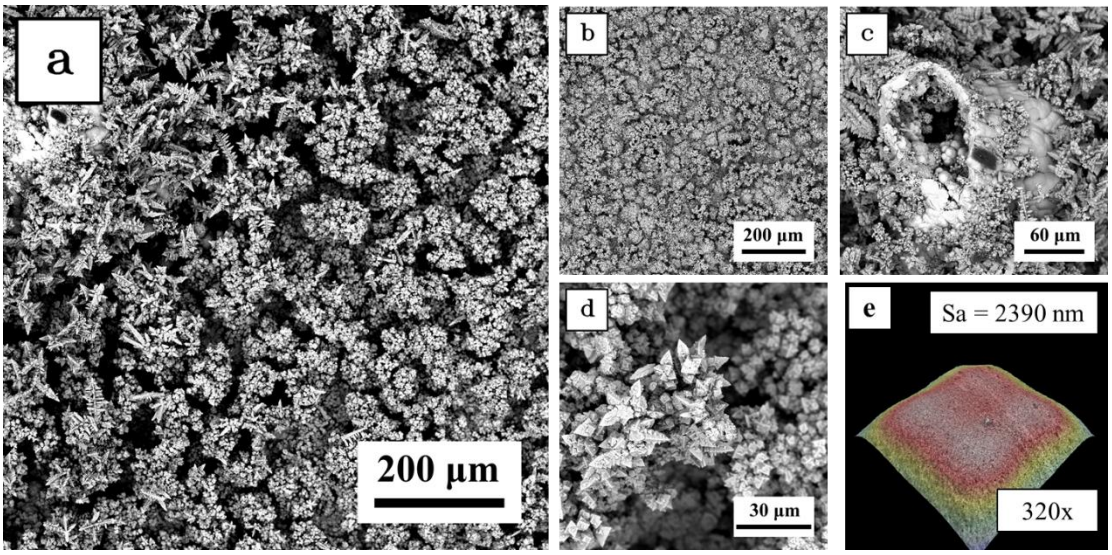

Figure A1.35 Pure Cu immersed in 3 wt.% NaCl with added 1mM SH-ImiMe solution for 60 days (a) surface under 320x magnification with all typical features (b) surface under 320x magnification (c) surface under 1000x magnification (d) surface 2500x magnification (e) 3D topography under 320x magnification by SEM

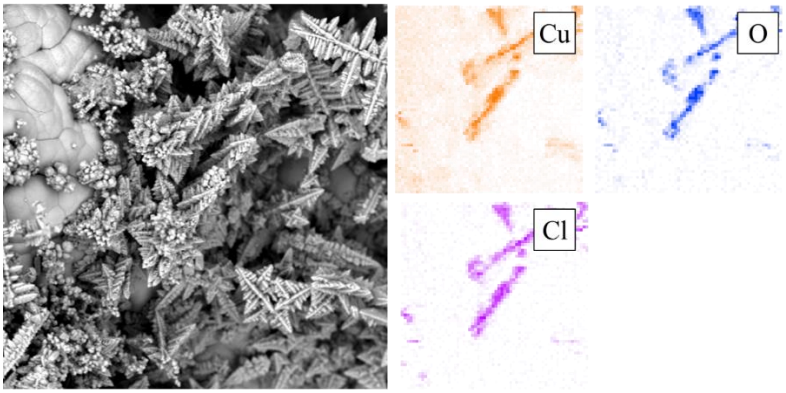

Figure A1.36 EDS elemental map analysis of pure Cu immersed in 3 wt.% NaCl solution with added 1mM SH-ImiMe for 60 days

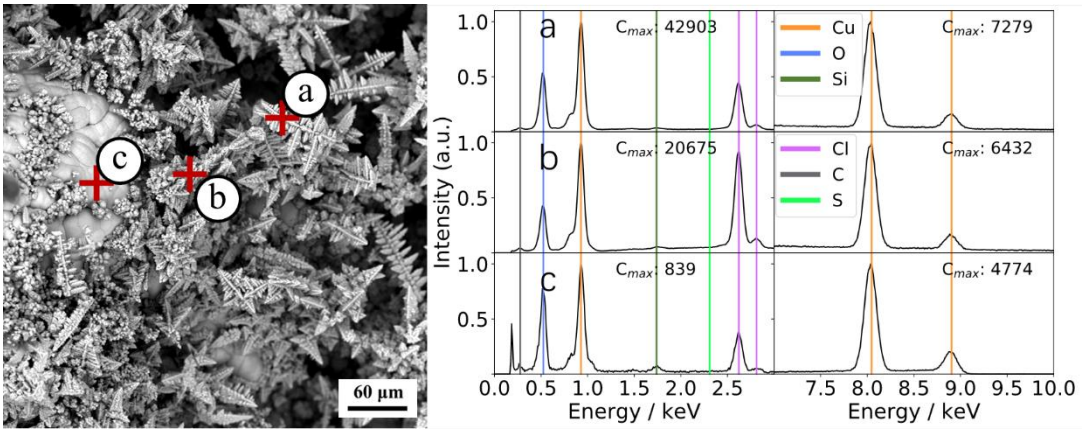

Figure A1.37 EDS elemental point analysis spectrum of pure Cu immersed in 3 wt.% NaCl solution with added 1mM SH-ImiMe for 60 days (a) (b) spectrum of point a and b, dendritic structure (c) spectrum of point c, white bulk.

Figure A1.38 shows the surface of pure Cu immersed in 3 wt.% NaCl with added 1mM OH-BimH for 60 days. **Figure A1.38** (a) and (c) shows the surface is mostly presents the same light grey, some part suffered for local attack and become darker. **Figure A1.38** (b) shows the 10000x magnification of surface, cubic crystal exists on the surface, and porous structure appears under the crystals. **Figure A1.38** (d) shows the local attacks on the surface. **Figure A1.39** shows the elemental map of the surface which is major composed of Cu and O. **Figure A1.40** is the point elemental analysis on different features. Compare with the cubic crystal on the surface, the porous structure presents less O, shown in point (a) and (b). Point (c) located on black part shows huge peak of Si indicates the exfoliation introduced local attack. OH-BimH is not effective inhibitor, which will assist the surface oxidation and keep this oxidation film during a long period.

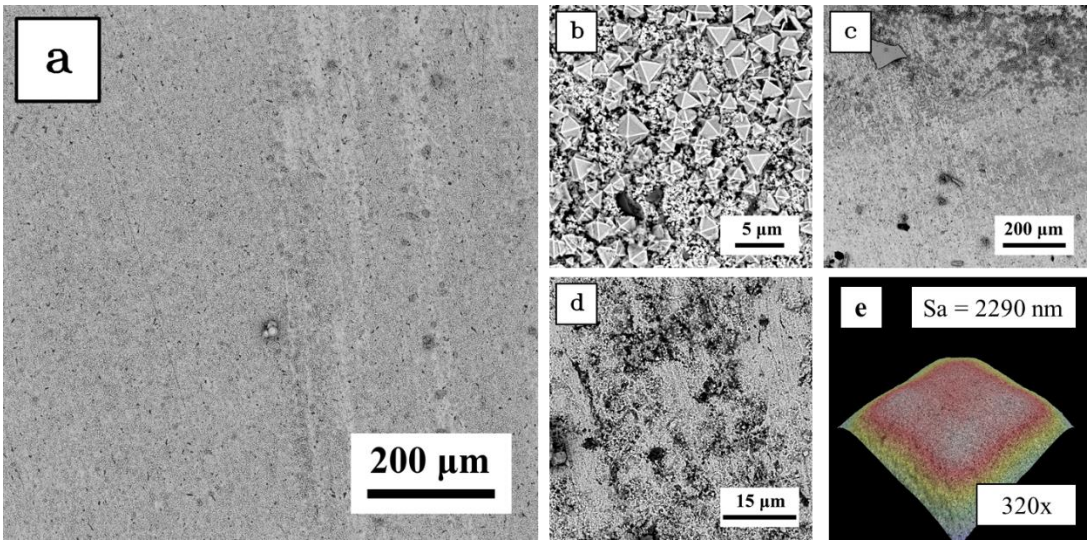

Figure A1.38 Pure Cu immersed in 3 wt.% NaCl with added 1mM OH-BimH solution for 60 days (a) surface under 320x magnification with all typical features (b) surface under 10000x magnification (c) surface with different features under 320x magnification (d) local attacks on the surface (e) 3D topography under 320x magnification by SEM

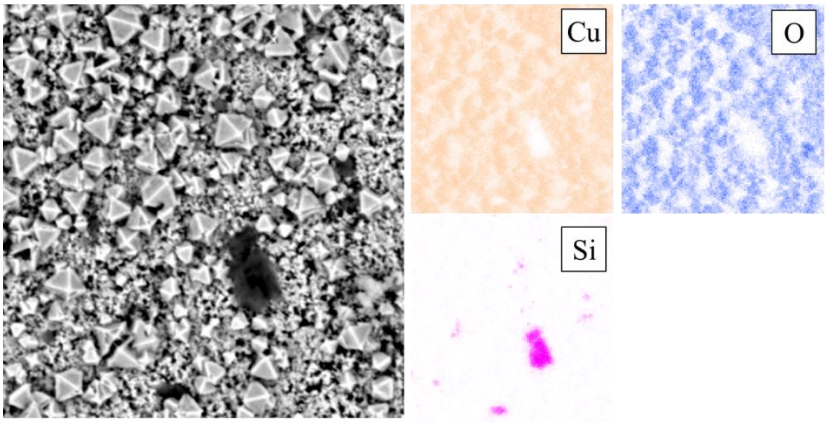

Figure A1.39 EDS elemental map analysis of pure Cu immersed in 3 wt.% NaCl solution with added 1mM OH-BimH for 60 days

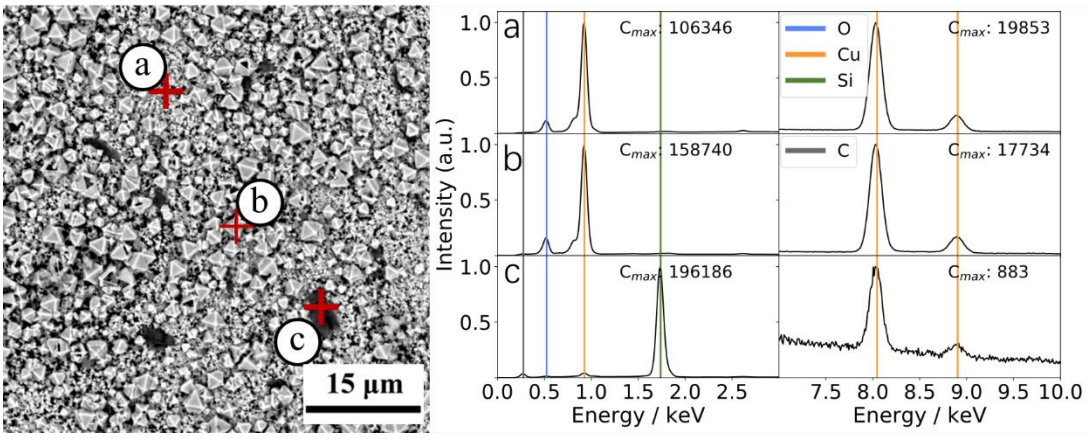

Figure A1.40 EDS elemental point analysis spectrum of pure Cu immersed in 3 wt.% NaCl solution with added 1mM OH-BimH for 60 days (a) spectrum of point a, porous surface (b) spectrum of point b, cubic particles on the surface (c) spectrum of point c, black part of the surface.

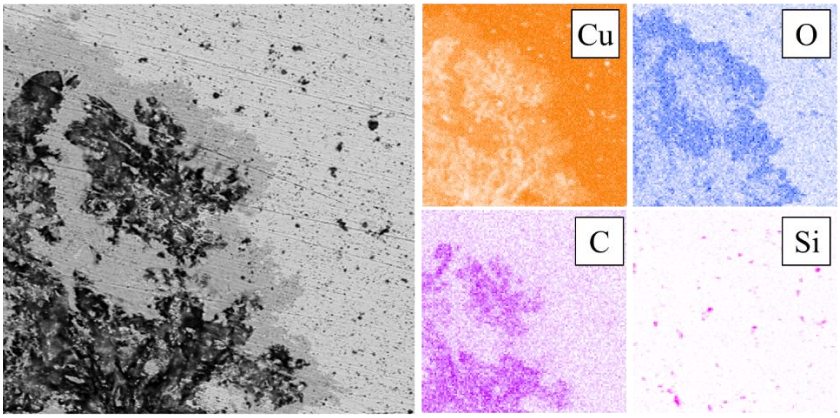

Figure A1.41 EDS elemental map analysis of pure Cu immersed in 3 wt.% NaCl solution with added 1mM OH-Me-BimH for 60 days

A1.2 Corrosion Inhibition of Zinc

A1.2.1 Short-term and long-term electrochemical tests

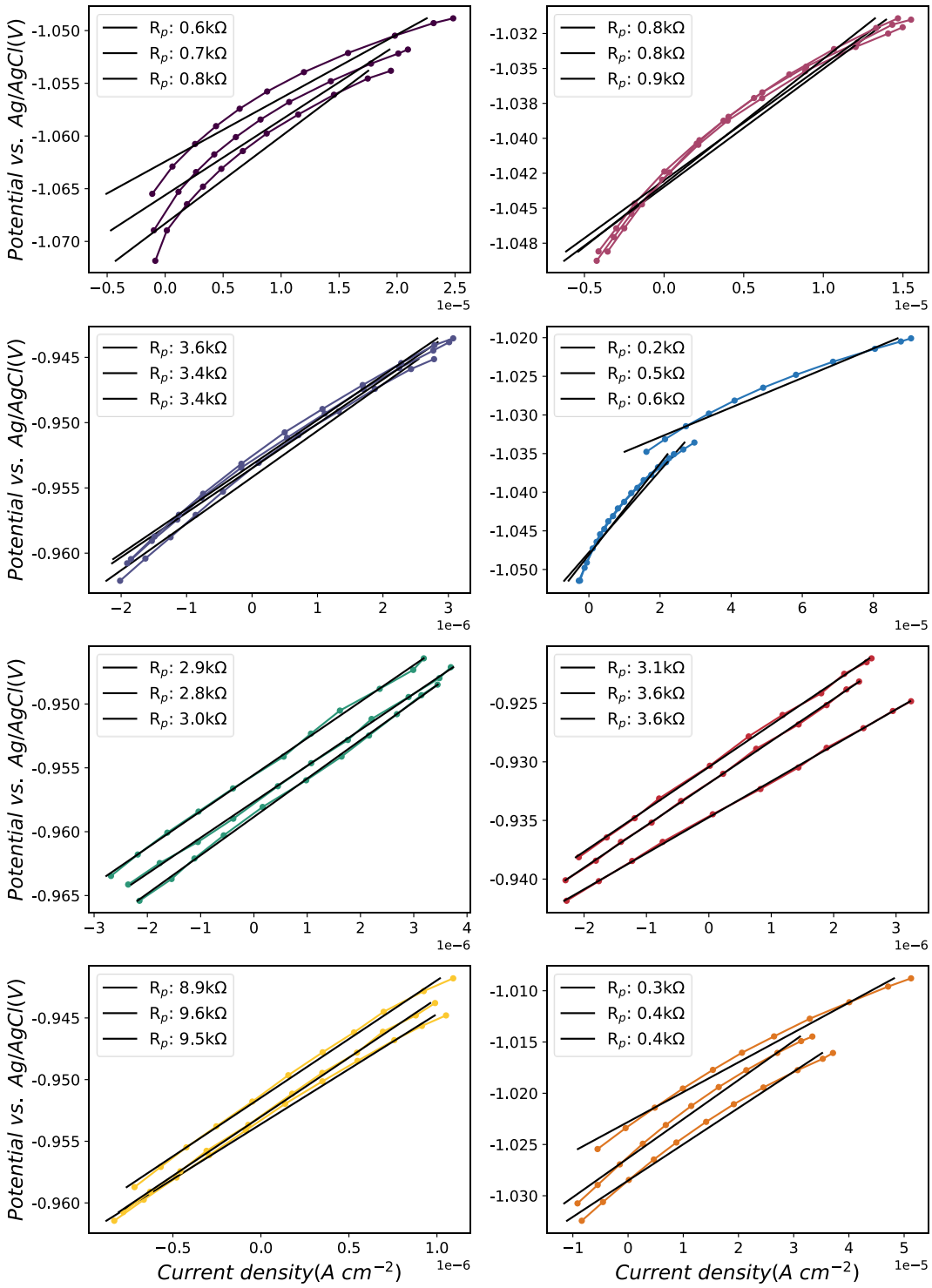

Figure A1.42 All linear polarization resistance curves of pure Zn with and without inhibitors in 3 wt.% NaCl solution after immersion for 1 h

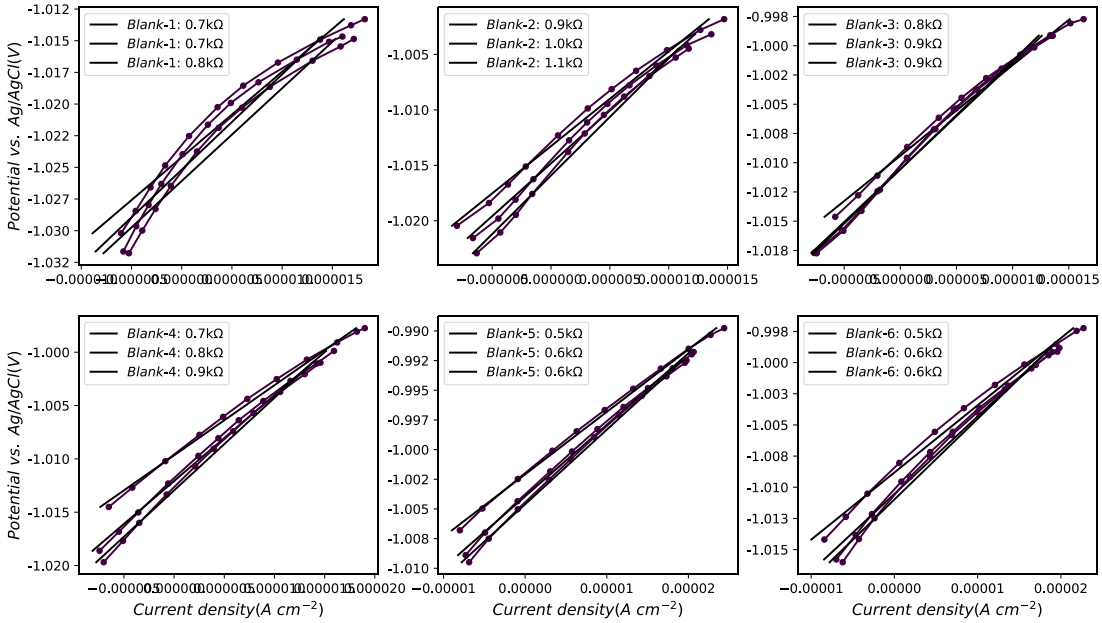

Figure A1.43 Long-term linear polarization curves of pure Zn under the 120h period of testing of the alloy in the presence of the inhibitor in the 3 wt.% NaCl aqueous solution without inhibitors

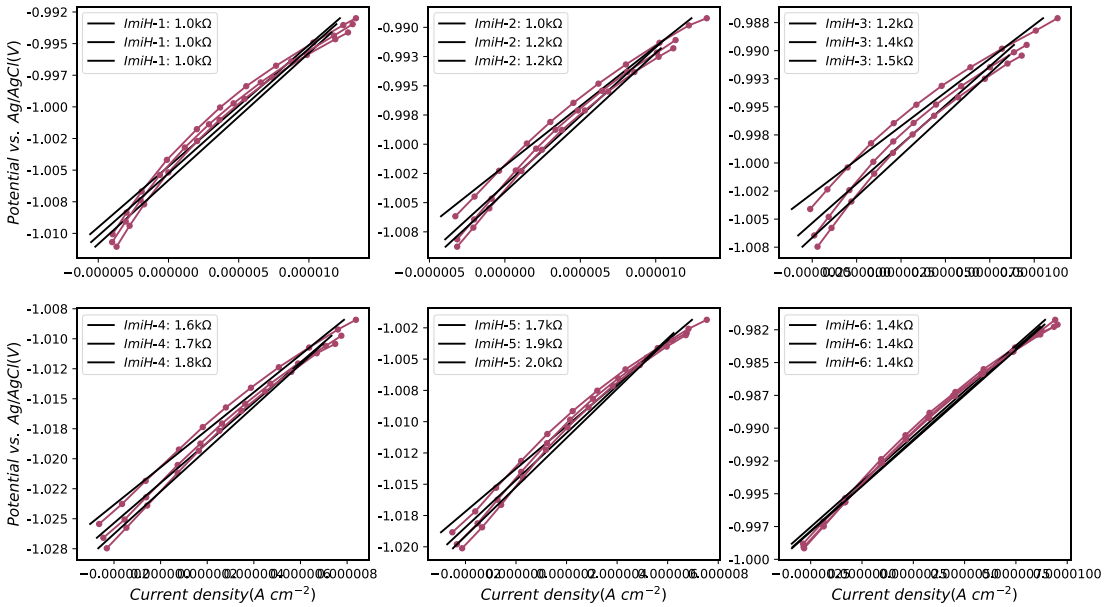

Figure A1.44 Long-term linear polarization curves of pure Zn under the 120h period of testing of the alloy in the presence of the inhibitor in the 3 wt.% NaCl aqueous solution with ImiH

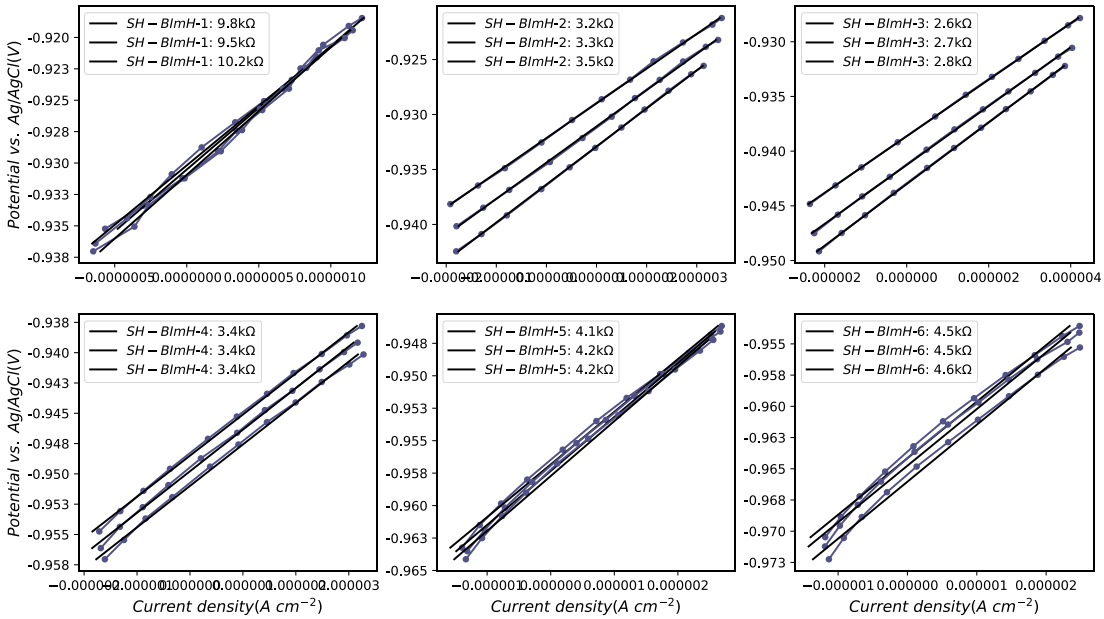

Figure A1.45 Long-term linear polarization curves of pure Zn under the 120h period of testing of the alloy in the presence of the inhibitor in the 3 wt.% NaCl aqueous solution with SH-BimH

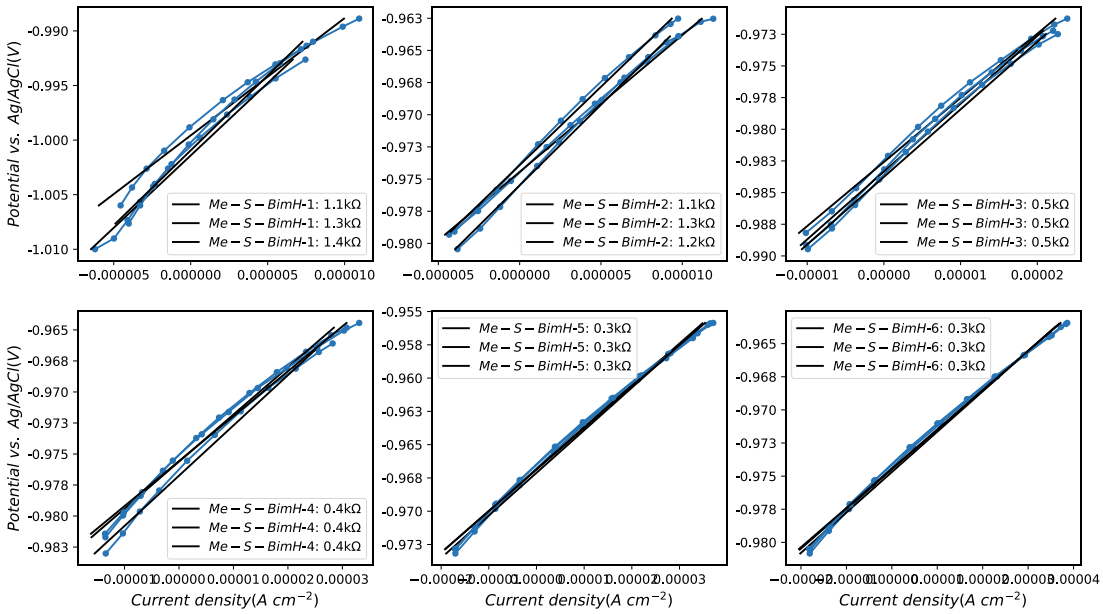

Figure A1.46 Long-term linear polarization curves of pure Zn under the 120h period of testing of the alloy in the presence of the inhibitor in the 3 wt.% NaCl aqueous solution with Me-S-BimH

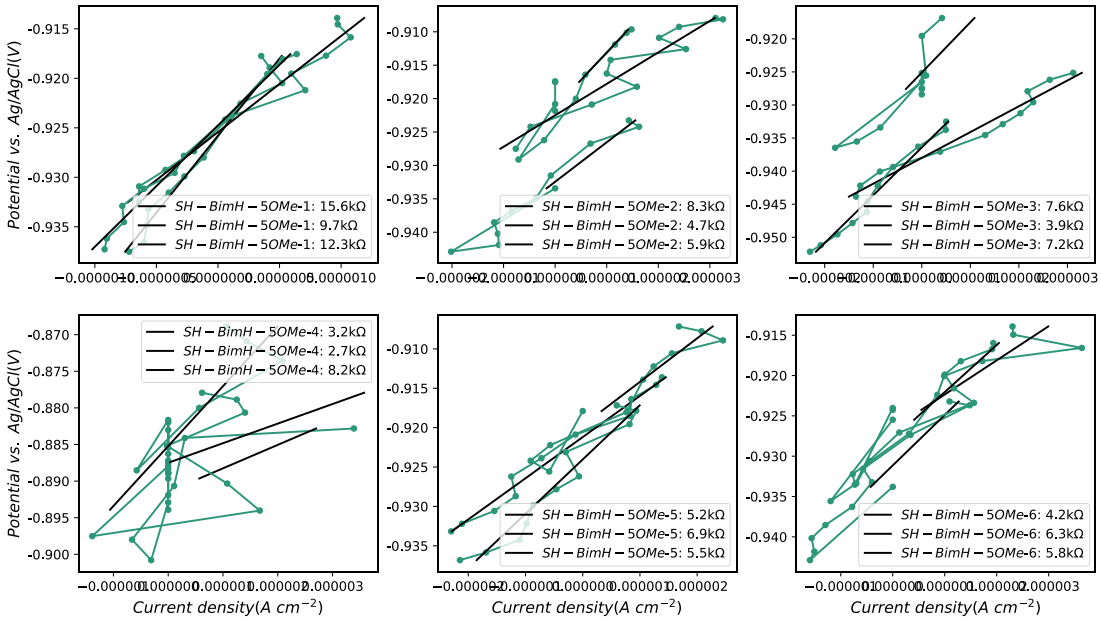

Figure A1.47 Long-term linear polarization curves of pure Zn under the 120h period of testing of the alloy in the presence of the inhibitor in the 3 wt.% NaCl aqueous solution with SH-BimH-5OMe

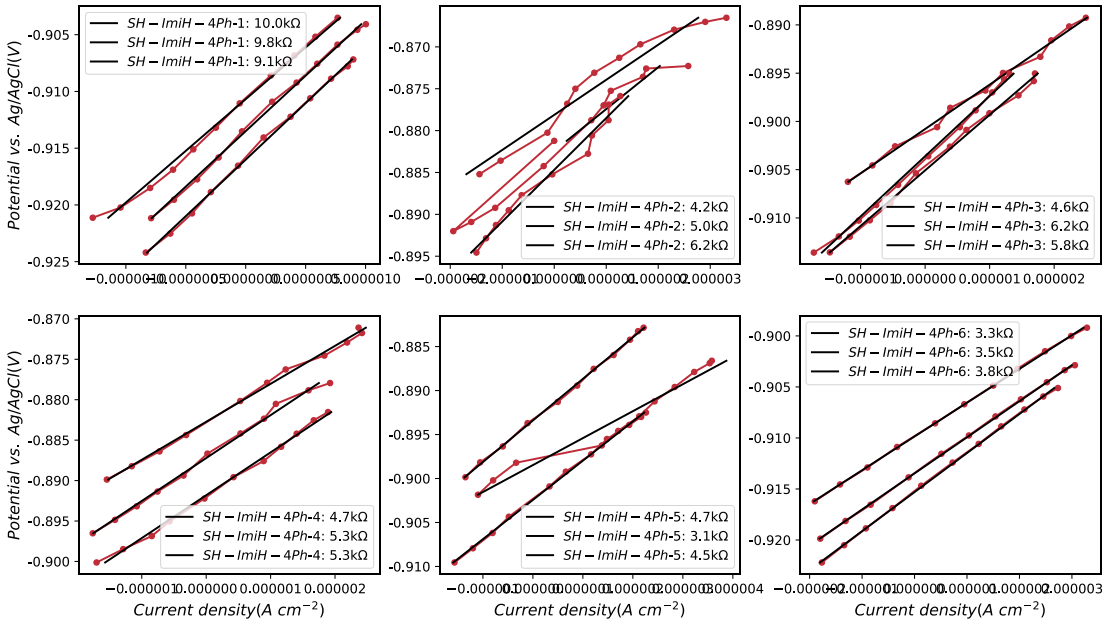

Figure A1.48 Long-term linear polarization curves of pure Zn under the 120h period of testing of the alloy in the presence of the inhibitor in the 3 wt.% NaCl aqueous solution with SH-ImiH-4Ph

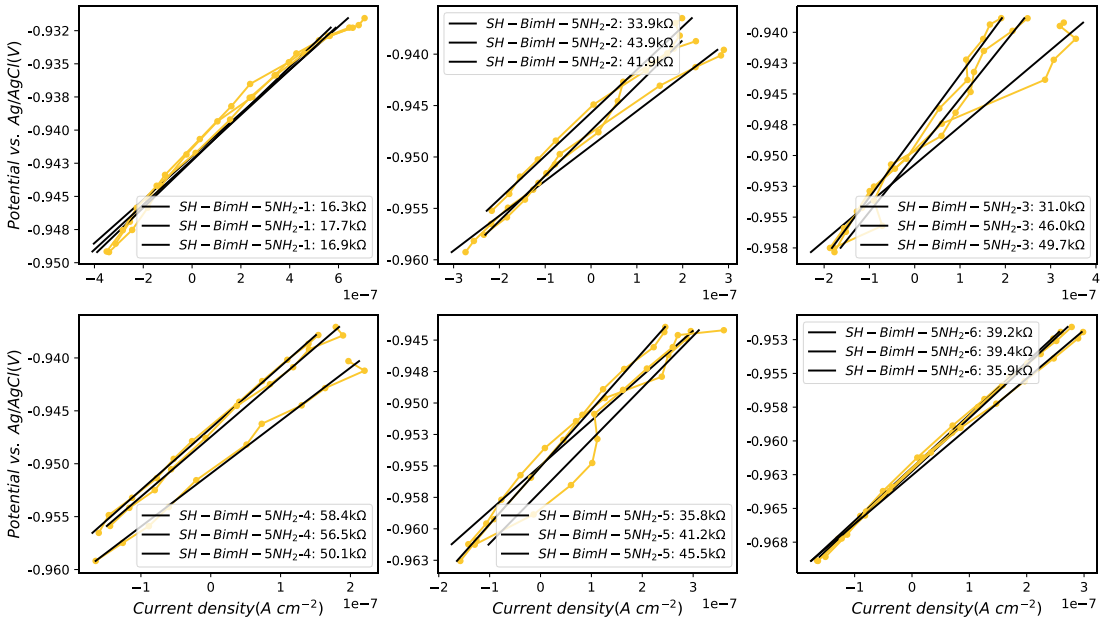

Figure A1.49 Long-term linear polarization curves of pure Zn under the 120h period of testing of the alloy in the presence of the inhibitor in the 3 wt.% NaCl aqueous solution with SH-BimH-5NH$_2$

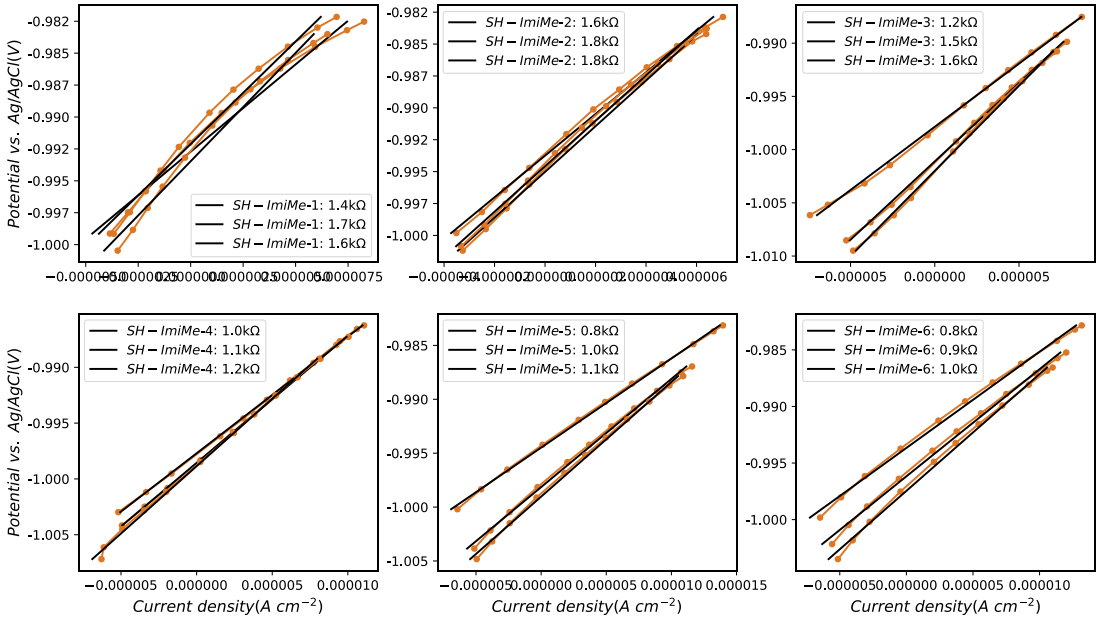

Figure A1.50 Long-term linear polarization curves of pure Zn under the 120h period of testing of the alloy in the presence of the inhibitor in the 3 wt.% NaCl aqueous solution with SH-ImiMe

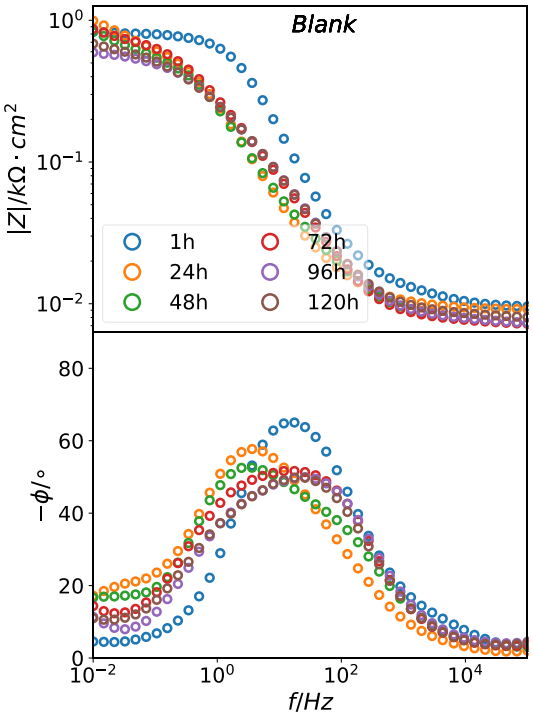

Figure A1.51 Long-term EIS impedance and phase diagram of pure Zn in NaCl, in period of 120h without inhibitor

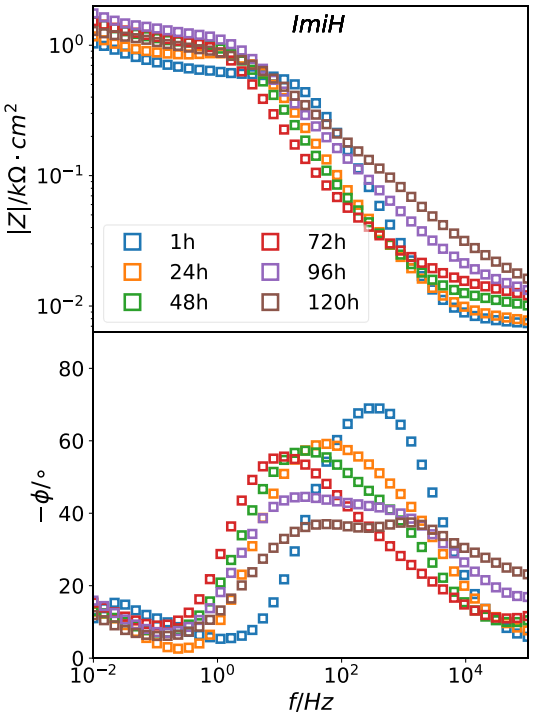

Figure A1.52 Long-term EIS impedance and phase diagram of pure Zn in NaCl, in period of 120h with ImiH

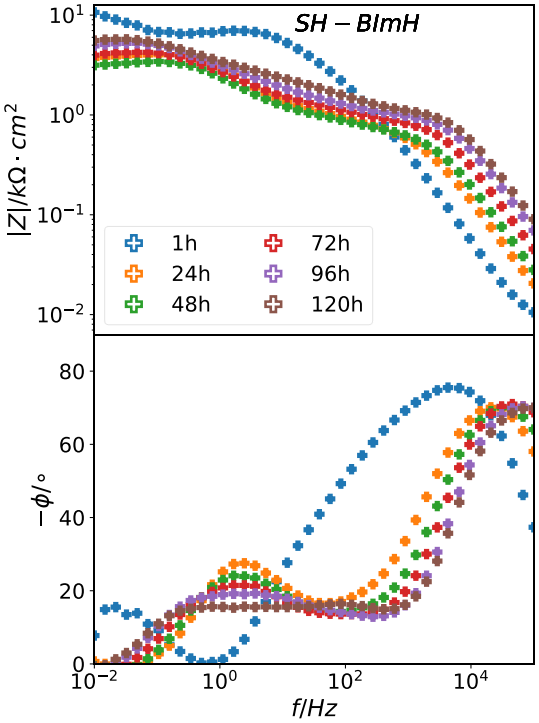

Figure A1.53 Long-term EIS impedance and phase diagram of pure Zn in NaCl, in period of 120h with SH-BimH

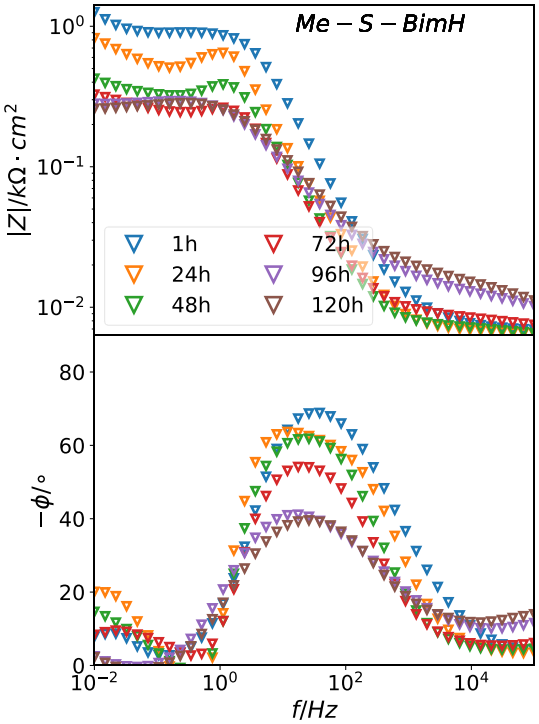

Figure A1.54 Long-term EIS impedance and phase diagram of pure Zn in NaCl, in period of 120h with Me-S-BimH

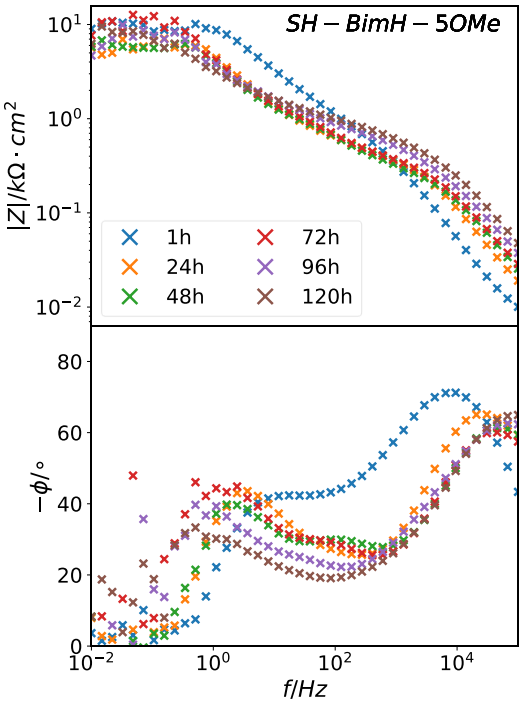

Figure A1.55 Long-term EIS impedance and phase diagram of pure Zn in NaCl, in period of 120h with SH-BimH-5OMe

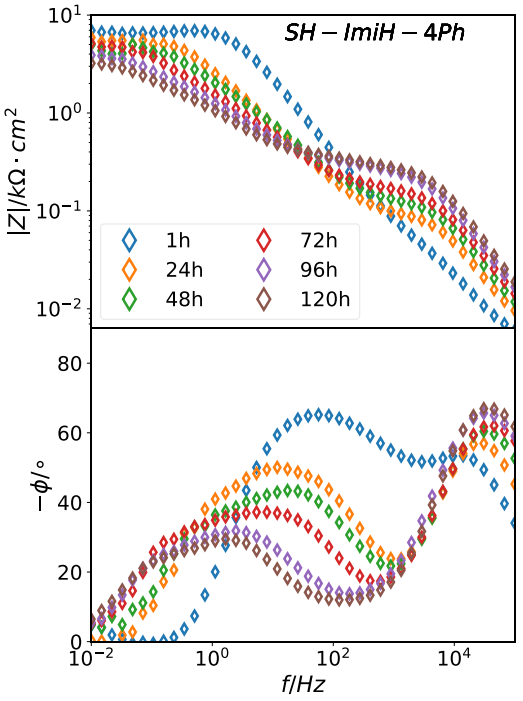

Figure A1.56 Long-term EIS impedance and phase diagram of pure Zn in NaCl, in period of 120h with SH-ImiH-4Ph

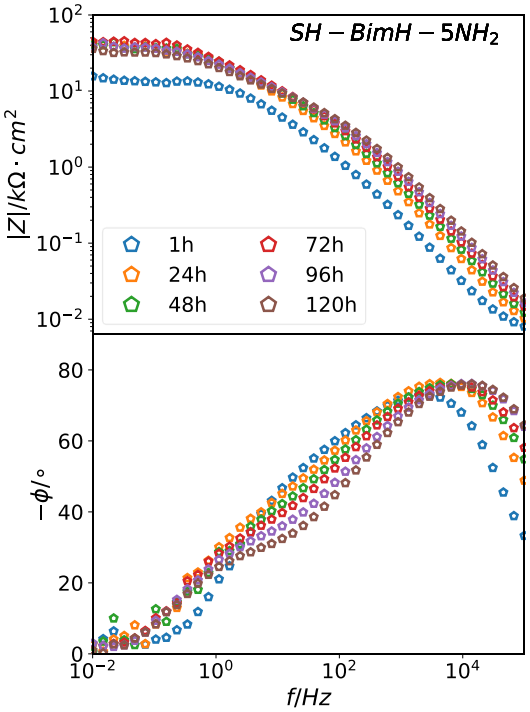

Figure A1.57 Long-term EIS impedance and phase diagram of pure Zn in NaCl, in period of 120h without SH-BimH-5NH_2

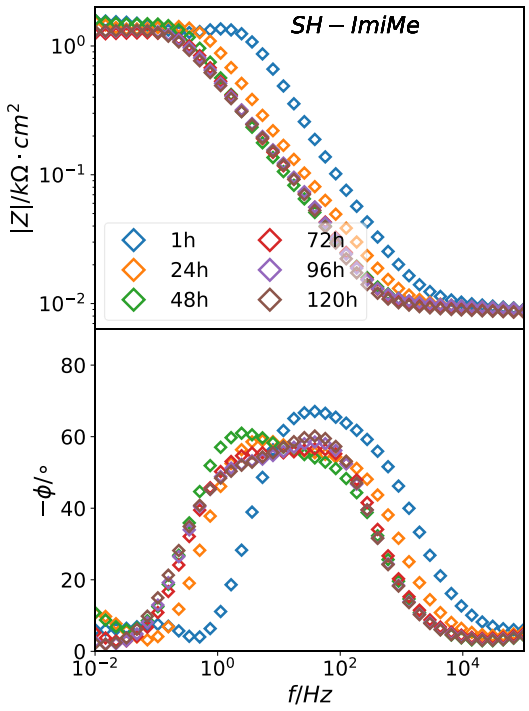

Figure A1.58 Long-term EIS impedance and phase diagram of pure Zn in NaCl, in period of 120h with SH-ImiMe

A1.2.2 Immersion test of pure Zn

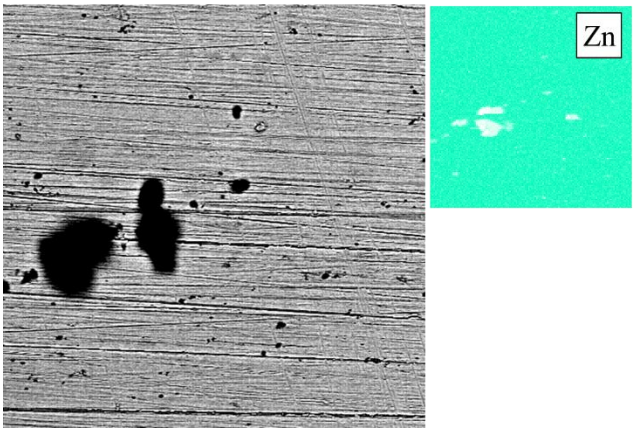

Figure A1.59 EDX elemental map analysis of the bare sample under 1000x magnification

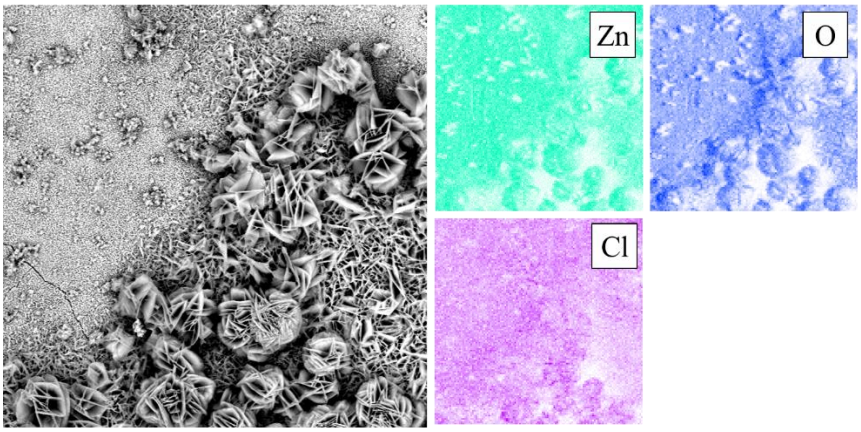

Figure A1.60 EDX elemental map analysis of Pure Zn immersed in 3 wt.% NaCl solution for 12 days

Figure A1.61 shows the surface of pure Zn immersed in 3 wt.% NaCl with added 1mM ImiH for 12 days. As shown in **Figure A1.61** (a) and (b), some big hemispheres appear on the surface. The surface is of hemispheres are composed of porous structure, see **Figure A1.61** (d). In **Figure A1.61** (c), cracks appear in some part along the surface. **Figure A1.62** shows the elemental map, and the distribution is similar to that of surface with 3 wt.% NaCl, that are Zn, Cl and O. **Figure A1.63** shows the point analysis of the surface, All three points show the same peaks and intensities. ImiH introduced a small scale porous surface which is not an inhibitor for pure Zn.

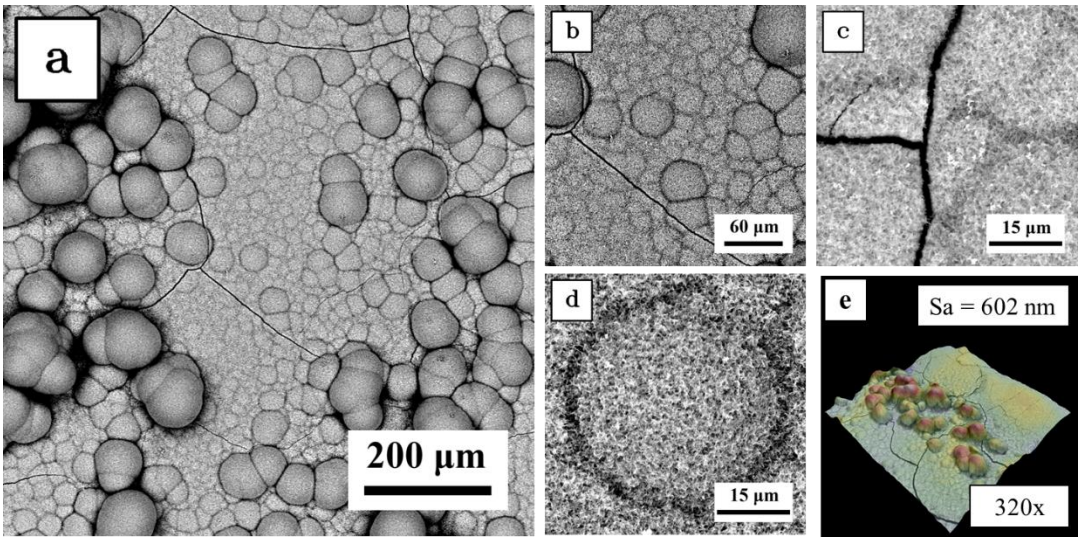

Figure A1.61 Pure Zn immersed in 3 wt.% NaCl with added 1mM ImiH solution for 12 days (a) surface under 320x magnification with all typical features (b) surface under 1000x magnification (c) cracks on the surface (d) hemisphere (e) 3D topography under 320x magnification by SEM

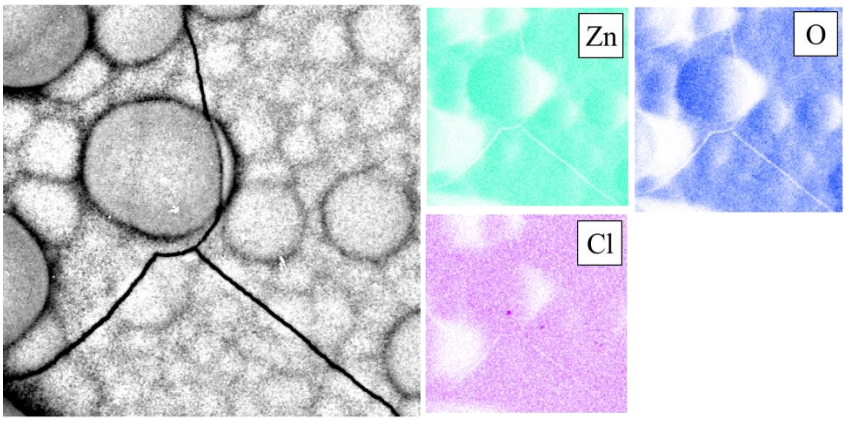

Figure A1.62 EDS elemental map analysis of Pure Zn immersed in 3 wt.% NaCl solution with added 1mM ImiH for 12 days

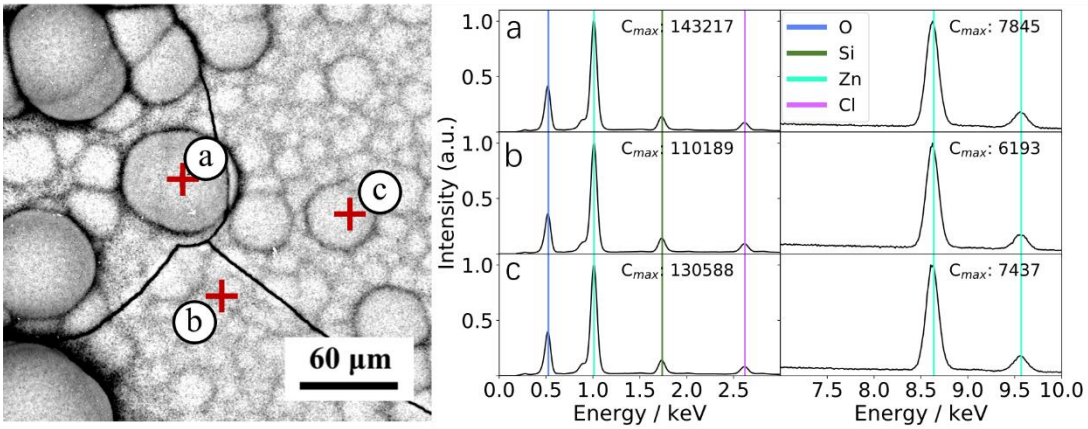

Figure A1.63 EDS elemental point analysis spectrum of Pure Zn immersed in 3 wt.% NaCl solution with added 1mM ImiH for 12 days (a) and (c) spectrum of point a and c, hemisphere on the surface (b) spectrum of point b, boundary between hemisphere

Figure A1.64 shows the surface of pure Zn after immersion in 3 wt.% NaCl with added SH-BimH for 12 days. As shown in **Figure A1.64** (a), some cracks appear, other parts are composed of dark grey and light grey under BSE. Scratches and exfoliations are disappeared in closer look in **Figure A1.64** (c) and (d), which indicates the surface is totally changed. **Figure A1.64** (e) shows the surface is a kind of plicated surface. **Figure A1.65** shows the elemental map of surface, Zn, Cl, O covered the surface, and present different concentration on different features. **Figure A1.66** shows the elemental point analysis on different features. Point (a) shows smallest Cl concentration than the rest ones, and it is on the light grey surface. As the darker of the surface, the ratio of Cl increases, shown in point (b) and (c). SH-BimH could not stop corrosion on pure Zn under this immersion condition.

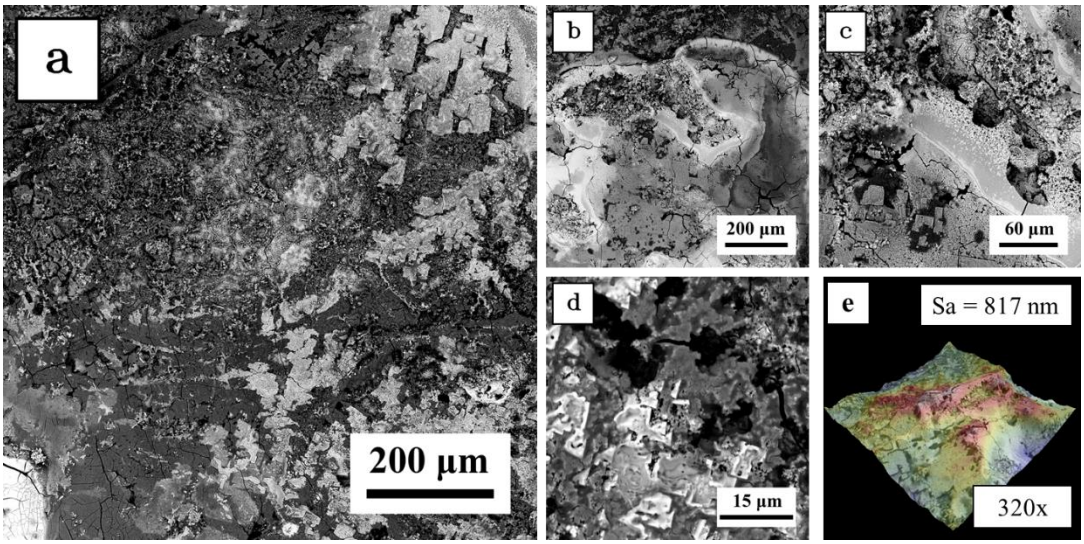

Figure A1.64 Pure Zn immersed in 3 wt.% NaCl with added 1mM SH-BimH solution for 12 days (a) surface under 320x magnification with all typical features (b) surface under 320x magnification (c) surface under 1000x magnification (d) cracks and holes on the surface (e) 3D topography under 1000x magnification by SEM

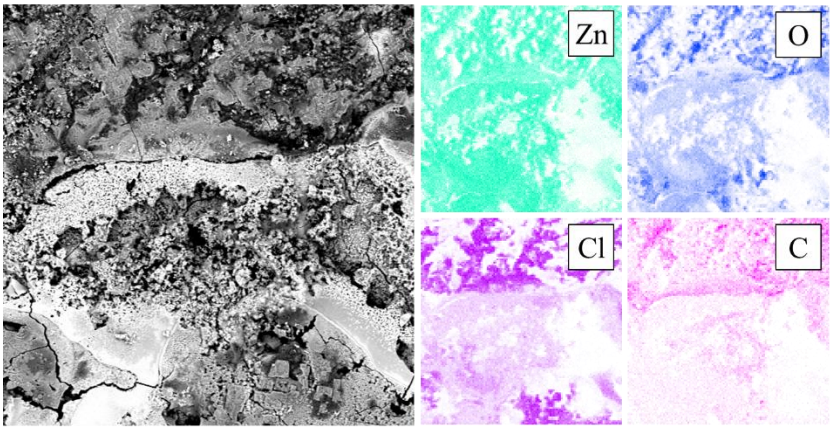

Figure A1.65 EDS elemental map analysis of Pure Zn immersed in 3 wt.% NaCl solution with added 1mM SH-BimH for 12 days

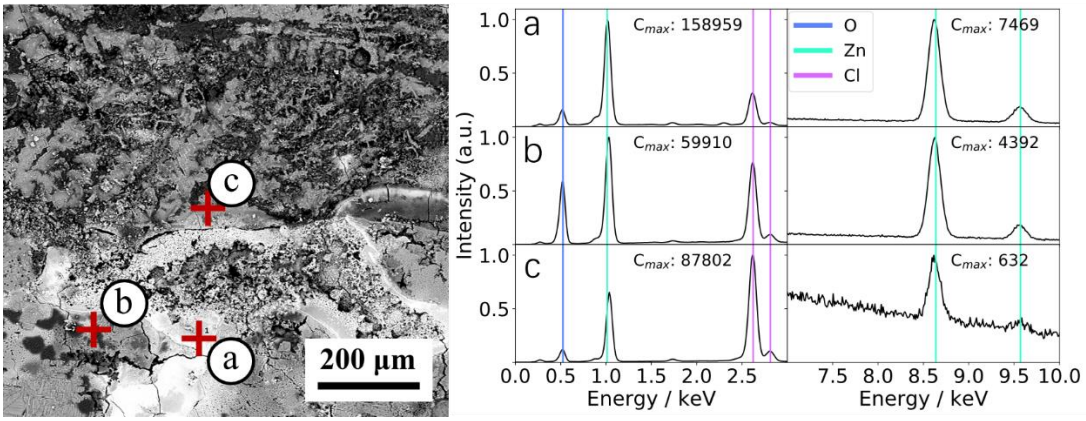

Figure A1.66 EDS elemental point analysis spectrum of Pure Zn immersed in 3 wt.% NaCl solution with added 1mM SH-BimH for 12 days (a) spectrum of point a, white part on the surface (b) spectrum of point b, black corroded part (c) spectrum of point c, grey part on the surface.

Figure A1.67 shows pure Zn surface immersed in 3wt. NaCl with added 1mM Me-S-BimH for 12 days. In **Figure A1.67** (a), big crack appears on the surface, and two different parts appear as well. The surface is destroyed in corrosive solution. As shown in **Figure A1.67** (b), (c) and (d), the two parts shows that the surface is full of porous and gaps. **Figure A1.68** shows the elemental map of the surface, light part contains much Zn and almost no O and Cl than that of dark part. Besides, point analysis in **Figure A1.69** shows the same results. Me-S-BimH could not improve the corrosion resistance for pure Zn in 3 wt.% NaCl.

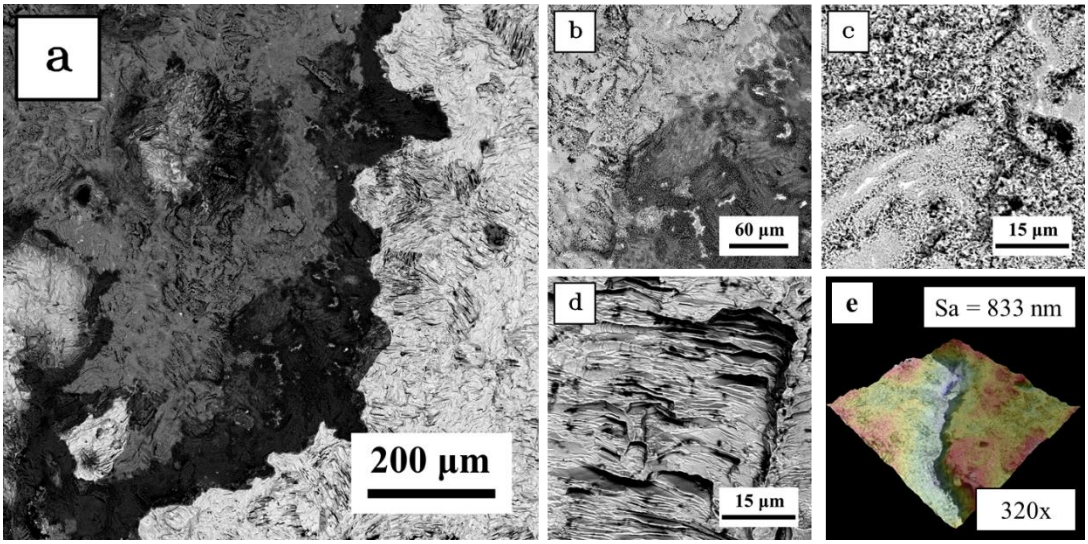

Figure A1.67 Pure Zn immersed in 3 wt.% NaCl with added 1mM Me-S-BimH solution for 12 days (a) surface under 320x magnification with all typical features (b) surface under 1000x magnification (c) surface under 5000x magnification (d) surface features on white part (e) 3D topography under 320x magnification by SEM

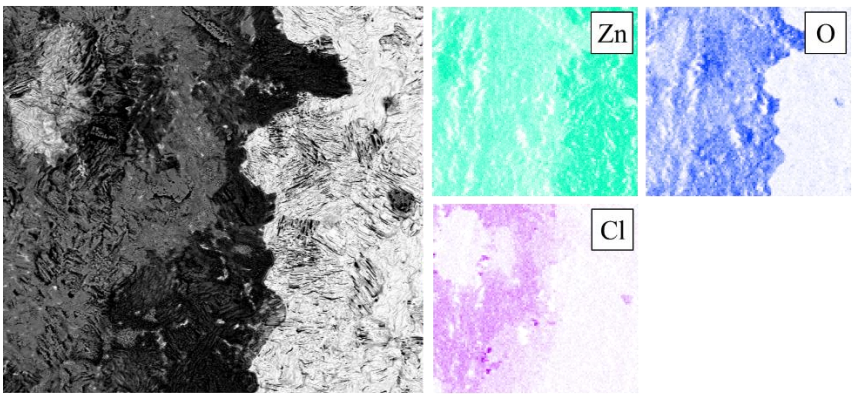

Figure A1.68 EDS elemental map analysis of Pure Zn immersed in 3 wt.% NaCl solution with added 1mM Me-S-BimH for 12 days

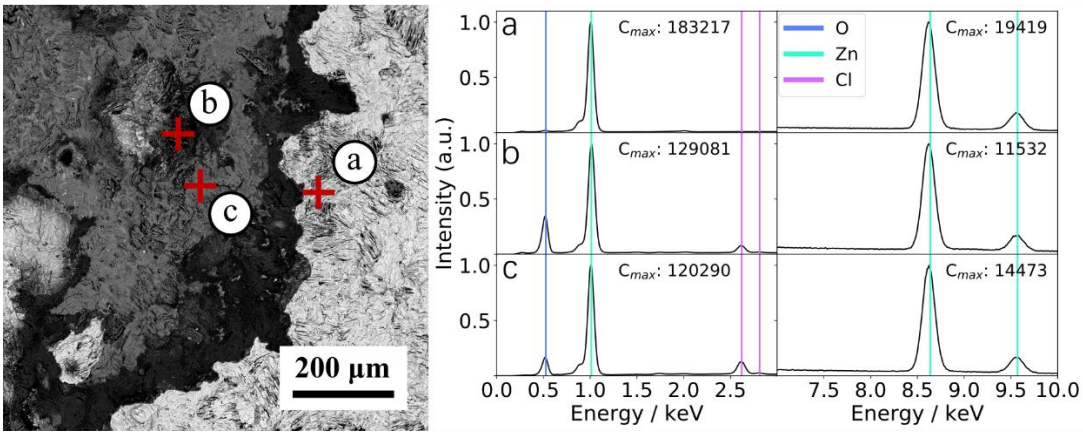

Figure A1.69 EDS elemental point analysis spectrum of Pure Zn immersed in 3 wt.% NaCl solution with added 1mM Me-S-BimH for 12 days (a) spectrum of point a, white part of the surface (b) spectrum of point b, black part of the surface (c) spectrum of point c, dark grey part of the surface.

Figure A1.70 shows the 12 days' immersed surface of pure Zn in 3 wt.% NaCl with added 1mM SH-BimH-5OMe solution. Different features such as cracks, dark part and long bulge, shown in **Figure A1.70** (a). As shown in **Figure A1.70** (c), little parts of the surface show inherited surface from the polished surface. In **Figure A1.70** (b) and (d), cracks and new substance appear on the surface. As shown in **Figure A1.70** (e), surface is fluctuant. **Figure A1.71** shows the existence of Zn, Cl, O, S, Si on the surface by elemental map. The point elemental analysis in **Figure A1.72** shows remained raw surface is covered by Zn, O, Cl in point (a). Besides, S appears which indicates the presence of inhibitor on the surface. Point (b) shows the bulge part is mostly Zn and O, which should be the redeposited Zn on the surface. Point (c) shows the adhesion of Zn-inhibitor complex on the cracks. SH-BimH-5OMe keeps some parts of the surface as raw condition, but most of the surface is destroyed. Furthermore, adhesion of Zn-inhibitor complex on local attack is found as well as on pure Cu.

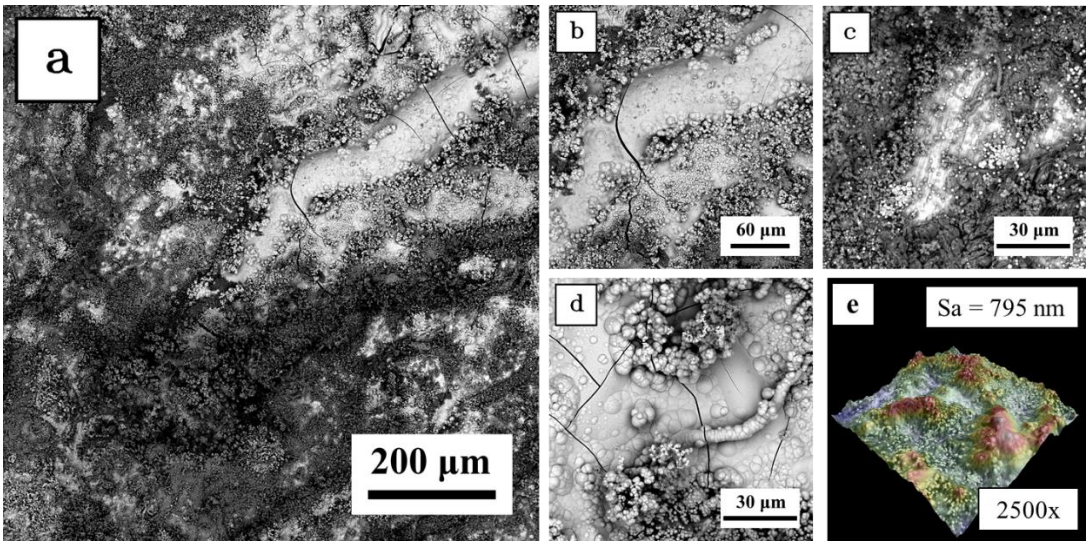

Figure A1.70 Pure Zn immersed in 3 wt.% NaCl with added 1mM SH-BimH-5OMe solution for 12 days (a) surface under 320x magnification with all typical features (b) long bulge on surface under 1000x magnification (c) white flat surface under 2500x magnification (d) cracks and corrosion products (e) 3D topography under 320x magnification by SEM

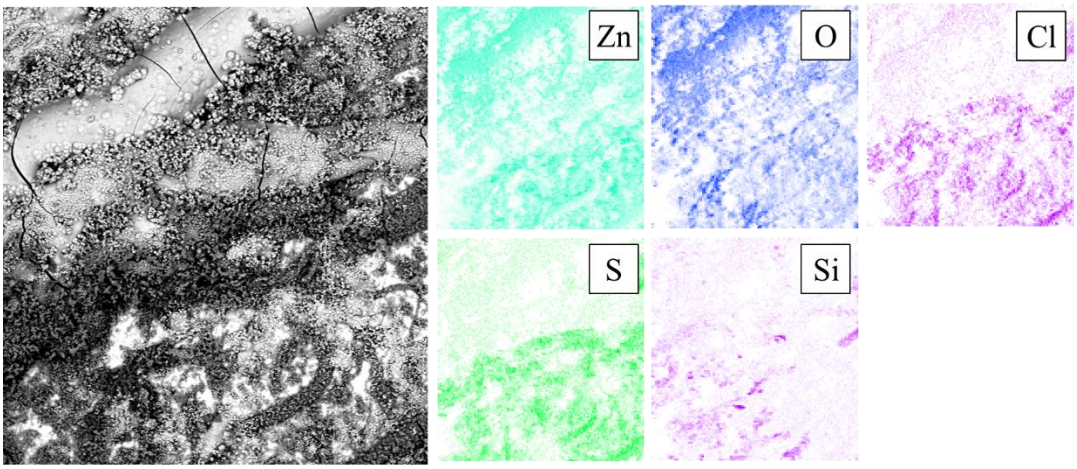

Figure A1.71 EDS elemental map analysis of Pure Zn immersed in 3 wt.% NaCl solution with added 1mM SH-BimH-5OMe for 12 days

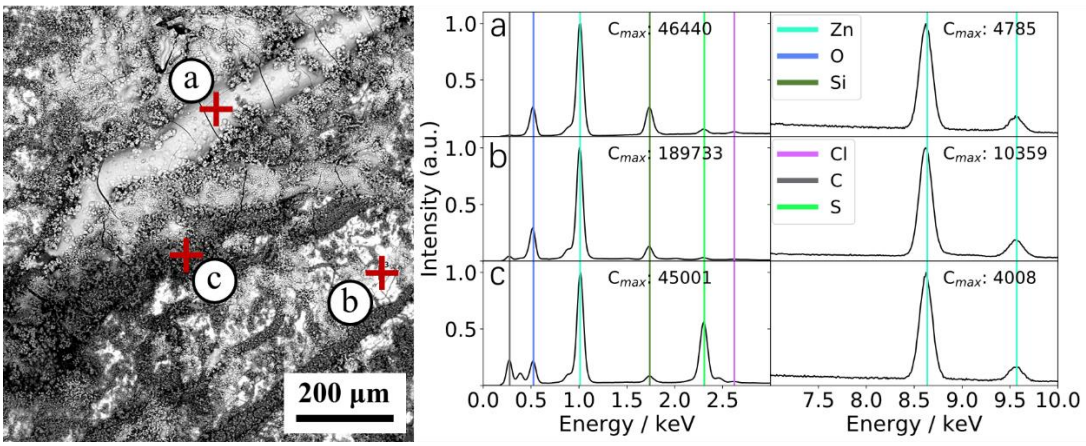

Figure A1.72 EDS elemental point analysis spectrum of Pure Zn immersed in 3 wt.% NaCl solution with added 1mM SH-BimH-5OMe for 12 days (a) spectrum of point a, white bulge on the surface (b) spectrum of point b, white flat surface (c) spectrum of point c, black corrosion products.

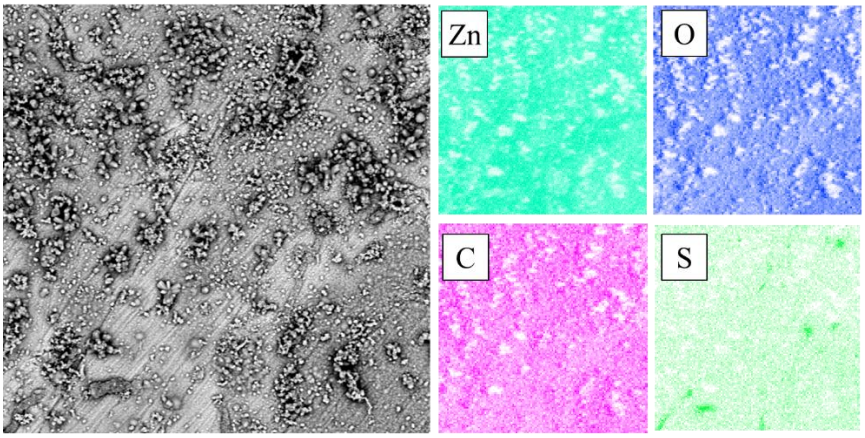

Figure A1.73 EDS elemental map analysis of Pure Zn immersed in 3 wt.% NaCl solution with added 1mM SH-ImiH-4Ph for 12 days

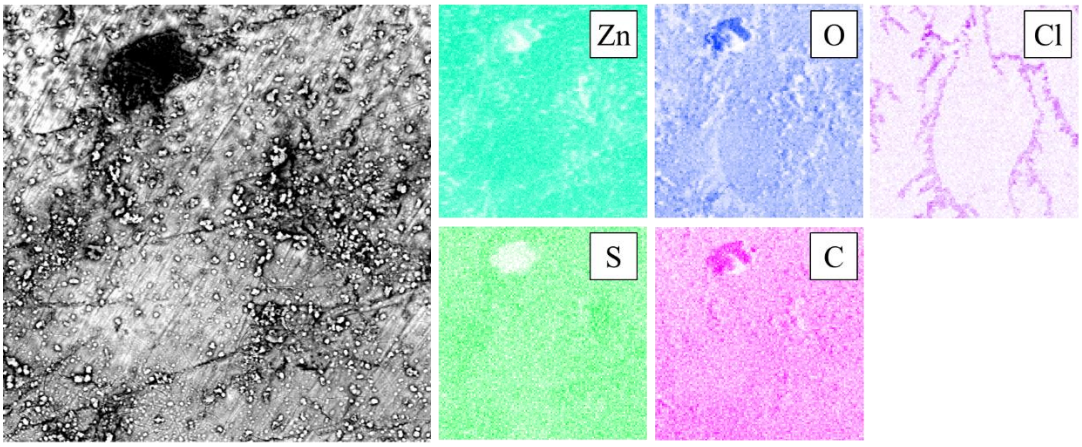

Figure A1.74 EDS elemental map analysis of Pure Zn immersed in 3 wt.% NaCl solution with added 1mM SH-BimH-5NH_2 for 12 days

Figure A1.75 shows the surface of pure Zn immersed in 3 wt.% NaCl with added SH-ImiMe for 12 days. As shown in **Figure A1.75** (a), the surface is reconstructed. Which is

different from the bare surface and shows a fluctuant look. The light part is condense as shown in **Figure A1.75** (c), and the dark parts present cracks and porous structure as shown in **Figure A1.75** (b) and (d). **Figure A1.76** and **Figure A1.77** show the elemental map and point analysis of the surface. They both confirm that the dark part is composed of O and Zn, and light part is close to pure Zn. SH-ImiMe could reconstruct or remove surface materials of pure Zn which indicates it is not an inhibitor for pure Zn.

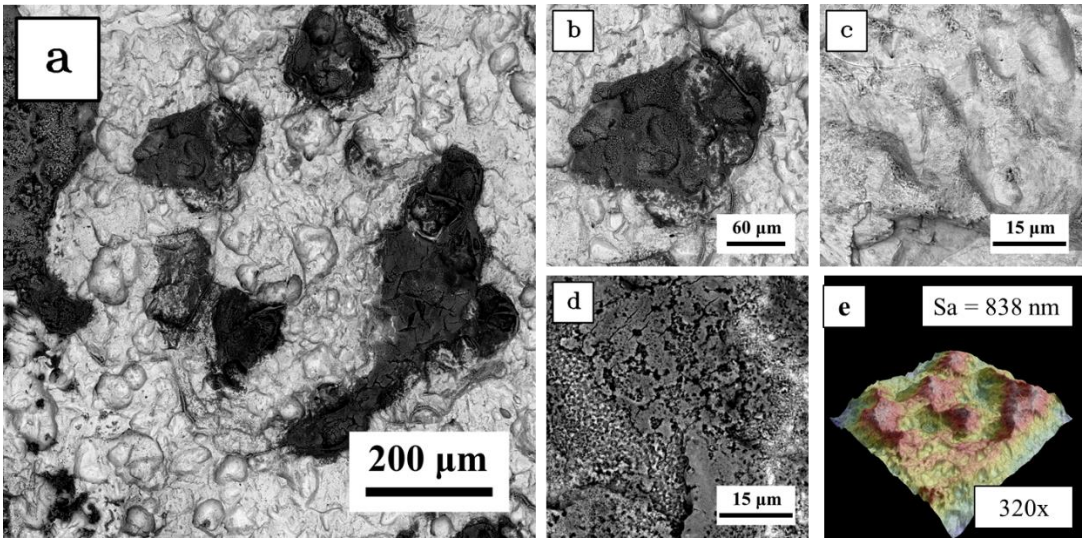

Figure A1.75 Pure Zn immersed in 3 wt.% NaCl with added 1mM SH-ImiMe solution for 12 days (a) surface under 320x magnification with all typical features (b) dark part of surface under 1000x magnification (c) white part of the surface under 5000x magnification (d) porous of dark part (e) 3D topography under 320x magnification by SEM

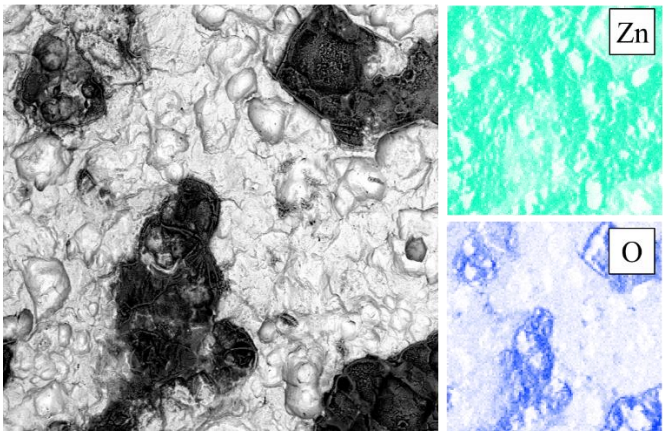

Figure A1.76 EDS elemental map analysis of Pure Zn immersed in 3 wt.% NaCl solution with added 1mM SH-ImiMe for 12 days

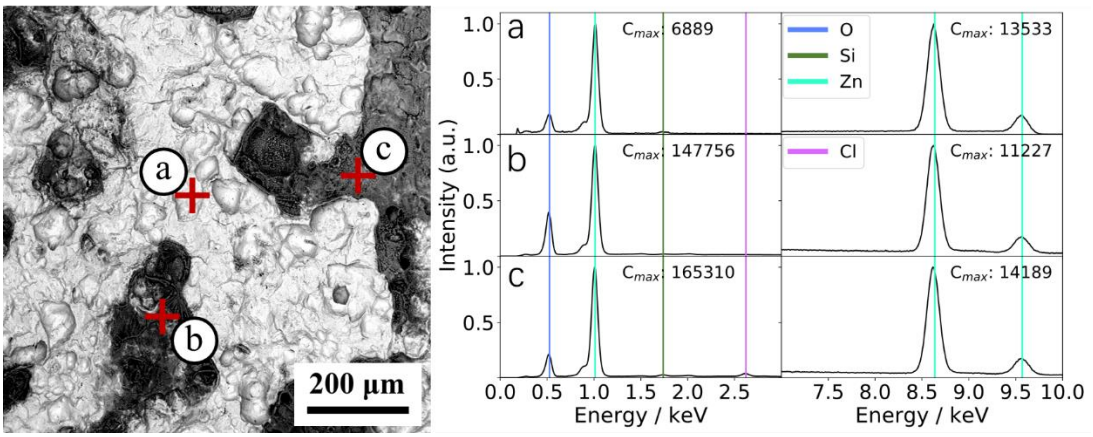

Figure A1.77 EDS elemental point analysis spectrum of Pure Zn immersed in 3 wt.% NaCl solution with added 1mM SH-ImiMe for 12 days (a) spectrum of point a, white part of the surface (b) spectrum of point b and c, dark part of the surface

A1.3 Corrosion Inhibition of Zirconium

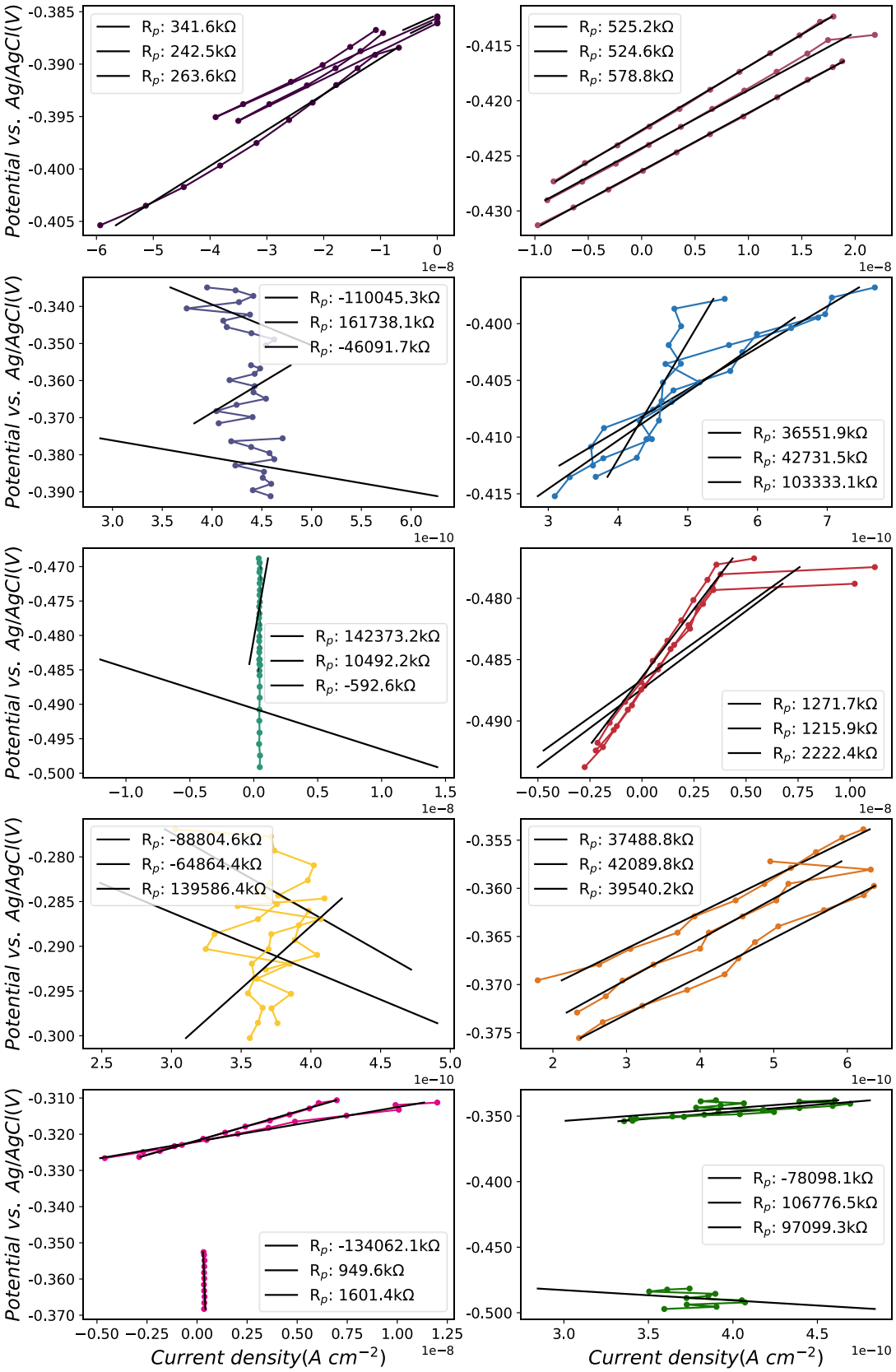

Figure A1.78 All linear polarization resistance curves of pure copper Zr with and without inhibitors

Appendix 2: Corrosion on CuZn alloys. Supplemental information.

A2.1 Short-term and long-term electrochemical tests of CuZn alloys

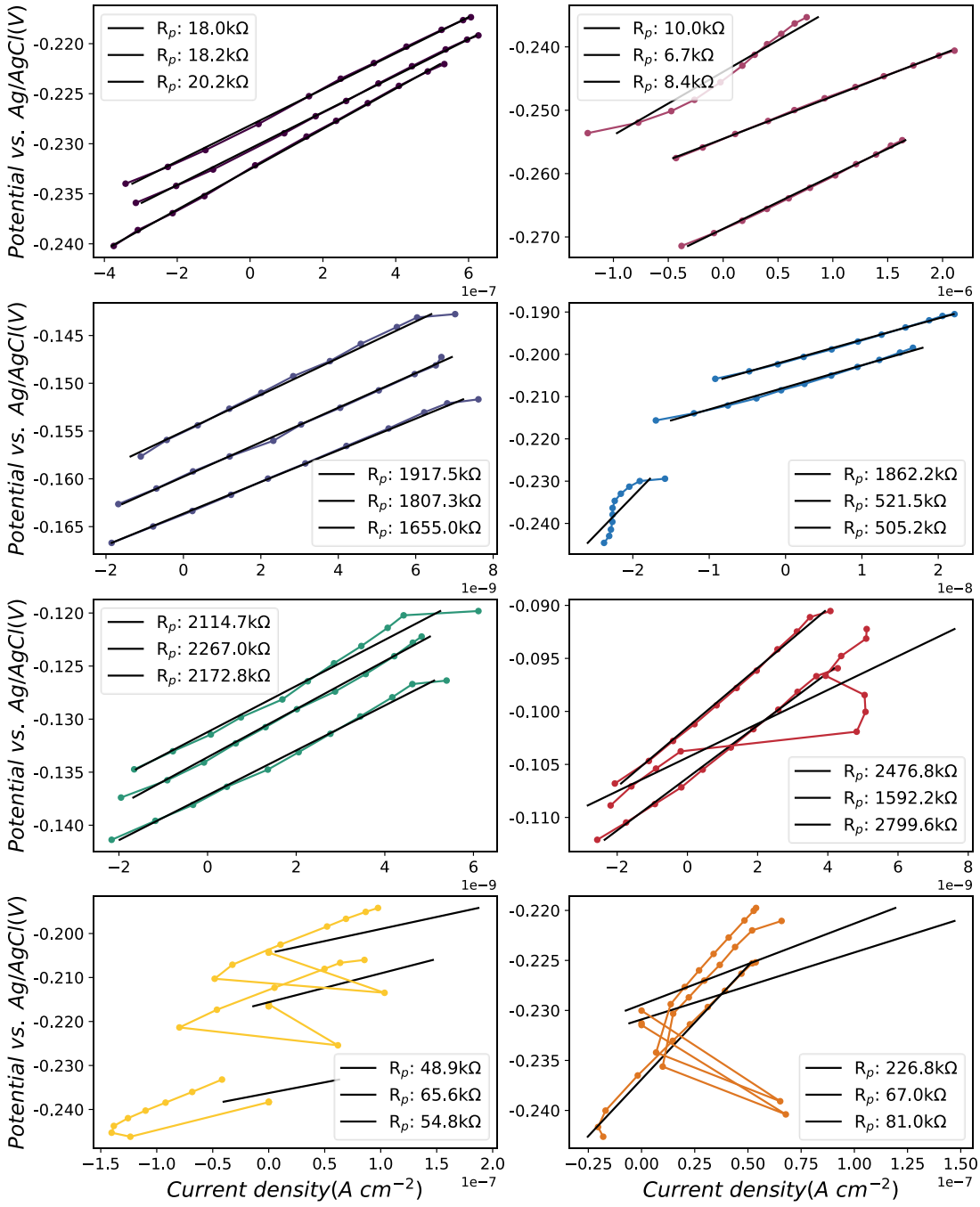

Figure A2.1 All linear polarization resistance curves of $Cu_{70}Zn_{30}$ alloy with and without inhibitors in 3 wt.% NaCl solution after immersion for 1 h

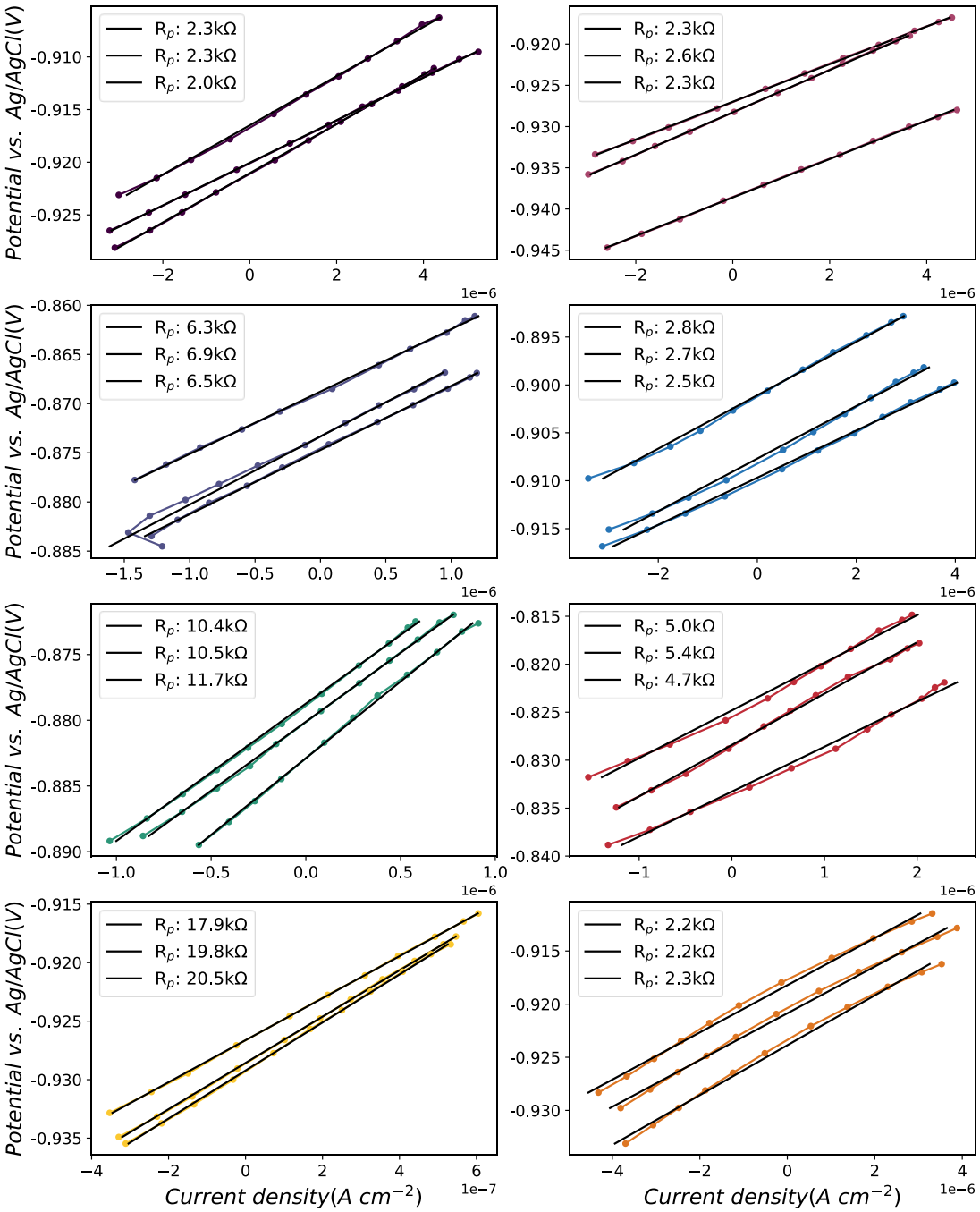

Figure A2.2 All linear polarization resistance curves of $Cu_{30}Zn_{70}$ alloy with and without inhibitors in 3 wt.% NaCl solution after immersion for 1 h

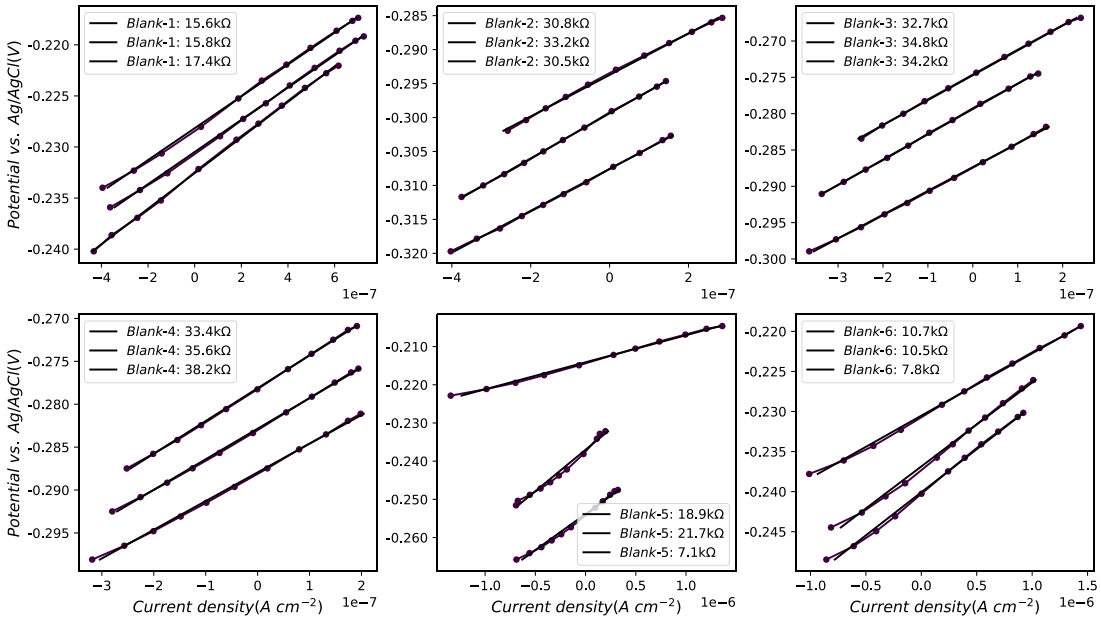

Figure A2.3 Long-term linear polarization curves of $Cu_{70}Zn_{30}$ alloy under the 120h period of testing of the alloy in the presence of the inhibitor in the 3 wt.% NaCl aqueous solution without inhibitors

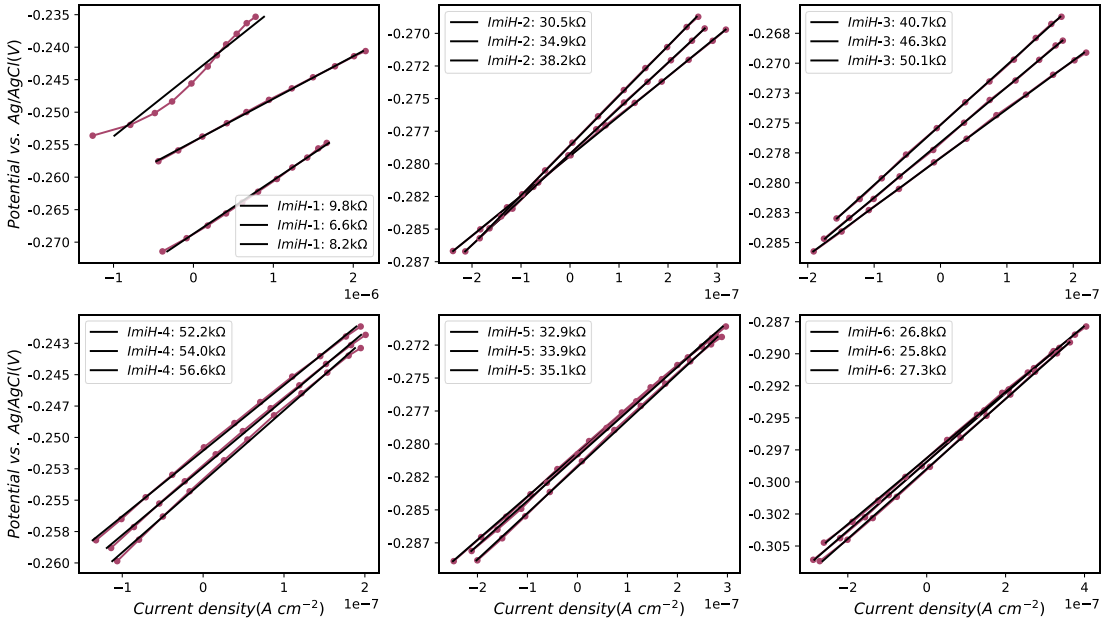

Figure A2.4 Long-term linear polarization curves of $Cu_{70}Zn_{30}$ alloy under the 120h period of testing of the alloy in the presence of the inhibitor in the 3 wt.% NaCl aqueous solution with ImiH

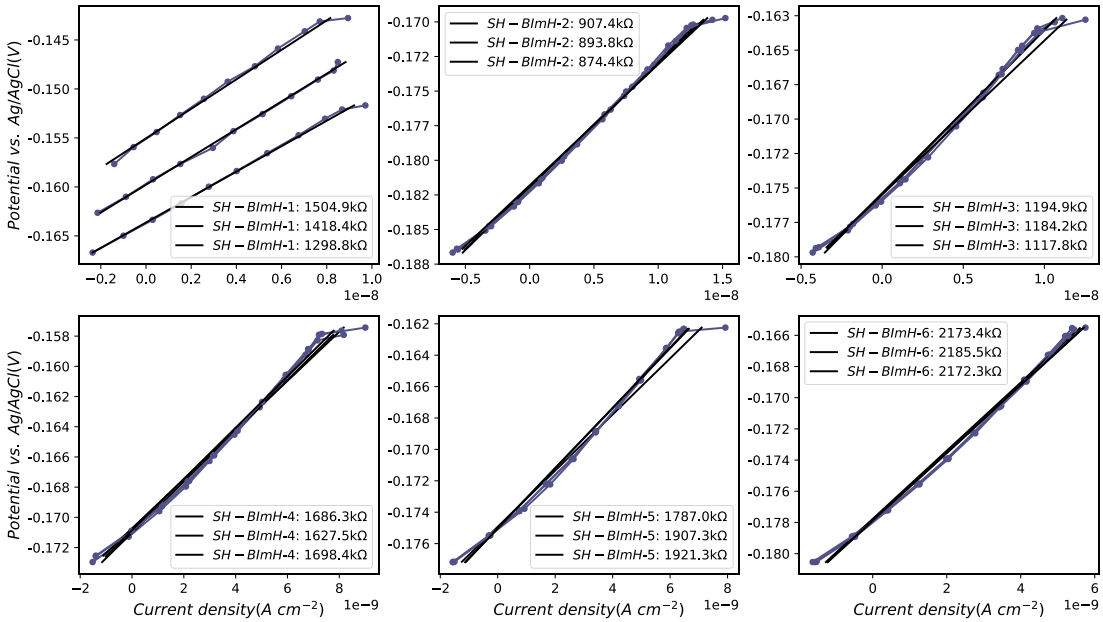

Figure A2.5 Long-term linear polarization curves of $Cu_{70}Zn_{30}$ alloy under the 120h period of testing of the alloy in the presence of the inhibitor in the 3 wt.% NaCl aqueous solution with SH-BimH

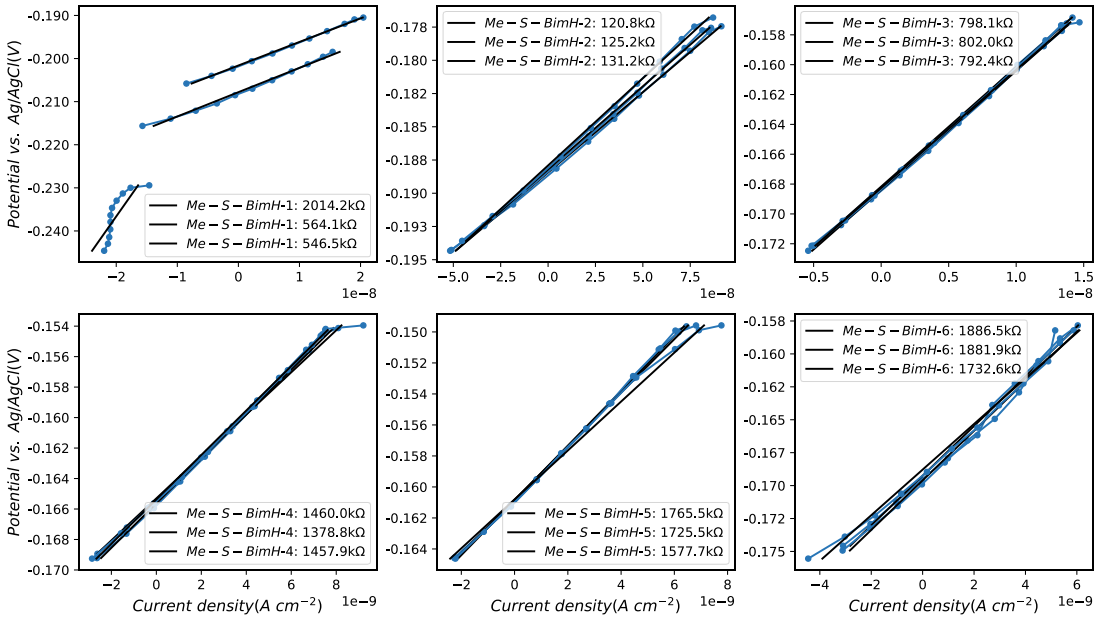

Figure A2.6 Long-term linear polarization curves of $Cu_{70}Zn_{30}$ alloy under the 120h period of testing of the alloy in the presence of the inhibitor in the 3 wt.% NaCl aqueous solution with Me-S-BimH

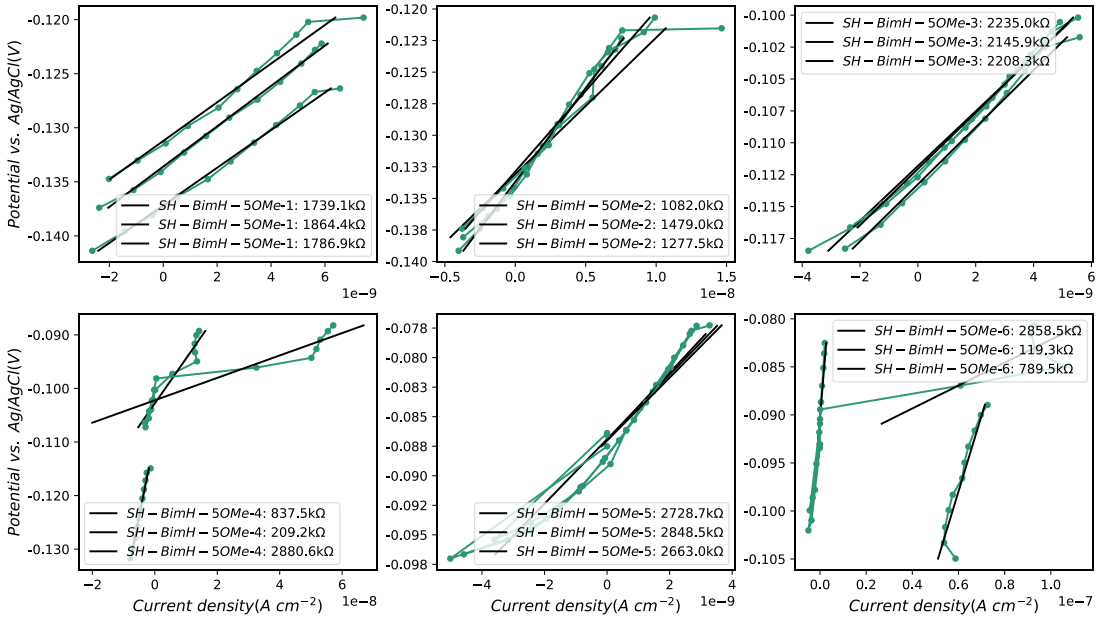

Figure A2.7 Long-term linear polarization curves of $Cu_{70}Zn_{30}$ alloy under the 120h period of testing of the alloy in the presence of the inhibitor in the 3 wt.% NaCl aqueous solution with SH-BimH-5OMe

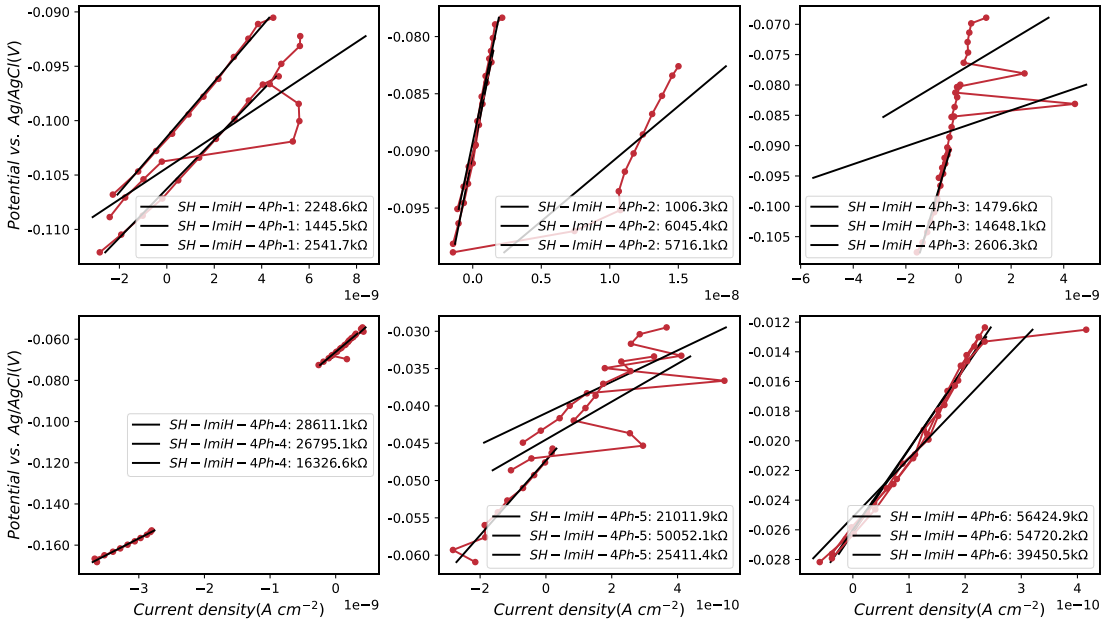

Figure A2.8 Long-term linear polarization curves of $Cu_{70}Zn_{30}$ alloy under the 120h period of testing of the alloy in the presence of the inhibitor in the 3 wt.% NaCl aqueous solution with SH-ImiH-4Ph

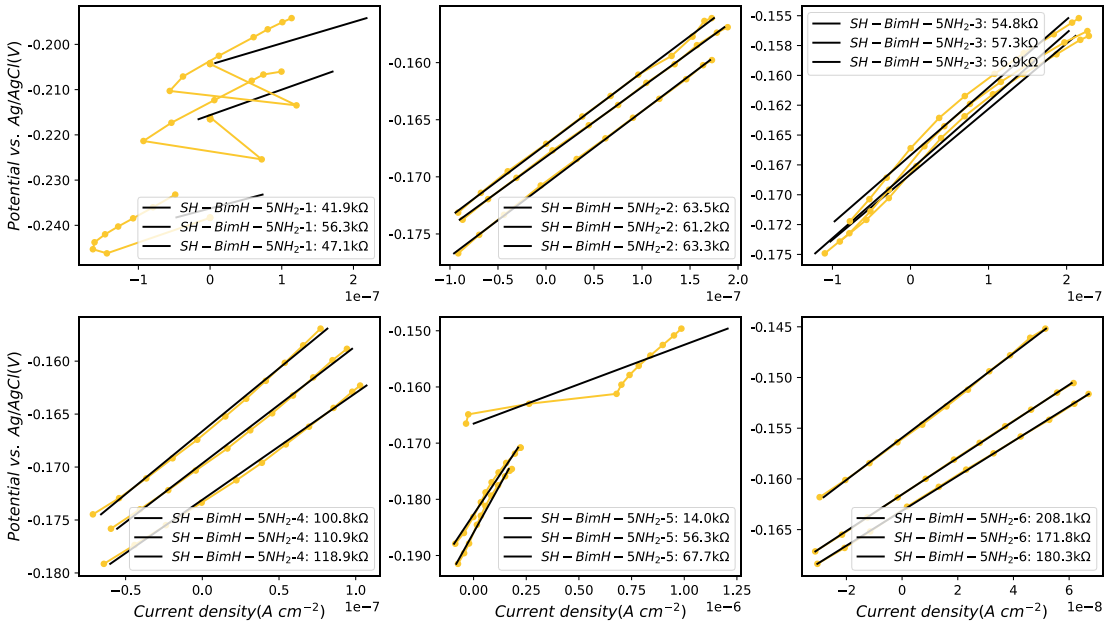

Figure A2.9 Long-term linear polarization curves of $Cu_{70}Zn_{30}$ alloy under the 120h period of testing of the alloy in the presence of the inhibitor in the 3 wt.% NaCl aqueous solution with SH-BimH-$5NH_2$

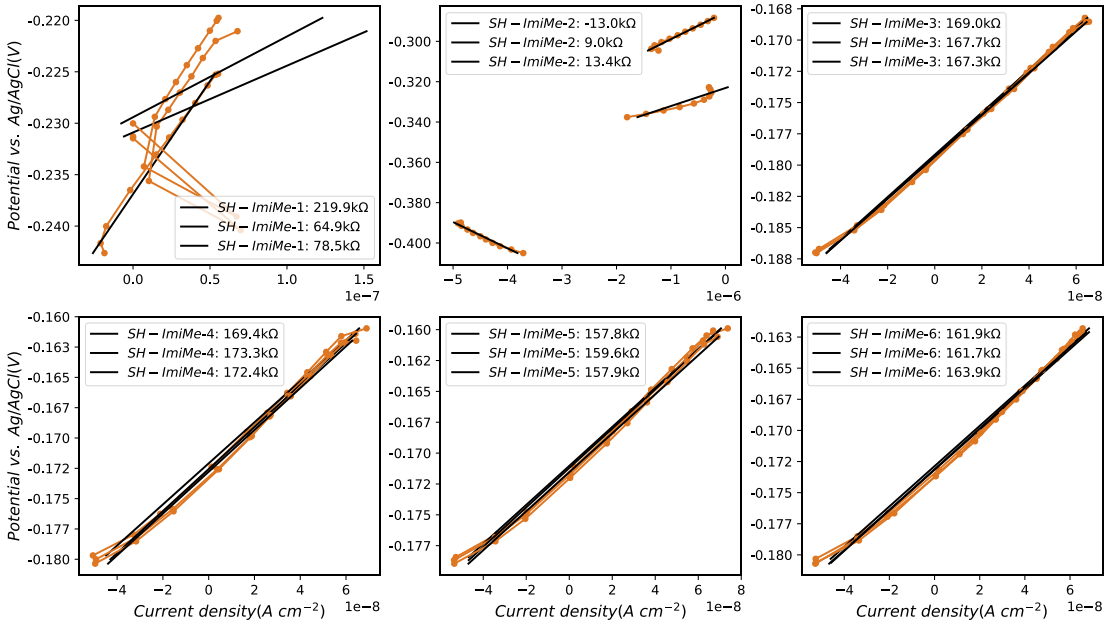

Figure A2.10 Long-term linear polarization curves of $Cu_{70}Zn_{30}$ alloy under the 120h period of testing of the alloy in the presence of the inhibitor in the 3 wt.% NaCl aqueous solution with SH-ImiMe

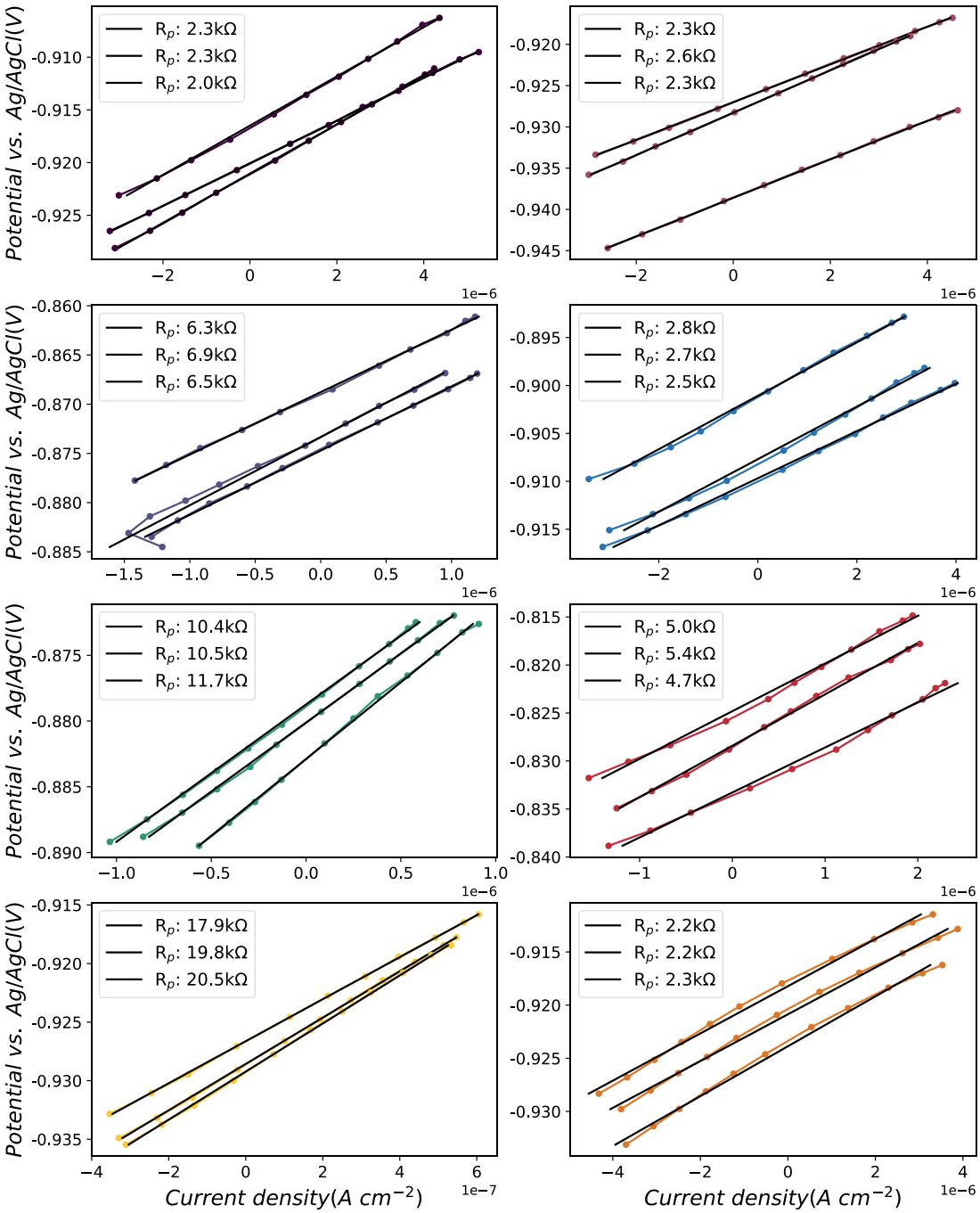

Figure A2.11 All linear polarization resistance curves of $Cu_{30}Zn_{70}$ alloy with and without inhibitors in 3 wt.% NaCl solution after immersion for 1 h

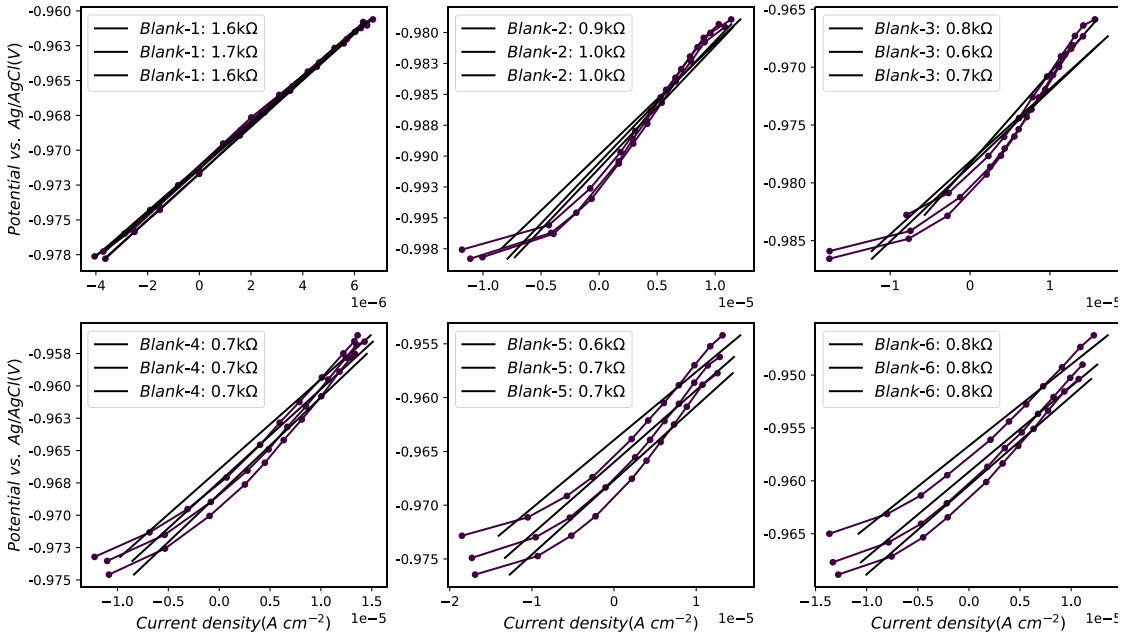

Figure A2.12 Long-term linear polarization curves of $Cu_{30}Zn_{70}$ alloy under the 120h period of testing of the alloy in the presence of the inhibitor in the 3 wt.% NaCl aqueous solution without inhibitors

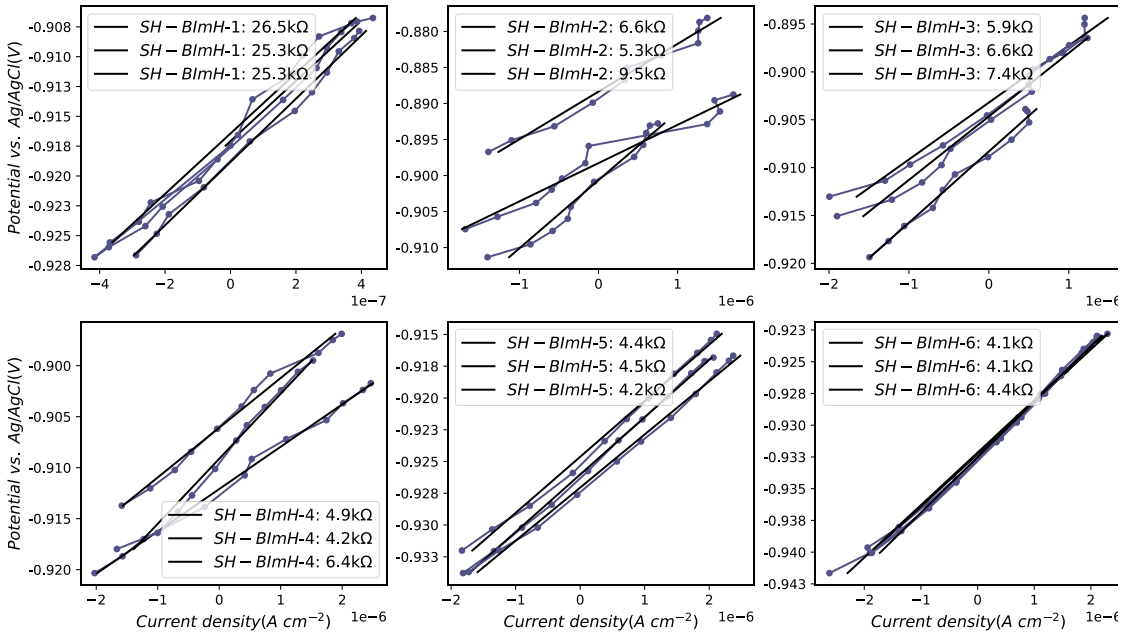

Figure A2.13 Long-term linear polarization curves of $Cu_{30}Zn_{70}$ alloy under the 120h period of testing of the alloy in the presence of the inhibitor in the 3 wt.% NaCl aqueous solution with SH-BImH

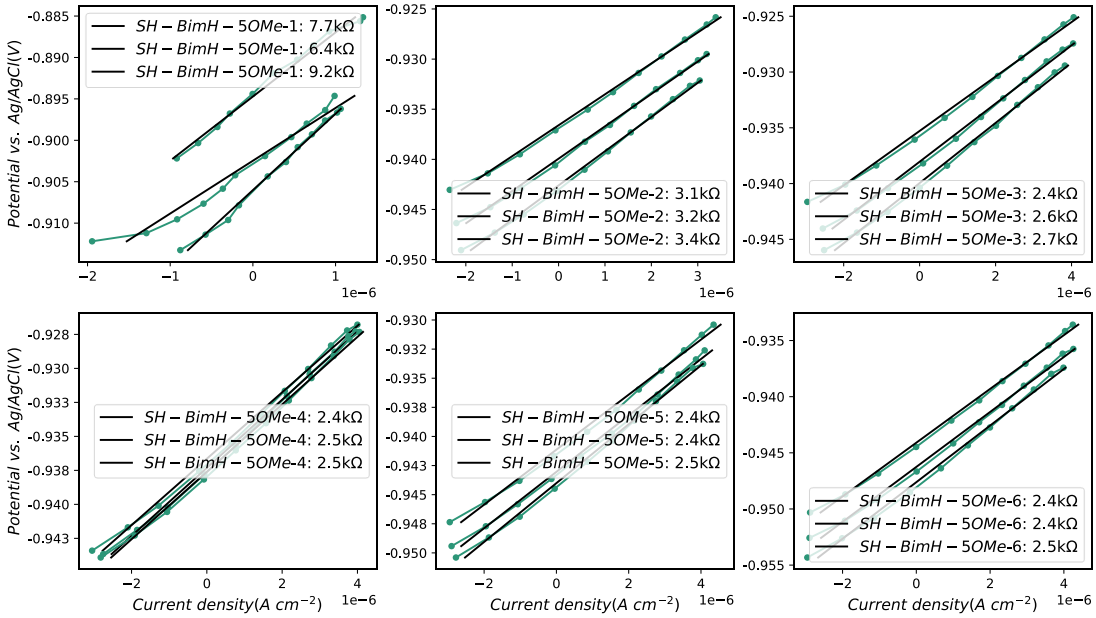

Figure A2.14 Long-term linear polarization curves of $Cu_{30}Zn_{70}$ alloy under the 120h period of testing of the alloy in the presence of the inhibitor in the 3 wt.% NaCl aqueous solution with SH-BimH-5OMe

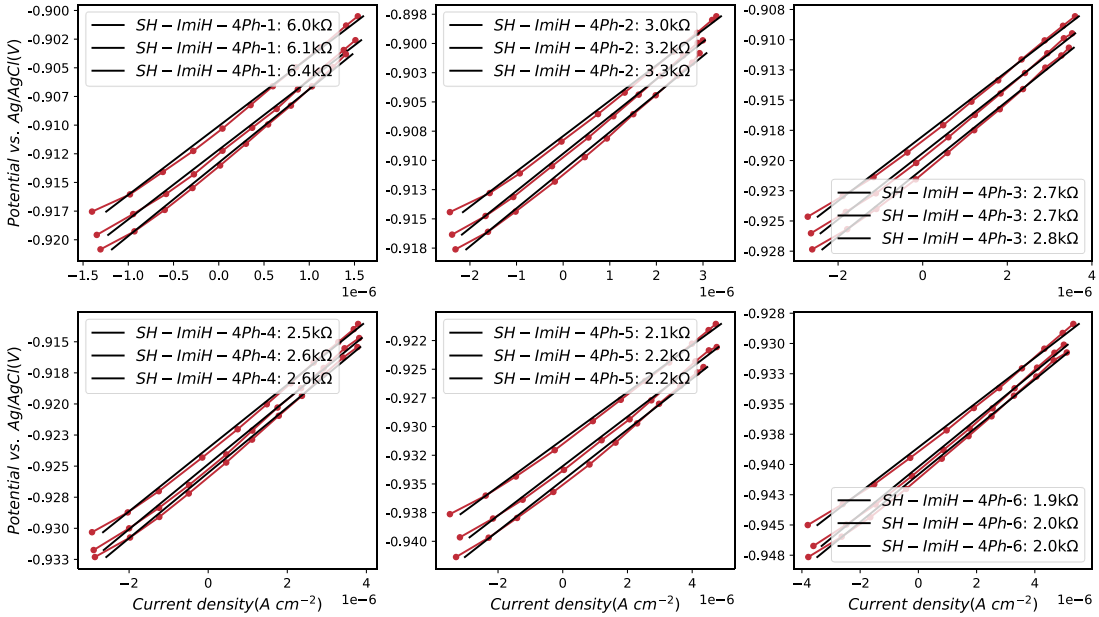

Figure A2.15 Long-term linear polarization curves of $Cu_{30}Zn_{70}$ alloy under the 120h period of testing of the alloy in the presence of the inhibitor in the 3 wt.% NaCl aqueous solution with SH-ImiH-4Ph

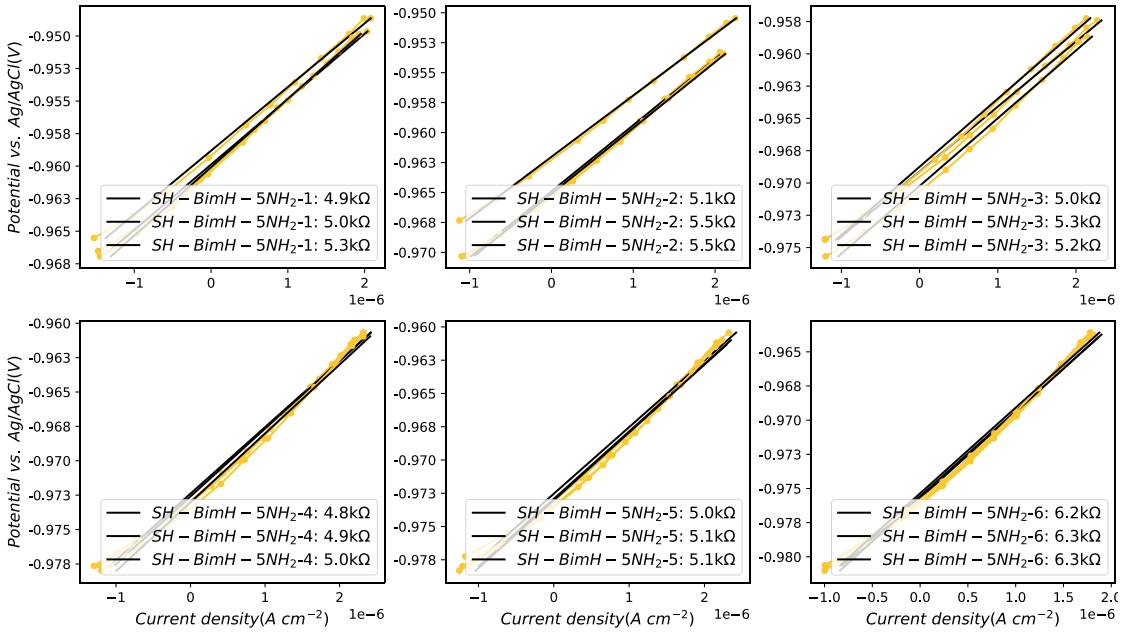

Figure A2.16 Long-term linear polarization curves of $Cu_{30}Zn_{70}$ alloy under the 120h period of testing of the alloy in the presence of the inhibitor in the 3 wt.% NaCl aqueous solution with SH-BimH-5NH_2

A2.2 Immersion test of CuZn alloy

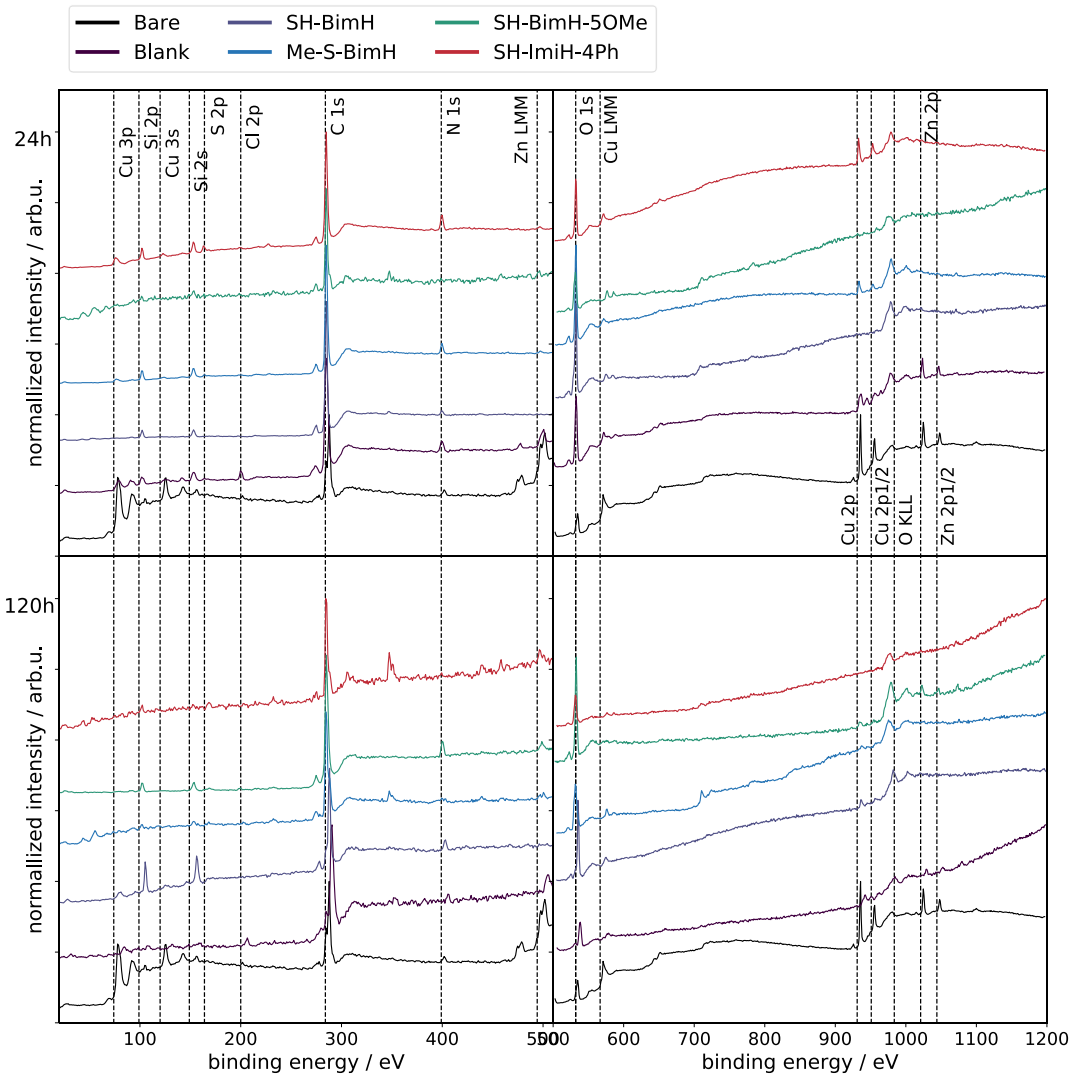

Figure A2.17 Normalized survey XPS spectrums for the surface of $Cu_{70}Zn_{30}$ alloy after polishing and pickling, and after immersion in 3wt.% NaCl with and without added of SH-BimH, Me-S-BimH, SH-BimH-5OMe and SH-ImiH-4Ph. Dash lines represent the position of peaks of reference compounds. Upper: Immersion for 24h. Down: Immersion for 120h.

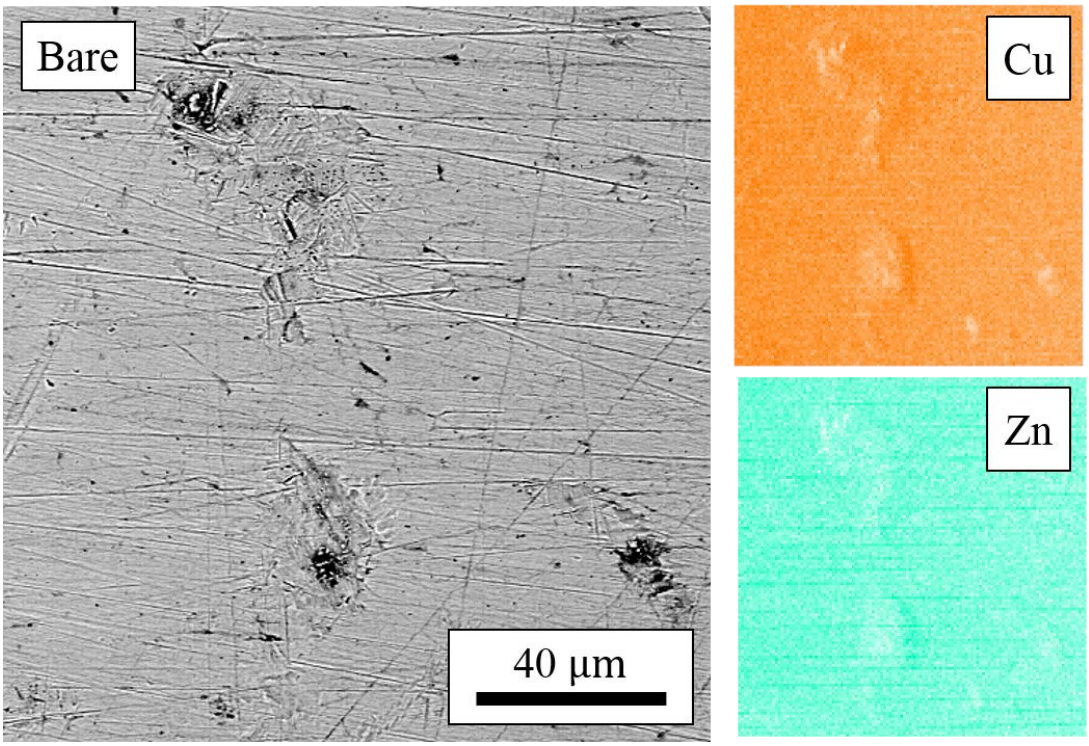

Figure A2.18 EDX elemental map analysis of the bare sample under 1000x magnification

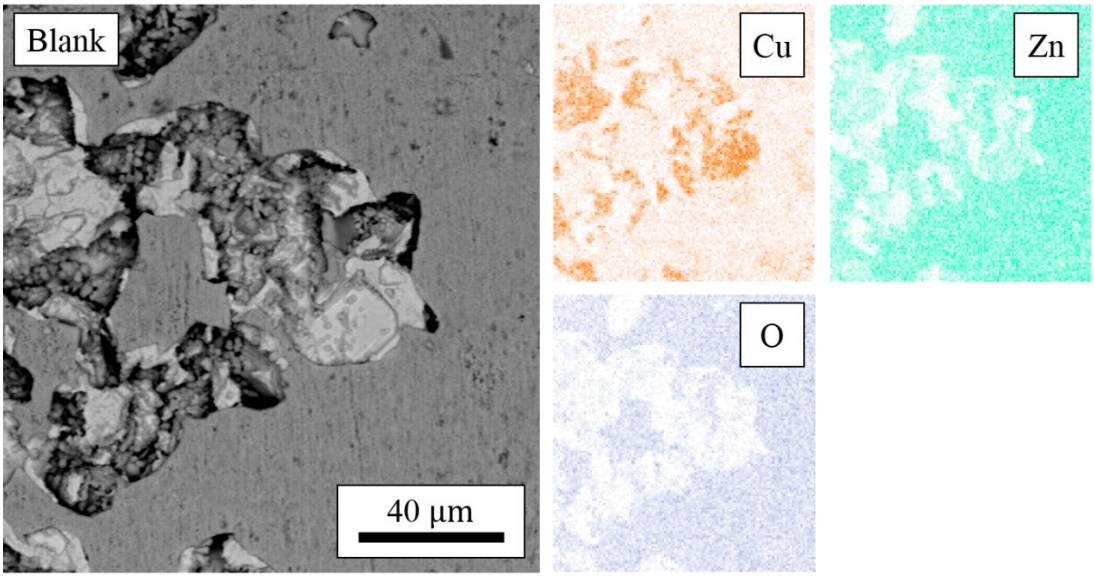

Figure A2.19 EDX elemental map analysis of $Cu_{70}Zn_{30}$ alloy immersed in 3 wt.% NaCl solution for 60 days

Figure A2.20 shows the BSE images of $Cu_{70}Zn_{30}$ alloy immersed in 3 wt.% NaCl with added 1mM ImiH for 60 days. **Figure A2.20** (a) shows three typical features: (A) shows clusters on the top, (B) are small cubes under the clusters, and (C) shows a light grey irregular piece. Subfigure (e) confirms the structure and shows a surface roughness Sa of

5.01 μm, the biggest one among all samples. As shown in **Figure A2.20** (b) and (c), the surface is covered by this kind of cluster island structure; the island size is around 20 – 60 μm. **Figure A2.20** (d) shows the cubic clusters on the surface. Furthermore, the holes near the cubic clusters seem very deep.

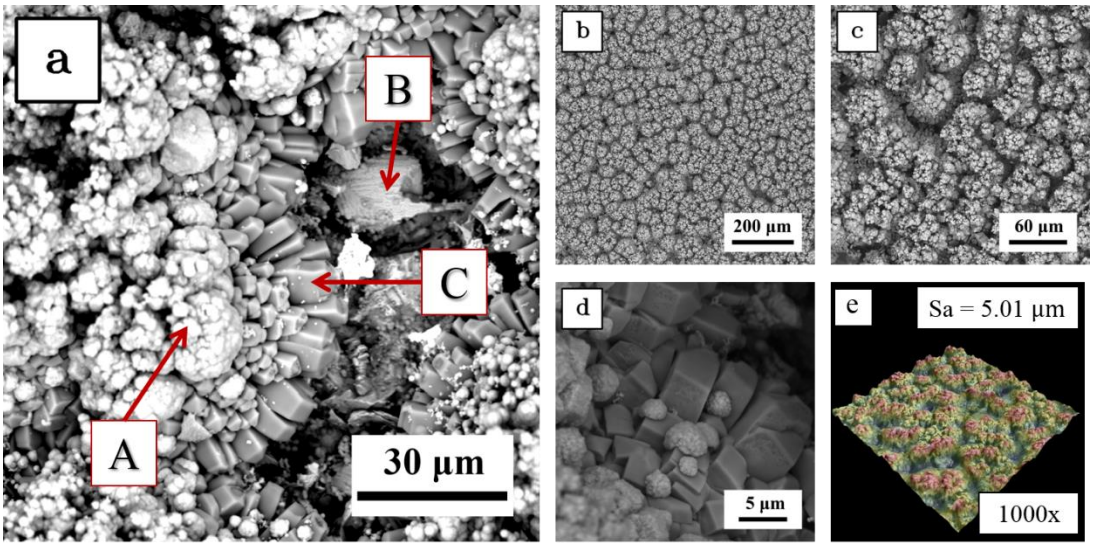

Figure A2.20 $Cu_{70}Zn_{30}$ alloy immersed in 3 wt.% NaCl with added 1mM ImiH solution for 60 days (a) surface under 2500x magnification with all typical features (b) surface under 320x magnification (c) surface under 1000x magnification (d) surface features in the valley (e) 3D topography under 1000x magnification by SEM

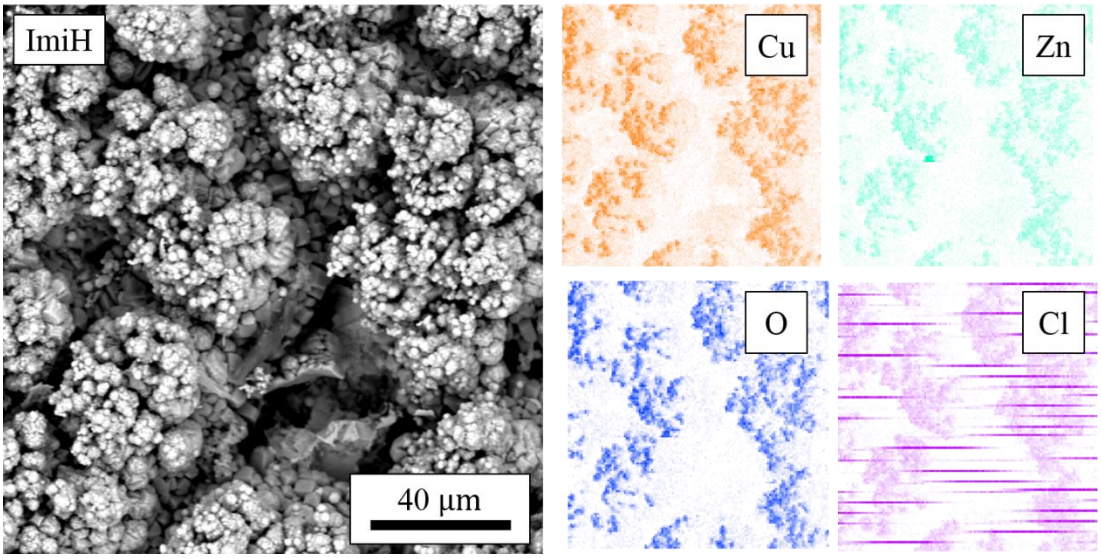

Figure A2.21 EDS elemental map analysis of $Cu_{70}Zn_{30}$ alloy immersed in 3 wt.% NaCl solution with added 1mM ImiH for 60 days

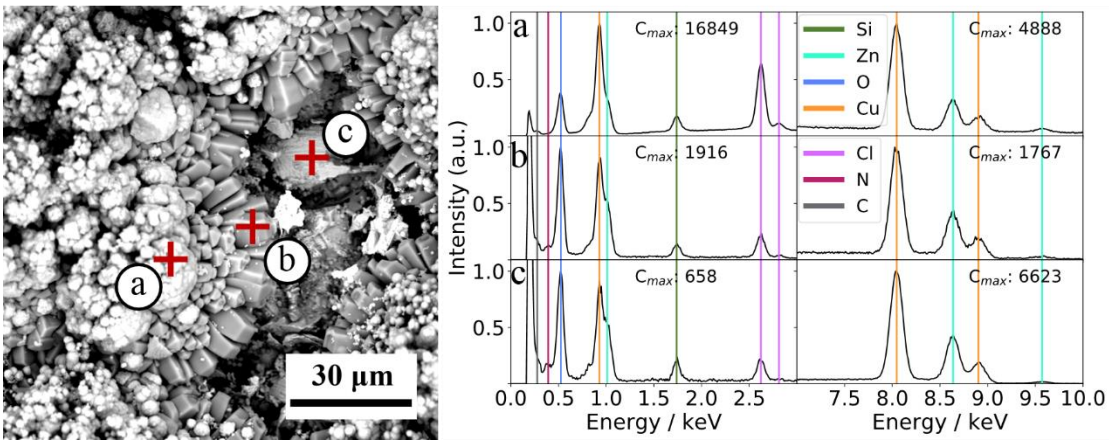

Figure A2.22 EDS elemental point analysis spectrum of $Cu_{70}Zn_{30}$ alloy immersed in 3 wt.% NaCl solution with added 1mM ImiH for 60 days (a) spectrum of point a, white clusters on the surface (b) spectrum of point b, grey cubic particles under the clusters (c) spectrum of point c, grey pieces in the valley.

Figure A2.21 shows the EDS elements map of Cu, Zn, O and Cl. The clusters are composed of Cu, Zn, O and Cl. However, there is less information from the map of the other areas. **Figure A2.22** is the EDS point spectrum of the features. Spectrum (a) is the cluster, showing oxygen, the chlorine peak with Cu and Zn that indicates that the cluster should be a complex. Spectrum (b) and (c) show the same large peak at less than 0.25 keV, and the Lα energy peak of Cu and Zn are both very small. This may be attributed to the fluorescence and absorption of x-ray by light elements. These two points are in the valley of the sample. Since the high roughness, the x-ray have to go throw the clusters before reaching the detector. We can see the C_{max} is quite small in low energy range, so the amount of Si, Cl and O should also lower than in point (a). The peak features are almost the same for these two positions, and the Zn/Cu ratio are the same (Zn/Cu: 0.58/1). None of these analyses can infer the precise compound. However, they prove the results of electrochemical measurements, namely that ImiH is not an efficient inhibitor for $Cu_{70}Zn_{30}$ alloy.

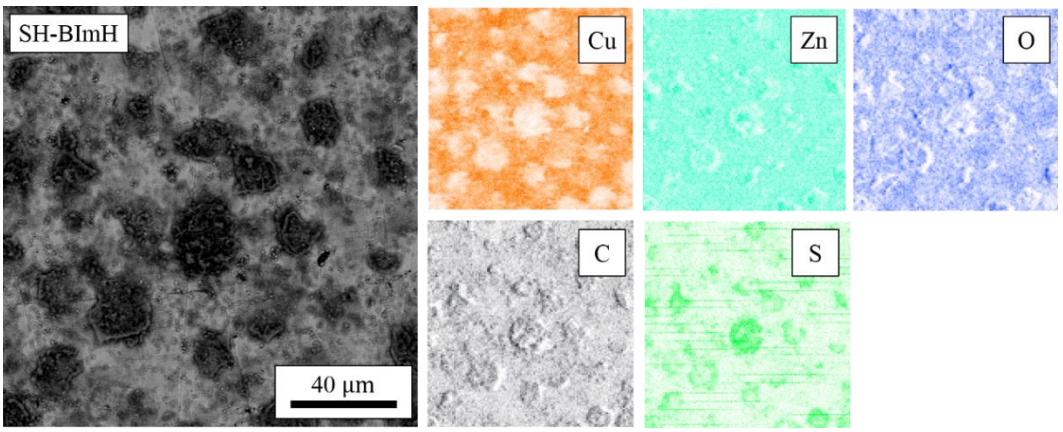

Figure A2.23 EDS elemental map analysis of Cu70Zn30 alloy immersed in 3 wt.% NaCl solution with added 1mM SH-BimH for 60 days

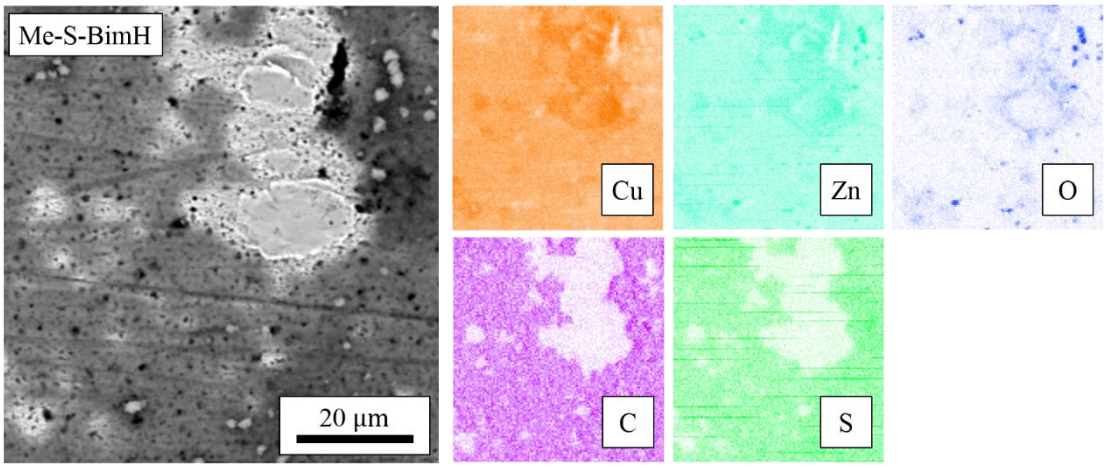

Figure A2.24 EDS elemental map analysis of $Cu_{70}Zn_{30}$ alloy immersed in 3 wt.% NaCl solution with added 1mM Me-S-BimH for 60 days

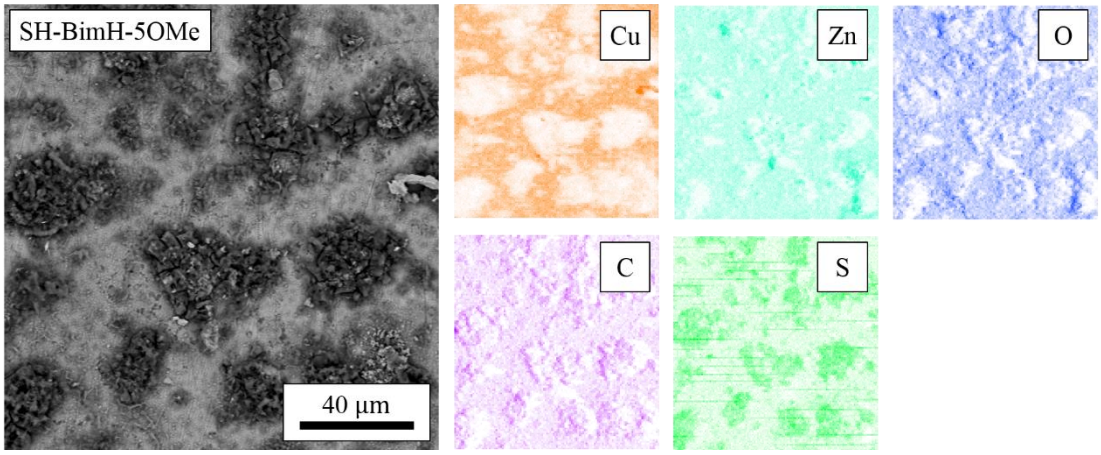

Figure A2.25 EDS elemental map analysis of $Cu_{70}Zn_{30}$ alloy immersed in 3 wt.% NaCl solution with added 1mM SH-BimH-5OMe for 60 days

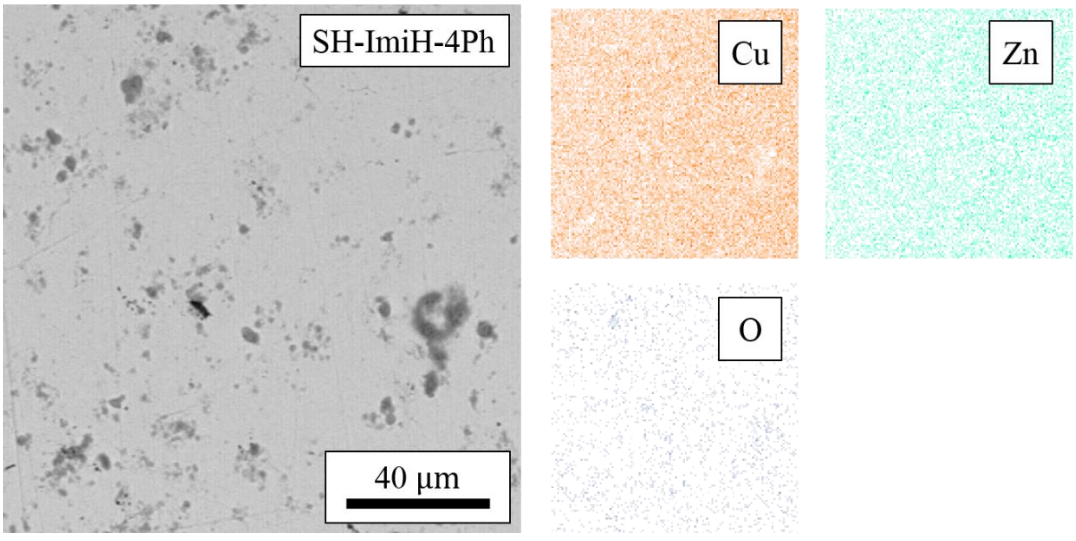

Figure A2.26 EDS elemental map analysis of $Cu_{70}Zn_{30}$ alloy immersed in 3 wt.% NaCl solution with added 1mM SH-ImiH-4Ph for 60 days

Figure A2.27 shows the BSE images of $Cu_{70}Zn_{30}$ alloy immersed in 3 wt.% NaCl aqueous solution with added 1mM SH-BimH-$5NH_2$ for 60 days. Three kinds of features are present on the surface, a flat grey area (A) under the black cracked film (B), and a porous part (C), as shown in subfigure (a) and (e). The surface roughness Sa is around 2.29 μm. In subfigure (b), it is shown that the black film is on the top of the grey surface, and the scratches are present on the grey surface, which means that in some parts the surface is protected by the black film. The black films are full of cracks, bubble-like bulges and holes, shown in subfigure (c). Subfigure (d) shows the porous structure, composed by polyhedron particles of a size around 5 μm.

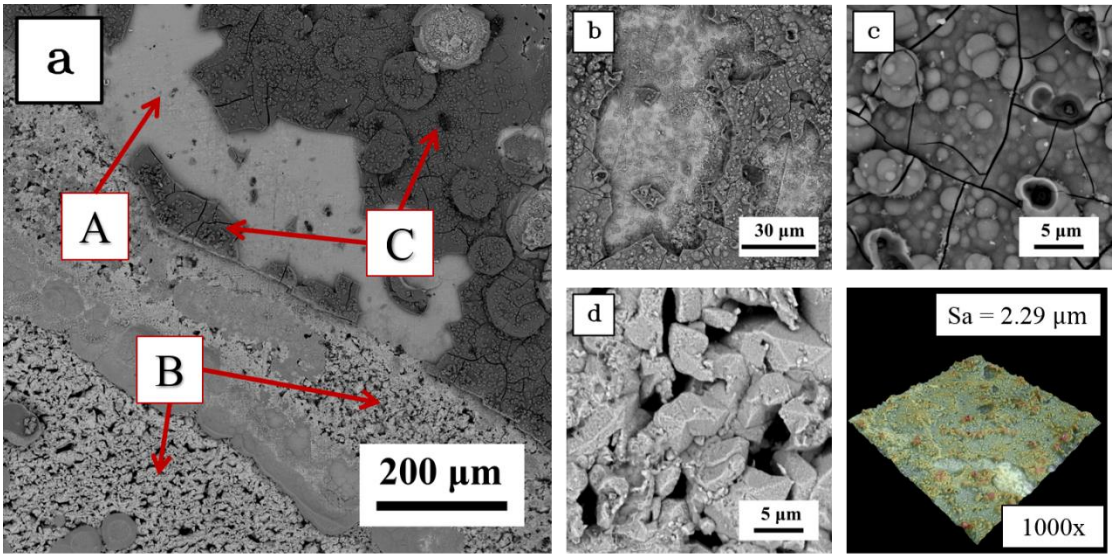

Figure A2.27 $Cu_{70}Zn_{30}$ alloy immersed in 3 wt.% NaCl with added 1mM SH-BimH-$5NH_2$ solution for 60 days (a) surface under 2500x magnification with all typical features (b) surface under 320x magnification (c) surface under 1000x magnification (d) surface features in the valley (e) 3D topography under 1000x magnification by SEM

Figure A2. 28 shows the EDS elemental map of C, O, S, Cl, Cu and Zn. The distribution of Zn is almost the same in the black film and the porous surface, showing a low amount of Zn. However, a region at the bottom of the image shows a high Zn concentration. Only O and Cu are observed in the porous region, which means the polyhedron particles are pure Cu with some oxides on the surface. Contrarily, C, S and Cl are the major components of the black. The area at the bottom of the image shows different features than the film under the black film. It appears to be a very flat surface, of different morphology than that of the raw material with an oxide surface. The major elements are Zn, Cl and O. **Figure A2.29** displays the EDS point spectrum of the features, (a) on the black film, (b) on the white porous part and (c) on the flat grey piece. Spectrum (a) shows the presence of C, N, O, Cu, Zn, S and Cl; Cu and Zn may form the background surface, and the film would be mostly formed by the inhibitor in the solution. The quantification result offers a Zn/Cu ratio of 0.439/1 close to the ratio of raw material, which confirms the estimation. Furthermore, the O may come from oxide on the CuZn surface under the black film. Spectrum (b) shows that there is neither Zn nor inhibitor in the porous region.

After dezincification, Cu particles may grow, and oxidation happens on the surface. The area at the bottom of the image shows the presence of Zn, O, Cl, and a little Cu. Since it locates on the top of porous area, the Cu peak may come from the porous, while Cl must come for the area itself. Therefore, this area may be a (Zn, Cl, O) compound formed during corrosion. The surface shows selective corrosion of the sample; this inhibitor introduces some new modes of corrosion and cannot adequately protect the surface. The protective black film did not show any regularity as well.

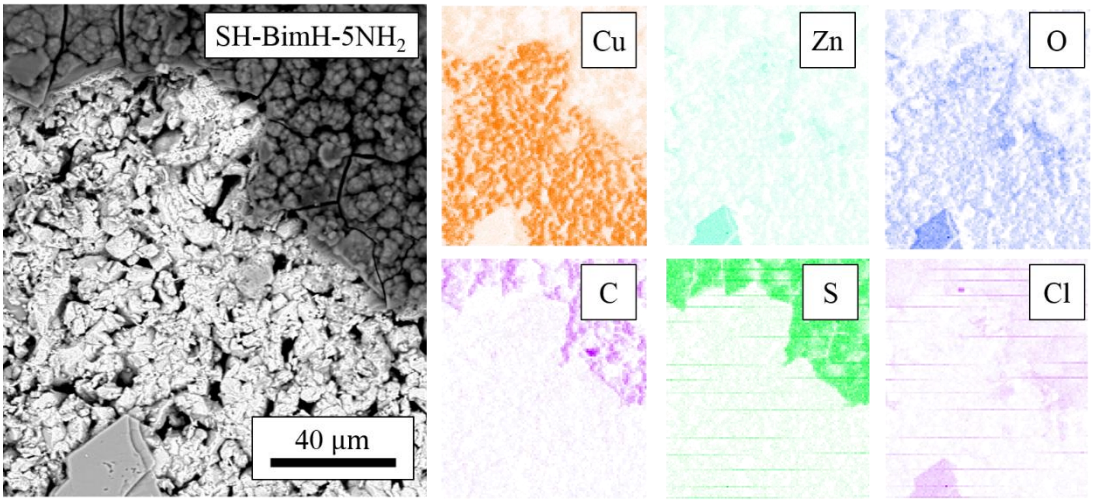

Figure A2. 28 EDS elemental map analysis of $Cu_{70}Zn_{30}$ alloy immersed in 3 wt.% NaCl solution with added 1mM SH-BimH-5NH_2 for 60 days

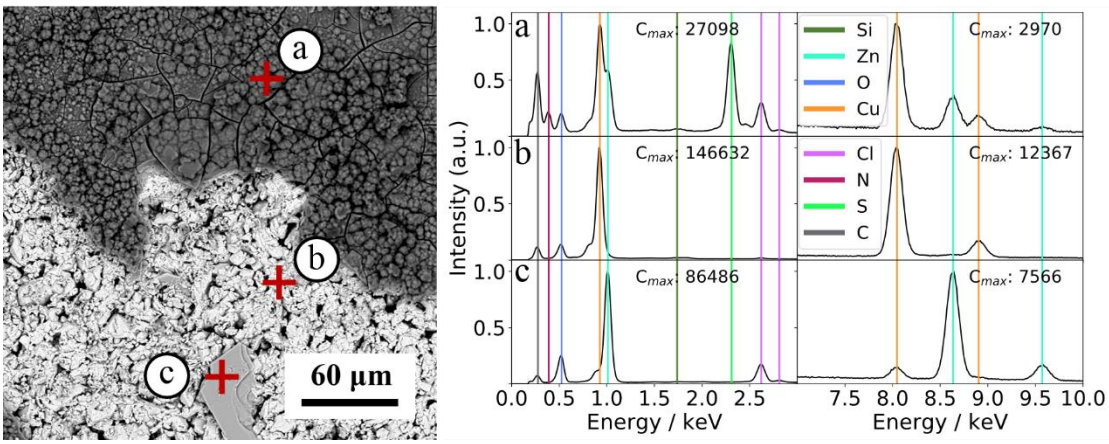

Figure A2.29 EDS elemental point analysis spectrum of Cu70Zn30 alloy immersed in 3 wt.% NaCl solution with added 1mM SH-BimH-5NH2 for 60 days (a) spectrum of point a, white part under BSE detector (b) spectrum of point b, grey film on the surface (c) spectrum of point c, particles in porous

Figure A2.30 shows the BSE images of the $Cu_{70}Zn_{30}$ alloy immersed in 3 wt.% NaCl aqueous solution with added 1mM SH-ImiMe for 60 days. According to subfigure (a) and (e), there are some flocs on the sample surface, most of them are white and the rest are

black. The flat surface is scratched, which means it is not severely corroded. The Sa roughness is 2.29 µm. As shown in subfigure (b), the flocs covered part of the surface. Moreover, under the floc, cracks may happen, see subfigure (c). The close-up subfigure (d) shows a porous structure under the flat surface. It indicates that selective dissolution happened in some locations in the surface. **Figure A2.31** shows the EDS elemental map of Cu, Zn, O, C, S and Cl. The flocs are all Cu-rich, and almost no Zn, O and Cl appear on the white flocs, which seems to be a (Cu, O, Cl) compound. Furthermore, the black flocs contain C, S and Cu, which may correspond to the inhibitor on Cu. The flat surface shows a Zn distribution with higher concentration than in the raw material, as well as the presence of O and Cl. This can be attributed to the development of ZnO over most of the surface during corrosion.

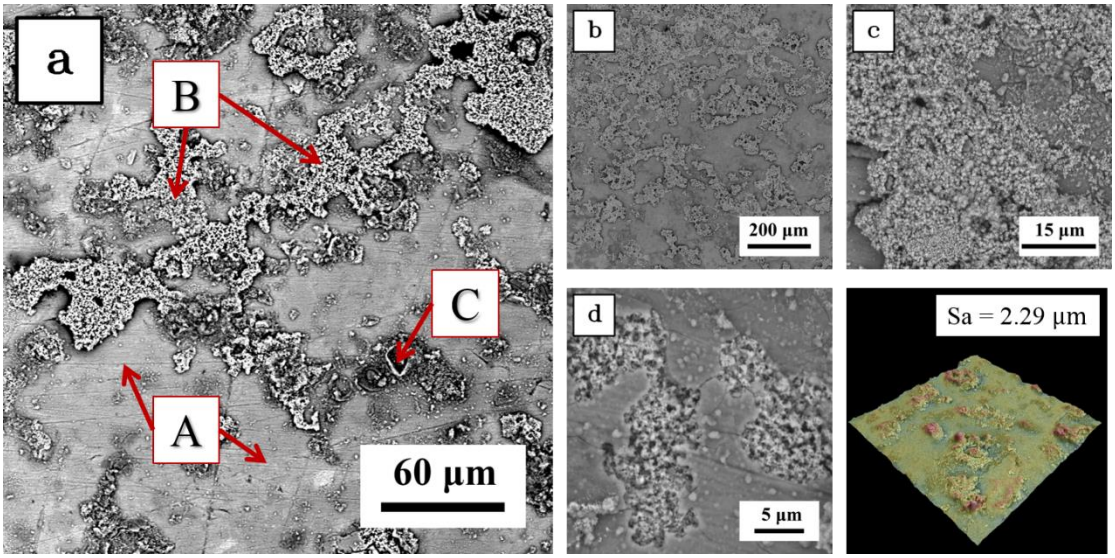

Figure A2.30 $Cu_{70}Zn_{30}$ alloy immersed in 3 wt.% NaCl with added 1mM SH-ImiMe solution for 60 days (a) surface under 2500x magnification with all typical features (b) surface under 320x magnification (c) surface under 1000x magnification (d) surface features in the valley (e) 3D topography under 1000x magnification by SEM

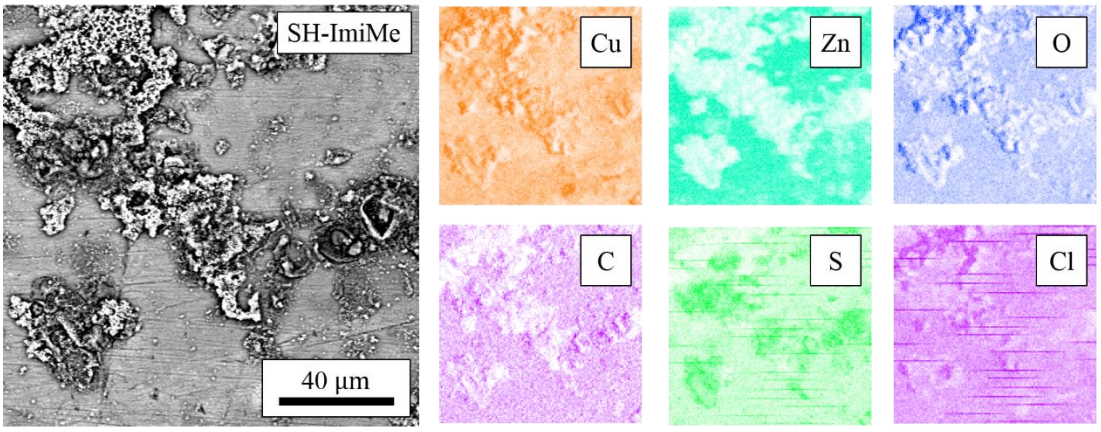

Figure A2.31 EDS elemental map analysis of $Cu_{70}Zn_{30}$ alloy immersed in 3 wt.% NaCl solution with added 1mM SH-ImiMe for 60 days

Figure A2.32 is the EDS point spectrum of the features, (a) on the white floc, (b) on the flat surface and (c) on the black floc. Spectrum (a) shows almost no Zn and high O, Cu, Cl concentrations in this position. It confirms the result of the EDS map. In spectrum (b), the small peaks of C and S denote the adsorption of inhibitors on the surface, but the existence of a Cl peak indicates this inhibitor reinforces the reaction of Cl^- ions with the sample. The spectrum (c) shows Cu and Zn peaks similar to that of the raw material in the 7 – 10 keV range, and high C, S, N peaks in the 0 – 3keV range, like some previous inhibitors. Thus, it appears that in the black flocs the organic compounds are on the surface, while under the surface an oxide layer develops with little corrosion products containing Cl; the Zn/Cu ratio of 0.488/1. This sample with SH-ImiMe shows a complex surface covered by corrosion products, organic compounds and an oxide film topped with inhibitor molecules. Moreover, small porous were found at some locations. This inhibitor may introduce the formation of the passive film like (B) region in 错误!未找到引用源。(a), but the passive layer only appears in some positions, therefore not protecting the whole surface. Furthermore, this passivation may also be responsible for the unstable signal recorded in the short-time electrochemical test.

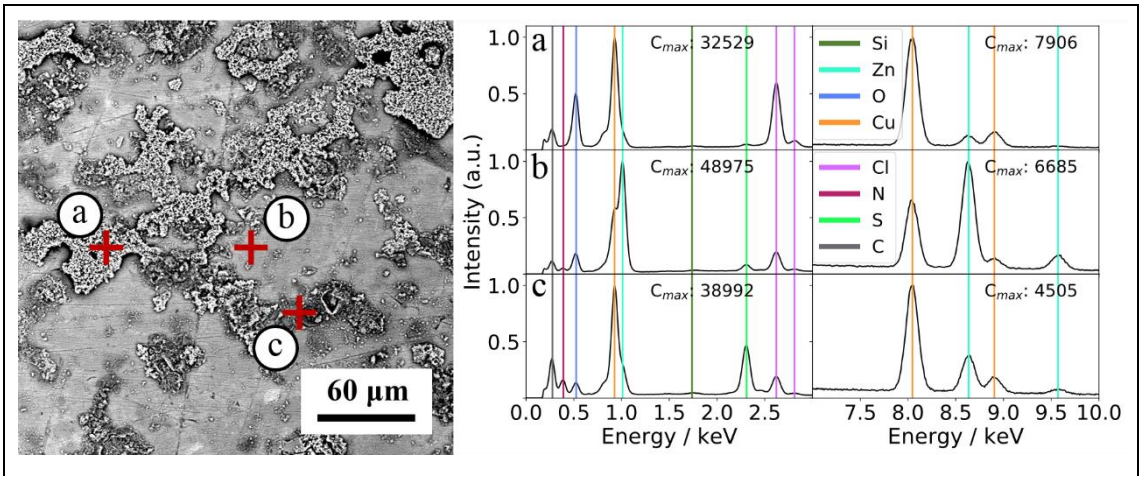

Figure A2.32 EDS elemental point analysis spectrum of $Cu_{70}Zn_{30}$ alloy immersed in 3 wt.% NaCl solution with added 1mM SH-ImiMe for 60 days (a) spectrum of point a, white part under BSE detector (b) spectrum of point b, grey film on the surface (c) spectrum of point c, particles in porous

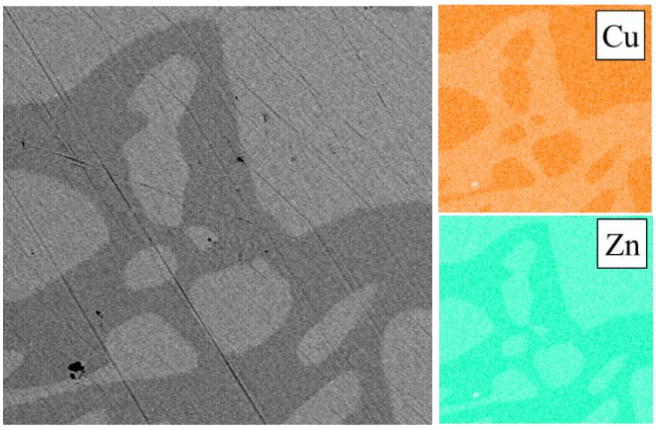

Figure A2.33 EDX elemental map analysis of the bare $Cu_{30}Zn_{70}$ alloy sample under 1000x magnification

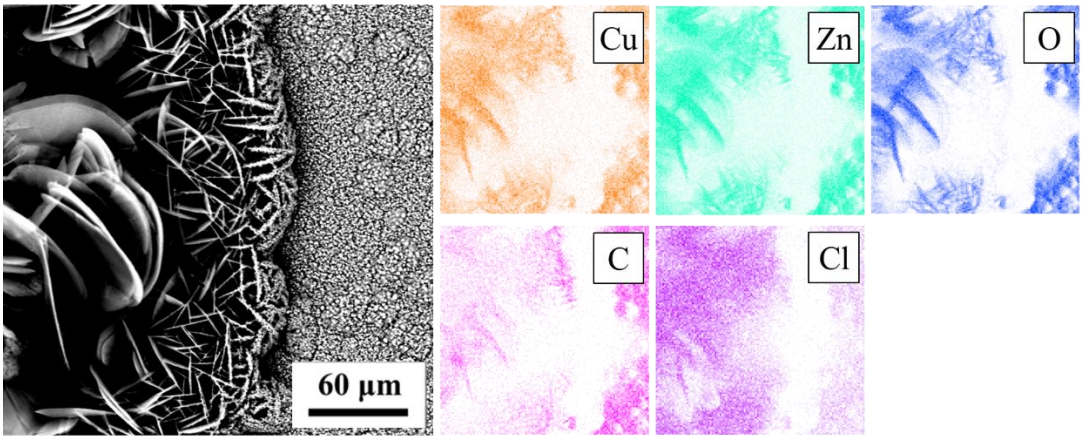

Figure A2.34 EDX elemental map analysis of $Cu_{30}Zn_{70}$ alloy immersed in 3 wt.% NaCl solution for 12 days

Figure A2.35 shows $Cu_{30}Zn_{70}$ alloy surface after immersion in 3 wt.% NaCl with added SH-BimH for 12 days. **Figure A2.35** (a) and (d) show global view of surface, there are some big bulk exist on the surface, And the scratches from polishing are disappeared. **Figure A2.35** (b) shows the flat surface in higher magnification, porous structure indicates corrosion happened on the surface. **Figure A2.35** (c) shows that the porous structure is a film on the surface and bulk material is under porous layer. **Figure A2.36** shows the elemental map of the surface, the porous layer is made of Zn, Cl, C and O. **Figure A2.37** shows the elemental point analysis. The bulk materials under porous layer is raw alloy with oxide surface in point (a). Point (b) and (c) show the substance on the surface and the porous layer are same, compose of Zn, Cl, O. SH-BimH did not work as inhibitor for $Cu_{30}Zn_{70}$ alloy.

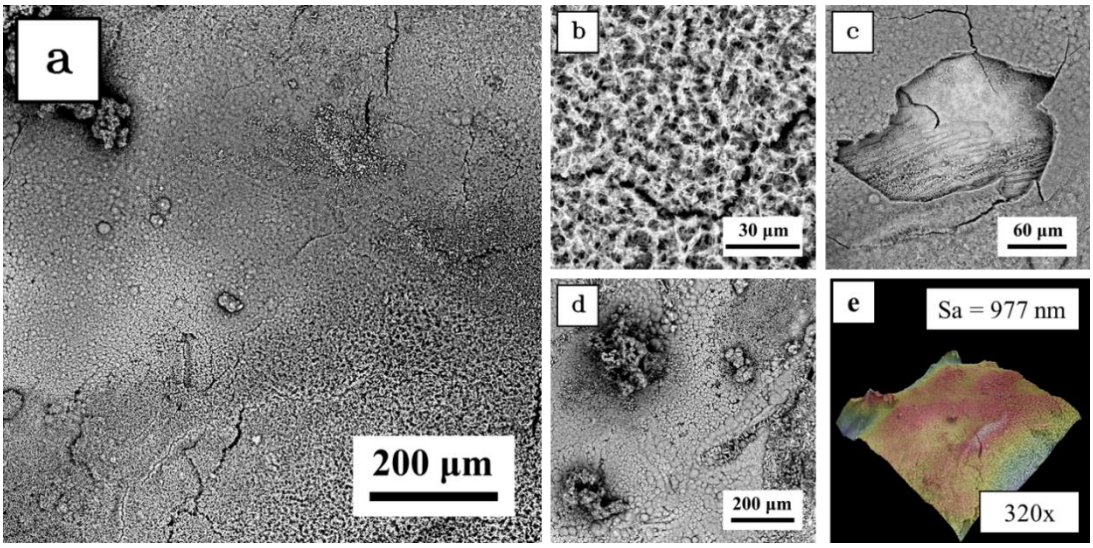

Figure A2.35 $Cu_{30}Zn_{70}$ alloy immersed in 3 wt.% NaCl with added 1mM SH-BimH solution for 12 days (a) surface under 320x magnification with all typical features (b) surface under 2500x magnification (c) bulk material under porous film (d) big corrosion products on the surface (e) 3D topography under 320x magnification by SEM

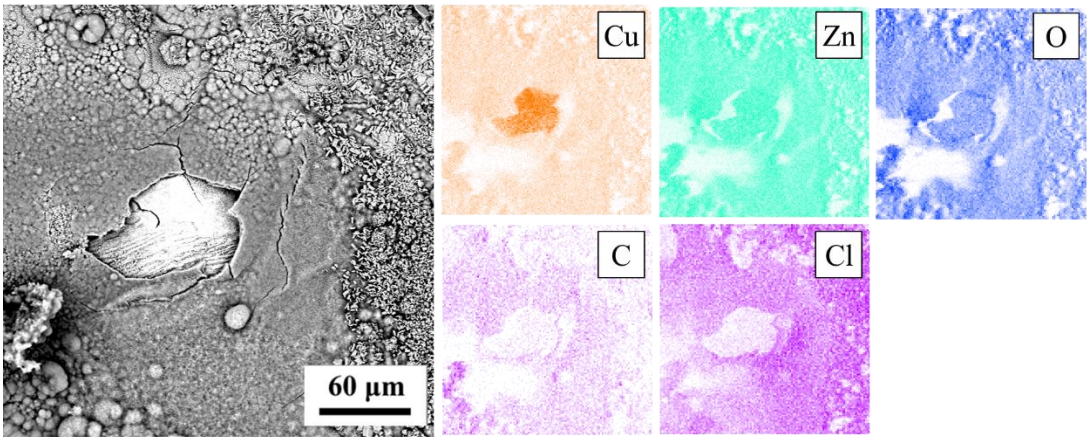

Figure A2.36 EDS elemental map analysis of $Cu_{30}Zn_{70}$ alloy immersed in 3 wt.% NaCl solution with added 1mM SH-BimH for 12 days

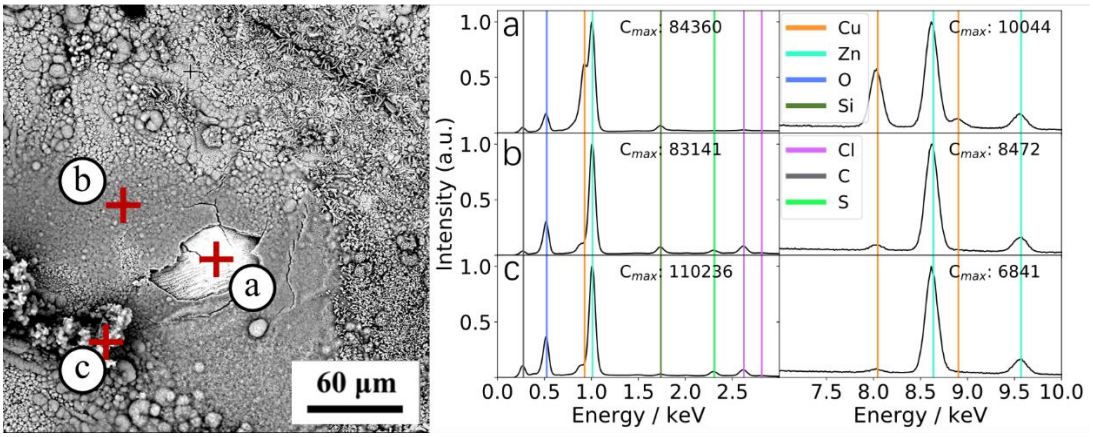

Figure A2.37 EDS elemental point analysis spectrum of $Cu_{30}Zn_{70}$ alloy immersed in 3 wt.% NaCl solution with added 1mM SH-BimH for 12 days (a) spectrum of point a, bulk material under the porous film (b) spectrum of point b, grey porous film (c) spectrum of point c, clusters on the surface.

Figure A2.38 shows the surface of $Cu_{30}Zn_{70}$ alloy immersed in 3 wt.% NaCl with added SH-BimH-5OMe for 12 days. As shown in **Figure A2.38** (a), cracks, particles and pits appear on the surface. In **Figure A2.38** (b) and (d), particles and porous film are clearer with 2500x magnification. Only little part of the surface maintains a better surface like in **Figure A2.38** (c). **Figure A2.39** shows the elemental map of the surface. Cu, Zn, O and S appear on the surface and there is no S on the porous part. **Figure A2.40** shows elemental point analysis on protected surface and porous parts. Point (a) is on the protected surface, S peak is high and almost no Cu peak appears, which indicates SH-BimH-5OMe combine with Zn and adhere to the surface. Point (b) and (c) show the same peaks, and the close to the analysis in surface with only 3 wt. NaCl. SH-BimH-5OMe is not effective inhibitor for $Cu_{30}Zn_{70}$ alloy even it can offer some protections.

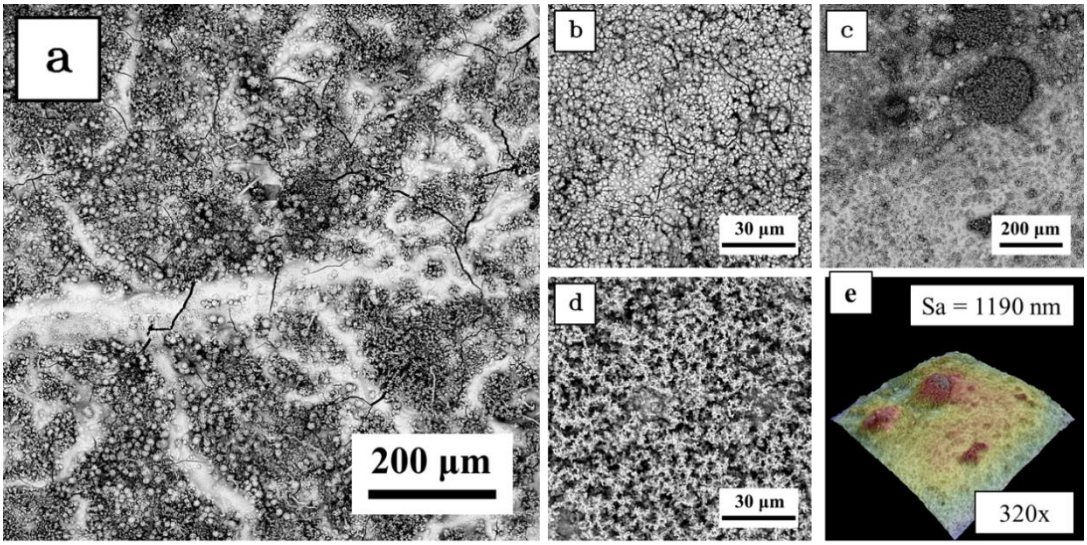

Figure A2.38 $Cu_{30}Zn_{70}$ alloy immersed in 3 wt.% NaCl with added 1mM SH-BimH-5OMe solution for 12 days (a) surface under 320x magnification with all typical

features (b) particles and cracks on the surface (c) surface under 320x magnification (d) porous structure of the surface (e) 3D topography under 320x magnification by SEM

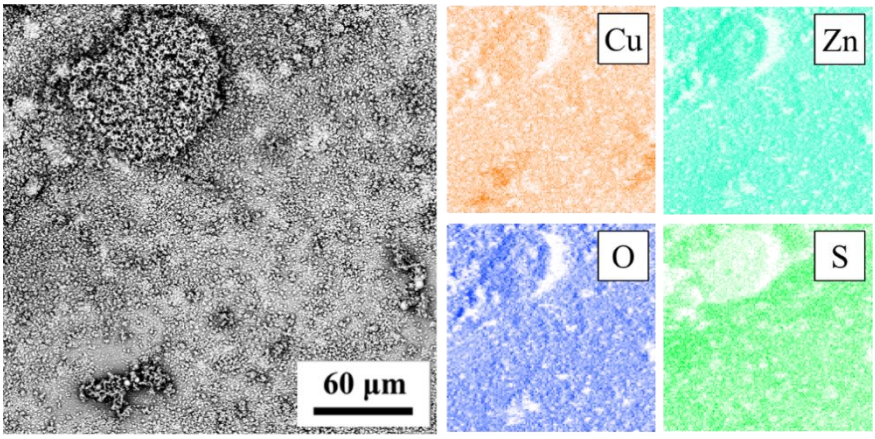

Figure A2.39 EDS elemental map analysis of $Cu_{30}Zn_{70}$ alloy immersed in 3 wt.% NaCl solution with added 1mM SH-BimH-5OMe for 12 days

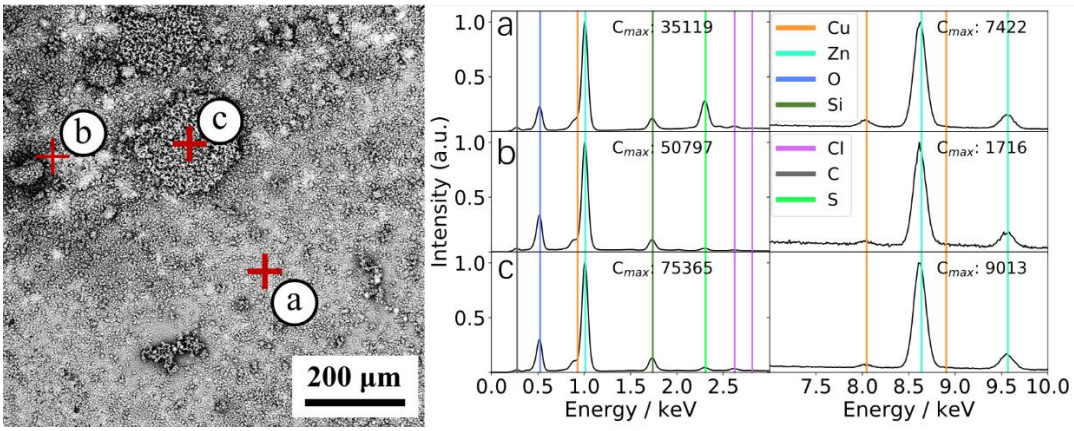

Figure A2.40 EDS elemental point analysis spectrum of $Cu_{30}Zn_{70}$ alloy immersed in 3 wt.% NaCl solution with added 1mM SH-BimH-5OMe for 12 days (a) spectrum of point a, grey flat surface (b) spectrum of point b, white flat surface (c) spectrum of point c, porous substance on the surface.

Figure A2.41 shows the surface of $Cu_{30}Zn_{70}$ alloy immersion for 60 days in 3 wt.% NaCl with added 1mM SH-ImiH-4Ph. All subplots show an interesting result, SH-ImiH-4Ph assist the formation of a flower-like structure similar to surface without inhibitor. And this structure is covered all surface. **Figure A2.42** is the elemental map of the surface. Combine with the elemental point analysis in **Figure A2.43**, the surface is covered by the same substance as sample with 3 wt.% NaCl. SH-ImiH-4Ph assists formation of corrosion products of (Cu, O, Cl) complex.

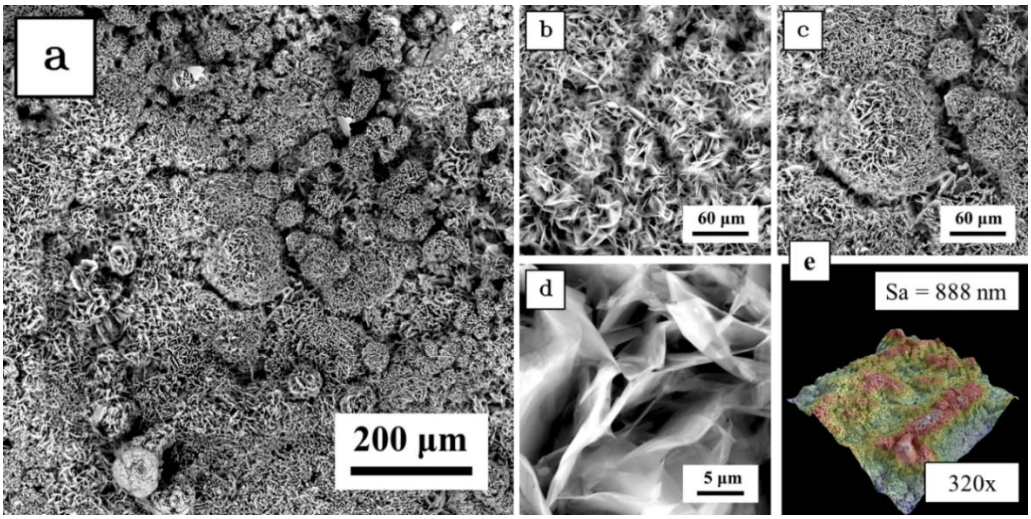

Figure A2.41 $Cu_{30}Zn_{70}$ alloy immersed in 3 wt.% NaCl with added 1mM SH-ImiH-4Ph solution for 12 days (a) surface under 320x magnification with all typical features (b) surface under 1000x magnification (c) surface under 1000x magnification (d) structure of flower-like substance (e) 3D topography under 320x magnification by SEM

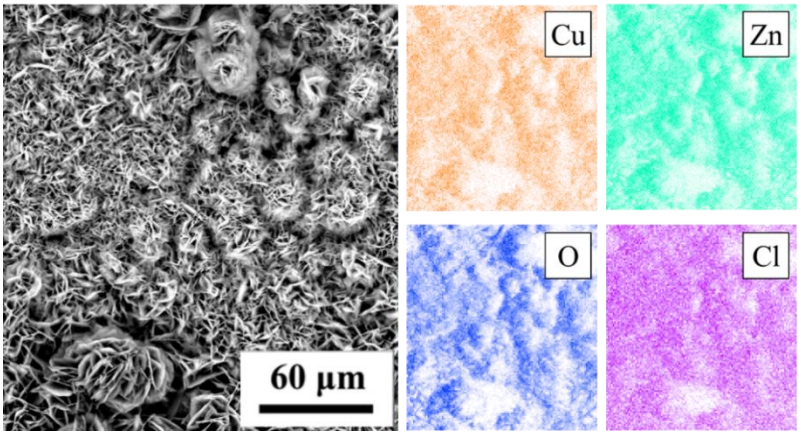

Figure A2.42 EDS elemental map analysis of $Cu_{30}Zn_{70}$ alloy immersed in 3 wt.% NaCl solution with added 1mM SH-ImiH-4Ph for 12 days

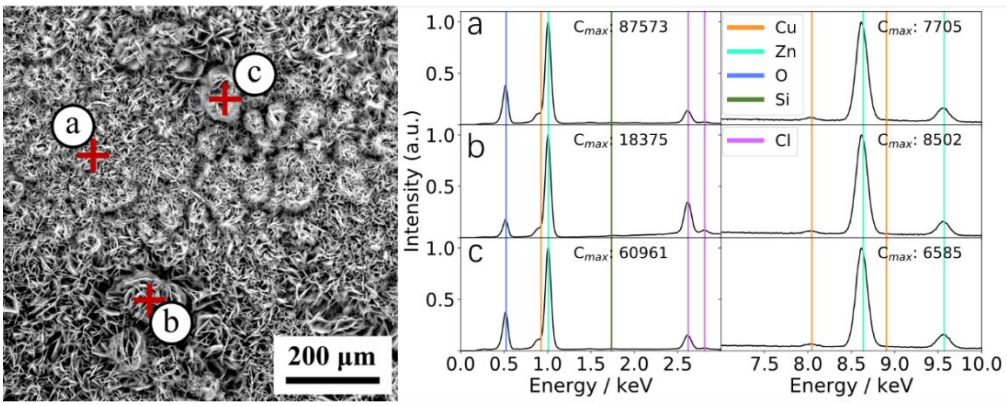

Figure A2.43 EDS elemental point analysis spectrum of $Cu_{30}Zn_{70}$ alloy immersed in 3 wt.% NaCl solution with added 1mM SH-ImiH-4Ph for 12 days (a) spectrum of point a, small flower-like substance (b) spectrum of point b and c, large flower-like substance.

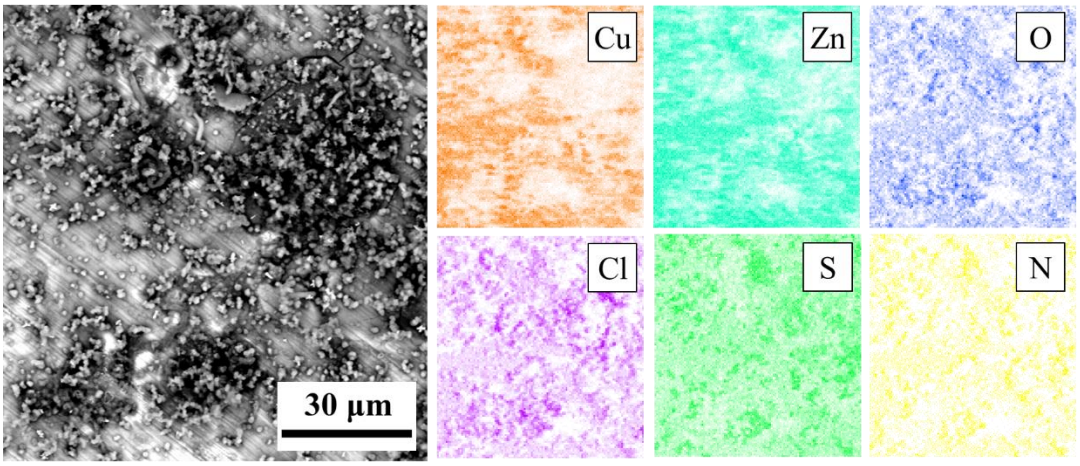

Figure A2.44 EDS elemental map analysis of $Cu_{30}Zn_{70}$ alloy immersed in 3 wt.% NaCl solution with added 1mM SH-BimH-$5NH_2$ for 12 days

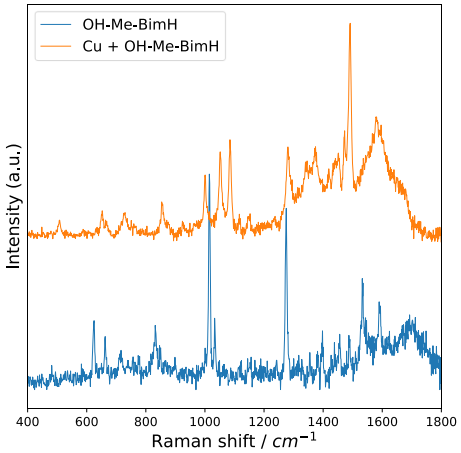

Figure A2.45 Raman spectrum of OH-Me-BimH powder (bottom), pure Cu surface after 60 days' immersion with added 1mM OH-Me-BimH (top).

Appendix 3: Corrosion on CuZr alloys. Supplemental information.

Table A3.7 $Cu_{40}Zr_{60}$ Crystalline Tafel Parameters (cf. **Figure 6.6**).

Solution	E_{corr} (mV) vs. Ag/AgCl	j_{corr} （μA/cm^2）	$-\beta_c$ (mV/dec)	βa (mV/dec)
3 wt.% NaCl	−405	0.117	105	174
ImiH	−402	0.152	86	185
SH-ImiMe	−494	8.737	133	141
SH-ImiH-4Ph	−429	0.256	45	306
SH-BimH	−530	0.100	299	177
SH-BimH-5OMe	−425	0.304	35	285
SH-BimH-5NH_2	−439	0.529	74	296
Me-S-BimH	−370	0.263	17	230
OH-BimH	−471	2.502	65	215
OH-Me-BimH	−443	1.406	42	218

Table A3.8 $Cu_{40}Zr_{60}$ Amorphous Tafel Parameters (cf. **Figure 6.6**).

Solution	E_{corr} (mV) vs. Ag/AgCl	j_{corr} （μA/cm^2）	$-\beta_c$ (mV/dec)	βa (mV/dec)
3 wt.% NaCl	−493	0.053	194	216
ImiH	−515	0.061	226	231
SH-ImiMe	−737	0.003	239	173
SH-ImiH-4Ph	−656	0.003	199	194
SH-BimH	−690	0.007	210	193
SH-BimH-5OMe	−690	0.010	202	192
SH-BimH-5NH_2	−662	0.005	229	202
Me-S-BimH	−679	0.006	187	206
OH-BimH	−480	0.091	324	242
OH-Me-BimH	−778	0.002	266	201

Table A3.9 $Cu_{50}Zr_{50}$ Crystalline Tafel Parameters (cf. **Figure 6.11**).

Solution	E_{corr} (mV) vs. Ag/AgCl	j_{corr} （μA/cm^2）	$-\beta_c$ (mV/dec)	β_a (mV/dec)
3 wt.% NaCl	−392	2.674	43	293
ImiH	−385	2.356	61	305
SH-ImiMe	−392	1.710	47	229
SH-ImiH-4Ph	−413	0.853	59	181
SH-BimH	−404	0.286	50	160
SH-BimH-5OMe	−373	0.830	24	253
SH-BimH-5NH_2	−476	1.501	133	109
Me-S-BimH	−391	1.799	54	253
OH-BimH	−411	1.791	42	159
OH-Me-BimH	−397	2.652	93	292

Table A3.10 $Cu_{50}Zr_{50}$ Amorphous Tafel Parameters (cf. **Figure 6.11**).

Solution	E_{corr} (mV) vs. Ag/AgCl	j_{corr} （μA/cm^2）	$-\beta_c$ (mV/dec)	β_a (mV/dec)
3 wt.% NaCl	−485	0.014	340	250
ImiH	−551	0.020	192	225
SH-ImiMe	−601	0.006	198	188
SH-ImiH-4Ph	−596	0.003	253	168
SH-BimH	−524	0.008	181	212
SH-BimH-5OMe	−588	0.003	201	174
SH-BimH-5NH_2	−547	0.004	187	192
Me-S-BimH	−512	0.007	184	210
OH-BimH	−438	0.037	460	279
OH-Me-BimH	−443	0.033	275	250

Table A3.11 $Cu_{64}Zr_{36}$ Crystalline Tafel Parameters (cf. **Figure 6.15**).

Solution	E_{corr} (mV) vs. Ag/AgCl	j_{corr} （μA/cm^2）	$-\beta_c$ (mV/dec)	β_a (mV/dec)
3 wt.% NaCl	−460	15.044	169	101
ImiH	-	-	-	-
SH-ImiMe	−523	18.264	116	182
SH-ImiH-4Ph	−573	2.571	95	183
SH-BimH	−471	1.214	73	159
SH-BimH-5OMe	−522	1.427	94	114
SH-BimH-5NH_2	−586	5.089	89	221
Me-S-BimH	−563	3.645	110	153
OH-BimH	-	-	-	-
OH-Me-BimH	−443	6.118	52	225

Table A3.12 $Cu_{64}Zr_{36}$ Amorphous Tafel Parameters (cf. **Figure 6.15**).

Solution	E_{corr} (mV) vs. Ag/AgCl	j_{corr} （μA/cm^2）	$-\beta_c$ (mV/dec)	β_a (mV/dec)
3 wt.% NaCl	-	-	-	-
ImiH	−343	0.029	176	185
SH-ImiMe	−386	0.030	275	188
SH-ImiH-4Ph	−387	0.014	241	183
SH-BimH	-	-	-	-
SH-BimH-5OMe	−302	0.161	2	408
SH-BimH-5NH_2	−485	0.013	216	188
Me-S-BimH	−334	0.029	248	206
OH-BimH	-	-	-	-
OH-Me-BimH	−392	0.016	203	182